THREE-DIMENSIONAL MODELING OF RIP CURRENT SYSTEMS

BY

KEVIN A. HAAS

AND

IB A. SVENDSEN

RESEARCH REPORT NO. CACR-00-06
DECEMBER 2000

CENTER FOR APPLIED COASTAL RESEARCH

Department of Civil and Environmental Engineering
University of Delaware
Newark, Delaware 19716, USA

TABLE OF CONTENTS

LIST OF FIGURES

LIST OF TABLES

ABSTRACT

This thesis analyzes the dynamics of rip current systems using both laboratory experiments and numerical modeling. The experiments primarily show the depth structure of rip currents. Offshore of the channel the rip current has strong depth variations, with strong seaward velocities near the surface and weak velocities near the bottom. The depth variations are shown to be sensitive to the total volume flux in the rip.

The nearshore circulation model SHORECIRC is applied for the rip currents case in a wave basin. The time-averaged flow properties show good agreement with the measurements. It is found that higher bottom stress leads to more stable flow where the rip current meanders less and fewer eddies are generated. Similar to the experiments, the flow in the two channels is found to behave differently because of the longshore variation in the topography. The wave current interaction creates forcing which prevents the rip currents from flowing too far offshore. The flow patterns are much more stable when the 3D dispersive mixing is included.

The vertical variations of the rip currents are modeled and show good agreement with the laboratory measurements. In the rip, the vertical variation of the current is governed by the convective accelerations in addition to the bottom stress and the short-wave forcing. The interaction of the currents and the waves, which was neglected in previous versions of SHORECIRC, turns out to play an important role in the vertical variation of the rip currents outside the breakers.

Finally, a study on the effects from varying topography and wave conditions is presented. When the channels are closer, a higher percentage of the total flux

is returned by the rip currents rather than the undertow over the bar. When the shoreline is closer to the bar, less flow is returned by the rip currents. Waves with an incident angle create a longshore current which, if sufficiently large, has enough inertia to pass the channel without producing a rip current. When the waves break in the channel, the longshore variation in the setup which, drives the rip current is much weaker, thereby creating weaker rip currents.

ACKNOWLEDGMENTS

This work was sponsored by Sea Grant, under Award No NA96RG0029 and by ONR (contract no N0014-99-1-0291).

Dr. Merrick Haller is gratefully acknowledged for providing his rip current laboratory data and providing guidance for our laboratory experiments. We also acknowledge Dr. Qun Zhao for her discussions and help with the model development.

Chapter 1

INTRODUCTION

The nearshore is a dynamic area which serves as an enjoyable leisure destination and yet contains many hazards for humans. The currents and waves pose many dangers for bathers, especially rip currents. According to the American Lifesaving Association, 80% of all rescues by lifeguards at surf beaches are the result of swimmers being caught in rip currents. A better understanding of the dynamics of rip currents and the education of the public could save countless lives.

In addition, since the middle of the twentieth century, the shores and beaches of the United States have been developing at an increasing rate. As a result of this economic build up, it is becoming more important to understand coastal processes, consisting of the wind, waves and currents as well as the motion of the sediments, in order to better protect the shore. Studying sediment transport is becoming increasingly essential beyond just the application to coastal erosion. Growing concerns over the transport of hazardous materials is requiring the scientific community to make learning how to model sediment transport a priority. In the nearshore region, the longshore and cross-shore currents (including rip currents) play a major role in the sediment motion.

It is imperative from a social, economic and environmental stand point, that we continue to learn more about nearshore circulation. The purpose of this study is to advance our knowledge about rip current dynamics by using both laboratory experiments and numerical modeling.

1.1 Undertow Versus Rip Currents

In the early part of the twentieth century there was much discussion about the cross-shore flow on beaches. Most of the debate was about whether there really was any cross-shore flow in the surf. In one article, Davis (1925a) dismisses the so-called undertow as a myth. He attributes the claims of this strong offshore current to poor swimmers being knocked down by large wave crests and being caught in the seaward flow within the wave trough. Jones (1925) replied that he agreed with Davis, arguing that undertow cannot exist because there is no shoreward flow in the water column and therefore continuity dictates that there cannot be any seaward flow.

Not everyone agreed with Davis. Quirke (1925) wrote that there are different types of waves and in the surf, "roll waves" carry water shoreward which must be balanced by a return flow, the undertow. In addition he gave a geological argument based on sediment distribution in the surfzone. Several other people replied based on personal experiences including Craig (1925) who had experienced a large cross-shore current created by a pier turning the longshore current seaward on a beach in Lake Michigan. Brant (1925) described strong offshore currents on a pocket beach on the west coast and Hite (1925) said that onshore winds push water towards the shore which is then returned to sea in narrow "rivers" of seaward flow.

Davis (1925b) replied to these observations of strong return flow and claimed that the localized return flow should not be called undertow. The discussion about undertow was laid to rest for more than a decade until Shepard (1936) described the rivers of return flows as rip currents replacing the name rip tides used by the general public. He described rip currents as largely being a surface phenomenon with eddying motion in the outer portion. He claimed that rip currents were responsible for draining the nearshore region and not the so-called undertow.

The argument over undertow was not through yet; Evans (1938) measured

return flows in ponds and lakes relating them to undertow in the surf. Shepard and LaFond (1939) responded with measurements of their own along the Scripps pier. They said that the strong offshore currents measured were not undertow because the velocity was never strong near the bottom but rather was confined near the surface like a rip current. However, they did call for more measurements under different conditions and locations.

Today the existence of undertow is generally accepted and it has been measured in the field by Wright *et al.* (1982), Guza and Thornton (1985), Greenwood and Osborne (1990) and Dyhr-Nielsen and Sørensen (1970) to name a few. It has been analyzed theoretically by Svendsen (1984b), Dally and Dean (1984), Svendsen *et al.* (1987), Svendsen and Hansen (1988), Okaysu *et al.* (1988) and Putrevu and Svendsen (1993) and recently by Garcez Faria *et al.* (2000) and Rattanapitikon and Shibayama (2000) among others. When considering undertow on a coast that also features rip currents, the old debate about how much flow is returned in undertow versus rip currents is not resolved yet, although Svendsen and Haas (1999), Svendsen *et al.* (2000) and the present study shed some light on this area.

1.2 Field Observations of Rip Currents

The first comprehensive documentation of rip currents and their circulation patterns in the field was given by Shepard *et al.* (1941). They describe the intermittent nature of rips and their tendency to become surface currents along the coast in southern California. In addition they note that rips are more pronounced during low tide and are increased in strength as the wave heights increase. Additional studies by Shepard and Inman (1950) notice that rips tend to have instabilities at multiple time scales. They also directly measured the vertical structure of rips using floats and triplanes finding that the current outside the breakers is much stronger at the surface than near the bottom. Shepard and Inman (1951) outlined a general study

on nearshore circulation in the San Diego area where they looked at currents on an open coast, near a submarine canyon and close to structures.

McKenzie (1958) described observations of rip currents on beaches in New South Wales, Australia. He relates the rip currents to the wave conditions and found that light and moderate swell conditions lead to numerous but weak rip currents whereas heavy swell leads to a few large rip currents. Sonu (1972) used observations from aerial photographs on beaches in Florida to describe meandering and pulsating rip currents. Using a bi-directional current meter he found that the absence of velocities in the lower half of the water column outside the breakers implied that rips had vertical structure. Cook (1970) observed rips in southern California and gave scenarios of wind and wave conditions under which rips were formed. Vos (1976) gave observations and a schematic analysis of short-lived transient rip currents in Western Australia.

Based on observations of rips in New South Wales, Australia, Short (1985) created classifications of two basic types of rip currents, erosion and accretion rips. Erosion rips are strong currents which are spatially and temporally unstable. Large erosion rips are classified as mega rips when only one or two rips drain the entire surfzone. On the other hand, accretion rips are weaker and much more stable with shorter spacing between rips. Typically a storm creates erosion type rips which become mega rips under strong enough wave conditions. Over time, as the wave conditions decrease, the rips become accretion rips and stay in their own channels until the channels are filled.

A large number of observations on numerous beaches in southeastern Australia are listed by Wright and Short (1984). They determine the state of the beach as to whether it is reflective or dissipative or somewhere in between. They identify the features of each beach state and document the transitions between the different beach states. A study on the Island of Sylt in the North Sea by Dette *et al.* (1995)

describes how the incident angle of the short waves is important in determining whether or not rip currents will be present. Smith and Largier (1995) used a sector scanning Doppler sonar to measure rip currents near the Scripps pier. Because they were able to obtain velocities over a large region, they found that the rips were episodic and were able to see vortices detach near the rip head.

Rip currents observed in Denmark by Aagaard *et al.* (1997) were found to depend on the degree of dissipation by the short waves, i.e. when the wave dissipation was weak the rips did not form or were weak. Brander (1999) measured rip currents on Palm Beach in Australia. He found that geometrical changes affected the rip flow. For example, reducing the cross-sectional area of the rip channel would increase the peak velocity in the rip. In addition he found that rips were tidally modulated such that they were stronger at low tide. Rip currents were observed at many other locations around the globe including Israel (Bowman *et al.*, 1988a,b, 1992), Jamaica (Huntley *et al.*, 1988) and India (Chandramohan *et al.*, 1997).

Measurements in the field are frequently of a qualitative nature, where only the location and the number of rips are noted. Several studies (i.e. Shepard and Inman (1950) and Sonu (1972)) note that rip currents have vertical structure and become surface currents outside the breakers However, this is based on discussions with lifeguards or inferred from measurements at single locations. Because of the lack of field measurements of rip currents the present study does not provide direct comparisons with rips in the field, but does compare the qualitative features such as meandering and eddy generation.

1.3 Theoretical Developments for Rip Current Dynamics

The first theoretical study of rip current dynamics was done by Arthur (1962) in which the vorticity equation was derived from the shallow water equations. Based upon the conservations of potential vorticity, the vortex stretching was found to be responsible for the rip current becoming narrower as it flowed offshore. Therefore,

the nonlinear inertial terms are of utmost importance in rip currents. Recently, the theoretical development and transport of the vorticity derived by Peregrine (1998, 1999) and Peregrine and Bokhove (1998) showed that the generation of the vorticity was linked to the breaking pattern in a well defined way.

Dalrymple (1978) created two basic classifications of the mechanisms for generating rip currents, wave interaction models and structural interaction models. The wave interaction models contain mechanisms such as edge waves interacting with incoming short waves, interacting wave trains and wave-current interaction models. The structural interaction models include rips created by the bottom topography and coastal structures.

In a pioneering paper, Bowen (1969b) showed that rip currents can be generated on a plane beach by longshore variations in the wave height. The larger waves generate a larger setup which drives water towards a rip current flowing seaward through the smaller setup generated by the smaller waves. Dalrymple (1975) identified a mechanism for generating the longshore varying conditions necessary for driving rips on an open coast, by deriving the expressions for the setdown and setup of two intersecting wave trains.

Wave current interaction was modeled by LeBlond and Tang (1974) by incorporating the energy exchange between the waves and rip current. They find that the energy exchange does not change the dynamics of the rip current systems, it only reduces the forcing for the rips resulting in weaker currents. Dalrymple and Lozano (1978) included refraction of the waves by the current which they claim is necessary to generate rip currents. These theories show that the wave current interaction can contribute to rip currents, however they make no mention of how the rips are initiated.

A simple model for rip currents on a barred beach with rip channels was derived by Dalrymple (1978). In this model, the waves are breaking over the bar,

creating a setup, but not in the channel which leads to a longshore pressure gradient driving the flow from behind the bar to the channels. The dynamics of rip current systems were also modeled by Tam (1973) using a similarity solution for the shallow water equations. The rip current cross-sections were found to be realistic. The rip head formation is linked to a sudden increase in the water depth or attributed to the rip encountering an opposing current such as a coastal current. In addition, he analyzes the turning of rips due to the entrainment of longshore flow. Similarly, Sasaki (1985) used the similarity solution while keeping more of the non-linear terms.

The theory for the formation of rip currents and beach cusps on a plane beach was derived by Hino (1974) using linear instability theory. He found that beach cusps were formed and the preferred wave length of the cusps was around four times the distance from the breakers to the shoreline which agreed well with the field data. Miller and Barcilon (1978) derived a model for circulation on a gently sloping plane beach with normal incident waves using steady linear stability theory. The eigen-wavenumbers, which represent the distance between rip currents, was found to depend on the rate at which the waves are dissipated as well as the bottom friction factor.

The formation of channels on a barred beach was analyzed by Deigaard (1990) through the use of linear instability analysis of the flow and sediment equations. He found that the spacing of the channels was similar to the distance from the bar to the shoreline. Deigaard *et al.* (1999) used a linear instability analysis on a barred beach with both normal and oblique incident waves. They found that an increase in the longshore currents lead to an increase in the preferred spacing between rip channels. In addition, they found that an increase in friction or lateral mixing gave a decrease in the spacing of the channels.

Huntley and Short (1992) found that the observed spacing between rip currents on Australian beaches was predicted well when the surf zone width was calculated based on the wave conditions and a profile model rather than estimated from visual observations. Zyserman *et al.* (1990) predict the spacing between rip channels based on an overall sediment balance.

Hence, much theoretical work on rip current dynamics has been done the past few decades using a variety of methods. Because rip currents are generated under different conditions, no one theory correctly predicts all types of rip currents. The present study enhances the previous work by using a more advanced model which allows for features such as unsteady and depth varying rips.

1.4 Laboratory and Numerical Modeling of Rip Currents

Because it is difficult to measure rip currents in the field, laboratory experiments are frequently used to obtain extensive measurements of rip current systems. One of the earliest rip current experiments was done by Bowen and Inman (1969). They used normally incident waves on a plane beach to generate edge waves which created the longshore variation required to create rip currents as theorized by Bowen (1969b). They found that usually only one edge wave mode would dominate the circulation.

Hansen and Svendsen (1986) pointed out that part of the shoreward flux over a longshore bar returns as undertow and part feeds the rip. A series of two-dimensional experiments in a wave flume simulated different amounts of net flux passing over the bar. The mean water level was found to have small variations for the different shear stresses associated with the various net fluxes over the bar because the shear stress was small relative to the cross-shore radiation stress forcing. Svendsen and Hansen (1986) used a two-dimensional numerical model to simulate the same situation which showed that the setup had little variation for the different current cases.

There have been experiments of plane jets in shallow waters, notably Giger *et al.* (1991) and Dracos *et al.* (1992). In these experiments the jet is unstable characterized by meandering and counter rotating vortices. In addition the velocities were typically depth uniform, contrary to the vertical variations found in typical rip currents.

The most comprehensive laboratory measurements of rip currents to date was done by Haller *et al.* (1997b,a) and Haller and Dalrymple (1999). These measurements were done in a directional wave basin with a longshore bar and two rip channels. The velocity and water level were measured inside the channel and behind the bar creating a clear picture of the circulation pattern of the rip current system. The rip currents were found to be unstable and this was related to the instabilities of a jet.

The vertical variation of rip currents has been measured in a few laboratory experiments. Sasaki (1985) measured the vertical variation of rip currents on a steep plane beach for normally incident waves where edge wave modes were excited. These measurements show little depth variation for the generated rip currents. Rip currents in a closed basin created by longshore currents encountering the side wall were measured by Wind and Vreugdenhil (1986). In this situation the rip current was bounded by the side and offshore walls. The vertical profiles showed weak depth variations where the current close to the surface was slightly larger than the current below. Drønen *et al.* (1999) ran an experiment with half of a rip channel and a longshore bar in a wave flume. The focus was on the depth variation of the flow inside the channel where the currents were mainly depth uniform.

The present study includes experimental measurements of the vertical variation of rip currents for the same conditions as Haller and Dalrymple (1999). The difference between the present measurements and the previous efforts are that unlike Sasaki (1985), these measurements are for topographically generated rip currents.

In addition the rips measured by Wind and Vreugdenhil (1986) were along the side wall and never were unbounded. The measurements by Drønen *et al.* (1999) were primarily in the channel whereas our measurements extend far outside the breakers.

Noda (1974) presented a circulation model for currents on a beach with longshore varying topography. The model is based on the shallow water equations and is solved for steady conditions. Both normal and oblique wave incidence are used and optimistic comparisons with field data are made. Numerical simulations by Tanaka and Wada (1984) were for cases of nearshore circulation with rip currents present. Sørensen *et al.* (1994) used a Boussinesq model to simulate the experiments by Hamm (1992) of directional nearshore waves propagating over a rip channel. Another Boussinesq model was used by Chen *et al.* (1999) to model the rip currents from the experiments by Haller and Dalrymple (1999). Sancho *et al.* (1995) found that small rip channels in longshore bars lead to longshore pressure gradients which are necessary for driving rip currents. Haas *et al.* (1998) models the experiments by Haller and Dalrymple (1999) and is a precursor to the present work while Haas *et al.* (2000) was done in parallel.

1.5 A Brief History of Nearshore Circulation Modeling

The concept of radiation stress was first introduced by Longuet-Higgins and Stewart (1962, 1964). The radiation stress was defined as the excess momentum flux due to the presence of waves. The radiation stress concept was used to theoretically model longshore currents by Longuet-Higgins (1970a,b), Bowen (1969a) and Thornton (1970).

The first numerical model for nearshore circulation was developed by Noda (1974). This model was for steady flow with longshore varying topography and was used successfully to model circulation patterns with rip currents. Some other notable early nearshore circulation models were by Ebersole and Dalrymple (1980), Wu and Liu (1985) and Wind and Vreugdenhil (1986).

The preceding models were all two-dimensional horizontal models (2DH) which essentially solve the shallow water equations. Development of the quasi-3D models began with De Vriend and Stive (1987) who divided the currents into primary and secondary components. The primary current was forced by the depth-invariant terms (i.e. the pressure gradient) while the secondary current was driven by the depth varying forcing. Alternatively, Svendsen and Lorenz (1989) assumed the cross-shore and longshore currents were weakly dependent on each other resulting in a current profile with a spiral shape. Svendsen and Putrevu (1990) solved for the vertical profiles analytically and used the result in a depth-averaged numerical model. This approach has since formed the basis for the development of the SHORECIRC (SC) model used in the present study. Sanchez-Arcilla *et al.* (1990, 1992) used a similar approach.

Svendsen and Putrevu (1994) found that the current-current and wave-current interaction terms were inducing non-linear mixing many times stronger than the turbulent mixing from wave breaking. A generalized version of these mixing terms were derived by Putrevu and Svendsen (1999) and is used in the present study. A simplified version of the 3D dispersive mixing is included in the original version of the nearshore circulation model SC first presented by Van Dongeren *et al.* (1994) and thoroughly documented by Van Dongeren and Svendsen (1997, 2000).

Further studies with nearshore circulation models have been done with SC and other models including Sancho and Svendsen (1997), Briand and Kamphuis (1993), Garcez Faria *et al.* (1995), Özkan-Haller and Kirby (1999), Slinn *et al.* (2000) and Van Dongeren and Svendsen (2000). Péchon *et al.* (1997) present an intercomparison between 7 European nearshore circulation models. The flow behind a breakwater is modeled and compared with data from a laboratory experiment. Recently Boussinesq models have been used to model nearshore circulation such as Madsen *et al.* (1997a,b), Sørensen *et al.* (1998) and Chen *et al.* (2000).

1.6 Outline of Present Work

Obviously there is much about rip current dynamics and their circulation patterns that is still unknown. The aim of the present study is to develop a better understanding of rip currents using both physical and numerical models. The goal of the numerical modeling is not to just match the experimental data but to learn more about the physics of rip current systems.

In Chapter 2 we present the laboratory experiments supplementing the experiments by Haller and Dalrymple (1999). The present experiments measure the vertical variation of the rip currents inside the channel and farther offshore. In addition a comparison between the behavior of the two rip currents is made.

In Chapter 3 the governing equations for SHORECIRC are derived for the horizontal momentum as well as the vertical profiles of the currents. Brief descriptions of the closure submodels are included.

In Chapter 4 the application of SHORECIRC for the rip currents in the wave basin is presented. The chapter focuses on the two-dimensional horizontal flow patterns and provides a direct comparison between the time-averaged model results and the experimental data. The sensitivity of the flow patterns to the physical mechanisms, such as the wave current interaction, is analyzed.

In Chapter 5 the modeled vertical variations of the rip currents are presented. An idealized symmetric topography and the real topography are used for analyzing the physics for the vertical variation of the rip currents. Comparisons between the model results and laboratory data are included.

In Chapter 6 a geometrical analysis of rip current systems is presented. The effect of the geometry of the topography as well as varying wave conditions are analyzed.

The final chapter summarizes the work presented and provides the conclusions drawn from the study.

Chapter 2

VERTICAL VARIATIONS OF RIP CURRENTS: EXPERIMENTS

Predicting where and when a rip current occurs is difficult, thereby making measurements of rip currents in the field a difficult task. When measurements of rip currents are made in a controlled laboratory environment, the use of fixed topography makes predicting the location of rip currents trivial.

This chapter discusses the results from the laboratory rip currents experiments which we performed. These experiments are an extension of the experiments first presented by Haller *et al.* (1997a,b) as well as Haller and Dalrymple (1999). The goal of the presented experiments is to investigate the vertical variation of rip currents.

The first section presents the laboratory setup for the investigation, including the background information about the experiment. In addition, the physical configuration and the experimental procedure are described.

The last section describes in detail the purpose of each experimental series. The results and in depth analysis for all the tests are provided in separate subsections. The final subsection summarizes the results of the four test series.

2.1 Experimental Setup

The laboratory experiment was performed in the directional wave basin located in the Ocean Engineering Laboratory at the University of Delaware. Details

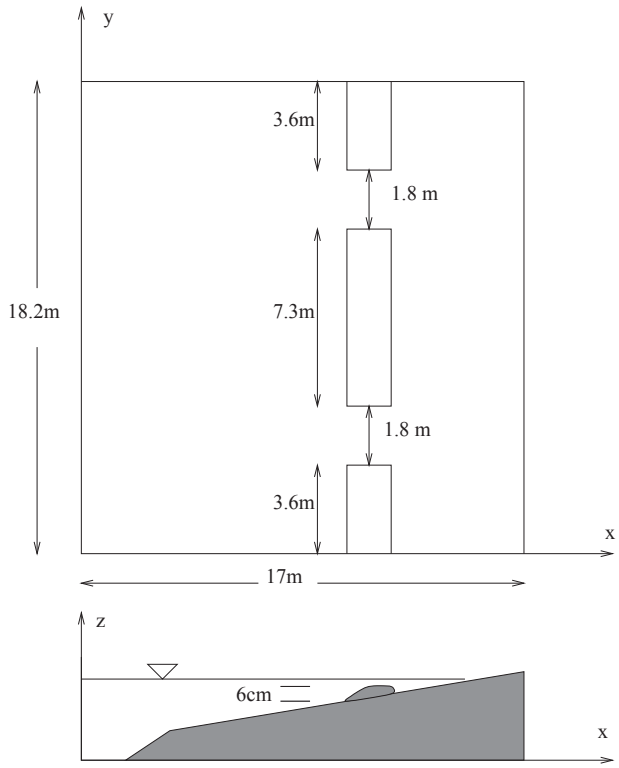

Figure 2.1: Design Topography.

about the designing and building of the experimental setup are found in Haller *et al.* (2000).

The design of the wave basin is seen in Figure 2.1. The waves are created by a multi-paddle wave maker located at the toe of a steep 1:5 slope preceding a milder 1:30 slope. A longshore bar of height 6 cm with two channels is centered about 11.8 m from the offshore wall and the two channels are approximately 1.8 m wide.

The original experiments by Haller and Dalrymple (1999) primarily focused on obtaining information about a horizontal spatial overview of the rip current circulation pattern. At most locations, measurements are only available for one depth which is selected to give a good representation of the depth-averaged currents. The time-averaged velocity vectors from these experiments are seen in Figure 2.2.

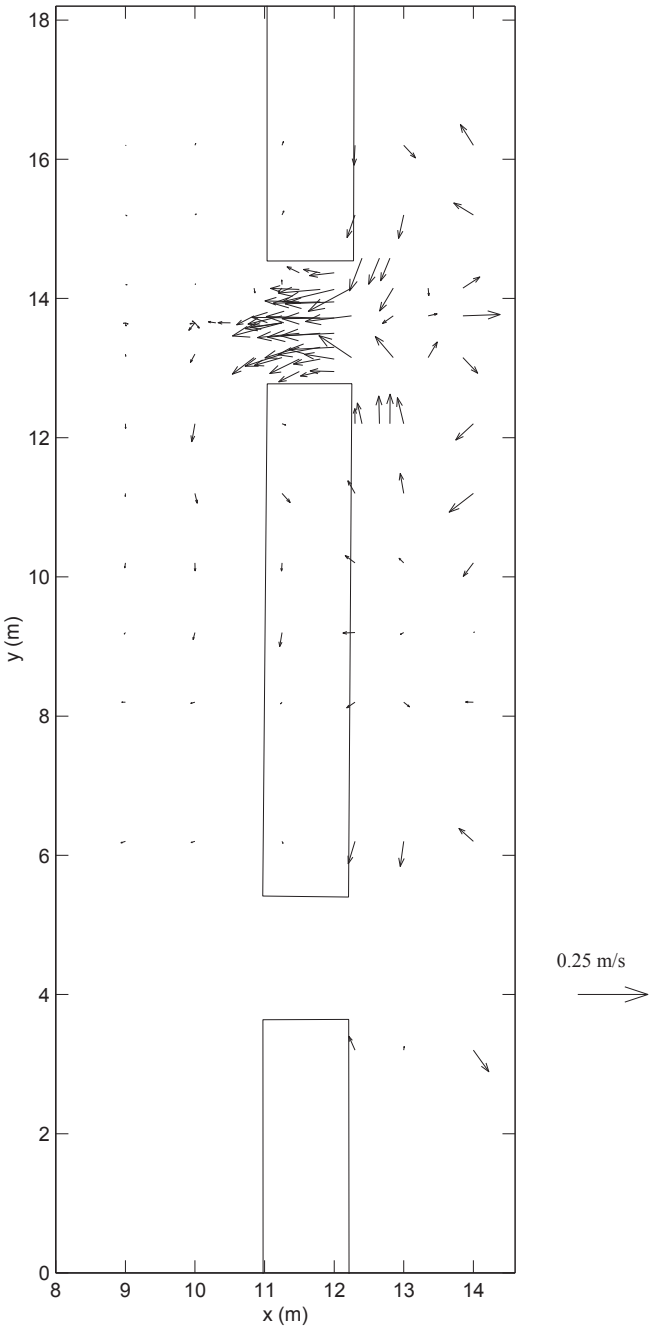

Figure 2.2: Time-averaged velocity vectors from Haller *et al.* (1997a,b).

The measurements span a large portion of the wave basin, providing a good spatial description of the rip current system. The primary focus lies within one of the rip channels, indicated by the dense number of measurements within that channel.

Because SHORECIRC calculates the depth varying currents, more information is needed about the depth variation of the rip currents to verify the numerical model. In the literature, such as Shepard and Inman (1950) and Sonu (1972), there are indications that although rip currents tend to be depth uniform inside the surf zone, outside the breaker rip currents tend to become surface currents. Measurements reported here are focused inside and offshore of the rip channel in order to learn about the evolution of the rip as it flows offshore. The purpose of the experiments is to gain understanding of the vertical variation of the rip currents. In addition, information is obtained about the temporal variation for the vertical profiles of rip currents. The goals are accomplished by performing experiments which supplement the experiments by Haller and Dalrymple (1999).

2.1.1 Instrumentation

The waves are generated by a multi-paddle wave maker consisting of 34 flap-type paddles using the Designer Waves theory by Dalrymple (1989). Shore normal wave conditions are used for all tests, therefore, the sidewall reflection aspect of the theory is not utilized.

Three Sontek Acoustic Doppler Velocimeters (ADV's) are used for measuring the velocities. The three ADV's are side-looking two-dimensional probes. The ADV's are mounted on a movable carriage in an arrangement indicated in Figure 2.3 such that they are as close to each other as possible ($\sim$ 7 cm). In order to measure the depth variation of the current, the probes are put at three different depths. The offshore gage (ADV 0) is placed near the bottom, the middle gage (ADV 1) is placed near the surface just below the trough level of the waves and the shoreward gage (ADV 2) is placed close to mid-depth. The measurements from the

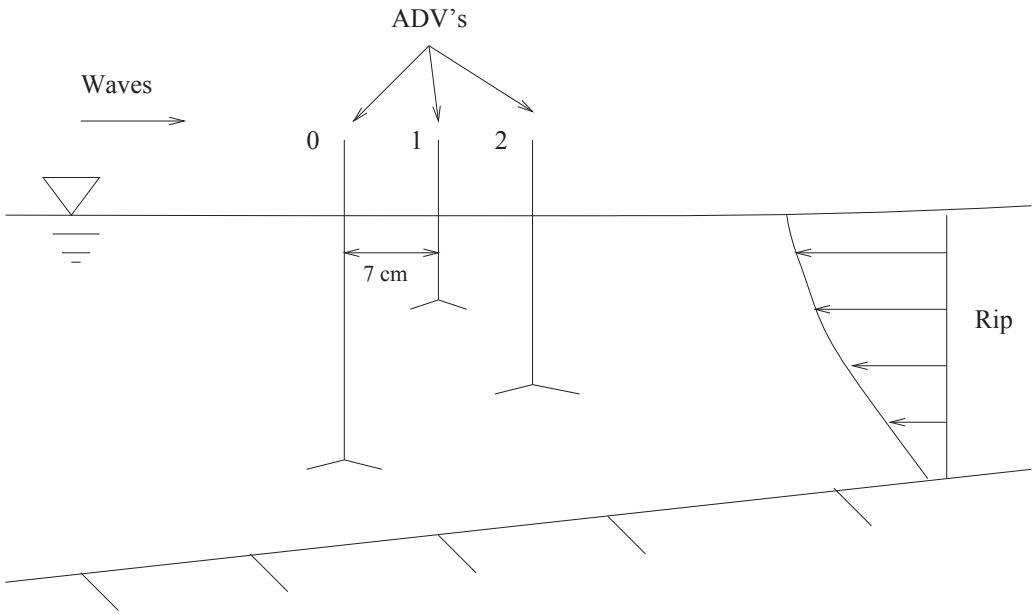

Figure 2.3: Setup for the ADV's.

three gages are used together to provide a vertical profile of the current assumed to be taken at the location of ADV 1.

The ADV's are placed and oriented by hand and the locations are measured with a ruler based upon markings on the bottom of the basin, which were determined from a prior survey of the basin. The depth of each gage and the still water level (SWL) at the center gage are measured with a ruler. The ADV's do not require any calibration.

The water level is measured using ten capacitance gages. These gages have a nearly linear voltage response to changes in the water level. Using the linear relationship allows for conversion of the voltage to water levels. The wave height as well as the mean water level (MWL) are extracted from the time series produced by these gages. Eight of the gages are mounted in a longshore row on a movable bridge. One gage is mounted on the same carriage as the ADV's providing water level measurements close to the velocity measurements. The final gage is located

offshore on a tripod providing wave height measurements which are used to verify repeatability of the experiments. The location of the gages are measured using a ruler. The gages require calibration to determine the slope of the voltage response. Every gage is calibrated daily prior to any measurements and recalibrated anytime they are relocated.

The capacitance gages are wired to the mainframe in the control room. The ADV's are hardwired into a data acquisition PC located next to the wave basin. The PC is linked to the mainframe by a cable, allowing the data acquisition to be synchronized. All data is recorded with a frequency of 10 Hz.

2.1.2 Procedure

The water level is checked and adjusted daily, prior to running any experiments, to maintain consistent depths. Next a few waves are run to stir up sediment and provide water motion. The ADV's are tested to ensure they are working properly. Once the water becomes still, the capacitance gages are calibrated. The following procedure is used for every test run to ensure consistency in the results.

1. Place all the capacitance gages and the ADV's at the desired locations.
2. After the water becomes still, calibrate the capacitance gages if they have been moved.
3. Take still water measurements for 1028 time steps at 10 Hz (102.8 seconds) with the capacitance gages in order to provide a zero reference level.
4. Start the waves and all data acquisition. The capacitance gages take 16384 data points at 10 Hz (27.3 minutes) while the ADV's are allowed to run longer if a rip current is present.
5. Once the basin oscillations have ceased the still water level is measured again.
6. Start over with step 1.

2.2 Experimental Results

Four series of tests are presented in this section and are divided as follows.

- Series R is the initial test series with wave conditions matching Haller and Dalrymple (1999) test B. The purpose of the velocity measurements is to cover a broad area in and offshore of the rip channel and provide an overview of the vertical variation of the rip.

- Series S has the same wave conditions as Series R. More detailed velocity measurements are taken along the centerline of the channel. Only enough wave measurements to verify repeatability are taken.

- Series T has larger wave conditions which do not specifically match any tests from Haller and Dalrymple (1999), therefore, a wide range of wave measurements are performed to get a broad view of the wave field. The velocity measurements are along the centerline of the rip channel.

- Series U has the same wave conditions as series R and S. Velocity and wave measurements are taken in each rip channel simultaneously to establish whether the two rips behave similarly and interact with each other.

All experiments have one offshore wave gage which is not moved to check repeatability of the tests. The individual waves heights are determined using a zero up-crossing method. These individual waves heights are averaged together to produce the mean wave height (H_m). The experiments are deemed repeatable if the offshore mean wave height has a low percent variation between realizations. The repeatability of the experiments is summarized in Table 2.1. The test series all have variations below 3%, therefore we believe the experiments are repeatable.

Test series R, S and U are designed to match series B from Haller and Dalrymple (1999). Series B has an offshore mean wave height of 4.11 cm. The last

Table 2.1: Repeatability of the experiments based on wave measurements at the offshore gage with the number of realizations n, the test name, the offshore mean wave height (H_m), the standard deviation (σ_H), the percent variation within each series and the percent variation from Haller and Dalrymple (1999) test B listed.

n	Test	H_m (cm)	σ_H (cm)	% var	%var B
18	R	4.04	0.08	2.0	1.7
30	S	4.06	0.07	1.7	1.2
16	T	5.79	0.12	2.1	n/a
4	U	4.20	0.12	2.8	2.2

column in Table 2.1 indicates that the percent variability between the present tests and Haller and Dalrymple (1999) is low. Therefore, we feel that we are reproducing the results from test series B.

2.2.1 Test R: Initial Test Series

The purpose of this series is to provide a broad overview in and offshore of the rip channel of the vertical variation of the rip. The locations of the measurements for Test R are shown in Figure 2.4. Each (x) in the figure represents the location of the ADV array comprised of the three ADV's as previously described. Each (x) on Figure 2.4 represent individual runs of the same experiment. The ADV arrays are located along 3 separate cross-shore lines containing 6 measurements each resulting in 18 total runs. This covers a broad range within and seaward of the channel.

The circles (o) in Figure 2.4 represent individual wave gages. One wave gage is always located offshore ($x = 6$ m, $y = 16.2$ m) and is used to check repeatability of the experiments. In order to provide water level data close to the current measurements, another wave gage is always placed close to the ADV array. Finally, 5 wave gages are placed on a bridge spanning the longshore direction which is located shoreward of the bar for half of the runs and seaward of bar for the rest of the runs. Tables giving the exact location for all gages are in Appendix A.

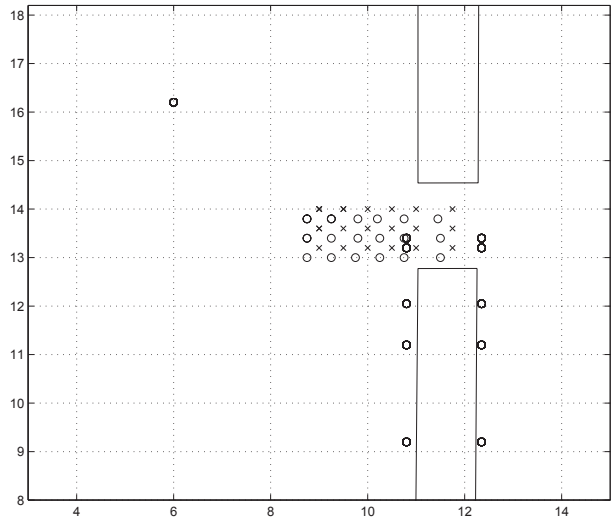

Figure 2.4: Location of the gages for Test R where (x) indicates ADV gage array locations and (o) indicates wave gage locations.

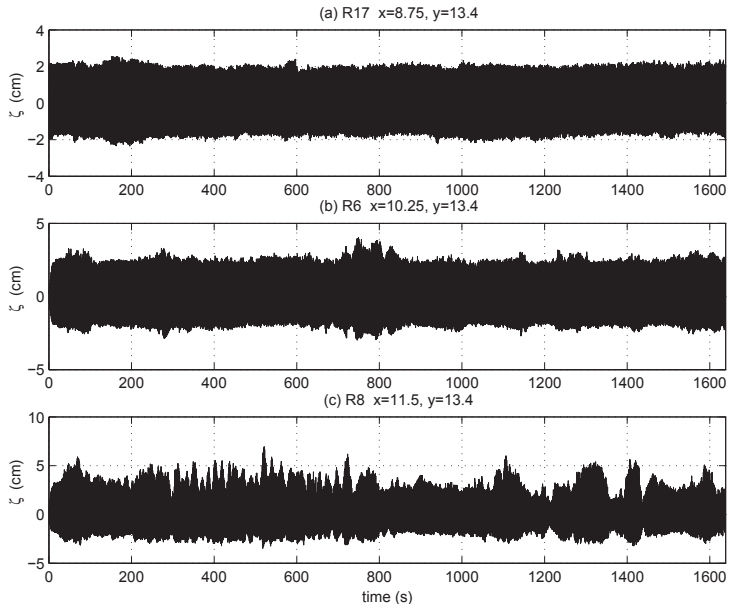

Figure 2.5: Raw water level (ζ) time series along the centerline of the channel. Subplot (a) is run R17 ($x = 8.75$ m), (b) is R6 ($x = 10.25$ m), and (c) is R8 ($x = 11.5$ m).

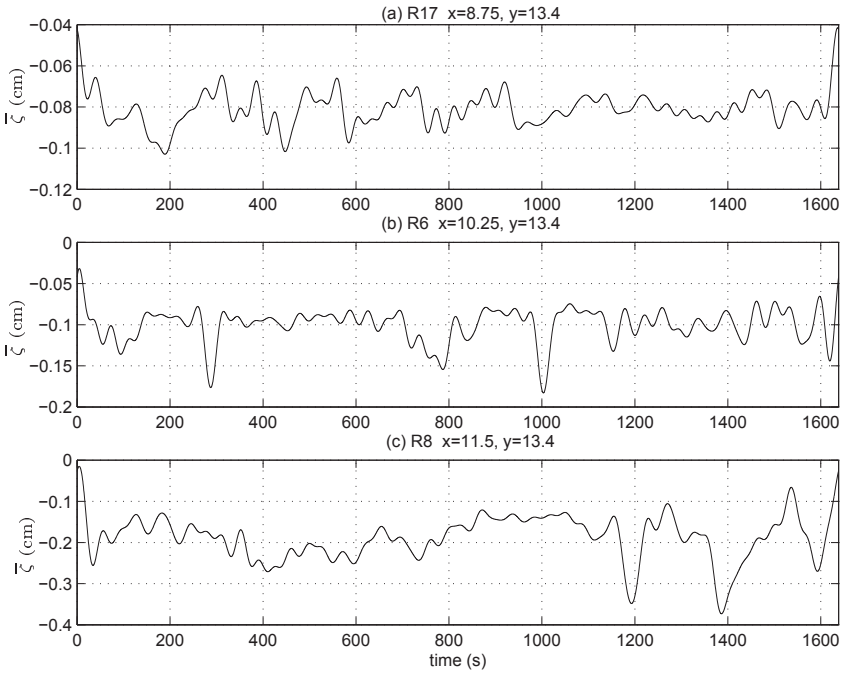

Figure 2.6: Low-pass filtered water level ($\overline{\zeta}$) time series along the centerline of the channel. Subplot (a) is run R17 ($x = 8.75$ m), (b) is R6 ($x = 10.25$ m), and (c) is R8 ($x = 11.5$ m).

The time series of the raw data for the water surface measurements (ζ) next to the velocity measurements for three runs are shown in Figure 2.5. The time series are from runs located along the centerline of the channel and range in the cross-shore direction from (a) 2.25 m offshore of the bar to (c) inside the channel. The signal for the short-waves causes the time series to take the appearance of thick solid blocks because the short-wave oscillations are not resolvable in the graphics. Nonetheless, indications of unsteady motion with longer time scales are evident. The time series in (a), the farthest location offshore, appears to be fairly steady with few minor variations. On the other hand, the time series in (c), for the location inside the surfzone, is unsteady with varying durations.

To facilitate analysis, the time series are low-pass filtered to remove the signal

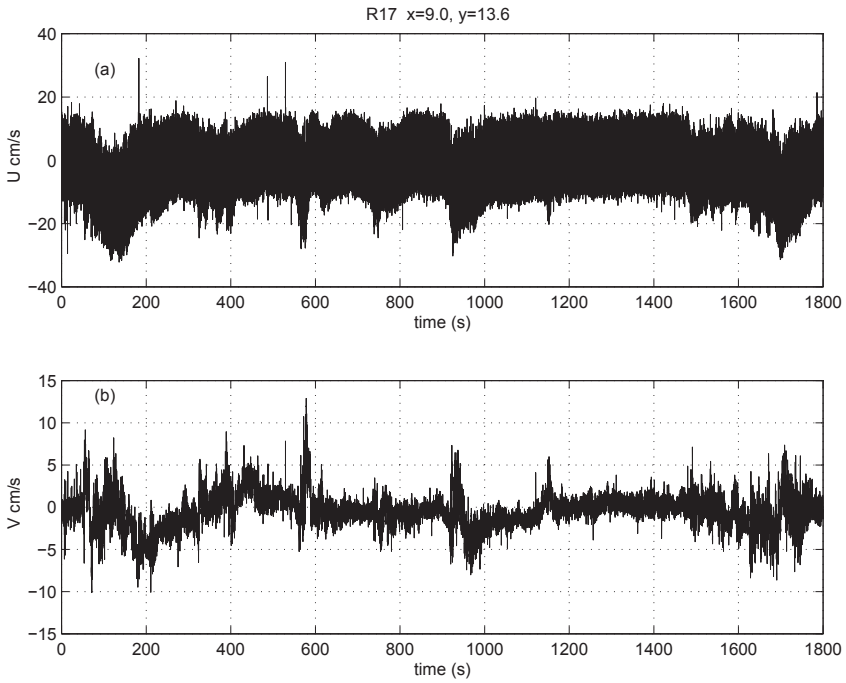

Figure 2.7: Raw velocity time series of cross-shore (a) and longshore (b) velocities for run R17 ($x = 9$ m, $y = 13.6$ m).

from the short-waves. The low-pass filter is accomplished by Fourier transforming the time series, setting the coefficients for frequencies above 0.03 Hz to zero and inverse transforming back to the time domain. The low-pass filtered time series is shown in Figure 2.6. The variation in the mean water level becomes apparent in this figure. Even the time series far offshore (a) has unsteady motions, although the amplitude of the variations offshore is much smaller than the variations inside the surfzone (c). It should be noted that the three time series shown in Figures 2.5 and 2.6 are from different test runs so no direct comparisons at specific times are possible.

The raw velocity time series measured close to the water surface along the centerline of the channel, 2 m offshore of the bar, is shown in Figure 2.7. Subplot (a) shows the cross-shore velocity (U) and (b) shows the longshore velocity (V). Similar

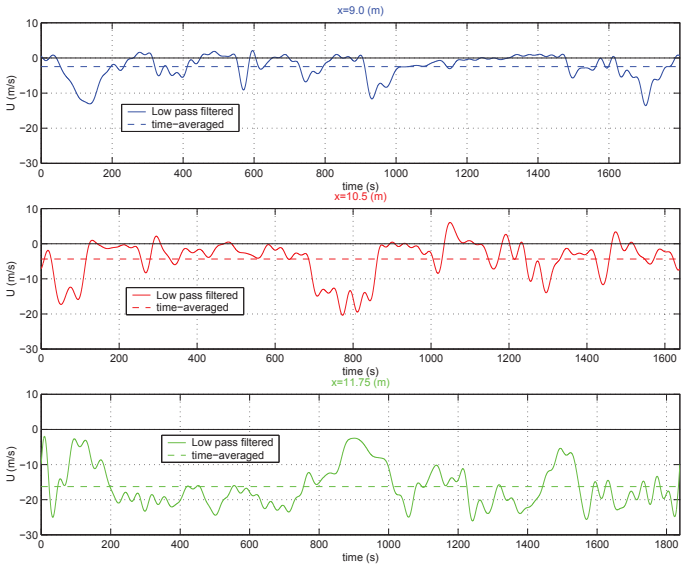

Figure 2.8: Low-pass filtered velocity time series with the long-term time-average along the centerline of the channel. Subplot (a) is run R17 ($x = 9$ m), (b) is run R6 ($x = 10.5$ m) and (c) is R8 ($x = 11.75$ m)

to the water level time series, the oscillations caused by the short-wave motion makes the signal look like a solid block. Because the waves are shore normal, the longshore signal has a relatively weak signal from the short waves. Both cross-shore and longshore velocities show plenty of variations at different time scales. Because the short-wave signal is weaker in the longshore direction, fluctuations in the longshore current are easier to view than fluctuations in the cross-shore current.

The velocity time series is also low-pass filtered to remove the short-wave oscillations. The low-pass filtered cross-shore velocity time series, measured close to the water surface, is shown in Figure 2.8 for the same three cross-shore locations as Figure 2.6. In addition, a line indicating the mean value of the current, averaged over the entire time series, is drawn on each plot (negative velocity indicates an offshore flow). These plots demonstrate that the flow in the rip varies significantly with time.

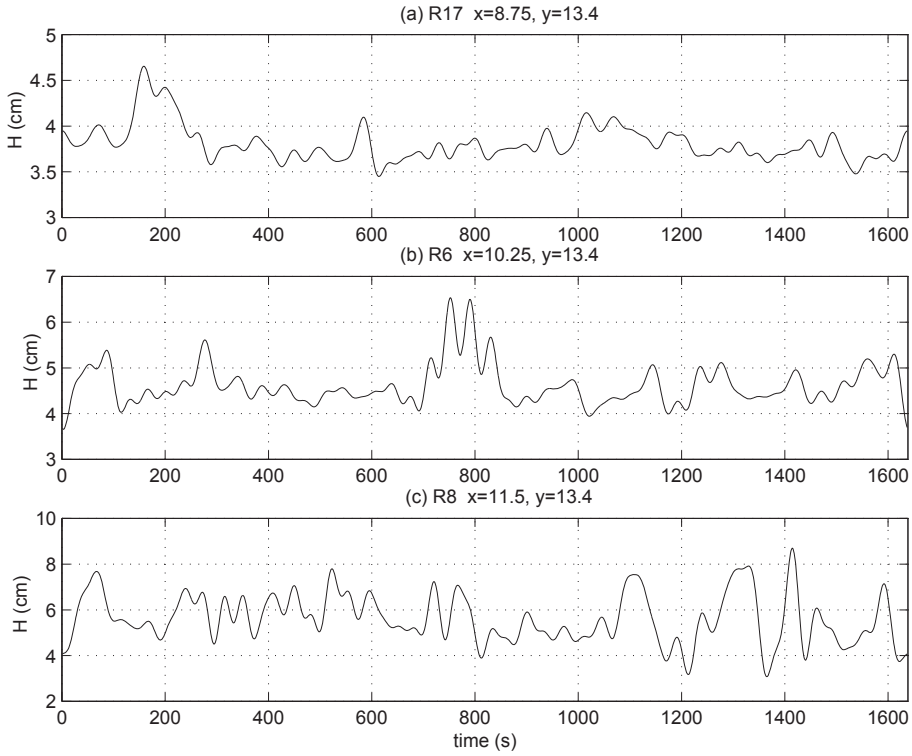

Figure 2.9: Wave height (H) time series. Subplot (a) is run R17 ($x = 8.75$ m), (b) is R6 ($x = 10.25$ m), and (c) is R8 ($x = 11.5$ m).

The offshore ($x = 9$ m) rip occurs sporadically in (a), therefore, the mean value of the velocity when averaged over the entire time period is small. The mean velocity is around 2 cm/s whereas the peak velocity in the rip reaches as high as 12 cm/s. This helps to explain why the time-averaged rip in Figure 2.2 appears to vanish offshore. Subplot (b) continues to show sporadic rip events although more frequently than in (a). Again, the mean velocity is small, reaching a value of 4 cm/s with the peak velocity being much larger, around 20 cm/s. Only the time series in the middle of the channel ((c) $x = 11.75$ m) has a mean velocity which is representative of the rip. The mean value is around 17 cm/s and the peak rip is about 25 cm/s.

At any given location the rip occurs sporadically, especially farther offshore. Even inside the channel the rip is not always present, around 100, 900 and 1500 seconds in Figure 2.8c the rip has vanished. When the rip velocity decreases in a time series it does not necessarily mean that the rip has vanished all together. The rip is moving from side to side, even inside the channel; therefore, as the rip moves past a gage, it shows up as a burst in the velocity. Visual observations during the experiments help confirm what happens to the rip. By watching the changes in the wave pattern the location of the rip is identified. The rip causes the waves to refract around the current. In addition, the wave height is increased due to the wave current interaction. We are able to watch the rip move from side to side within and offshore of the channel. There are times when the rip moves out of the channel and over the bar or even vanishes all together.

Because of the observed relationship between the wave height and the rip current, the time series of the wave height should correlate with the time series of the rip velocity. The time series of the wave height is created by using a zero up-crossing method on the water level data to identify individual waves. The wave height is calculated with

$$H = \zeta_{max} - \zeta_{min} \tag{2.1}$$

where H is the wave height, ζ_{max} is the maximum water level or the crest of the wave and ζ_{min} is the minimum water level or the trough of the wave. Because we are using regular waves with a 1 second period, the wave height time series is put through a low-pass filter eliminating all frequencies above 0.03 Hz. Figure 2.9 shows time series of the wave height along the centerline of the channel for the same locations as Figures 2.6 and 2.8. The wave heights at all three locations vary substantially over time. Comparisons between Figures 2.9 and 2.8 show that at all three x values the wave height increases when the rip velocity increases. For example, in Figure 2.8b between $t = 700$ and 800 seconds a rip current is present

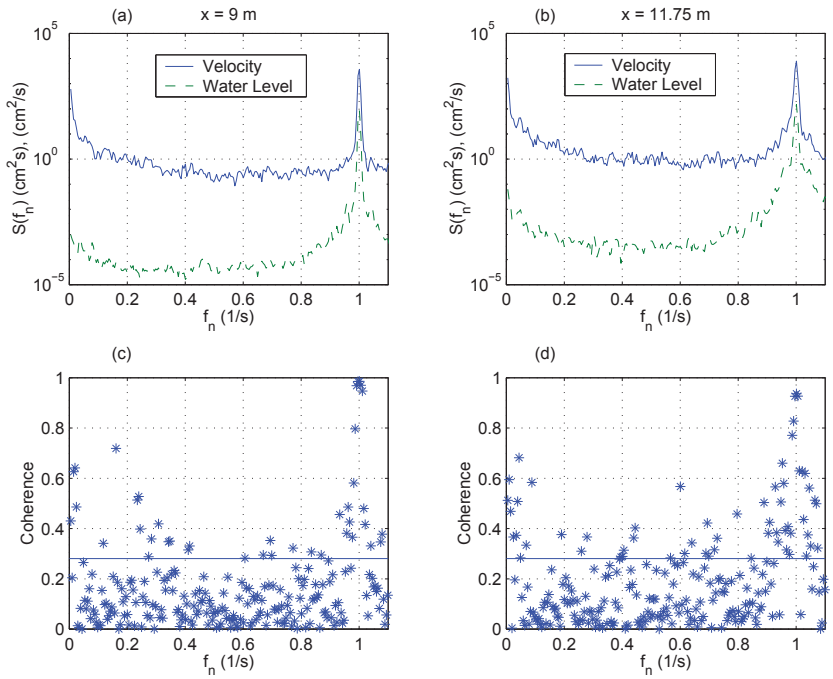

Figure 2.10: Energy spectra with 16 degrees of freedom (a and b) and coherence (c and d) for the current and water level in the rip at $x = 9$ m (a and c), and $x = 11.75$ m (b and d). The straight line indicates the limit of 90% confidence of nonzero coherence

for a long duration. Correspondingly, Figure 2.9b shows an increased wave height for the same span of time. The wave height also shows the same higher frequency oscillations superimposed on the the longer oscillation. The slight phase shift in the higher frequency oscillations results from the cross-shore and the longshore offset between the velocity and wave measurements.

The relationship between the rip current velocity and the wave height is quantified statistically by finding the coherence between the two signals. The coherence (γ_{12}^2) is defined as

$$\gamma_{12}^2 = \frac{|\Phi_{12}(n)|^2}{\Phi_{11}\Phi_{22}} \tag{2.2}$$

where Φ_{12} is the cross-spectrum and Φ_{11} and Φ_{22} are the auto-spectra defined by

$$\Phi_{12} = F_1^*(n)F_2(n) \tag{2.3}$$

with $F_1(n)$ defined as the Fourier transform of the data record containing n points and $F_1^*(n)$ defined as the complex conjugate. The coherence ranges from 0 to 1, where 1 indicates the signals are coherent and 0 indicates that the signals are statistically unrelated.

The energy spectra and the coherence of cross-shore velocity and water level for locations offshore and inside the channel are shown in Figure 2.10. The spectra are calculated using Fast Fourier Transform techniques and utilizing a Hanning window with Bartlett averaging. The resulting spectra have 16 degrees of freedom. The peak energy for both the velocity and the water level occurs at $f_n = 1$ Hz. This is expected because that is the frequency of the short waves. However, the lower frequencies ($f_n < 0.2$ Hz) also have relatively large amounts of energy for both the velocity and the water level. There is no clearly defined peak in energy for the lower frequencies because the rip current is not periodic. The rip events are sporadic, thus they show up in the spectra as broad bands of increased energy in the lower frequencies. Haller and Dalrymple (1999) found that the natural oscillation modes of the basin contribute to the low frequency energy although concentrated closer to the shoreline. Furthermore, Haller and Dalrymple (1999) found a consistent concentration of low frequency motion contained in the rip channel indicating a local source of low frequency variance.

The coherence between the water level and rip velocity is shown in Figures 2.10c and 2.10d. The wave height is part of the water level signal, therefore, this figure also represents the coherence between the wave height and the rip velocity. The straight line on the coherence plot indicates the limit of 90% confidence of nonzero coherence defined as

$$c = 1 - .1^{\frac{1}{\alpha - 1}} \tag{2.4}$$

by Thompson (1979) where α is the number of blocks used in the Bartlett averaging. Both the measurements offshore of the bar (c) and inside the channel (d) have high coherence for the frequencies around $f_n = 1$ Hz which is the frequency of the short waves. The lower frequencies, which also contain significant energy, demonstrate coherence as well. This is in the frequency range ($f_n < 0.1$ Hz) for the variations in the wave height due to the interaction with the rip currents. There is a clear coherence between the slow variation of H and U which suggest that wave current interaction plays a key role in the slow time variation of the rip currents.

Velocity measurements were taken at three depths for all locations, and time series for all three depths are examined. Figure 2.11 shows the cross-shore and longshore low pass filtered velocities for all three depths measured at the centerline of the channel, offshore of the bar at $x = 9$ m. In Figure 2.11, strong depth variations clearly exist in the cross-shore velocity. For example, around $t = 950$ seconds there is a strong rip occurrence. The cross-shore velocity closest to the surface is large, around 12 cm/s, but at mid-depth, the cross-shore velocity is smaller, only around 4 cm/s. Yet, close to the bottom, the cross-shore velocity is approximately 2 cm/s and even directed shoreward. The trend of shoreward velocity at the bottom continues throughout most of the time series, with only a few exceptions of offshore flow. Throughout this time series at the offshore location, the cross-shore velocity in the rip rarely penetrates to the bottom of the water column. On the other hand, the longshore velocity in Figure 2.11b demonstrates fairly depth uniform behavior. This eliminates the possibility of flow separation, because when flow separates from the bottom there should be similar depth variation in both the cross-shore and longshore velocities.

Similarly, Figure 2.12 shows the low-pass filtered velocities inside the surfzone at $x = 11.75$ m. The cross-shore velocities inside the channel shown in Figure 2.12a clearly indicate depth uniform flow. More depth variation occurs in the longshore

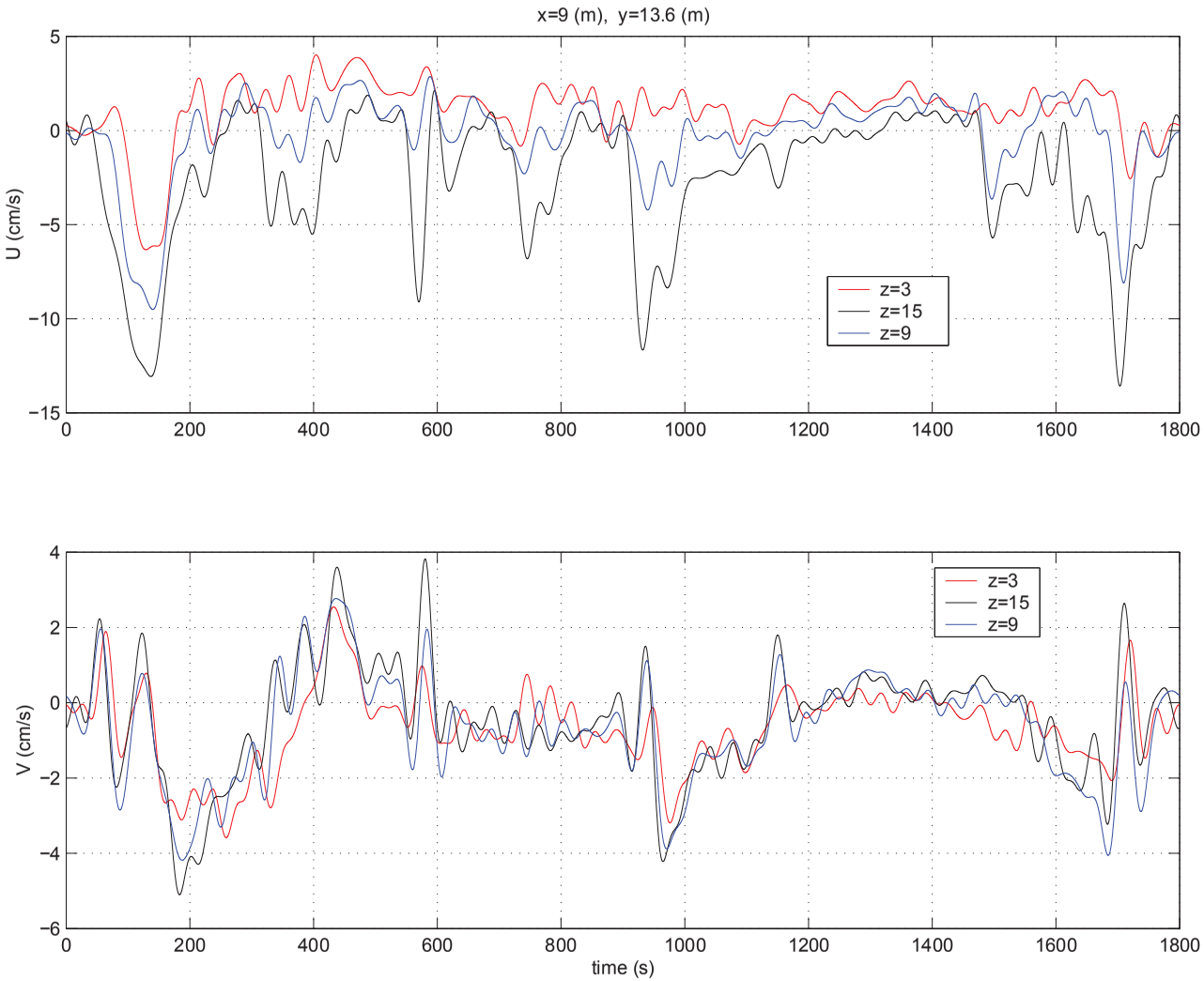

Figure 2.11: Low-pass filtered velocity time series at three depths for run R17 ($x = 9$ m). The top shows cross-shore velocities (U) and the bottom shows longshore velocities (V). z is 0 at the bottom and is positive upwards.

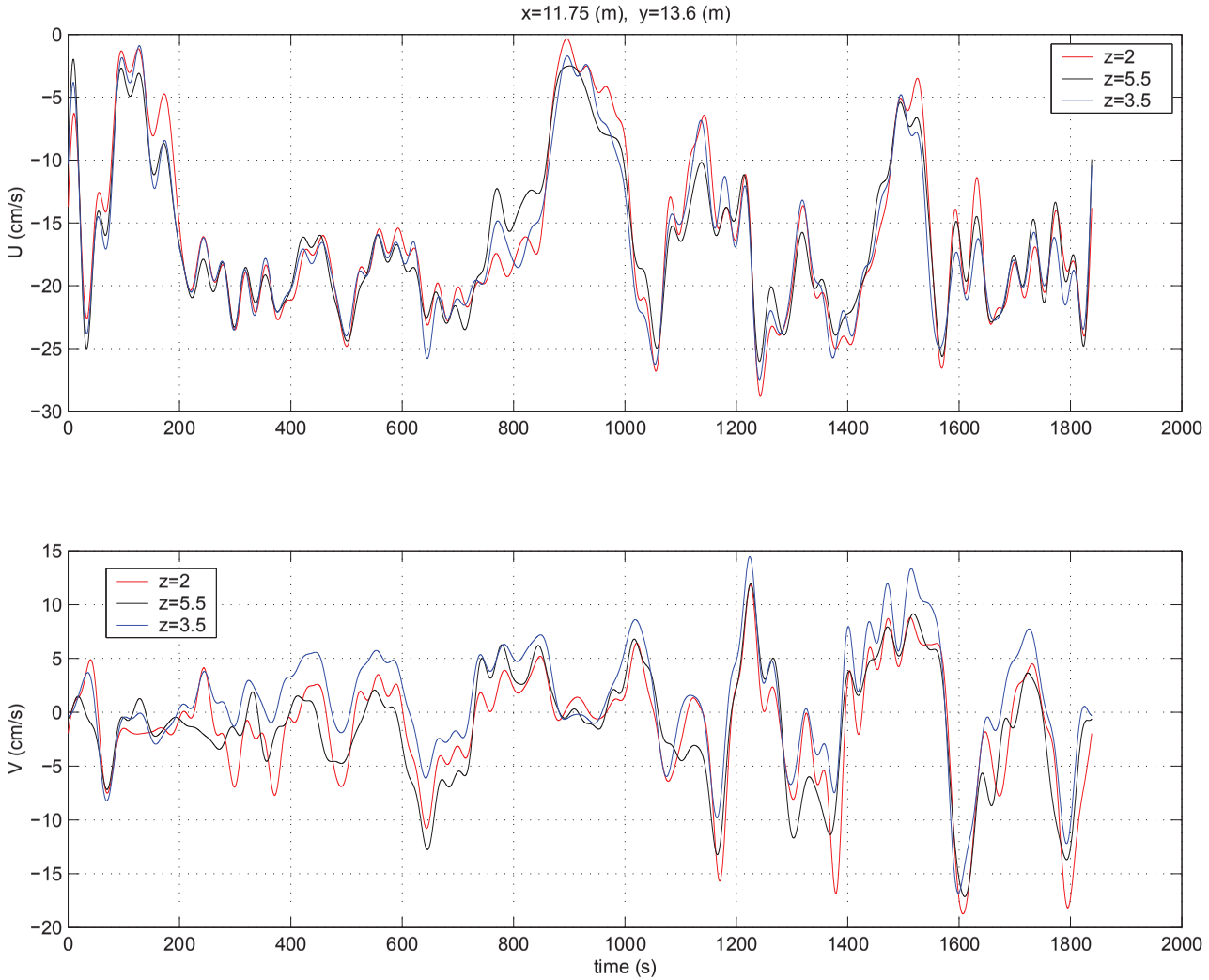

Figure 2.12: Low-pass filtered velocity time series at three depths for run R8 (x = 11.75 m). The top shows cross-shore velocities (U) and the bottom shows longshore velocities (V). z is 0 at the bottom and is positive upwards.

flow shown in (b) than in the cross-shore flow in (a). In addition, the magnitude of the longshore current is similar to the magnitude of the cross-shore current.

The depth variations also give another reason why the rip current vanishes shortly offshore of the channel for the time-averaged velocities in Figure 2.2. Most of the measurements used to generate the velocity vectors in this figure were taken at mid-depth or lower. As seen in Figure 2.11, measurements at mid-depth or lower offshore of the channel have much lower velocities than the measurements taken close to the surface. This leads to the possibility that the rip does not vanish as it flows offshore, it passes over the top of the gages located lower in the water column. It should be noted that the focus of the study by Haller and Dalrymple (1999) is on the rip velocities in the channel, where, as indicated in Figure 2.12, the velocities are nearly uniform over depth so that measurements lower in the water column are representative of the velocity over all depths.

The velocities are measured at each horizontal location during separate runs which prevents direct comparisons between the time series. In addition the rip behavior is not identical between runs, i.e., even measurements at the same location for separate runs are different. The repeatable aspect of the experiments is the time-averaged properties and not the instantaneous flow patterns. In addition, as previously mentioned, time-averaging the velocity records over the length of the experiments eliminates the rip signal outside the surfzone.

In order to analyze the cross-shore variation of the rip current profiles a bin-averaging technique is utilized. The velocity profiles are sorted into bins based on the magnitude of the cross-shore velocity measured closest to the surface (U_1). The bins are defined using the following criteria,

$$\begin{array}{lll} \text{if} & U_1 > 25 & \text{bin25} \\ \text{if} & 25 > U_1 > 20 & \text{bin20} \\ \text{if} & 20 > U_1 > 15 & \text{bin15} \end{array}$$

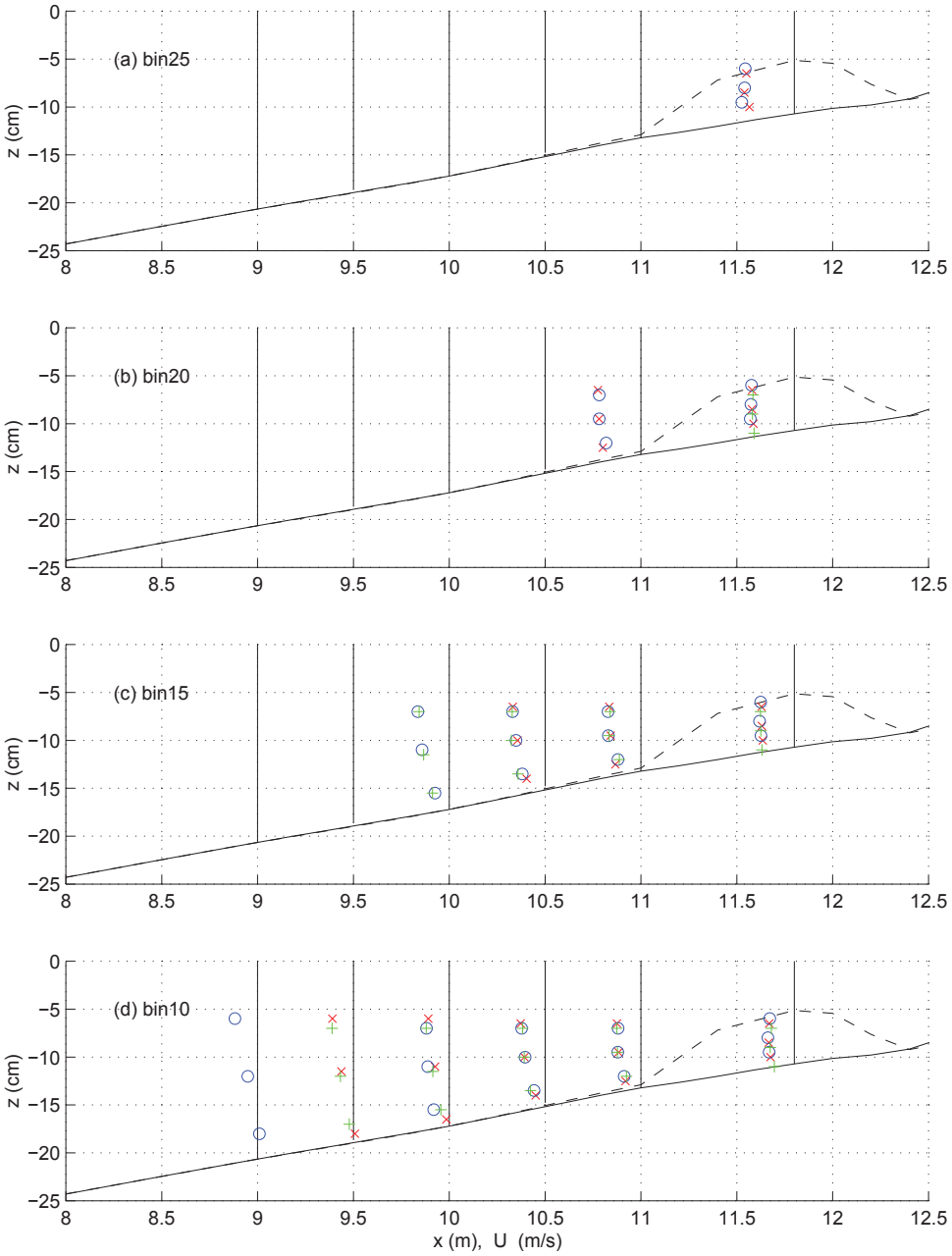

Figure 2.13: Bin-averaged offshore velocity profiles along three cross-shore lines from Test R for (a) bin25, (b) bin20, (c) bin15 and (d) bin10. The symbols are defined as (x) - $y = 13.2$, (o) - $y = 13.6$ and (+) - $y = 14.0$. The vertical lines are the reference lines for each location.

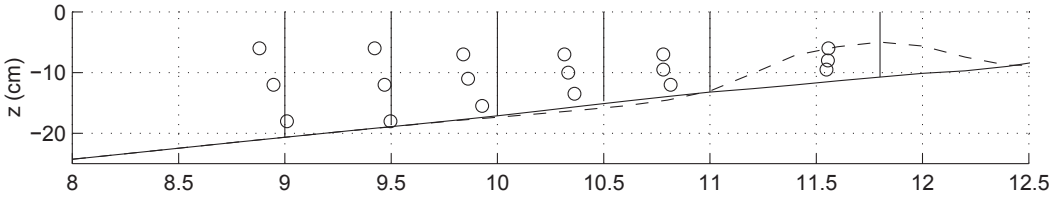

Figure 2.14: Maximum averaged offshore velocity profiles for Test R

$$\text{if} \quad 15 > U_1 > 10 \quad \text{bin10}.$$

The velocity profiles are averaged within each bin producing four velocity profiles, one for each bin. The bin averaging is done at each measurement location allowing for direct comparisons between the velocity profiles at different locations. The intention is to group the profiles based on physical similarities.

Figure 2.13 shows the velocity profiles for each bin at all of the locations. The cross-shore velocity near the surface does not meet the criteria for the bins at all the locations, which explains the absence of many profiles, especially for bin25 in (a). The three profiles at any given cross-shore location show little variation implying that regardless of where the rip passes in the longshore direction, the vertical profile of the rip remains unchanged. Measurements at different longshore locations within the region where the rip passes produce the same velocity profile whenever the rip is present, therefore, further experiments will focus primarily on one cross-shore section, along the centerline of the channel.

The cross-shore transition of the depth variation is evident, particularly in bin10. Inside the channel the velocity is virtually depth uniform whereas the velocity exhibits strong depth variations farther offshore. The profiles represent the bin-averaged velocity and are not an indication of the instantaneous depth variations. Therefore, Figure 2.13d does not represent the actual instantaneous depth variation of a rip current flowing offshore.

Another technique which gives more physical representations of the cross-shore variation of the vertical current profiles is to average the maximum profile at each location. Any profile which is within 3 cm/s of the maximum velocity at the surface for a given cross-shore location is grouped together and averaged. This is based on the premise that the maximum averaged profile represents the decrease in velocity as the rip flows seaward into deeper water.

Figure 2.14 shows the maximum averaged current profiles from Test R. The peak velocity decreases as the rip flows offshore. The variation of the vertical profile is evident, there is little variation inside the channel and progressively larger depth variation farther offshore. For the location furthest offshore ($x = 9$ m) the velocity at the bottom becomes shoreward.

Variations of the velocity profiles in time can be compared at any given location. Because the gages are offset by 7 cm in the cross-shore direction, the measurements contain some phase shift between the different depths. For this reason, instantaneous profiles are calculated by averaging the velocity over 5 seconds which is usually much more than the time it takes the flow to pass from one gage to the other. However, this time scale is much shorter than the time variations of the rip flow, therefore, little information is lost from the averaging process.

Vertical profiles of velocity from eight times during a rip event at the location 2 m offshore of the bar are shown in Figure 2.15. The vertical lines are the reference lines. The horizontal lines are vectors indicating both the magnitude and direction of the current. The projections of the cross-shore and longshore velocities are included as well. The largest offshore (negative) current is located at the top whereas the weakest or onshore (positive) current is at the bottom. The cross-shore velocities exhibit the strong depth variations but the longshore velocity remains fairly depth uniform. The striking features is that the current is twisting over depth with the surface velocity going mainly offshore and the bottom current going in the negative

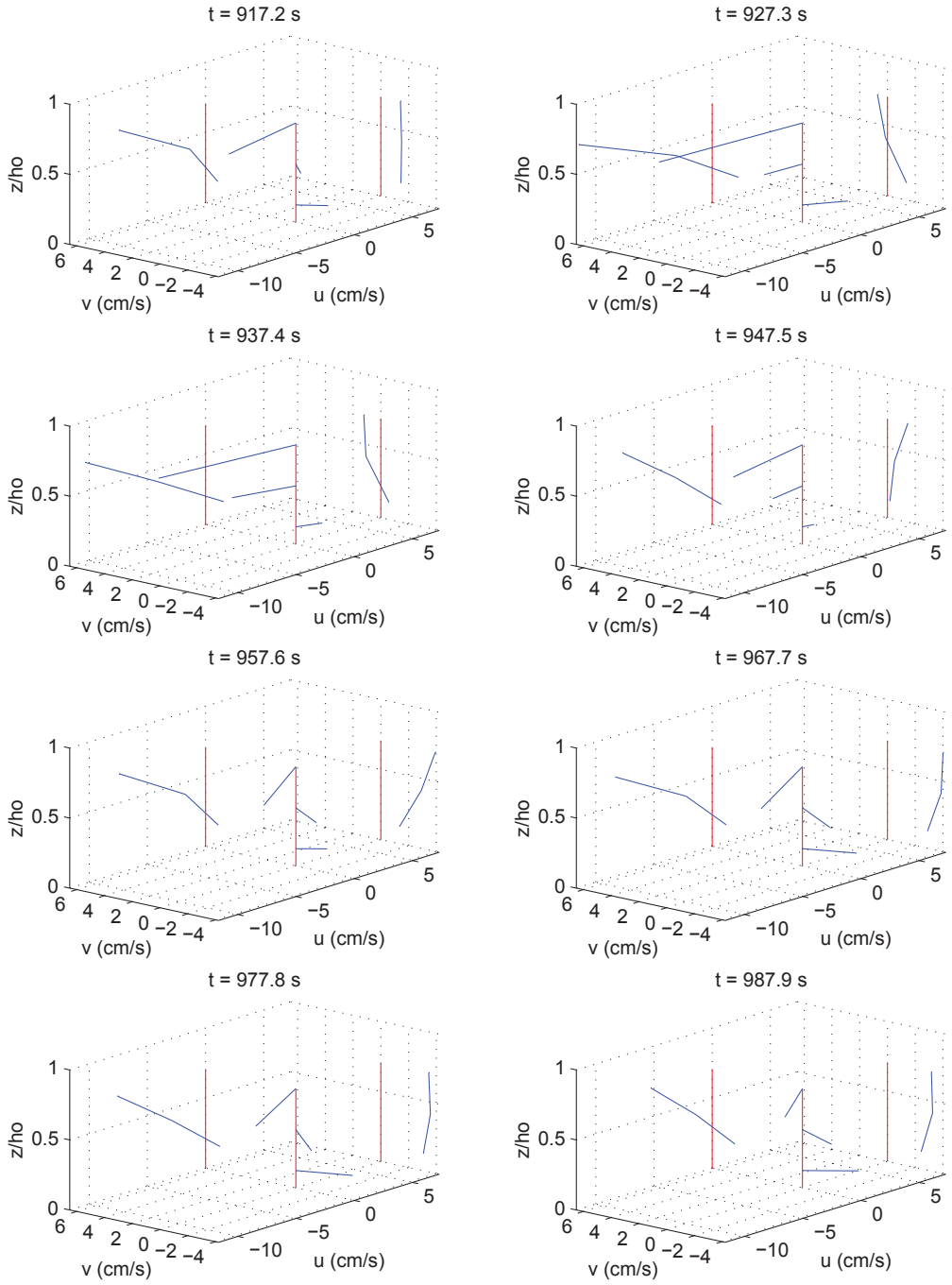

Figure 2.15: Snapshots of the velocity vectors with projections of the cross-shore and longshore currents for run R17 2 m offshore of the channel ($x = 9$, $y = 13.6$ m).

longshore direction and slightly shoreward.

In contrast, Figure 2.16 shows vertical profiles of velocity at eight times during a rip event inside the channel. Here the vertical profiles tend to be depth uniform with little twisting of the current evident. During the initial surge of the rip, the peak current is occurring at mid-depth, although as the velocity reduces, the peak tends to move toward the surface.

The results of Test R are summarized as follows:

- The rip currents are unstable with multiple time scales.
- The wave heights increase when rip currents are present due to wave current interaction.
- The mean water level has a depression as rip currents pass by.
- Rip currents show a strong depth variation outside the breakers and little depth variation inside the channel.
- Bin-averaging and maximum averaging provide good spatial descriptions of the profiles.
- The instantaneous profiles twist over depth farther offshore and are fairly uniform in the channel.

2.2.2 Test S: Higher Resolution Test Series

Because the bin-averaged rip current profiles remain the same along the three cross-shore sections in Test R, the focus is now along a single cross-shore section. More measurements are taken making for a higher resolution of the depth variations of the rip currents. The locations of the measurements for Test S are shown in Figure 2.17. The ADV arrays are located along the centerline of the channel at 17 locations spaced 20 cm apart. In order to get better resolution of the vertical current profiles,

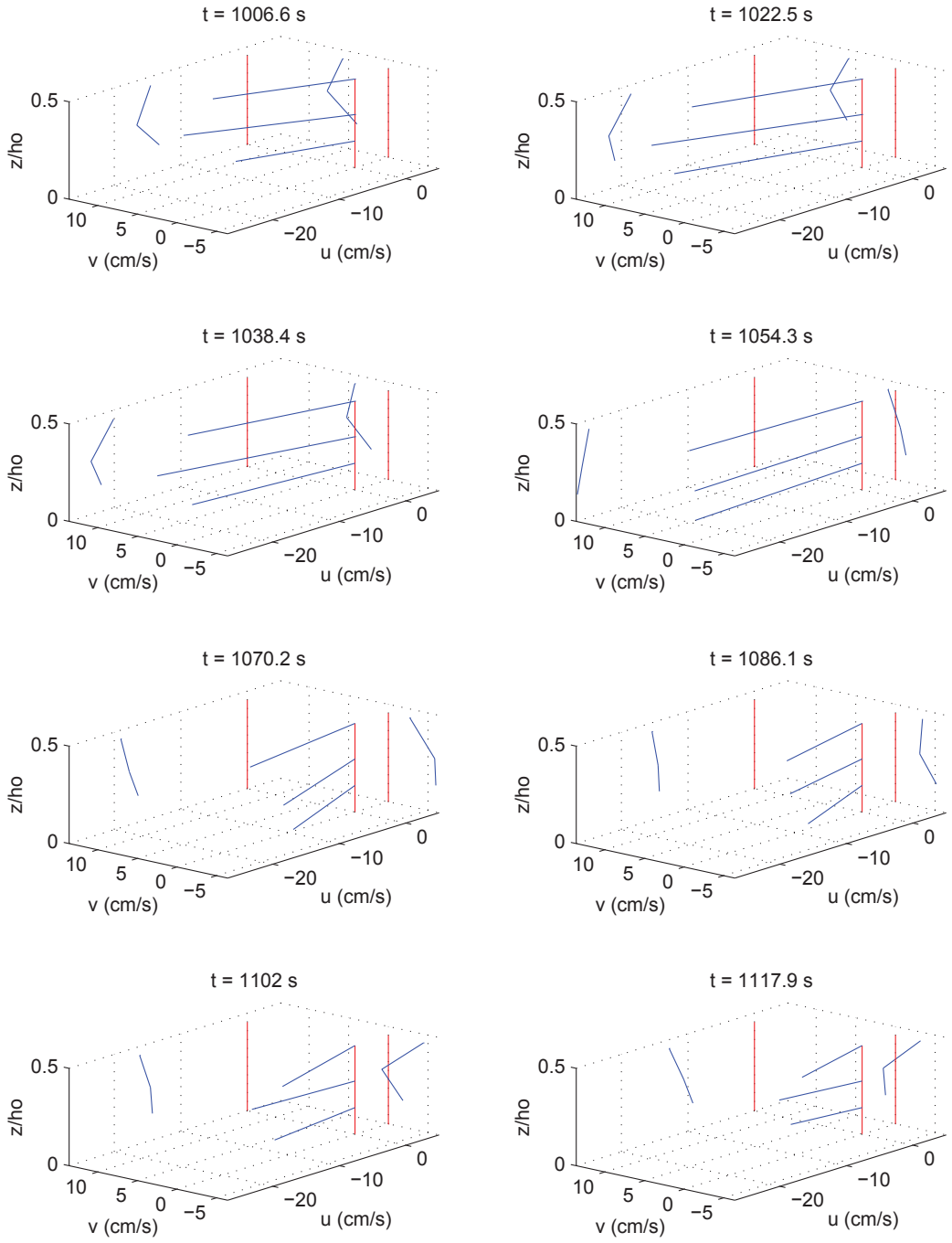

Figure 2.16: Snapshots of the velocity vectors with projections of the cross-shore and longshore currents for run R8 in the channel ($x = 11.75$, $y = 13.6$ m).

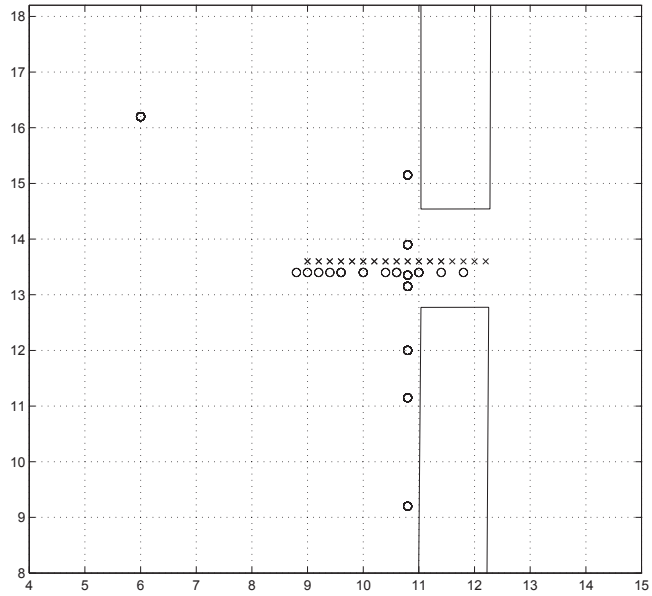

Figure 2.17: Location of the gages for Test S where (x) indicates ADV gage array locations and (o) indicates wave gage locations.

13 of the locations have 6 measurements over depth from two separate runs. Gage 1 was kept close to the same depth to allow for direct comparison between the two runs. This yields velocity measurements at 5 depths for each of these locations. The other 4 locations were in too shallow of water to allow for more than 3 measurements over depth.

The circles (o) in Figure 2.17 represent individual wave gages. As before, one wave gage is always located offshore (x = 6 m, y = 16.2 m) and is used to check repeatability of the experiments. In order to provide water level data close to the velocity measurements, another wave gage is always placed close to the ADV array. Finally, 6 wave gages are placed on a bridge spanning the longshore direction in front of the bar. These gages are removed for the second half of the runs because of the large amount of wave data already available for these wave conditions. Tables giving the exact location for all gages are in Appendix A.

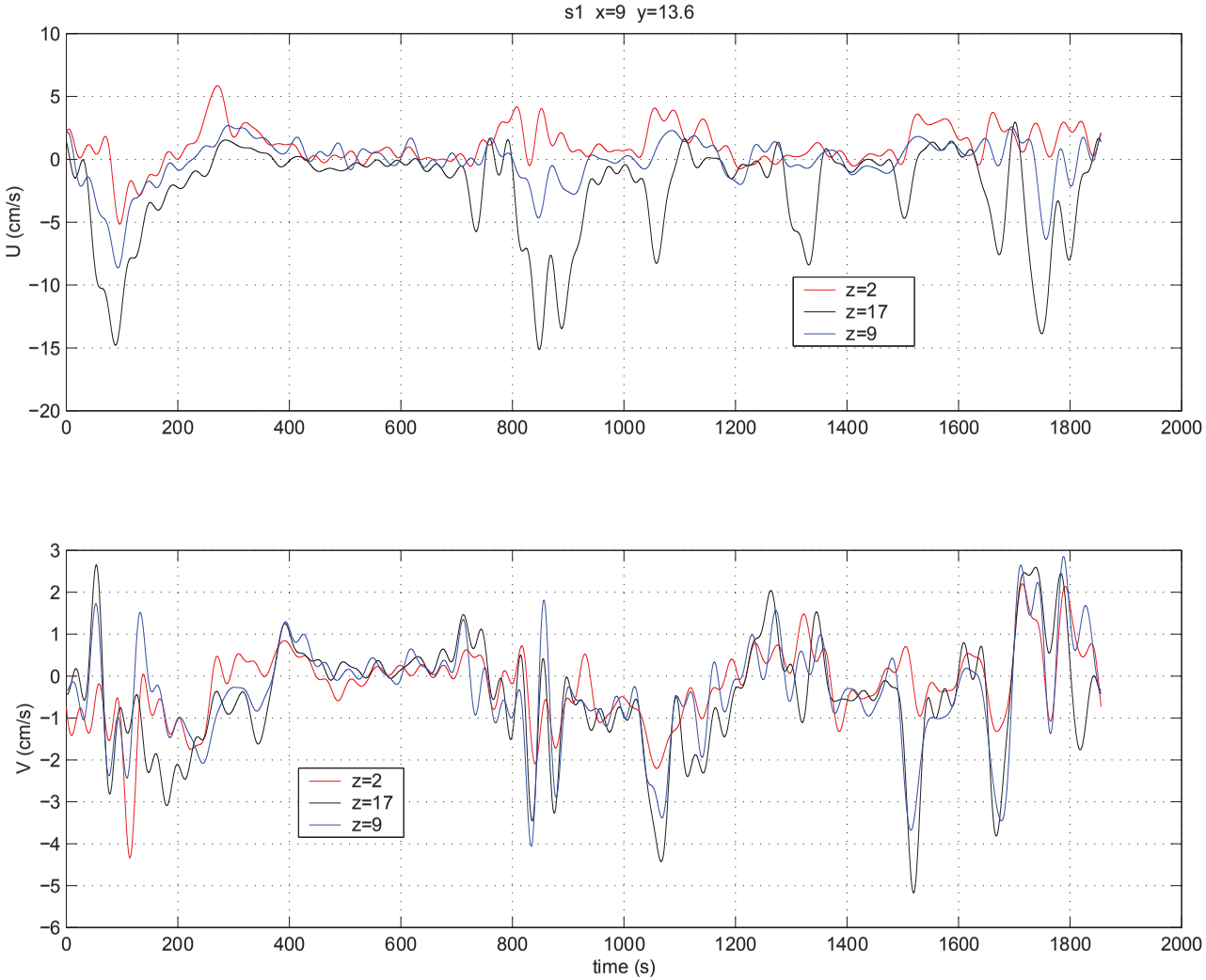

Figure 2.18: Low-pass filtered velocity time series at three depths for run S1 ($x = 9.0$ m). The top shows cross-shore velocities (U) and the bottom shows longshore velocities (V). z is 0 at the bottom and is positive upwards.

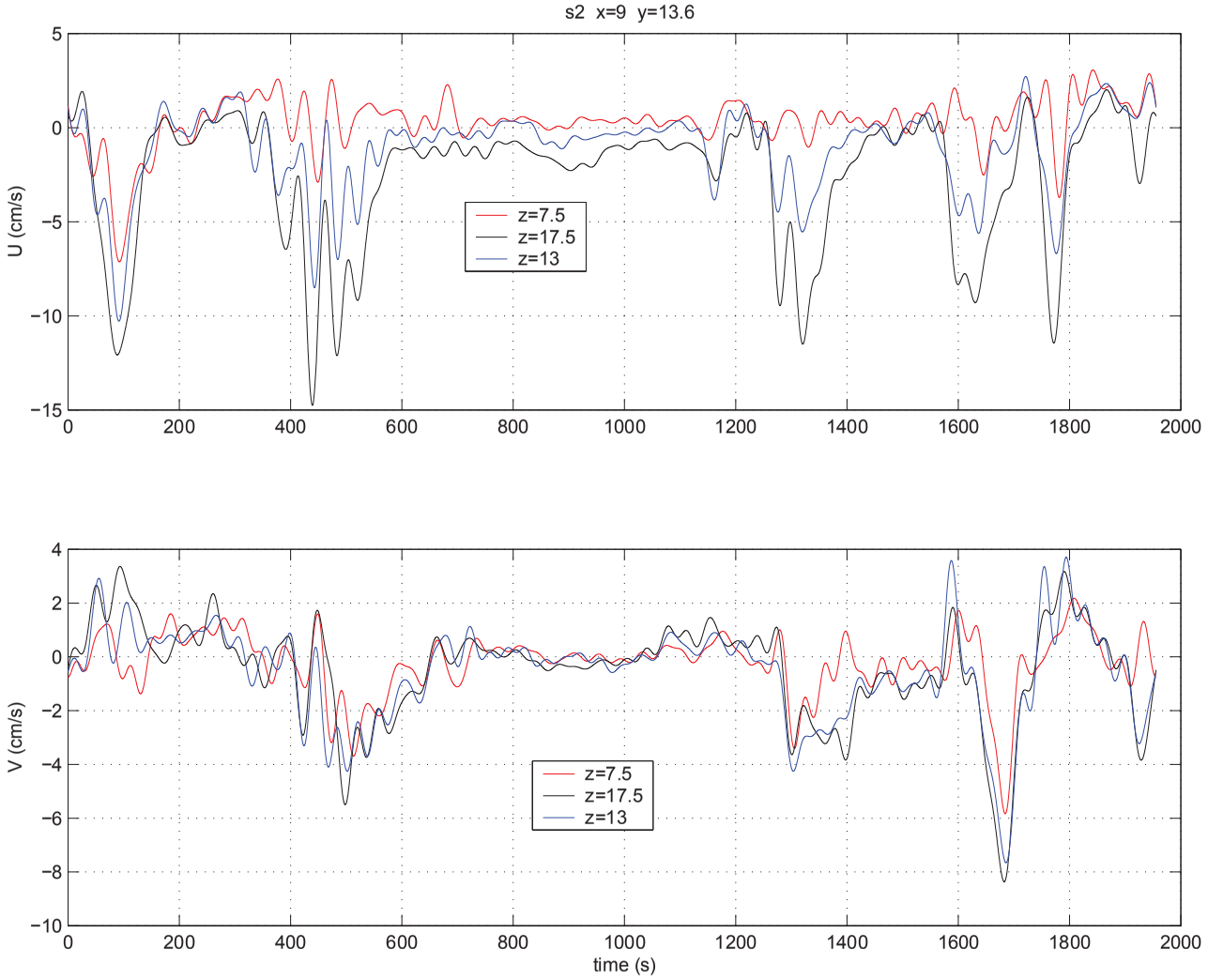

Figure 2.19: Low-pass filtered velocity time series at three depths for run S2 ($x = 9.0$ m). The top shows cross-shore velocities (U) and the bottom shows longshore velocities (V). z is 0 at the bottom and is positive upwards.

Low-pass filtered time series of the cross-shore and longshore velocities are shown in Figures 2.18 and 2.19. These figures are for two individual runs with the gages located at the same cross-shore and longshore positions ($x = 9$ m, $y = 13.6$ m) but the gages are at different depths. However, the gage closest to the surface is at the same depth for both realizations which allows for a direct comparison. The still water depth at this location, 2 m offshore from the bar along on centerline of the channel, is 21.0 cm.

The strong depth variations are evident in both figures. The velocity at the surface gage reaches up to 15 cm/s while the velocity lower in the water column is much smaller. The cross-shore velocity closest to the bottom, plotted in red in Figure 2.18, is virtually always shoreward. Only the gages closest to the surface in both figures and the mid-depth gage in Figure 2.19 record velocities which exceed 5 cm/s during the rip events. This indicates that the larger currents in the rip penetrate less than half of the water column at this offshore location.

Even though the wave conditions for the two experimental runs are identical, comparing the time series for the gage closest to the surface in both figures shows that the individual rip events differ. Both time series have an initial event near the beginning which is due to the drainage from the initial surge of water shoreward when the waves are begun. The time series in Figure 2.18 does not have another significant rip event until around $t = 800$ s while the time series in Figure 2.19 has a rip event before $t = 400$ s. Because rip events at the same location do not occur at the same time in separate runs, direct comparisons of the time varying currents are not possible.

Figures 2.20 and 2.21 show time series of the low-pass filtered velocity 1 m offshore of the bar at the centerline of the channel. The surface measurements are taken at the same depth while the other four measurements are taken at different depths. The still water depth at this location is 17.5 cm.

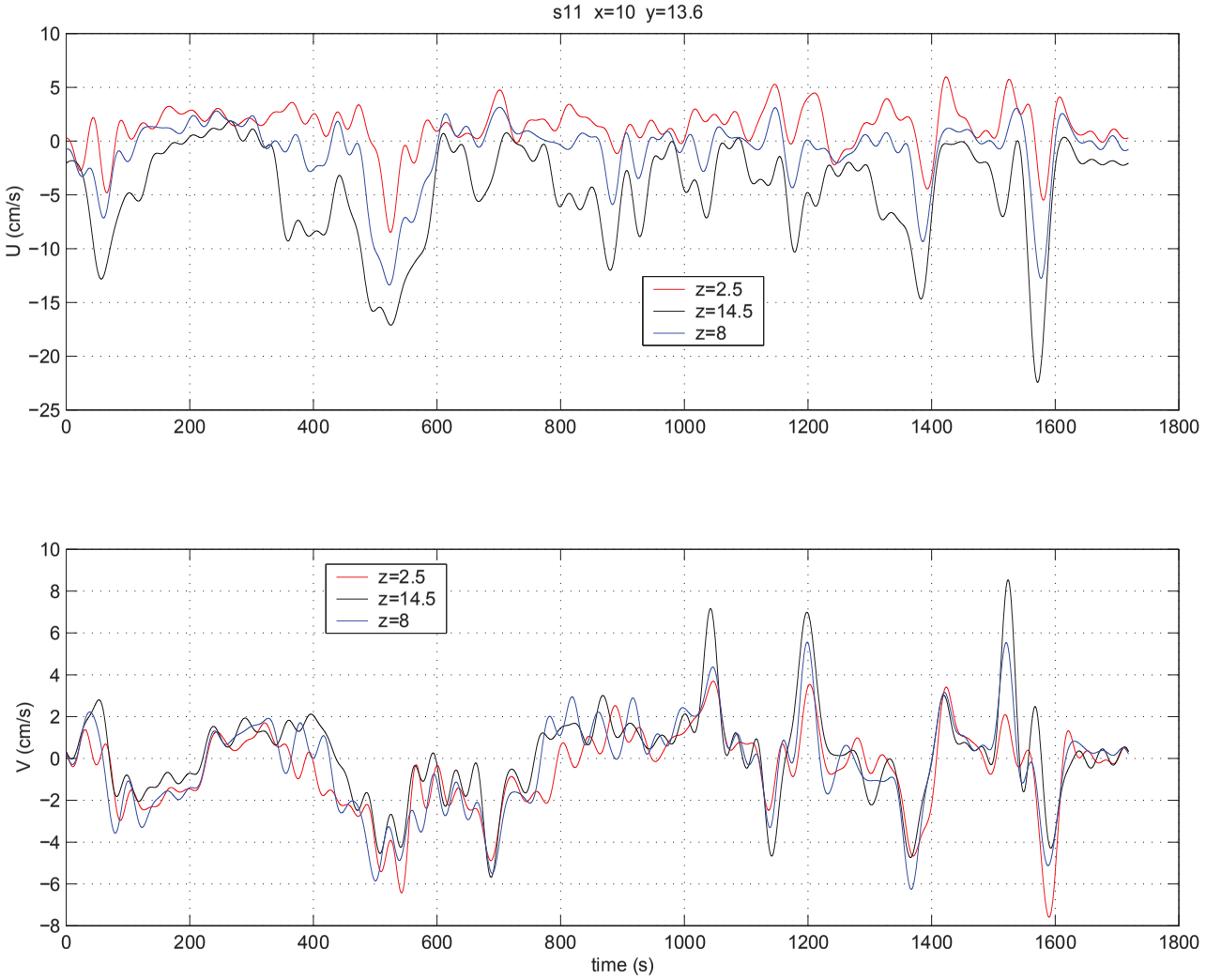

Figure 2.20: Low-pass filtered velocity time series at three depths for run S11 (x = 10.0 m). The top shows cross-shore velocities (U) and the bottom shows longshore velocities (V). z is 0 at the bottom and is positive upwards.

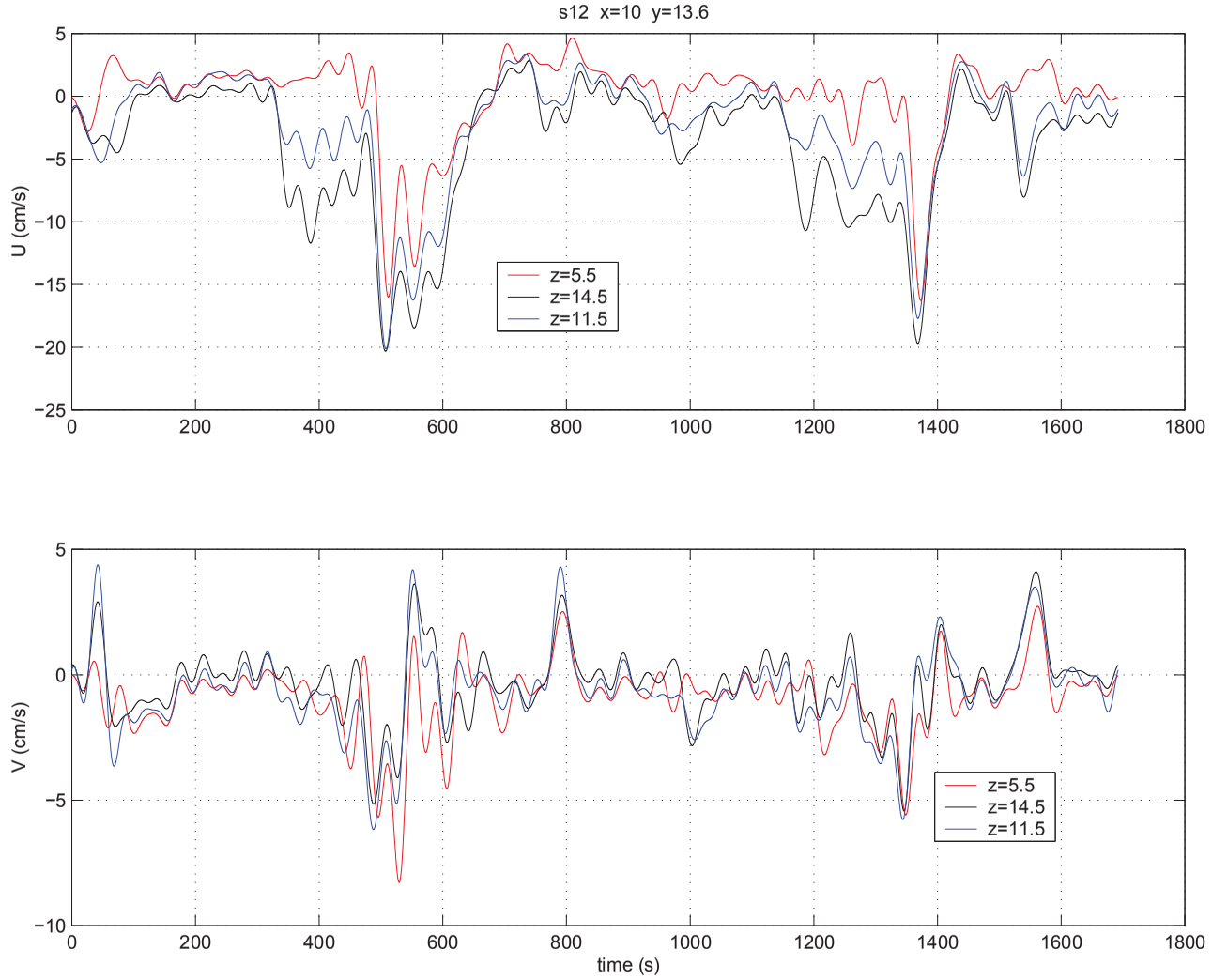

Figure 2.21: Low-pass filtered velocity time series at three depths for run S12 (x = 10.0 m). The top shows cross-shore velocities (U) and the bottom shows longshore velocities (V). z is 0 at the bottom and is positive upwards.

At this location the rip events are sporadic and the velocities are largest close to the surface. It is interesting to note that in Figure 2.20 there are frequent small rip events with only a few large events with short durations. On the other hand in Figure 2.21, there are a few large rip events with longer durations and almost no small rip events. Even though the measurements are taken at the same location under the same wave conditions, the rip behavior has remarkable variations.

Time series of the low-pass filtered velocity measured inside the channel at $x = 11.4$ m are shown in Figures 2.22 and 2.23. The velocities from the gage closest to the surface are measured at the same depths while the other gages are at four different depths. The still water depth at this location is 12.25 cm.

During rip events in these figures, the velocities are similar at all depths. This indicates nearly depth uniform flow for the rip inside the channel. The velocities during the lulls between rip events, however, demonstrate some depth variation with the velocity closest to the bottom being weaker or even shoreward. The frequency of rip events is similar in both figures although in Figure 2.22 there is a long stretch without any rip activity for $600 < t < 800$ s. There is no such lull in rip activity in Figure 2.23.

The velocities are separated into bins following the method outlined by (2.5). At the cross-shore locations where two individual runs are performed, the gage closest to the surface is at the same depth for both runs. This is the velocity record which is used to sort the velocity profiles into the bins. Because the sorting is based on velocities at the same depth, the profiles from both runs are combined to give a resulting profile with velocities at five depths.

Figure 2.24 shows the vertical profiles of the cross-shore velocity for the four bins. In bin20, the current profile shows strong depth variation at $x = 10$ m, but weak variations for $x > 11.6$ m. The profiles in bin10, however, show depth variations from $x = 9$ m all the way to $x = 11$ m. This indicates that stronger burst

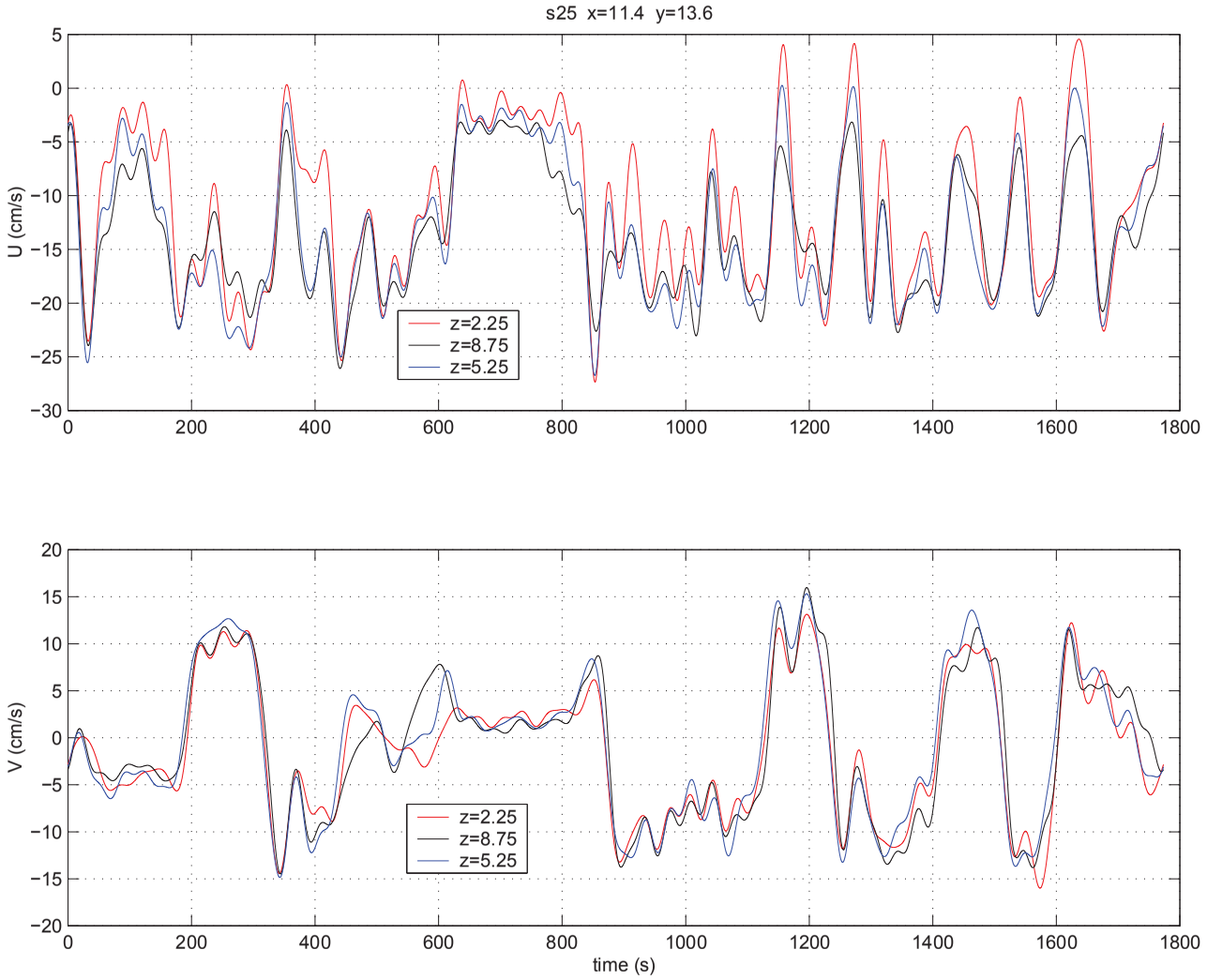

Figure 2.22: Low-pass filtered velocity time series at three depths for run S25 (x = 11.4 m). The top shows cross-shore velocities (U) and the bottom shows longshore velocities (V). z is 0 at the bottom and is positive upwards.

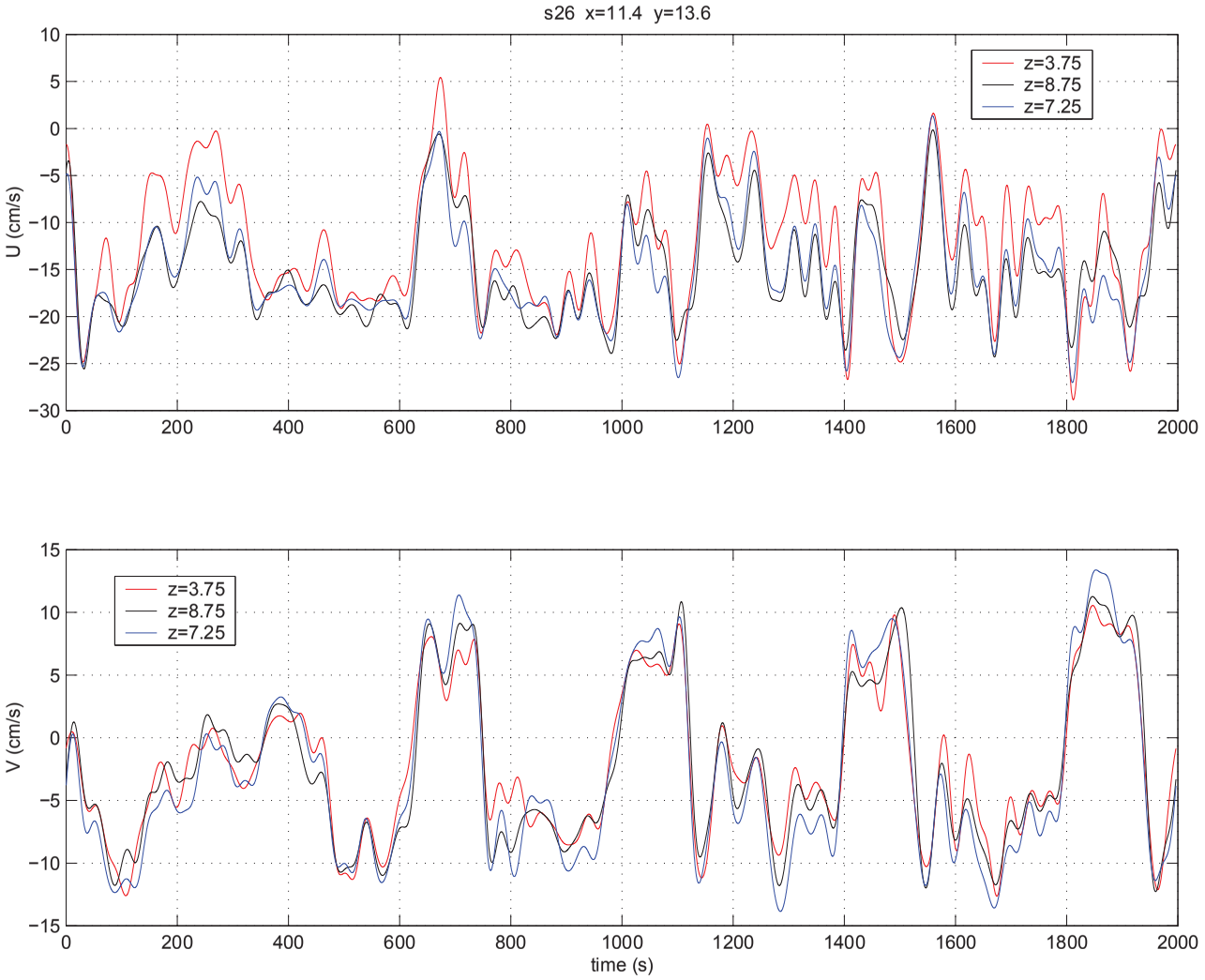

Figure 2.23: Low-pass filtered velocity time series at three depths for run S26 (x = 11.4 m). The top shows cross-shore velocities (U) and the bottom shows longshore velocities (V). z is 0 at the bottom and is positive upwards.

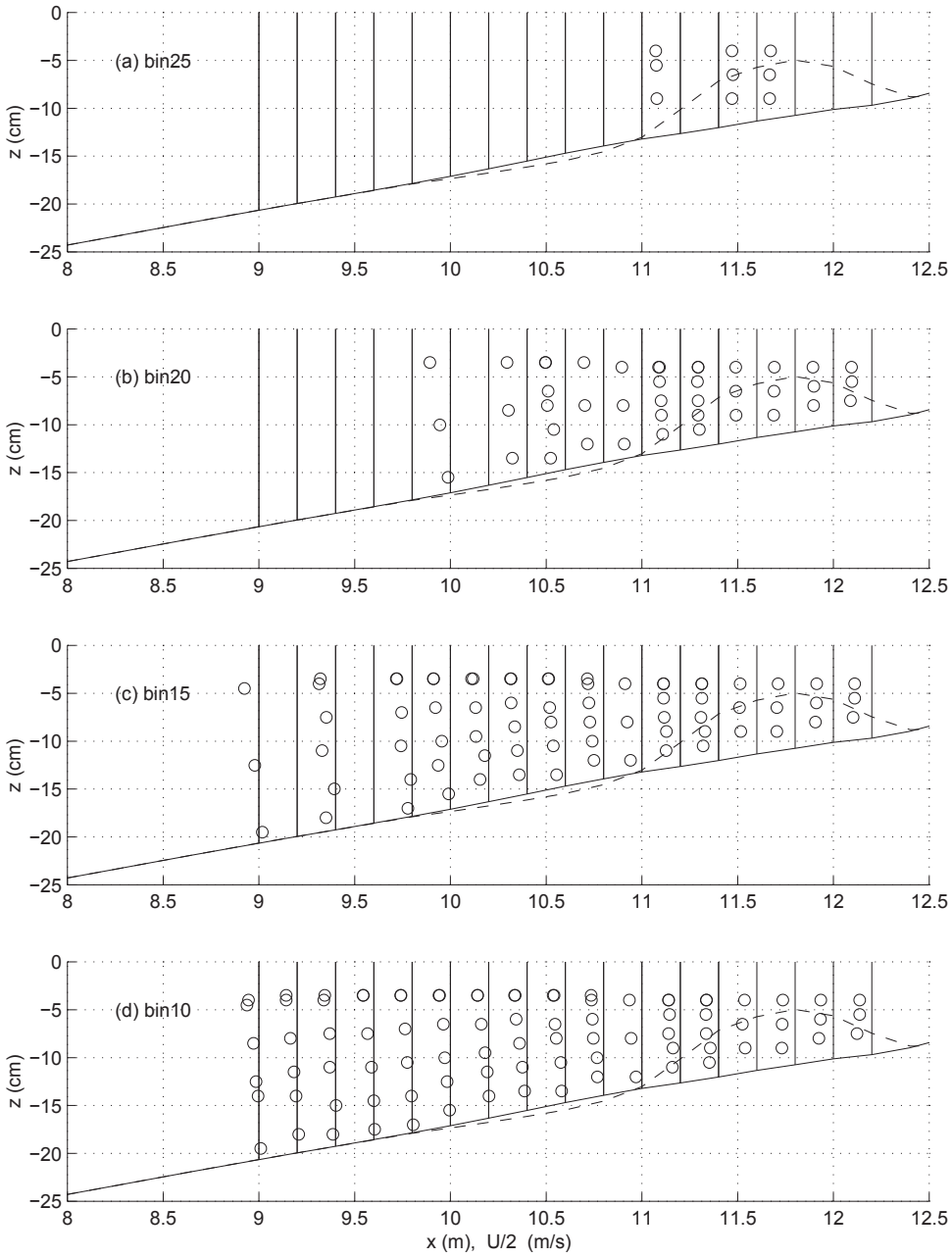

Figure 2.24: Bin-averaged rip current profiles from Test S for (a) bin25, (b) bin20, (c) bin15 and (d) bin10. The vertical lines are the reference lines for each location.

of rip flow penetrates farther down the water column. Therefore, the vertical profile is somewhat dependent on the total volume flux of the rip flow.

At most locations the combining of the separate runs to create a single profile appears to be acceptable with only a few strange looking profiles. Most importantly, the bin-averaged velocity for the surface measurements have good agreement even though they are from individual runs. Although the time series of rip events for separate runs at the same location have varying frequency and duration of rip events, the bin-averaged velocity at the surface remains unchanged.

Test series S showed that even at the same location, the rip events were different for separate runs. This series also provide much more detailed vertical profiles. It is found that the larger rip bursts containing more volume flux has less depth variation than smaller rip burst at the same location.

2.2.3 Test T: Large Wave Test Series

This test represents a situation characterized by larger waves. The larger waves carry more water over the bar leading to greater offshore discharge in the rip currents. Because the depth is the same as for the smaller wave case, the larger discharge leads directly to larger velocities in the rip current. The purpose of this test is to analyze the sensitivity of the vertical profile to increased total flux in the rip current. The locations of the measurements for Test T are shown in Figure 2.25. The ADV arrays are located along a single cross-shore line at 7 locations spaced 50 cm apart along the centerline of the channel. Each marked ADV location represents current velocities at three separate depths.

The circles (o) in Figure 2.25 represent individual wave gages. One wave gage is again located offshore ($x = 6$ m, $y = 16.2$ m) and is used to check repeatability of the experiments. In order to provide water level data close to the velocity measurements, another wave gage is always placed close to the ADV array. Six wave gages are placed on a bridge spanning the longshore direction behind the bar. Because

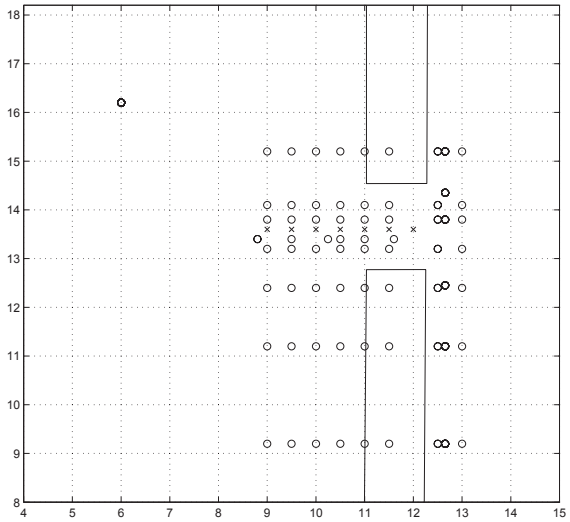

Figure 2.25: Location of the gages for Test T where (x) indicates ADV gage array locations and (o) indicates wave gage locations.

this is a new wave condition which has not been previously measured, the wave field must be documented over a larger region. After the current measurements are completed, 7 wave gages are placed on the bridge spanning the longshore direction. This bridge is moved to 8 different locations providing information about the wave field over a broad area. Tables giving the exact location for all gages are in Appendix A.

The time-averaged wave heights and water levels $\overline{\zeta}$ from test T are shown in Figure 2.26. The wave heights closest to the shoreline are facing toward the front of the figure whereas the offshore region of the water level is shown facing toward the front of the figure. The increase of wave height due to the presence of the rip current is evident around $y = 13.6$ m. The decrease in the wave height as the waves break over the bar ($x = 12$ m) is seen as well. The water level in (b) shows a setdown offshore of the breaking followed by setup closer to the shoreline. In the trough region behind the bar ($x > 12$ m), the setup is larger behind the bar ($y < 13$ m) than behind the channel ($y = 13.6$ m) leading to a longshore pressure gradient

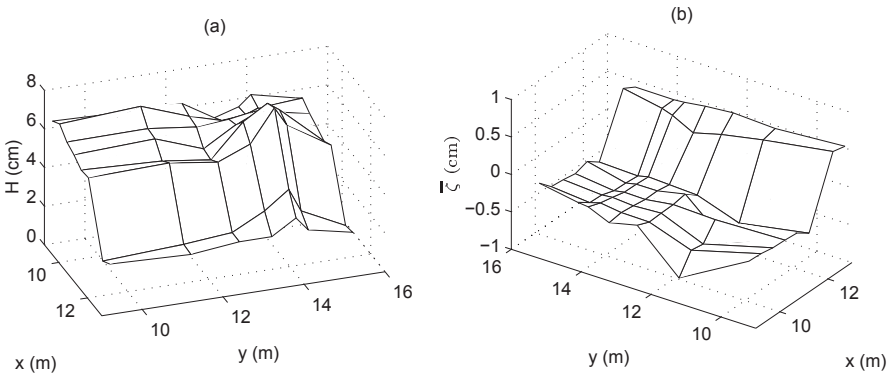

Figure 2.26: Mesh plots of the time-averaged (a) wave height H and (b) mean water level $\overline{\zeta}$ for test series T. Note that in (a) the shoreline is facing toward the front of the figure and in (b) the shoreline is facing toward the back of the figure. The rip channel is centered at $y = 13.6$ m.

toward the channel.

A more detailed view of the cross-shore variation of the time-averaged wave heights and water levels is shown in Figure 2.27. As the waves approach the offshore edge of the bar ($x = 11$ m), the wave height in the channel is increasing rapidly whereas the wave height over the bar is actually decreasing slightly. The exact location of the breaking is difficult to identify because of the coarse resolution of the measurements. The waves which passed over the bar seem to be reforming and increase slightly in height for $x > 12.5$ m. The waves passing through the channel, however, have wave heights which are decreasing between $x = 12.5$ and $x = 13$ m indicating that the waves are still breaking.

Cross-shore sections of the mean water level over the bar and channel are shown in Figure 2.27b. Offshore from the bar ($x < 11$ m), there is little longshore difference in the setdown. Once breaking commences and a setup is created, the longshore variation of $\overline{\zeta}$ in the trough behind the bar for $x \geq 12.5$ m as indicated

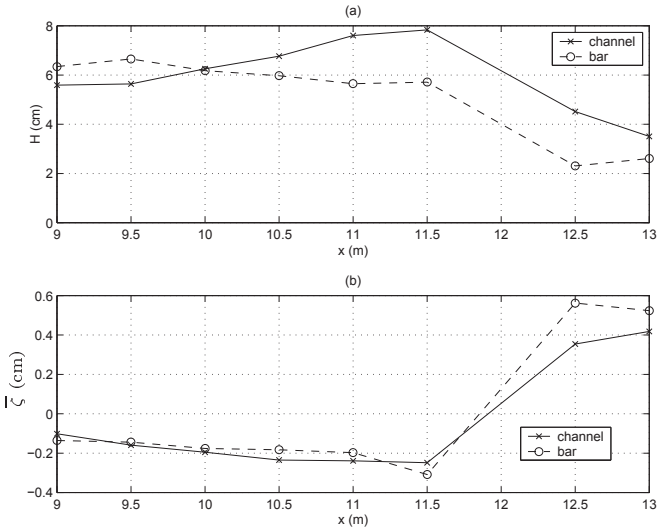

Figure 2.27: Cross-shore sections of the time-averaged (a) wave height H and (b) the mean water level $\overline{\zeta}$ through the channel ($y = 13.5$ m) and over the center of the bar ($y = 9$ m). The bar is located at $11 < x < 12.4$ m.

in Figure 2.26 becomes evident. For $x \geq 12.5$ m, the setup behind the bar is significantly larger than the setup behind the channel. At the shoreward most point the difference between the water levels is smaller indicating that further measurements closer to the shoreline would show a reversal of the longshore pressure gradient.

Two low-pass filtered time series taken during the same realization of the cross-shore velocity from the gage closest to the surface and of $\overline{\zeta}$ are shown in Figure 2.28 for a location approximately 2 m offshore from the bar ($x = 9$ m). The rip events at this offshore location occur much more frequently than for the smaller wave conditions in Figure 2.8a. A close inspection of this figure reveals that the oscillations in the two signals are related to one another. During burst of large rip flow (negative velocities), the water level decreases.

Similarly, Figure 2.29 shows low-pass filtered time series of the velocity and water level inside the channel. Note that the cross-shore offset between the velocity

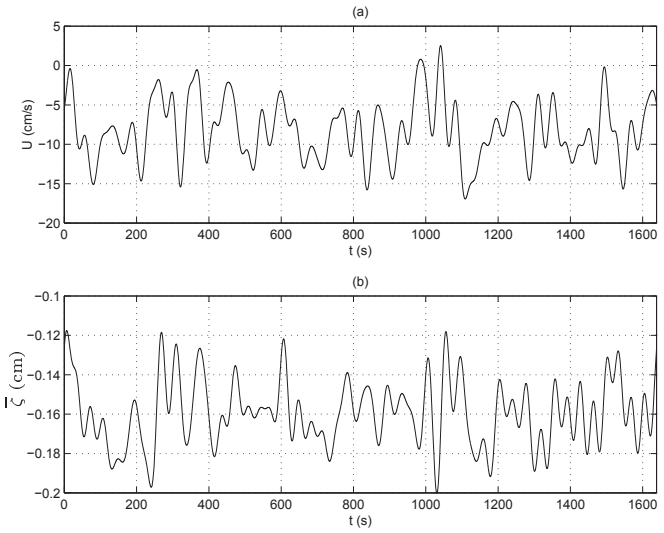

Figure 2.28: Synchronized time series 2 m offshore of the bar on the centerline of the channel of (a) the cross-shore velocity U ($x = 9$ m and $y = 13.6$ m), and (b) the mean water level $\overline{\zeta}$ ($x = 8.8$ m and $y = 13.4$ m).

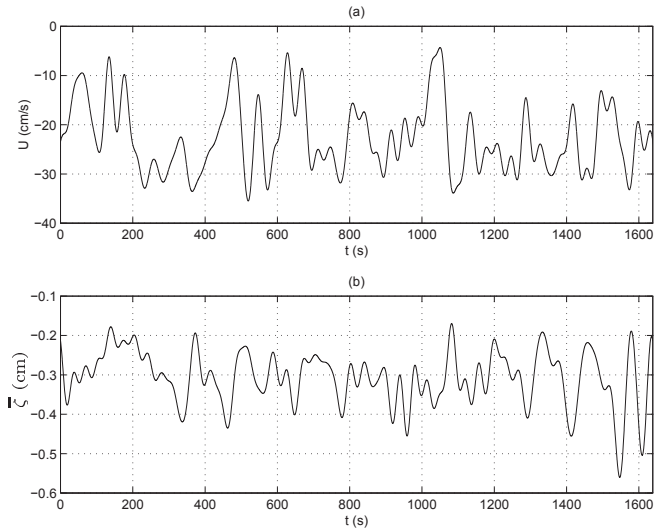

Figure 2.29: Synchronized time series in the channel on the centerline of the channel of (a) the cross-shore velocity U ($x = 11.5$ m and $y = 13.6$ m), and (b) the mean water level $\overline{\zeta}$ ($x = 11$ m and $y = 13.4$ m).

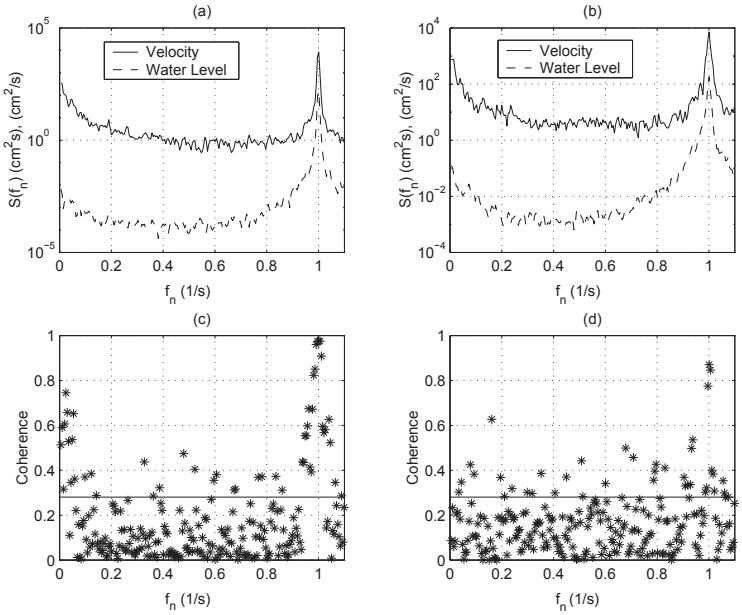

Figure 2.30: Energy spectra with 16 degrees of freedom (a and b) and coherence (c and d) for the current and water level outside the breakers (a and c) at $x = 9$ m (U) and $x = 8.8$ m ($\overline{\zeta}$) and inside the channel at $x = 11.5$ m (U) and $x = 11.0$ m ($\overline{\zeta}$).

and the water level is 50 cm which is larger than in Figure 2.28. Even with the large offset there appears to be a relationship between the two signals. Rip events in the velocity signal, which are nearly continuous, do occur slightly earlier than the depression in the water surface because the rip reaches the velocity gage, which is located shoreward of the wave gage, first.

Figure 2.30 shows the energy spectra for the cross-shore velocities and the water levels offshore and in the channel. Comparing this figure with the energy spectra for the smaller wave conditions in Figure 2.10 reveals that the energy is much larger for the bigger waves for both the incident frequency ($f_n = 1$ Hz) and the lower frequencies ($f_n < 0.2$ Hz) as could be expected. The reason for this is

that the larger wave condition is transporting more water shoreward, increasing the offshore discharge in the rip. The larger total flux in the rip leads to larger velocities and more energy. Larger waves input more energy leading to more energy in the rip currents.

The relationship between the current and the water level is quantified statistically by calculating the coherence as defined by (2.2). The coherence is shown in Figure 2.30 which is similar to Figure 2.10 for the smaller wave conditions. For the offshore location, (c), the coherence is high around 1 Hz, the short-wave frequency, as well as at the lower frequencies, $f_n < 0.2$ Hz. The low frequencies correspond to the instabilities and meandering of the rip current. Inside the channel the coherence is lower, most likely due to the larger offset between the gages.

Time series of the low-pass filtered velocity for three depths measured 2 m offshore of the channel ($x = 9$ m) are shown in Figure 2.31. Comparing this figure to Figure 2.11 reveals that for the larger wave conditions the rip occurs much more frequently and has stronger velocities. The figure also shows that cross-shore velocity measured by the bottom gage is usually shoreward, although, for a few strong burst the velocity is seaward. Similar to the weaker wave conditions, the longshore current shows less depth variation than the cross-shore current.

Figure 2.32 shows the similar low-pass filtered time series at three depths for the current inside the channel. Here the rip is much stronger inside the channel compared to the rip for the smaller waves in Figure 2.12. The current exceeds 35 cm/s whereas before the maximum current is only 25 cm/s. The current inside the channel has weak depth variations for both the small and large wave conditions.

The current profiles are sorted into bins based on the velocity from the gage closest to the surface following the method defined by (2.5). The resulting profiles for each bin are shown in Figure 2.33. The profiles from $x = 10.5$ are not included because of problems with the synchronization of the gages at that location.

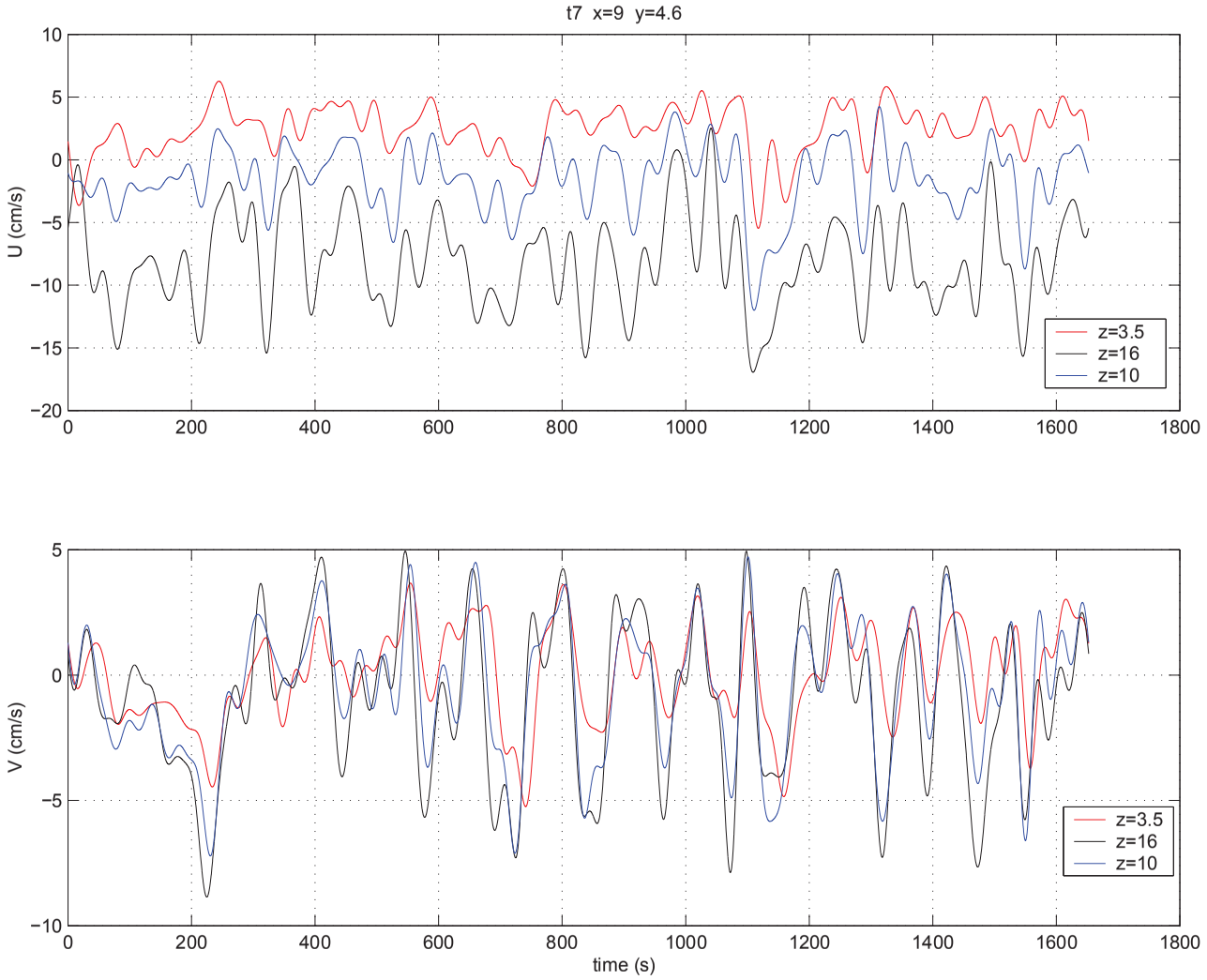

Figure 2.31: Low-pass filtered velocity time series at three depths for run T7 ($x = 9.0$ m). The top shows cross-shore velocities (U) and the bottom shows longshore velocities (V). z is 0 at the bottom and is positive upwards.

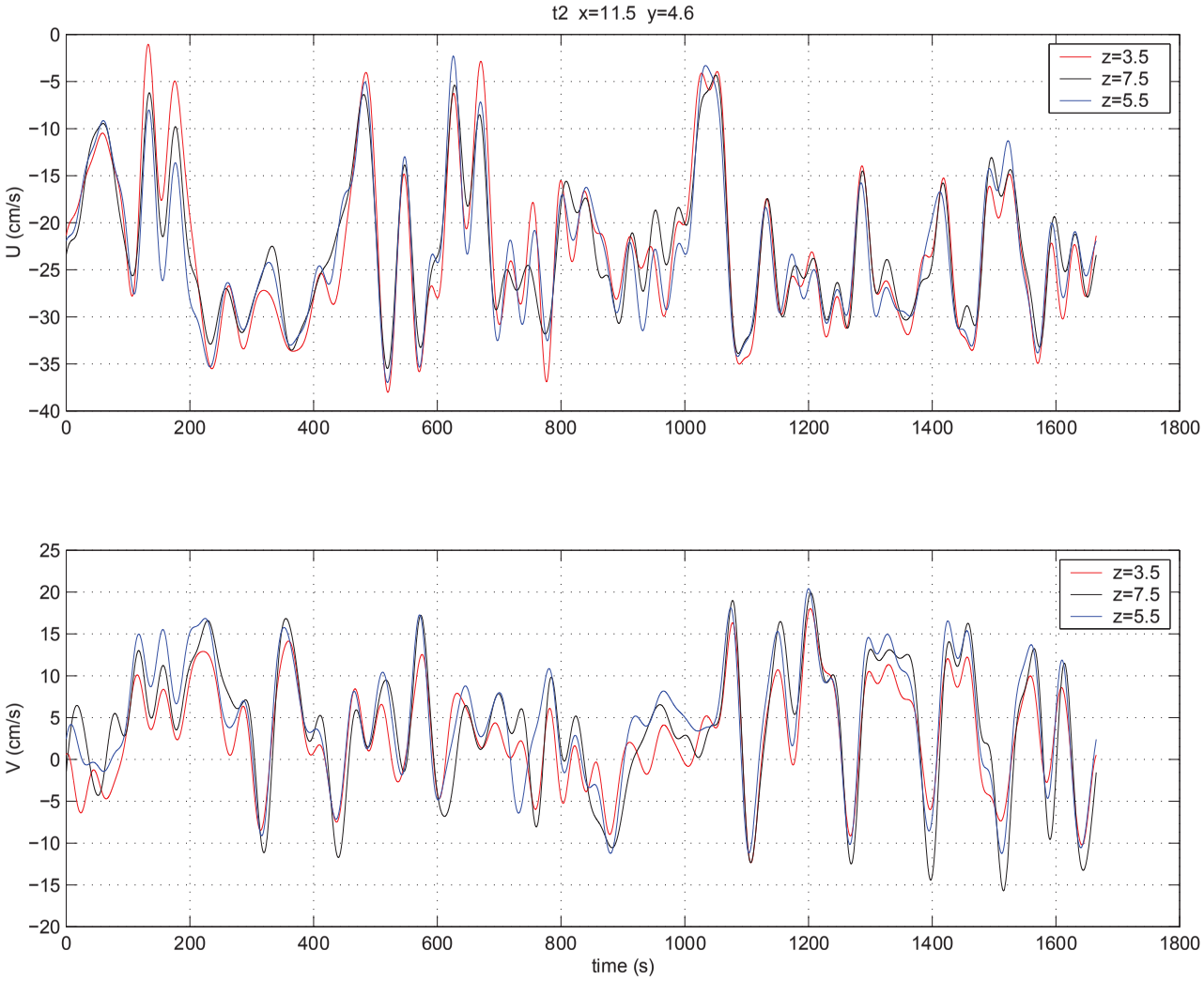

Figure 2.32: Low-pass filtered velocity time series at three depths for run T2 ($x = 11.5$ m). The top shows cross-shore velocities (U) and the bottom shows longshore velocities (V). z is 0 at the bottom and is positive upwards.

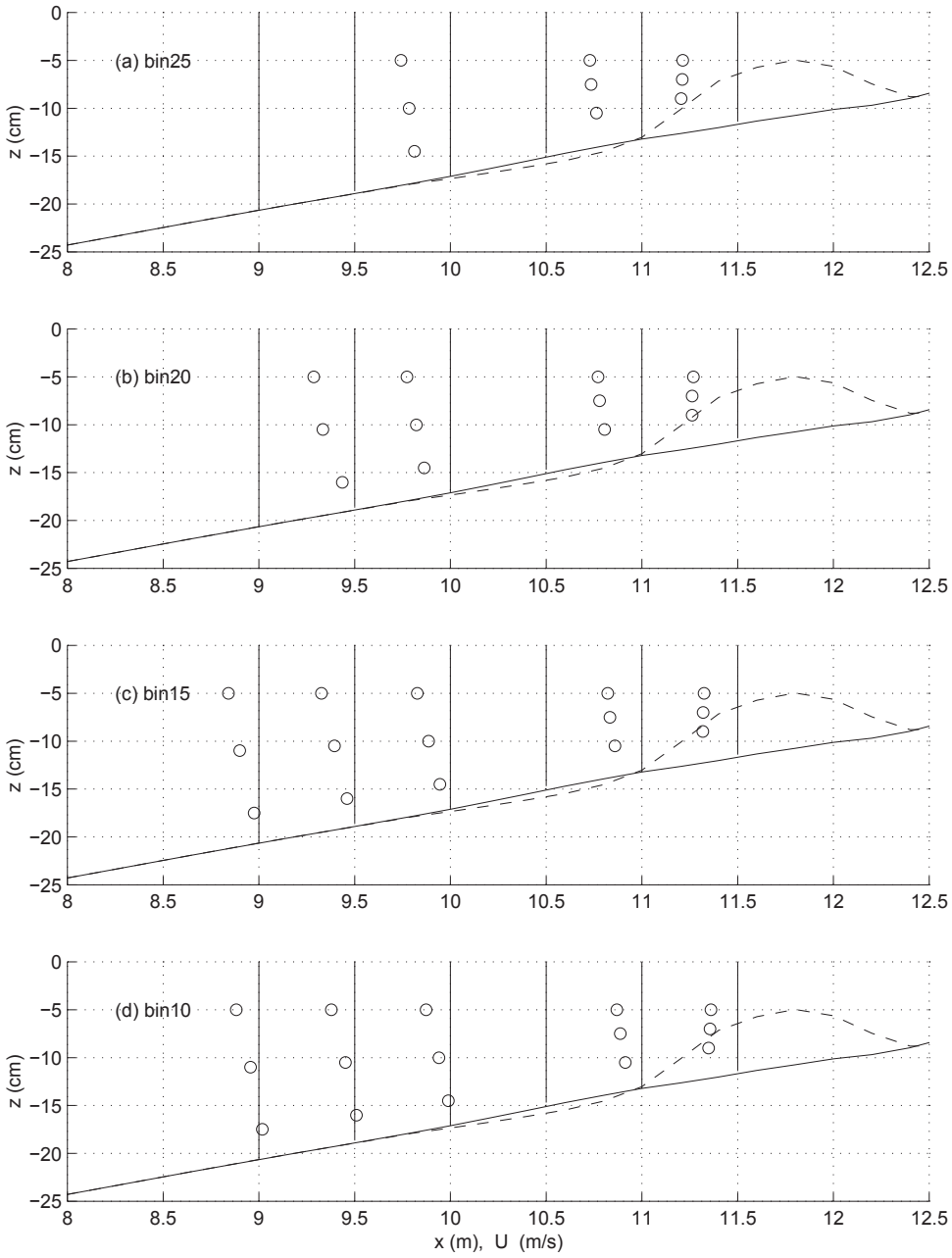

Figure 2.33: Bin-averaged rip current profiles from test T for (a) bin25, (b) bin20, (c) bin15 and (d) bin10. The vertical lines are the reference lines for each location.

In this case the bins contain more profiles because of the larger velocities associated with the bigger waves. However, the profiles in bin10 are similar to the profiles for the smaller wave conditions in Figure 2.13. These profiles have strong depth variations in the offshore region ($x \leq 10$ m) with larger velocities close to the surface and weaker or shoreward velocities near the bottom. At $x = 10$ m, the profile in bin25 shows weaker depth variations than the profile in bin10. The profile in bin25 represents the maximum burst of rip flow whereas the profile in bin10 represents either the beginning or the ending of a rip burst. For all the bins the profiles inside the channel are nearly depth uniform.

The larger waves carry more water over the bar leading to greater offshore discharge in the rip currents. Because the depth is the same as for the smaller wave case, the larger discharge leads directly to larger velocities in the rip current. In addition, the larger flux in the rip causes the velocity at the bottom to be increased leading to weaker vertical variation of the profiles.

2.2.4 Test U: Comparison Between the Two Rips

The purpose of this test series is to determine if the flow in the two rip channels behave similarly and are interacting. The locations of the measurements for Test U are shown in Figure 2.34. In this figure the (x) indicates locations of individual ADV's. In order to compare the behavior of each rip simultaneously, one ADV is placed at the same cross-shore position inside each channel. The third ADV is placed behind the bar at the center of the basin. These measurements are done for four runs at three different cross-shore positions.

The circles (o) in Figure 2.25 represent individual wave gages. One wave gage is again always located offshore ($x = 6$ m, $y = 16.2$ m) and is used to check repeatability of the experiments. In order to compare the wave conditions throughout the entire basin simultaneously, 7 wave gages are placed along a cross-shore line symmetrically about the centerline of the basin. The four runs from this series are

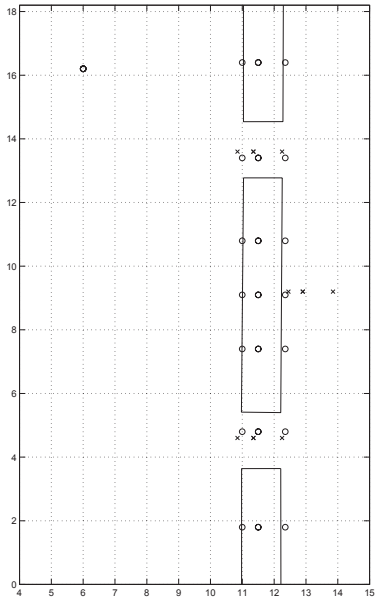

Figure 2.34: Location of the gages for Test U where (x) indicates ADV locations and (o) indicates wave gage locations.

done at three different cross-shore locations. Tables giving the exact location for all gages are in Appendix A.

Figure 2.35 shows longshore sections of the time-averaged wave heights for the four test cases. The measurements of the wave heights in (a) are taken at the offshore edge of the bar. Comparing the time-averaged wave heights at each rip reveals that the waves in the upper rip ($y = 4.6$ m) are around 5 cm and the waves in the lower rip (13.6 m) are only 4 cm. The other sections have similar trends, especially (c) where the wave height in the upper rip is around 5 cm and the wave height for the lower rip is around 3.5 cm. Wave current interaction plays a role in increasing the wave heights, therefore this disparity in the heights may indicate differences in the strength of the rip currents. Further analysis about the disparity between the rips using a numerical model is shown in Chapter 4.

Low-pass filtered time series of the mean water level are shown in Figure

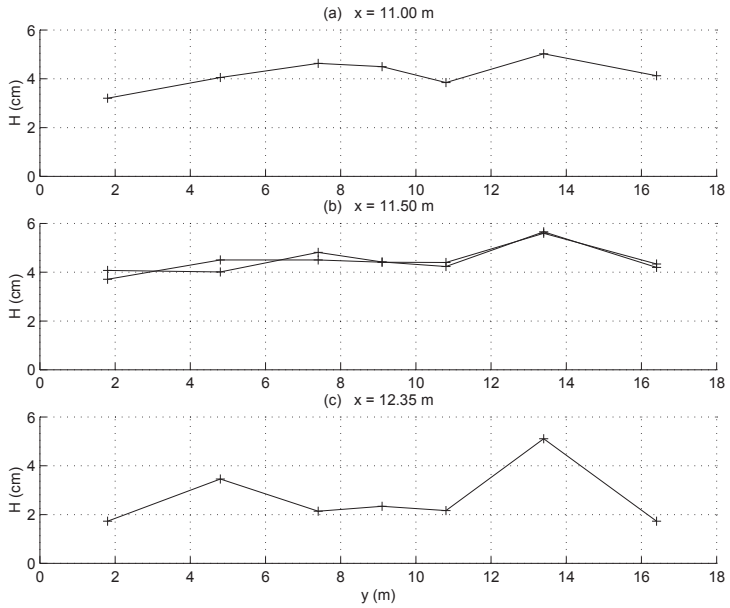

Figure 2.35: Time-averaged wave heights from series U for (a) $x = 11$, (b) $x = 11.5$ and (c) $x = 12.35$.

2.36 for the four test cases. Upon inspection it is immediately obvious that the variations of the water level in the two rips are distinctly different. The water level in the upper rip, $y = 13.6$ m, shows more large variations than the lower rip, $y = 4.6$. Rip currents cause the water level to decrease slightly so the dips in $\overline{\zeta}$ indicate rip currents. The water level variations signify that the upper channel has much more rip activity than the lower channel.

The energy for the water level is quantified in the frequency spectra shown in Figure 2.37. As expected, the low frequency energy for the water level in the upper rip channel is much larger than in the lower channel, particularly, the energy for the frequencies below 0.03 Hz. This frequency corresponds to the slow meandering as well as the appearance and disappearance of the rip current.

Figure 2.38 shows the low-pass filtered time series of the velocity from test

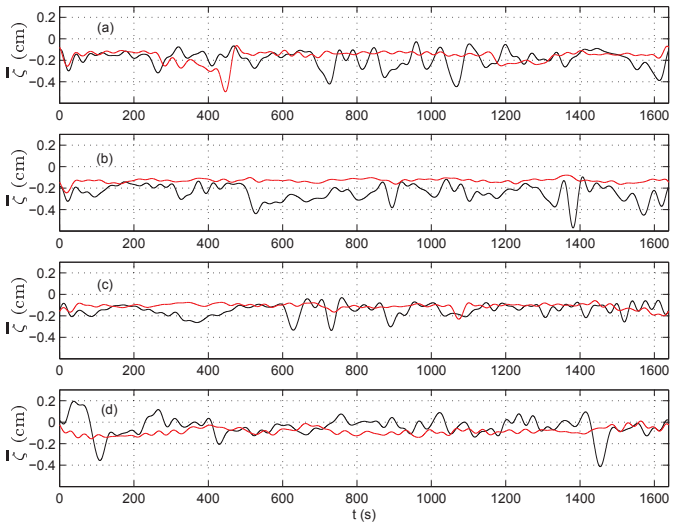

Figure 2.36: Low-pass filtered time series of the mean water level in each rip for (a) U1 $x = 11.35$, (b) U2 $x = 11.35$, (c) U3 $x = 10.85$ and (d) U4 $x = 12.25$ at the (red) lower rip $y = 4.6$ and (black) upper rip $y = 13.6$.

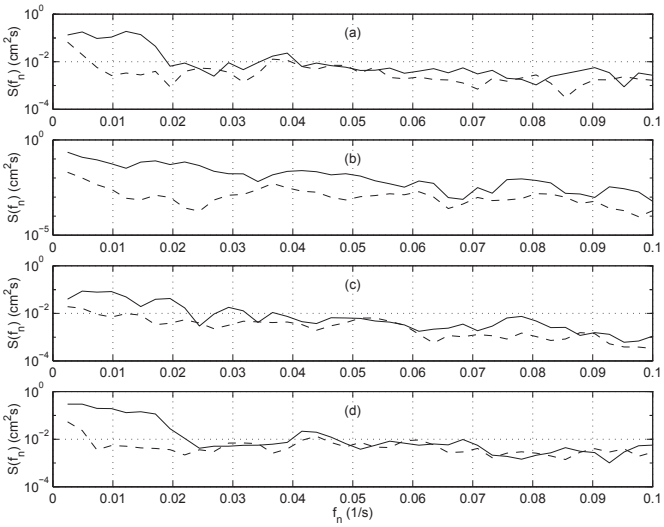

Figure 2.37: Energy spectra (16 degrees of freedom) for the water level in each rip for (a) U1 $x = 11.35$, (b) U2 $x = 11.35$, (c) U3 $x = 10.85$ and (d) U4 $x = 12.25$ with (-) upper rip $y = 13.6$ and (- -) lower rip $y = 4.6$.

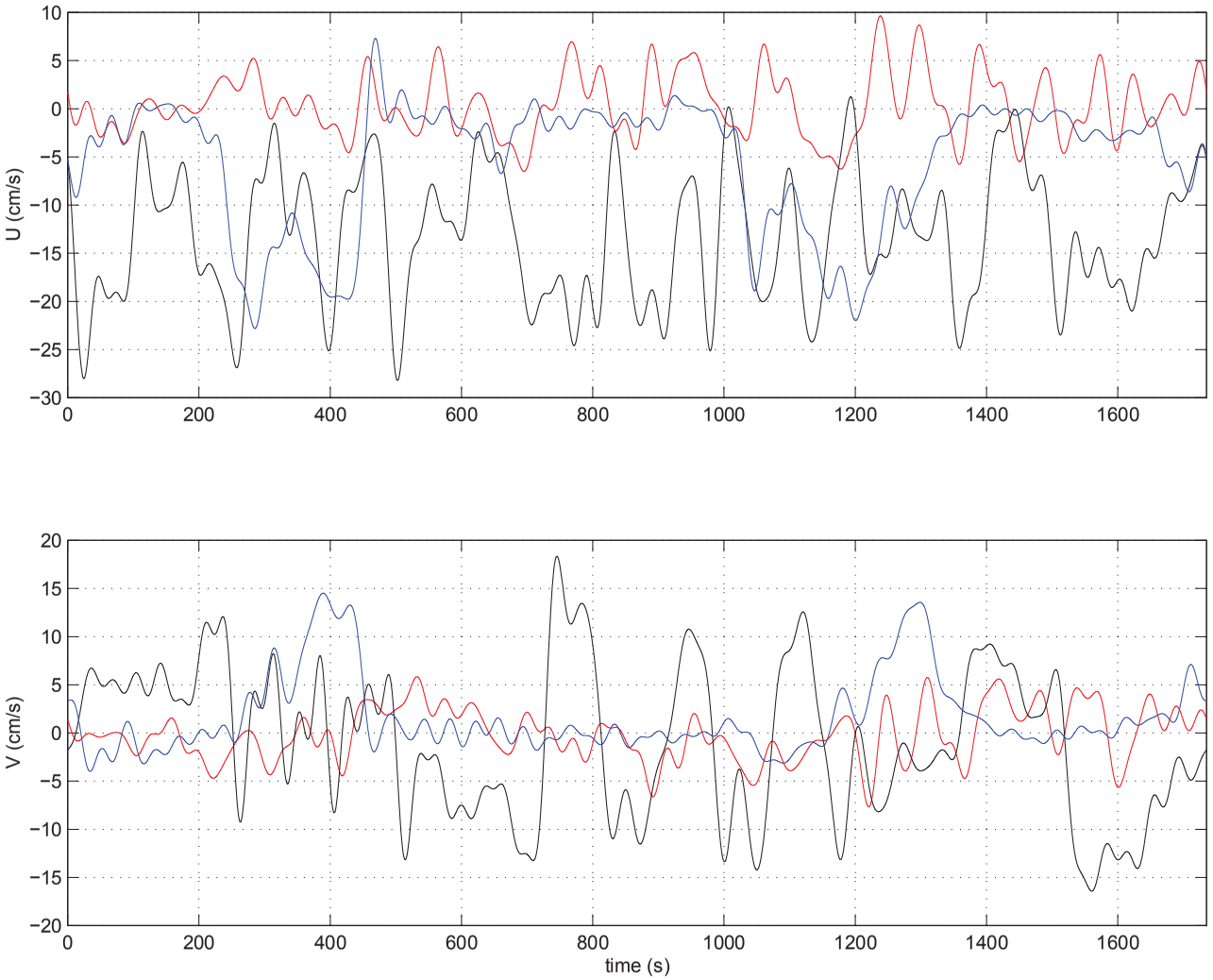

Figure 2.38: Low-pass filtered velocity time series at three depths for run U1. The top shows cross-shore velocities (U) and the bottom shows longshore velocities (V) with (red) between the rips $x = 12.9$, $y = 9$, (black) upper rip $x = 11.35$, $y = 13.6$ and (blue) lower rip $x = 11.35$, $y = 4.6$.

U1 where the measurements are taken in the middle of the channels. The cross-shore velocities show much more frequent rip events for the upper rip (black) than the lower rip (blue). The longshore velocity becomes large when the rip current appears, therefore, the longshore velocity for the lower rip (blue) is only significant during the two rip events between $300 < t < 500$ and $1100 < t < 1300$. The flow in the two rips appear to be unrelated and no obvious connection between the flow behind the bar (red) and the two rips is observed. Because the time scale of the rip events is long, usually several hundred seconds, the length of the time series is too short to produce any reliable correlations between the rips.

Because the differences between the two rips were so striking, the experiment was repeated for the same measurement locations. The time series of low-pass filtered velocities for the second test case, U2, is shown in Figure 2.39. Again, the lower rip has little activity whereas the upper rip has frequent events confirming the results from the previous test.

Time series of the low-pass filtered velocities at the offshore edge of the channels are shown in Figure 2.40. The frequency as well as the magnitude of the rip events in the lower channel ($y = 4.6$ m) are much lower than for the upper channel ($y = 13.6$ m). There does not appear to be any relationship between the two rips, such as flow alternating between the two channels. During the first rip event in the lower channel ($t = 700$ s) there is a strong rip in the upper channel. However, during the second rip event in the lower channel ($t = 1500$ s) there is no rip in the upper channel.

Finally Figure 2.41 shows the time series of the low-pass filtered velocities for test U4 where the measurements are taken at the shoreward edge of the channel. The lower channel again has fewer rip events than the upper channel. In addition, the peak velocities for the upper rip are substantially larger than the peak velocities in the lower rip. The longshore velocity in the lower channel is always negative

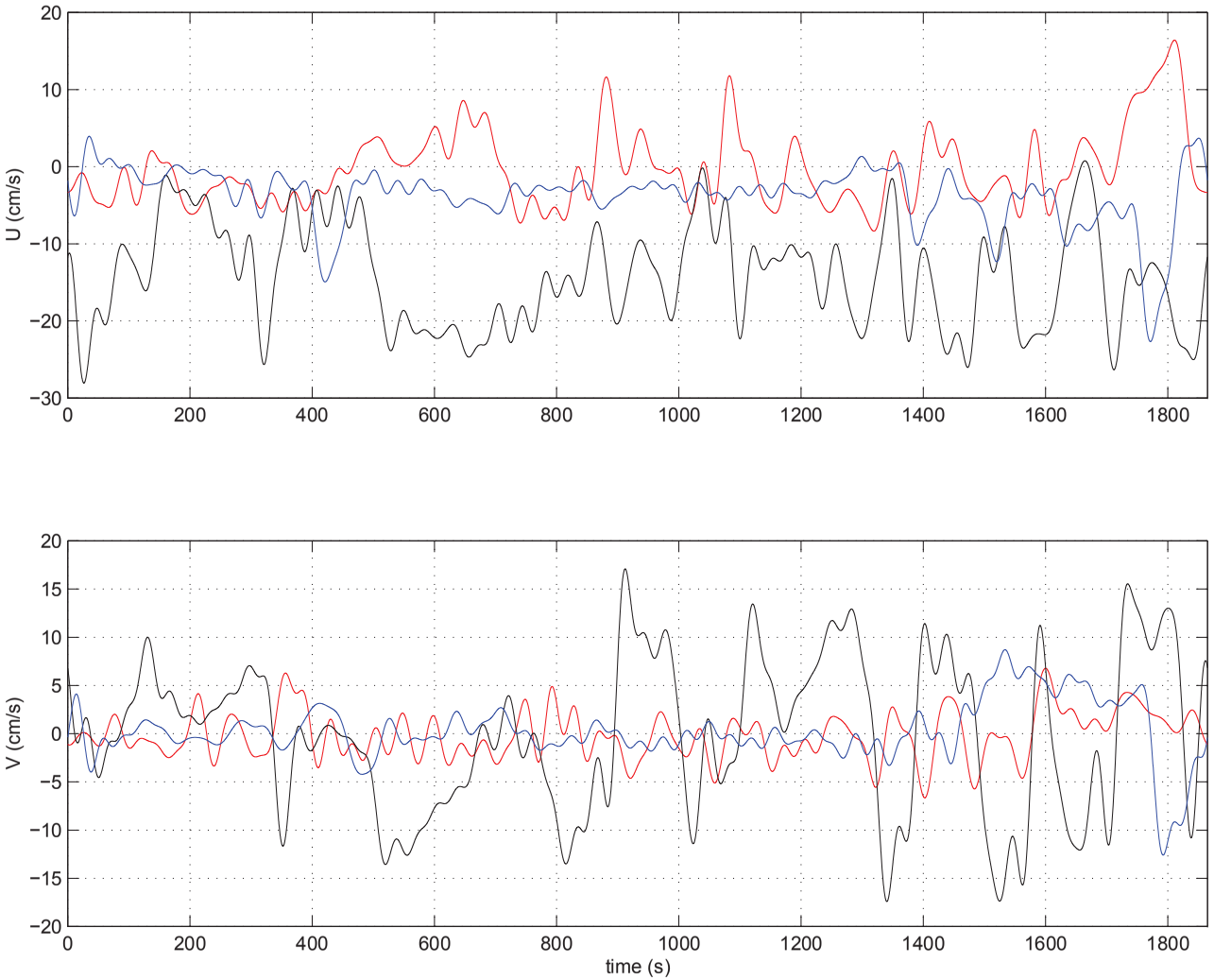

Figure 2.39: Low-pass filtered velocity time series at three depths for run U2. The top shows cross-shore velocities (U) and the bottom shows longshore velocities (V) with (red) between the rips $x = 12.9$, $y = 9$, (black) upper rip $x = 11.35$, $y = 13.6$ and (blue) lower rip $x = 11.35$, $y = 4.6$).

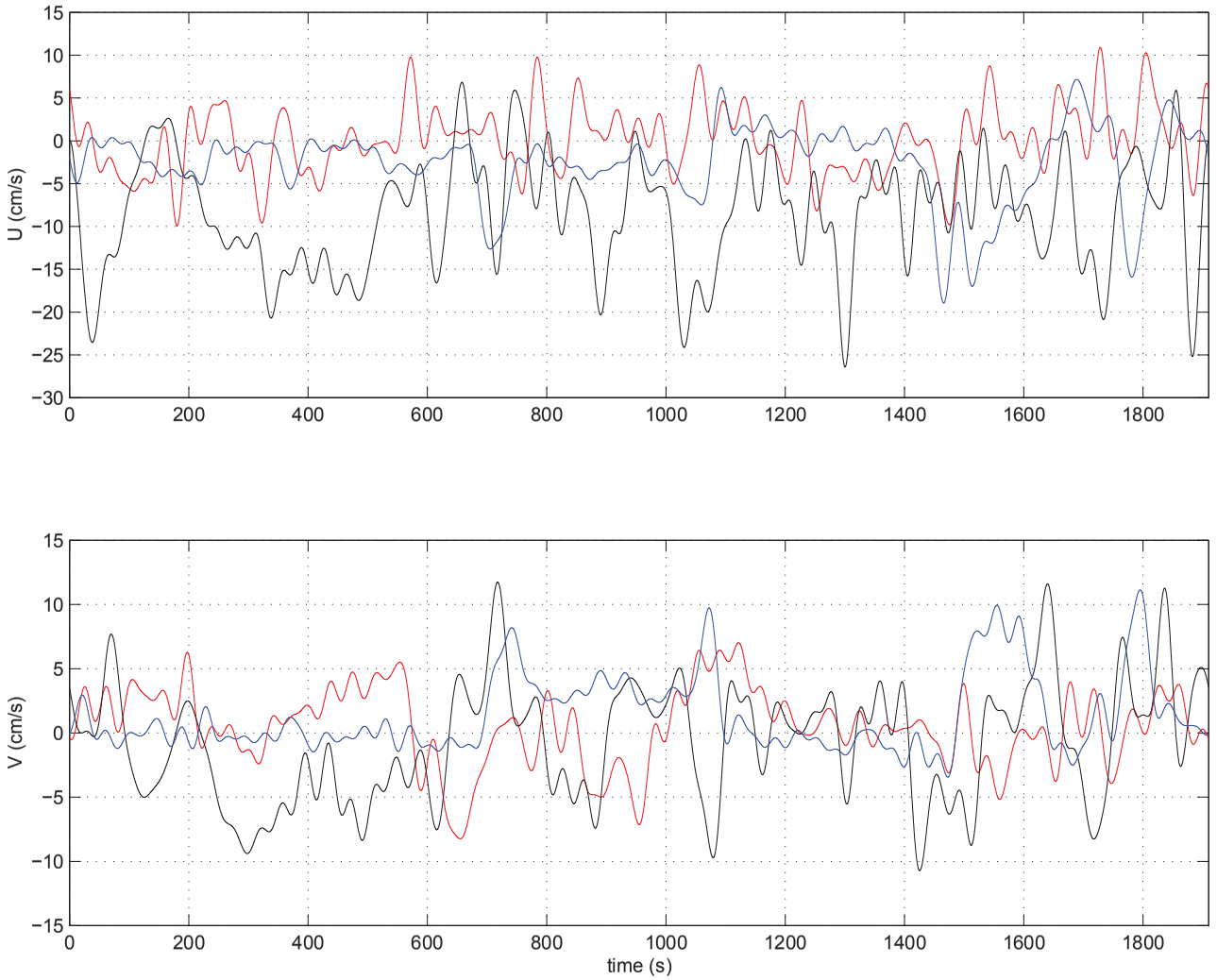

Figure 2.40: Low-pass filtered velocity time series at three depths for run U3. The top shows cross-shore velocities (U) and the bottom shows longshore velocities (V) with (red) between the rips $x = 12.45$, $y = 9$, (black) upper rip $x = 10.85$, $y = 13.6$ and (blue) lower rip $x = 10.85$, $y = 4.6$.

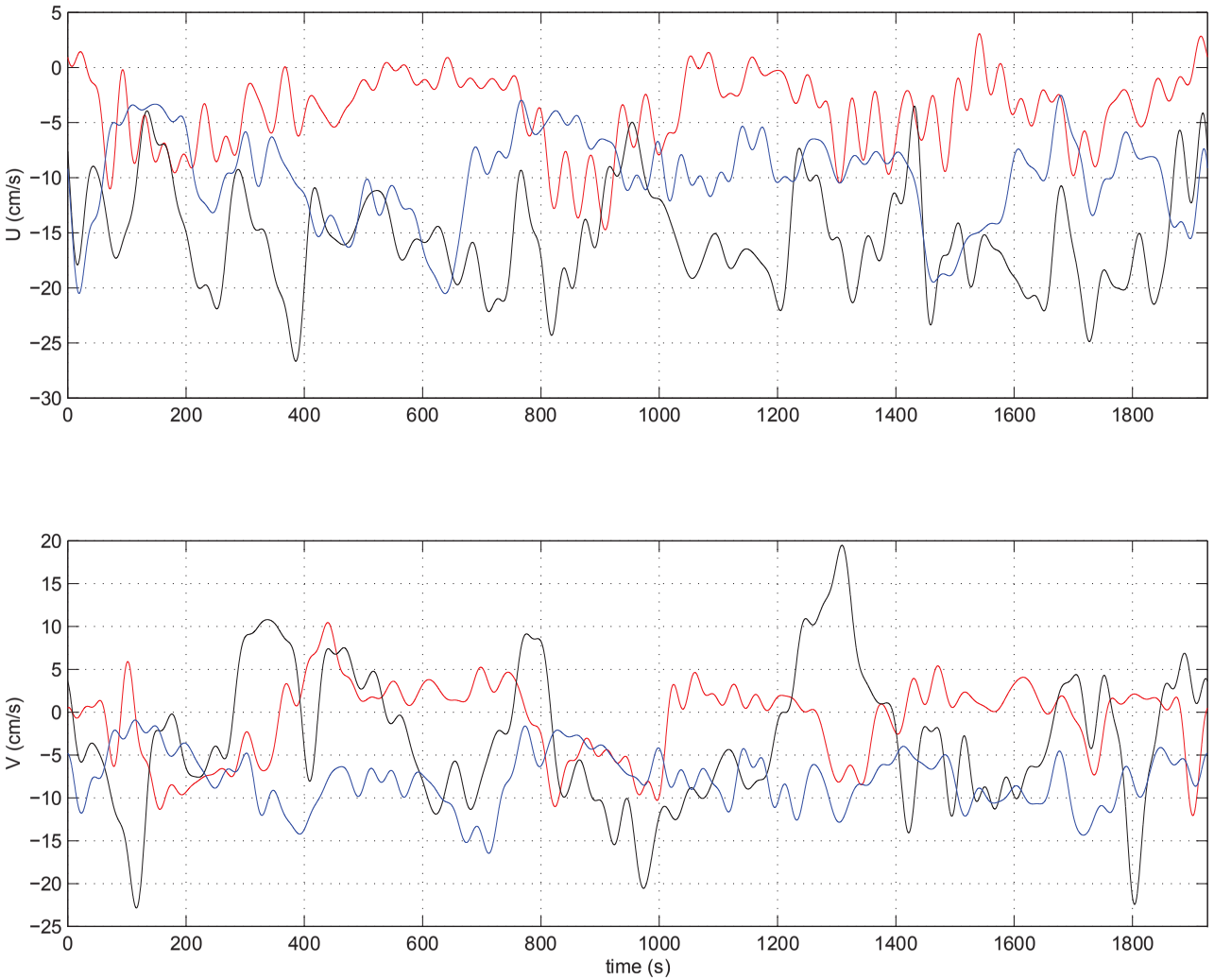

Figure 2.41: Low-pass filtered velocity time series at three depths for run U4. The top shows cross-shore velocities (U) and the bottom shows longshore velocities (V) with (red) between the rips $x = 13.85$, $y = 9$, (black) upper rip $x = 12.25$, $y = 13.6$ and (blue) lower rip $x = 12.25$, $y = 4.6$.

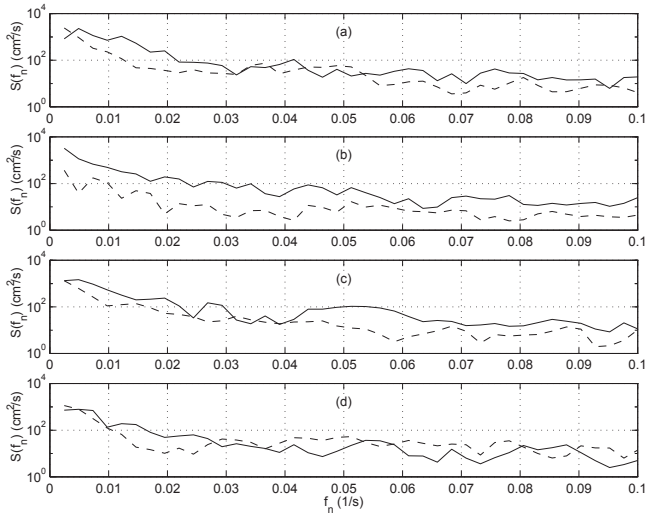

Figure 2.42: Energy spectra (16 degrees of freedom) for the cross-shore currents in each rip for (a) U1 $x = 11.35$, (b) U2 $x = 11.35$, (c) U3 $x = 10.85$ and (d) U4 $x = 12.25$ with (-) upper rip $y = 13.6$ and (- -) lower rip $y = 4.6$.

signifying that the current is passing through the channel at an angle. However, the longshore current in the upper rip fluctuates between positive and negative indicating that there is no dominant direction for the flow in this channel.

Figure 2.42 shows the energy spectra of the cross-shore flow in the two rips for the four test cases. As expected the low frequency energy in the upper rip is considerably higher than the energy in the lower rip. The fluctuations for the two rips are similar for test U4, therefore in (d), the energy for both rips are similar for $f_n > 0.03$ Hz.

The coherence between the cross-shore flow in the two rip channels is shown in Figure 2.43 for the four test cases. The coherence is below the 90% confidence limit for the majority of frequencies. This is an indication that the flow in the two channels are not interacting with each other.

It is interesting to note that the rip events in the upper channel, where the

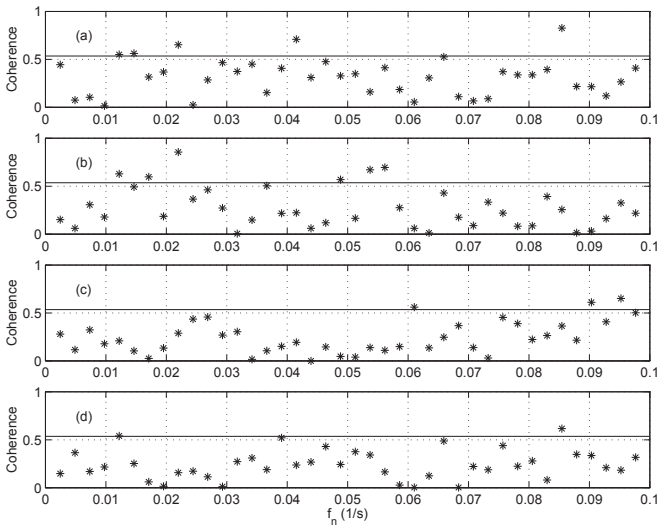

Figure 2.43: Coherence between for the cross-shore currents in each rip for (a) U1 $x = 11.35$, (b) U2 $x = 11.35$, (c) U3 $x = 10.85$ and (d) U4 $x = 12.25$. The straight line indicates the limit of 90% confidence of nonzero coherence

vast majority of previous measurements were made, appear sporadically. There is no particular pattern to when rips appear in this channel. However, the rip in the lower channel, at least in these four test series, is more predictable in the sense that for every time series there are two separate rip events. No comments about the regularity of these rip events can be made without running the experiments longer allowing for more possible rip events.

This test series showed that the flow in the two rip channels behave differently. The upper rip channel, where the vast majority of measurements have been made, is much more energetic than the lower rip channel. In addition, the two rips do not seem to be interacting with each other.

2.2.5 Summary

This subsection summarizes the results of the four experimental test series. Test series R was the initial series and found that the rip currents were unstable with multiple time scales. The rip currents caused the wave heights to increase and the mean water level to decrease. The rip currents had strong depth variations outside the breakers with large offshore velocity near the surface and weak or shoreward velocity near the bottom. Inside the channel, however, the rip current had nearly depth uniform velocities. Bin-averaging and maximum averaging provided good spatial descriptions of the profiles. The instantaneous profiles showed that the currents outside the breakers twist over the depth but are essentially depth uniform inside the channel.

Test series S showed that even at the same location, the rip events were different for separate runs. This series also provide much more detailed vertical profiles. It is found that the larger rip bursts containing more volume flux has less depth variation than smaller rip burst at the same location.

In test series T it was found that the larger waves carry more water over the bar leading to greater offshore discharge in the rip currents. Because the depth is the same as for the smaller wave case, the larger discharge leads directly to larger velocities in the rip current. In addition, the larger flux in the rip causes the velocity at the bottom to be increased leading to weaker vertical variation of the profiles.

Test series U showed that the flow in the two channels do not appear to be interacting with each other. In addition, this series showed that the two rips are different from one another. The rip where the majority of the measurements were made is much more active than the other rip.

Chapter 3

SHORECIRC GOVERNING EQUATIONS

This chapter outlines the derivations of the governing equations used in SHORECIRC (SC). The first section shows the derivation for the time-averaged and depth-integrated equations. We follow the method outlined in detail by Putrevu and Svendsen (1991). The derivation of the mass equation is given in detail, for brevity however, the derivation of the momentum equation is only outlined.

The second section derives the equations for the vertical variation of the currents. This derivation follows the method given by Putrevu and Svendsen (1999), although using a different definition for the splitting of the current velocity.

The third section derives the expressions for the 3D dispersive mixing coefficients. This derivation also follows Putrevu and Svendsen (1999) but again utilizes a different definition for the currents.

The next section presents the simplifications that we make in order to solve the equations in SC. The final forms of the governing equations are also shown.

The final section discusses the closure models used by SC when solving the governing equations. This section primarily focuses on how the subgrid stresses (SGS) are modeled. A more detailed discussion for the rest of the closure models is found in Sancho and Svendsen (1997).

3.1 Time-Averaged Depth-Integrated Equations

We follow the technique outlined by Lesieur and Métais (1996), Wilcox (1998) and Rogallo and Moin (1984) for obtaining equations similar to the Reynolds equations. We begin with the Navier-Stokes equations. The mass equation is given as

$$\frac{\partial u_\alpha}{\partial x_\alpha} = 0 \tag{3.1}$$

and the momentum equation is given by

$$\frac{\partial u_\alpha}{\partial t} + \frac{\partial u_\alpha u_\beta}{\partial x_\beta} = -\frac{1}{\rho}\frac{\partial p}{\partial x_\alpha} + \frac{1}{\rho}\frac{\partial \tau^v_{\alpha\beta}}{\partial x_\beta} \tag{3.2}$$

where α and β are indices for the horizontal directions, u_α is the velocity in the α direction, x_α is the spatial coordinate in the α direction, t is time, ρ is density, p is pressure and $\frac{1}{\rho}\tau^v_{\alpha\beta}$ is the viscous stress.

The subgrid fluctuations are eliminated using a method similar to Reynold's averaging. We use a low-pass filter function G characterized by

$$\widehat{u_\alpha}(x_\alpha, t) = \int G(x_\alpha - \xi_\alpha) u_\alpha(\xi_\alpha, t) d\xi_\alpha \tag{3.3}$$

where $\widehat{u_\alpha}$ is the resolvable filtered velocity. Numerically speaking, the resolvable velocity is the velocity at the discrete points on the grid. The fluctuations relative to $\widehat{u_\alpha}$ is defined as

$$u'_\alpha = u_\alpha - \widehat{u_\alpha}. \tag{3.4}$$

u'_α essentially represents the velocity variations with subgrid length scale.

Applying the filter to the continuity equation,(3.1), results in the following equation,

$$\frac{\partial \widehat{u_\alpha}}{\partial x_\alpha} = 0. \tag{3.5}$$

After applying the filter to equation (3.2), the momentum equation becomes,

$$\frac{\partial \widehat{u_\alpha}}{\partial t} + \frac{\partial \widehat{u_\alpha}\,\widehat{u_\beta}}{\partial x_\beta} = -\frac{1}{\rho}\frac{\partial \widehat{p}}{\partial x_\alpha} + \frac{1}{\rho}\frac{\partial \widehat{\tau^v_{\alpha\beta}}}{\partial x_\beta} + \frac{1}{\rho}\frac{\partial T_{\alpha\beta}}{\partial x_\beta} \tag{3.6}$$

where $T_{\alpha\beta}$ is defined by

$$T_{\alpha\beta} = \rho(\widehat{u_\alpha}\,\widehat{u_\beta} - \widehat{u_\alpha u_\beta}) \tag{3.7}$$

which is the subgrid stress tensor. This subgrid stress is created by the shear in the flow as well as the bottom friction and the wave breaking. Therefore, several closure models are required and are discussed in section 3.5. In addition, we assume that

$$T_{\alpha\beta} > \widehat{\tau^v_{\alpha\beta}} \tag{3.8}$$

therefore, the viscous stresses $(\widehat{\tau^v_{\alpha\beta}})$ are neglected which results in the momentum equation written as

$$\frac{\partial \widehat{u_\alpha}}{\partial t} + \frac{\partial \widehat{u_\alpha}\,\widehat{u_\beta}}{\partial x_\beta} = -\frac{1}{\rho}\frac{\partial \widehat{p}}{\partial x_\alpha} + \frac{1}{\rho}\frac{\partial T_{\alpha\beta}}{\partial x_\beta}. \tag{3.9}$$

The difference between equation (3.9) and the Reynold's momentum equation is in the shear stress term (3.7). When using Reynold's averaging the convective term becomes

$$\widehat{u_\alpha u_\beta} = \widehat{u_\alpha}\,\widehat{u_\beta} + \widehat{u'_\alpha u'_\beta}\,. \tag{3.10}$$

Alternatively, applying the filter to the convective term results in

$$\widehat{u_\alpha u_\beta} = \widehat{u_\alpha}\,\widehat{u_\beta} + L_{\alpha\beta} + C_{\alpha\beta} + R_{\alpha\beta} \tag{3.11}$$

where

$$L_{\alpha\beta} = \widehat{\widehat{u_\alpha}\,\widehat{u_\beta}} - \widehat{u_\alpha}\,\widehat{u_\beta} \tag{3.12}$$

$$C_{\alpha\beta} = \widehat{\widehat{u_\alpha}\,u'_\beta} + \widehat{u'_\alpha\,\widehat{u_\beta}} \tag{3.13}$$

$$R_{\alpha\beta} = \widehat{u'_\alpha u'_\beta} \tag{3.14}$$

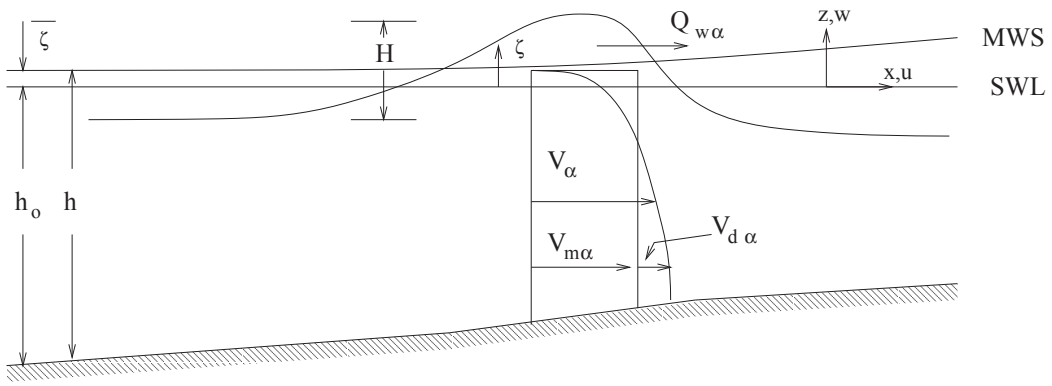

Figure 3.1: Definition sketch.

$L_{\alpha\beta}$ is the Leonard stress, $C_{\alpha\beta}$ is the cross-term stress and $R_{\alpha\beta}$ is the SGS Reynold's stress (Wilcox, 1998). The Leonard stress is implicitly included in the numerical scheme, therefore no further modeling of that term is needed. The cross-term and SGS Reynold's stresses are usually modeled together. Ultimately the difference between the Reynold's approach and the filtering approach is the addition of more turbulence accounting for dissipation by the unresolved eddies.

3.1.1 Mass Equation

This section derives the depth-integrated wave-averaged mass equation. We begin with equation (3.5) and rewrite it such that α and β are the indices for the horizontal components only. Dropping the overbraces for convenience gives the following equation,

$$\frac{\partial u_\alpha}{\partial x_\alpha} + \frac{\partial w}{\partial z} = 0 \tag{3.15}$$

where w is the vertical component of the velocity and z is the vertical direction defined as positive from the still water level (SWL) up, as indicated in Figure 3.1.

Integrating this equation from the bottom, $z = -h_o$, to the instantaneous surface, $z = \zeta$, gives

$$\int_{-h_o}^{\zeta} \frac{\partial u_\alpha}{\partial x_\alpha} dz + w(\zeta) - w(-h_o) = 0 \tag{3.16}$$

Using the Leibniz Rule on the first term results in

$$\int_{-h_o}^{\zeta} \frac{\partial u_\alpha}{\partial x_\alpha} dz = \frac{\partial}{\partial x_\alpha} \int_{-h_o}^{\zeta} u_\alpha dz - \frac{\partial \zeta}{\partial x_\alpha} u_\alpha(\zeta) + \frac{\partial(-h_o)}{\partial x_\alpha} u_\alpha(-h_o). \tag{3.17}$$

In addition, the bottom boundary condition is defined as

$$w(-h_o) + u_\alpha(-h_o) \frac{\partial h_o}{\partial x_\alpha} = 0 \tag{3.18}$$

and the kinematic free surface boundary condition is defined as

$$w(\zeta) - u_\alpha(\zeta) \frac{\partial \zeta}{\partial x_\alpha} = \frac{\partial \zeta}{\partial t}. \tag{3.19}$$

Substituting equations (3.17),(3.18) and (3.19) into equation (3.16) gives

$$\frac{\partial \zeta}{\partial t} + \frac{\partial}{\partial x_\alpha} \int_{-h_o}^{\zeta} u_\alpha dz = 0 \tag{3.20}$$

The total volume flux Q_α is defined as

$$Q_\alpha \equiv \int_{-h_o}^{\zeta} u_\alpha dz. \tag{3.21}$$

Substituting equation (3.21) into equation (3.20) and averaging over a wave period yields the final form of the continuity equation

$$\frac{\partial \overline{\zeta}}{\partial t} + \frac{\partial \overline{Q_\alpha}}{\partial x_\alpha} = 0 \tag{3.22}$$

with the overbar is defined as

$$\overline{\cdot} = \frac{1}{T} \int_0^T \cdot \, dt \tag{3.23}$$

where T is the short wave period.

The velocity u_α is split into two components

$$u_\alpha = V_\alpha + u_{w\alpha} \tag{3.24}$$

where V_α is the current component and $u_{w\alpha}$ is the short-wave component. In addition, the distribution of the short-wave velocity is defined such that

$$\overline{u_{w\alpha}} = 0 \quad \text{below trough.} \tag{3.25}$$

The short-wave induced volume flux is defined as

$$Q_{w\alpha} \equiv \overline{\int_{\zeta_t}^{\zeta} u_{w\alpha}\, dz} \tag{3.26}$$

where ζ_t indicates the trough level.

3.1.2 Horizontal Momentum Equations

This subsection outlines the derivation of the depth-integrated wave-averaged horizontal momentum equations. We follow the procedure outlined by Putrevu and Svendsen (1991), which is an extension of the methods by Phillips (1977) and Mei (1983).

We begin with the filtered Navier-Stokes momentum equations, (3.9), which are rewritten here dropping the overbraces for convenience,

$$\frac{\partial u_\alpha}{\partial t} + \frac{\partial u_\alpha u_\beta}{\partial x_\beta} + \frac{\partial u_\beta w}{\partial z} = -\frac{1}{\rho}\frac{\partial p}{\partial x_\alpha} + \frac{1}{\rho}\left(\frac{\partial T_{\alpha\beta}}{\partial x_\beta} + \frac{\partial T_{\alpha z}}{\partial z}\right) \tag{3.27}$$

where α and β are index notation for the horizontal directions.

The derivation proceeds with the following steps:

- The momentum equation is integrated from the bottom ($-h_o$) to the surface (ζ).
- The Leibniz Rule is used to move the partial derivatives outside the integrals, similar to equation (3.17).

- The bottom boundary condition, equation (3.18) and the kinematic free surface boundary condition equation (3.19) are used to eliminate the boundary terms resulting from the application of Leibniz Rule. In addition the dynamic boundary conditions at the bottom and the free surface are applied to get the equations in terms of the bottom and surface shear stresses.

The resulting equation is then time-averaged over the short-wave period to yield

$$\frac{\partial}{\partial t}\overline{\int_{-h_o}^{\zeta} u_\alpha dz} + \frac{\partial}{\partial x_\beta}\overline{\int_{-h_o}^{\zeta} u_\alpha u_\beta \, dz} = \frac{1}{\rho}\overline{p(-h_o)}\frac{\partial h_o}{\partial x_\alpha}$$
$$-\frac{1}{\rho}\frac{\partial}{\partial x_\beta}\overline{\left(\int_{-h_o}^{\zeta} p\delta_{\alpha\beta} - T_{\alpha\beta}dz\right)} + \frac{\tau_\alpha^S}{\rho} - \frac{\tau_\alpha^B}{\rho} \tag{3.28}$$

where the overbar is the time-average as defined by equation (3.23).

In order to eliminate the pressure take the vertical momentum equation

$$\frac{\partial w}{\partial t} + \frac{\partial w u_\beta}{\partial x_\beta} + \frac{\partial w^2}{\partial z} = -\frac{1}{\rho}\frac{\partial p}{\partial z} - g + \frac{1}{\rho}\left(\frac{\partial T_{z\beta}}{\partial x_\beta} + \frac{\partial T_{zz}}{\partial z}\right) \tag{3.29}$$

and integrate it from a level z to the free surface ζ. Using the Leibniz Rule and the surface boundary conditions yield the following expression for the pressure

$$p(z) = \rho g(\zeta - z) - \rho w^2 + T_{zz} + \frac{\partial}{\partial t}\int_z^\zeta \rho w dz + \frac{\partial}{\partial x_\beta}\int_z^\zeta (\rho u_\beta w - T_{\beta z})dz. \tag{3.30}$$

Using equation (3.30) to find the pressure at the bottom and time-averaging over a wave period yields

$$p(-h_o) = \rho g(\overline{\zeta} + h_o) + \frac{\partial}{\partial x_\beta}\overline{\int_z^\zeta (\rho u_\beta w - T_{\beta z})dz} \simeq \rho g(\overline{\zeta} + h_o). \tag{3.31}$$

We assume that over a wave period the weight of the water column is supported by itself and is not transfered to its neighbor. Therefore, the second term is small and the wave-averaged pressure at the bottom is essentially hydrostatic. Substitute (3.31) into the horizontal momentum equation (3.28) to get

$$\frac{\partial}{\partial t}\overline{\int_{-h_o}^{\zeta} u_\alpha dz} + \frac{\partial}{\partial x_\beta}\overline{\int_{-h_o}^{\zeta} u_\alpha u_\beta \, dz} =$$
$$-gh\frac{\partial \overline{\zeta}}{\partial x_\alpha} - \frac{1}{\rho}\frac{\partial}{\partial x_\beta}\left(\overline{\int_{-h_o}^{\zeta} p\delta_{\alpha\beta} dz} - \delta_{\alpha\beta}\frac{1}{2}\rho g h^2\right)$$
$$+\frac{1}{\rho}\frac{\partial}{\partial x_\beta}\overline{\int_{-h_o}^{\zeta} T_{\alpha\beta} dz} + \frac{\tau_\alpha^S}{\rho} - \frac{\tau_\alpha^B}{\rho} \tag{3.32}$$

where h is the total water depth as defined by

$$h \equiv h_o + \overline{\zeta}. \tag{3.33}$$

Substituting (3.24) into (3.21) and time averaging the result yields

$$\overline{Q_\alpha} = \overline{\int_{-h_o}^{\zeta} V_\alpha dz} + \overline{\int_{\zeta_t}^{\zeta} u_{w\alpha} dz} = \overline{\int_{-h_o}^{\zeta} V_\alpha dz} + Q_{w\alpha}. \tag{3.34}$$

Introducing the velocity split, equation (3.24) into the convective acceleration terms produces the following formulation

$$\overline{\int_{-h_o}^{\zeta} u_\alpha u_\beta \, dz} = \overline{\int_{-h_o}^{\zeta} V_\alpha V_\beta dz} + \overline{\int_{-h_o}^{\zeta} u_{w\alpha} u_{w\beta} dz} + \overline{\int_{\zeta_t}^{\zeta} u_{w\alpha} V_\beta + u_{w\beta} V_\alpha dz}. \tag{3.35}$$

The horizontal momentum equation (3.32) is rewritten using (3.24), (3.34) and (3.35) to get

$$\frac{\partial \overline{Q}_\alpha}{\partial t} + \frac{\partial}{\partial x_\beta}\overline{\int_{-h_o}^{\zeta} V_\alpha V_\beta dz} + \frac{\partial}{\partial x_\beta}\overline{\int_{\zeta_t}^{\zeta} u_{w\alpha} V_\beta + u_{w\beta} V_\alpha dz} =$$
$$-gh\frac{\partial \overline{\zeta}}{\partial x_\alpha} - \frac{1}{\rho}\frac{\partial}{\partial x_\beta}\left[S_{\alpha\beta} - \overline{\int_{-h_o}^{\zeta} T_{\alpha\beta} dz}\right] + \frac{\tau_\alpha^S}{\rho} - \frac{\tau_\alpha^B}{\rho} \tag{3.36}$$

where the radiation stress $S_{\alpha\beta}$ is defined as

$$S_{\alpha\beta} \equiv \overline{\int_{-h_o}^{\zeta} p\delta_{\alpha\beta} + \rho u_{w\alpha} u_{w\beta} \, dz} - \delta_{\alpha\beta}\frac{1}{2}\rho g h^2. \tag{3.37}$$

3.1.3 Choices for Splitting the Current

In the previous section, the momentum equation (3.36) is written in terms of a current velocity, V_α and a short-wave velocity, $u_{w\alpha}$ using the split defined by

(3.24). It is convenient to split the velocity further by dividing the current into depth uniform and depth varying components. This subsection discusses the two choices proposed by Svendsen and Putrevu (1996) for performing this split.

The first choice, which is the method used in previous versions of SC (i.e. Svendsen and Putrevu (1994), Van Dongeren and Svendsen (1997), Sancho and Svendsen (1997) and Putrevu and Svendsen (1999)) is to split the current using

$$V_\alpha(z) = \tilde{V}_\alpha + V_{1\alpha}(z) \tag{3.38}$$

where we define

$$\tilde{V}_\alpha \equiv \frac{1}{h}\overline{\int_{-h_o}^{\zeta} u_\alpha \, dz} = \frac{\overline{Q}_\alpha}{h}. \tag{3.39}$$

This implies

$$\overline{\int_{-h_o}^{\zeta} V_{1\alpha} \, dz} = -Q_{w\alpha}. \tag{3.40}$$

Substituting (3.38) into (3.36) yields

$$\begin{aligned}
&\frac{\partial \overline{Q}_\alpha}{\partial t} + \frac{\partial}{\partial x_\alpha}\left(\frac{\overline{Q}_\alpha \overline{Q}_\beta}{h}\right) + \frac{\partial}{\partial x_\beta}\overline{\int_{-h_o}^{\zeta} V_{1\alpha}V_{1\beta}dz} \\
&+\frac{\partial}{\partial x_\beta}\overline{\int_{\zeta_t}^{\zeta} u_{w\alpha}V_{1\beta} + u_{w\beta}V_{1\alpha}dz} = \\
&-gh\frac{\partial \overline{\zeta}}{\partial x_\alpha} - \frac{1}{\rho}\frac{\partial}{\partial x_\beta}\left[S_{\alpha\beta} - \overline{\int_{-h_o}^{\zeta} T_{\alpha\beta}dz}\right] + \frac{\tau_\alpha^S}{\rho} - \frac{\tau_\alpha^B}{\rho}.
\end{aligned} \tag{3.41}$$

The second option is to split the current as follows,

$$V_\alpha(z) = V_{m\alpha} + V_{d\alpha}(z) \tag{3.42}$$

where we define

$$V_{m\alpha} \equiv \frac{\overline{Q}_\alpha - Q_{w\alpha}}{h}. \tag{3.43}$$

Similar to (3.40) we find that

$$\overline{\int_{-h_o}^{\zeta} V_{d\alpha} \, dz} = 0. \tag{3.44}$$

Substituting (3.42) into (3.36) yields

$$\frac{\partial \overline{Q}_\alpha}{\partial t} + \frac{\partial}{\partial x_\alpha}\left(\frac{\overline{Q}_\alpha \overline{Q}_\beta}{h}\right) + \frac{\partial}{\partial x_\beta}\overline{\int_{-h_o}^{\zeta} V_{d\alpha} V_{d\beta} dz}$$
$$+\frac{\partial}{\partial x_\beta}\overline{\int_{\zeta_t}^{\zeta} u_{w\alpha} V_{d\beta} + u_{w\beta} V_{d\alpha} dz} =$$
$$-gh\frac{\partial \overline{\zeta}}{\partial x_\alpha} - \frac{1}{\rho}\frac{\partial}{\partial x_\beta}\left[S'_{\alpha\beta} - \overline{\int_{-h_o}^{\zeta} T_{\alpha\beta} dz}\right] + \frac{\tau^S_\alpha}{\rho} - \frac{\tau^B_\alpha}{\rho} \tag{3.45}$$

where a modified radiation stress similar to the definition used by Phillips (1977) is defined as,

$$S'_{\alpha\beta} = S_{\alpha\beta} - \frac{Q_{w\alpha} Q_{w\beta}}{h}. \tag{3.46}$$

It is first emphasized that both methods include all terms in the full equations. The differences between the two methods for splitting the velocity are subtle, but important. First of all, the velocity $\tilde{V}_\alpha$ is a non-physical current that cannot be measured, whereas the current $V_{m\alpha}$ can be measured directly by integrating velocity measurements over depth and averaging them over a wave period.

When simplifying the model to depth uniform currents it is apparent from (3.40) that the current $V_{1\alpha}$ reduces to $\frac{-Q_{w\alpha}}{h}$. The integral terms in (3.41) then reduce to $-\frac{Q_{w\alpha} Q_{w\beta}}{h}$.

On the other hand, because of (3.44), $V_{d\alpha}$ vanishes for the depth uniform current case. This means that the integral terms in (3.45) vanish as well. The contribution from the integral terms for the depth uniform currents are already included in the modified radiation stress as evident in (3.46).

It is fairly straightforward to find the relationship between the two methods for splitting the current. By using (3.39) and (3.43) together we find

$$V_{m\alpha} = \tilde{V}_\alpha - \frac{Q_{w\alpha}}{h} \tag{3.47}$$

and by using (3.38), (3.42) and (3.47) we find

$$V_{d\alpha} = V_{1\alpha} + \frac{Q_{w\alpha}}{h}. \tag{3.48}$$

Hence, it is evident that the only difference between the two methods for splitting the current is the choice of which current term contains the contribution from the short-wave volume flux ($-\frac{Q_{w\alpha}}{h}$). The best method for understanding where this short-wave contribution comes from is to take the example of one-dimensional undertow for normally incident waves. In this example there is no net cross-shore flow, therefore, the return flow must equal the short-wave volume flux. The depth integral of the undertow is given as

$$\overline{\int_{-h_o}^{\zeta} V_\alpha \, dz} = -Q_{w\alpha}. \tag{3.49}$$

The difference between the two methods for splitting the current is in which current component will satisfy condition (3.49). The first method includes it with the depth varying term ($V_{1\alpha}$) as (3.40). This has an advantage because it simplifies the solution for the depth varying currents. On the other hand, the second method includes it with the depth uniform term ($V_{m\alpha}$) as (3.44) indicates.

The previous versions of SC used the $\tilde{V}_\alpha$ and $V_{1\alpha}$ method because of the simplifications in the derivations. Here we use the alternate method with $V_{m\alpha}$ and $V_{d\alpha}$ because it is a more physical current split. It also has advantages in the calculation of the 3D dispersive mixing terms that will be evident in section 3.4.

3.2 Solution for the Vertical Velocity Profiles

The momentum equations given by (3.45) are all in terms of depth-averaged properties except for the integral terms. In this section expressions for the depth varying current $V_{d\alpha}$ are derived. The derivation closely follows the method from Putrevu and Svendsen (1999) although it uses the alternate velocity split. Therefore, once we introduce the split for the current, the governing equation for the vertical variation will include several extra terms. In addition, the boundary conditions for the vertical varying current will be different.

We begin with the local horizontal momentum balance as given by (3.27) which is rewritten here for convenience,

$$\frac{\partial u_\alpha}{\partial t} + \frac{\partial u_\alpha u_\beta}{\partial x_\beta} + \frac{\partial u_\alpha w}{\partial z} = -\frac{1}{\rho}\frac{\partial p}{\partial x_\alpha} + \frac{1}{\rho}\left(\frac{\partial T_{\alpha\beta}}{\partial x_\beta} + \frac{\partial T_{\alpha z}}{\partial z}\right) \tag{3.50}$$

Next we introduce the velocity split given by (3.24), time-average and assume hydrostatic short-wave-averaged pressure

$$\overline{p} = \rho g(\overline{\zeta} - z) \tag{3.51}$$

to get

$$\begin{aligned} &\frac{\partial V_\alpha}{\partial t} + \frac{\partial}{\partial x_\beta}\left(V_\alpha V_\beta + \overline{u_{w\alpha}u_{w\beta}}\right) + \frac{\partial}{\partial z}\left(V_\alpha W + \overline{u_{w\alpha}w_w}\right) \\ &= -\frac{1}{\rho}\frac{\partial \overline{\zeta}}{\partial x_\alpha} + \frac{1}{\rho}\left(\frac{\partial \overline{T_{\alpha\beta}}}{\partial x_\beta} + \frac{\partial \overline{T_{\alpha z}}}{\partial z}\right). \end{aligned} \tag{3.52}$$

By using the local continuity

$$\frac{\partial V_\alpha}{\partial x_\alpha} + \frac{\partial W}{\partial z} = 0 \tag{3.53}$$

we rewrite (3.52) as

$$\begin{aligned} &\frac{\partial V_\alpha}{\partial t} + V_\beta\frac{\partial V_\alpha}{\partial x_\beta} + W\frac{\partial V_\alpha}{\partial z} + \frac{\partial}{\partial x_\alpha}(\overline{u_{w\alpha}u_{w\beta}}) + \frac{\partial}{\partial z}(\overline{u_{w\alpha}w_w}) = \\ &-\frac{1}{\rho}\frac{\partial \overline{\zeta}}{\partial x_\alpha} + \frac{1}{\rho}\left(\frac{\partial \overline{T_{\alpha\beta}}}{\partial x_\beta} + \frac{\partial \overline{T_{\alpha z}}}{\partial z}\right). \end{aligned} \tag{3.54}$$

Introducing the split for the current given by (3.42) and expressing the turbulent stresses using an eddy viscosity model,

$$\overline{T_{\alpha\beta}} = \rho(\nu_t + \nu_s)\left(\frac{\partial V_\beta}{\partial x_\alpha} + \frac{\partial V_\alpha}{\partial x_\beta}\right) \tag{3.55}$$

$$\overline{T_{\alpha z}} = \rho(\nu_t + \nu_s)\left(\frac{\partial V_{d\alpha}}{\partial z} + \frac{\partial W}{\partial x_\alpha}\right) \tag{3.56}$$

with ν_t being the the eddy viscosity representing the turbulence created by the bottom friction and the short-wave breaking, and ν_s being the eddy viscosity created by the shear in the flow, results in

$$\begin{aligned}\frac{\partial V_{d\alpha}}{\partial t} - \frac{\partial}{\partial z}\left((\nu_t + \nu_s)\frac{\partial V_{d\alpha}}{\partial z}\right) = &-\left(\frac{\partial V_{m\alpha}}{\partial t} + V_{m\beta}\frac{\partial V_{m\alpha}}{\partial x_\beta} + g\frac{\partial \overline{\zeta}}{\partial x_\alpha} + f_\alpha\right)\\ &-\left(V_{m\beta}\frac{\partial V_{d\alpha}}{\partial x_\beta} + V_{d\beta}\frac{\partial V_{m\alpha}}{\partial x_\beta} + V_{d\beta}\frac{\partial V_{d\alpha}}{\partial x_\beta} + W\frac{\partial V_{d\alpha}}{\partial z}\right)\\ &+\frac{\partial}{\partial x_\alpha}\left((\nu_t + \nu_s)\left(\frac{\partial V_\alpha}{\partial x_\beta} + \frac{\partial V_\beta}{\partial x_\alpha}\right)\right) + \frac{\partial}{\partial z}\left((\nu_t + \nu_s)\frac{\partial W}{\partial x_\alpha}\right).\end{aligned} \tag{3.57}$$

We define f_α, which is the local contribution to the radiation stress, as

$$f_\alpha = \frac{\partial}{\partial x_\alpha}(\overline{u_{w\alpha}u_{w\beta}}) + \frac{\partial}{\partial z}(\overline{u_{w\alpha}w_w}). \tag{3.58}$$

Using the definition for $V_{m\alpha}$ (3.43) in (3.57) yields

$$\begin{aligned}\frac{\partial V_{d\alpha}}{\partial t} - \frac{\partial}{\partial z}\left((\nu_t + \nu_s)\frac{\partial V_{d\alpha}}{\partial z}\right) = &-\left(\frac{\partial \frac{\overline{Q}_\alpha}{h}}{\partial t} + \frac{\overline{Q}_\beta}{h}\frac{\partial \frac{\overline{Q}_\alpha}{h}}{\partial x_\beta} + g\frac{\partial \overline{\zeta}}{\partial x_\alpha} + f_\alpha\right)\\ &-\left(\frac{\overline{Q}_\beta}{h}\frac{\partial V_{d\alpha}}{\partial x_\beta} + V_{d\beta}\frac{\partial \frac{\overline{Q}_\alpha}{h}}{\partial x_\beta} + V_{d\beta}\frac{\partial V_{d\alpha}}{\partial x_\beta} + W\frac{\partial V_{d\alpha}}{\partial z}\right)\\ &+\left(\frac{\partial \frac{Q_{w\alpha}}{h}}{\partial t} + \frac{\overline{Q}_\beta}{h}\frac{\partial \frac{Q_{w\alpha}}{h}}{\partial x_\beta} + \frac{Q_{w\beta}}{h}\frac{\partial \frac{\overline{Q}_\alpha}{h}}{\partial x_\beta} - \frac{Q_{w\beta}}{h}\frac{\partial \frac{Q_{w\alpha}}{h}}{\partial x_\beta} + \frac{Q_{w\beta}}{h}\frac{\partial V_{d\alpha}}{\partial x_\beta} + V_{d\beta}\frac{\partial \frac{Q_{w\alpha}}{h}}{\partial x_\beta}\right)\\ &+\frac{\partial}{\partial x_\alpha}\left((\nu_t + \nu_s)\left(\frac{\partial V_\alpha}{\partial x_\beta} + \frac{\partial V_\beta}{\partial x_\alpha}\right)\right) + \frac{\partial}{\partial z}\left((\nu_t + \nu_s)\frac{\partial W}{\partial x_\alpha}\right).\end{aligned} \tag{3.59}$$

Using continuity (3.22) the depth-integrated momentum equation, (3.45) is rewritten as

$$\frac{\partial \frac{\overline{Q}_\alpha}{h}}{\partial t} + \frac{\overline{Q}_\beta}{h}\frac{\partial \frac{\overline{Q}_\alpha}{h}}{\partial x_\beta} + g\frac{\partial \overline{\zeta}}{\partial x_\alpha} = -\frac{1}{\rho h}\frac{\partial}{\partial x_\beta}\left[S'_{\alpha\beta} - \overline{\int_{-h_o}^{\zeta} T_{\alpha\beta} dz}\right] + \frac{\tau_\alpha^S}{\rho h} - \frac{\tau_\alpha^B}{\rho h} - \frac{1}{h}\frac{\partial}{\partial x_\beta}\overline{\int_{-h_o}^{\zeta} V_{d\alpha}V_{d\beta}dz} - \frac{1}{h}\frac{\partial}{\partial x_\beta}\overline{\int_{\zeta_t}^{\zeta} u_{w\alpha}V_{d\beta} + u_{w\beta}V_{d\alpha}dz} \quad (3.60)$$

which is then used to rewrite (3.59) as

$$\begin{aligned}
\frac{\partial V_{d\alpha}}{\partial t} - \frac{\partial}{\partial z}\left((\nu_t + \nu_s)\frac{\partial V_{d\alpha}}{\partial z}\right) &= \left\{\frac{1}{\rho h}\frac{\partial S'_{\alpha\beta}}{\partial x_\beta} - \frac{\tau_\alpha^S}{\rho h} + \frac{\tau_\alpha^B}{\rho h} - f_\alpha\right\} \\
&\quad - \left\{\left(\frac{\overline{Q}_\beta}{h}\frac{\partial V_{d\alpha}}{\partial x_\beta} + V_{d\beta}\frac{\partial \frac{\overline{Q}_\alpha}{h}}{\partial x_\beta} + V_{d\beta}\frac{\partial V_{d\alpha}}{\partial x_\beta} + W\frac{\partial V_{d\alpha}}{\partial z}\right)\right. \\
&\quad - \left(\frac{\partial \frac{Q_{w\alpha}}{h}}{\partial t} + \frac{\overline{Q}_\beta}{h}\frac{\partial \frac{Q_{w\alpha}}{h}}{\partial x_\beta} + \frac{Q_{w\beta}}{h}\frac{\partial \frac{\overline{Q}_\alpha}{h}}{\partial x_\beta} - \frac{Q_{w\beta}}{h}\frac{\partial \frac{Q_{w\alpha}}{h}}{\partial x_\beta} + \frac{Q_{w\beta}}{h}\frac{\partial V_{d\alpha}}{\partial x_\beta} + V_{d\beta}\frac{\partial \frac{Q_{w\alpha}}{h}}{\partial x_\beta}\right) \\
&\quad \left. - \frac{1}{h}\frac{\partial}{\partial x_\beta}\overline{\int_{-h_o}^{\zeta} V_{d\alpha}V_{d\beta}dz} - \frac{1}{h}\frac{\partial}{\partial x_\beta}\overline{\int_{\zeta_t}^{\zeta} u_{w\alpha}V_{d\beta} + u_{w\beta}V_{d\alpha}dz}\right\} \\
&\quad + \left\{\frac{\partial}{\partial x_\alpha}\left((\nu_t + \nu_s)\left(\frac{\partial V_\alpha}{\partial x_\beta} + \frac{\partial V_\beta}{\partial x_\alpha}\right)\right) + \frac{\partial}{\partial z}\left((\nu_t + \nu_s)\frac{\partial W}{\partial x_\alpha}\right)\right\}. \quad (3.61)
\end{aligned}$$

The previous equation governs the vertical structure of $V_{d\alpha}$. Solving (3.61) requires boundary conditions for the current $V_{d\alpha}$. We match the shear stress at the bottom and specify no net flow per (3.44) which is written as

$$(\nu_t + \nu_s)\frac{\partial V_{d\alpha}}{\partial z}\bigg|_{z=-h_o} = \frac{\tau_\alpha^B}{\rho}, \qquad \int_{-h_o}^{\overline{\zeta}} V_{d\alpha} = 0. \quad (3.62)$$

Equations (3.61) and (3.62) are similar to the equations governing $V_{1\alpha}$ (19) and (20) in Putrevu and Svendsen (1999). The terms in the third line of (3.61) are new. In addition, the depth integral boundary condition in (3.62) is equal to zero whereas in Putrevu and Svendsen (1999) (20) it is equal to $-Q_{w\alpha}$.

We solve these equations for the vertical variation of $V_{d\alpha}$ by assuming time variations slow enough to allow us to neglect $\frac{\partial}{\partial t}$. This results in

$$-\frac{\partial}{\partial z}\left((\nu_t + \nu_s)\frac{\partial V_{d\alpha}}{\partial z}\right) = F_\alpha^{(0)} + F_\alpha^{(1)} + F_\alpha^{(2)} \quad (3.63)$$

where the forcing on the right hand side is given by

$$F_\alpha^{(0)} = \left\{ \frac{1}{\rho h}\frac{\partial S'_{\alpha\beta}}{\partial x_\beta} - \frac{\tau_\alpha^S}{\rho h} + \frac{\tau_\alpha^B}{\rho h} - f_\alpha \right\} \tag{3.64}$$

$$\begin{aligned} F_\alpha^{(1)} = -\Bigg\{ & \left(\frac{\overline{Q}_\beta}{h}\frac{\partial V_{d\alpha}}{\partial x_\beta} + V_{d\beta}\frac{\partial \frac{\overline{Q}_\alpha}{h}}{\partial x_\beta} + V_{d\beta}\frac{\partial V_{d\alpha}}{\partial x_\beta} + W\frac{\partial V_{d\alpha}}{\partial z} \right) \\ & - \left(\frac{\overline{Q}_\beta}{h}\frac{\partial \frac{Q_{w\alpha}}{h}}{\partial x_\beta} + \frac{Q_{w\beta}}{h}\frac{\partial \frac{\overline{Q}_\alpha}{h}}{\partial x_\beta} - \frac{Q_{w\beta}}{h}\frac{\partial \frac{Q_{w\alpha}}{h}}{\partial x_\beta} + \frac{Q_{w\beta}}{h}\frac{\partial V_{d\alpha}}{\partial x_\beta} + V_{d\beta}\frac{\partial \frac{Q_{w\alpha}}{h}}{\partial x_\beta} \right) \\ & - \frac{1}{h}\frac{\partial}{\partial x_\beta}\overline{\int_{-h_o}^{\zeta} V_{d\alpha}V_{d\beta}dz} - \frac{1}{h}\frac{\partial}{\partial x_\beta}\overline{\int_{\zeta_t}^{\zeta} u_{w\alpha}V_{d\beta} + u_{w\beta}V_{d\alpha}dz} \Bigg\} \end{aligned} \tag{3.65}$$

$$F_\alpha^{(2)} = \left\{ \frac{\partial}{\partial x_\alpha}\left((\nu_t + \nu_s)\left(\frac{\partial V_\alpha}{\partial x_\beta} + \frac{\partial V_\beta}{\partial x_\alpha} \right) \right) + \frac{\partial}{\partial z}\left((\nu_t + \nu_s)\frac{\partial W}{\partial x_\alpha} \right) \right\}. \tag{3.66}$$

A rigorous discussion about the scaling of the problem is given by Putrevu and Svendsen (1999) and the details are omitted here. It suffices here to say that the relative size of the forcing is as follows

$$F_\alpha^{(0)} \gg F_\alpha^{(1)} \gg F_\alpha^{(2)}. \tag{3.67}$$

This allows us to solve (3.63) using a perturbation method where we utilize

$$V_{d\alpha} = V_{d\alpha}^{(0)} + V_{d\alpha}^{(1)} + \ldots \tag{3.68}$$

The equation governing $V_{d\alpha}^{(0)}$ is then

$$-\frac{\partial}{\partial z}\left((\nu_t + \nu_s)\frac{\partial V_{d\alpha}^{(0)}}{\partial z} \right) = F_\alpha^{(0)} \tag{3.69}$$

with the boundary conditions

$$(\nu_t + \nu_s)\frac{\partial V_{d\alpha}^{(0)}}{\partial z}\bigg|_{z=-h_o} = \frac{\tau_\alpha^B}{\rho}, \qquad \int_{-h_o}^{\overline{\zeta}} V_{d\alpha}^{(0)} = 0. \tag{3.70}$$

The solution method for $V_{d\alpha}^{(0)}$ is the same as shown by Putrevu and Svendsen (1999) for $V_{1\alpha}^{(0)}$. It gives the following result

$$\begin{aligned} V_{d\alpha}^{(0)} = \quad & \frac{\tau_\alpha^B}{\rho}\left(\int_{-h_o}^{z}\frac{dz'}{(\nu_t+\nu_s)} - \frac{1}{h}\int_{-h_o}^{\overline{\zeta}}\int_{-h_o}^{z}\frac{dz'}{(\nu_t+\nu_s)}dz\right) \\ & - \int_{-h_o}^{z}\frac{1}{(\nu_t+\nu_s)}\int_{-h_o}^{z'}F_\alpha^{(0)}dz'dz \\ & + \frac{1}{h}\int_{-h_o}^{\overline{\zeta}}\int_{-h_o}^{z}\frac{1}{(\nu_t+\nu_s)}\int_{-h_o}^{z'}F_\alpha^{(0)}dz''dz'dz \end{aligned} \tag{3.71}$$

This equation is the same as the steady solution for $V_{1\alpha}^{(0)}$ given by Putrevu and Svendsen (1999) (34) without the $-\frac{Q_{w\alpha}}{h}$ term.

Similarly, the equation governing $V_{d\alpha}^{(1)}$ is

$$-\frac{\partial}{\partial z}\left((\nu_t+\nu_s)\frac{\partial V_{d\alpha}^{(1)}}{\partial z}\right) = F_\alpha^{(1)} \tag{3.72}$$

with the boundary conditions

$$(\nu_t+\nu_s)\frac{\partial V_{d\alpha}^{(1)}}{\partial z}\bigg|_{z=-h_o} = 0, \qquad \int_{-h_o}^{\overline{\zeta}} V_{d\alpha}^{(1)} = 0 \tag{3.73}$$

where we substitute $V_{d\alpha}^{(0)}$ for $V_{d\alpha}$ in the equation for $F_\alpha^{(1)}$. The solution method is the same as for $V_{d\alpha}^{(0)}$ with the following result

$$\begin{aligned} V_{d\alpha}^{(1)} = \quad & - \int_{-h_o}^{z}\frac{1}{(\nu_t+\nu_s)}\int_{-h_o}^{z'}F_\alpha^{(1)}dz'dz \\ & + \frac{1}{h}\int_{-h_o}^{\overline{\zeta}}\int_{-h_o}^{z}\frac{1}{(\nu_t+\nu_s)}\int_{-h_o}^{z'}F_\alpha^{(1)}dz''dz'dz. \end{aligned} \tag{3.74}$$

This equation is the same as Putrevu and Svendsen (1999) (42) for $V_{1\alpha}^{(1)}$.

Now we have solutions for the depth varying currents in terms of the depth-integrated properties. This allows us to solve the depth-integrated equations in terms of depth-integrated currents only. Therefore, we include the effect of the three-dimensional currents but we only have to perform the calculations in two-dimension. The detailed derivation of expressions in terms of depth-integrated quantities for (3.71) and (3.74) are included in Appendix B.

3.3 Calculation of the Integral Terms

This section utilizes the equations for the solutions of the vertical variation of the currents to find expressions for the integral terms in (3.45).

We are focusing on wave-driven flows so we exclude the wind-driven flows, therefore from this point on, we neglect the surface stress. In addition we make the following approximations,

$$\overline{\int_{-h_o}^{\zeta} V_{d\alpha}\, dz} \approx \int_{-h_o}^{\overline{\zeta}} V_{d\alpha}\, dz \tag{3.75}$$

$$\begin{aligned} \overline{\int_{-h_o}^{\zeta} V_{d\alpha} V_{d\beta} dz} \quad & + \overline{\int_{\zeta_t}^{\zeta} u_{w\alpha} V_{d\beta} + u_{w\beta} V_{d\alpha} dz} \approx \\ & \int_{-h_o}^{\overline{\zeta}} V_{d\alpha} V_{d\beta} dz + V_{d\beta}(\overline{\zeta}) Q_{w\alpha} + V_{d\alpha}(\overline{\zeta}) Q_{w\beta}. \end{aligned} \tag{3.76}$$

This essentially assumes that $V_{d\alpha}$ remains constant between ζ_t and ζ. In the first place it is not clear how we should define $V_{d\alpha}$ above trough level. However, when the surface stresses are neglected this is probably not a bad approximation.

Substituting the split for the current given by (3.42) into the integral terms results in

$$\begin{aligned} \int_{-h_o}^{\overline{\zeta}} V_{d\alpha} V_{d\beta} dz + \quad & V_{d\beta}(\overline{\zeta}) Q_{w\alpha} + V_{d\alpha}(\overline{\zeta}) Q_{w\beta} = \\ & \int_{-h_o}^{\overline{\zeta}} V_{d\alpha}^{(0)} V_{d\beta}^{(0)} dz + V_{d\beta}^{(0)}(\overline{\zeta}) Q_{w\alpha} + V_{d\alpha}^{(0)}(\overline{\zeta}) Q_{w\beta} \\ & + \int_{-h_o}^{\overline{\zeta}} V_{d\alpha}^{(0)} V_{d\beta}^{(1)} + V_{d\alpha}^{(1)} V_{d\beta}^{(0)}\, dz \\ & + V_{d\alpha}^{(1)}(\overline{\zeta}) Q_{w\beta} + V_{d\beta}^{(1)}(\overline{\zeta}) Q_{w\alpha} + O(V_d^{(1)})^2. \end{aligned} \tag{3.77}$$

Omitting many steps which are outlined in Putrevu and Svendsen (1999) in terms of $V_{1\alpha}^{(0)}$, the expression for the integrals is written in terms of $V_{d\alpha}^{(0)}$ as follows

$$\int_{-h_o}^{\overline{\zeta}} V_{d\alpha}V_{d\beta}dz + \quad V_{d\beta}(\overline{\zeta})Q_{w\alpha} + V_{d\alpha}(\overline{\zeta})Q_{w\beta} =$$
$$\int_{-h_o}^{\overline{\zeta}} V_{d\alpha}^{(0)}V_{d\beta}^{(0)}dz + V_{d\beta}^{(0)}(\overline{\zeta})Q_{w\alpha} + V_{d\alpha}^{(0)}(\overline{\zeta})Q_{w\beta}$$
$$\int_{-h_o}^{\overline{\zeta}} \left(\int_{-h_o}^{z} F_{\alpha}^{(1)}dz'\right)\left(\int_{-h_o}^{z} V_{d\beta}^{(0)} - \frac{Q_{w\beta}}{h}\,dz'\right)\frac{1}{(\nu_t+\nu_s)}dz$$
$$\int_{-h_o}^{\overline{\zeta}} \left(\int_{-h_o}^{z} F_{\beta}^{(1)}dz'\right)\left(\int_{-h_o}^{z} V_{d\alpha}^{(0)} - \frac{Q_{w\alpha}}{h}\,dz'\right)\frac{1}{(\nu_t+\nu_s)}dz. \tag{3.78}$$

$F_{\alpha}^{(1)}$ is then found by substituting $V_{d\alpha}^{(0)}$ for $V_{d\alpha}$ in (3.65),

$$F_{\alpha}^{(1)} = -\left\{\left(\frac{\overline{Q}_{\beta}}{h}\frac{\partial V_{d\alpha}^{(0)}}{\partial x_{\beta}} + V_{d\beta}^{(0)}\frac{\partial \frac{\overline{Q}_{\alpha}}{h}}{\partial x_{\beta}} + V_{d\beta}^{(0)}\frac{\partial V_{d\alpha}^{(0)}}{\partial x_{\beta}} + W\frac{\partial V_{d\alpha}^{(0)}}{\partial z}\right)\right.$$
$$-\left(\frac{\overline{Q}_{\beta}}{h}\frac{\partial \frac{Q_{w\alpha}}{h}}{\partial x_{\beta}} + \frac{Q_{w\beta}}{h}\frac{\partial \frac{\overline{Q}_{\alpha}}{h}}{\partial x_{\beta}} - \frac{Q_{w\beta}}{h}\frac{\partial \frac{Q_{w\alpha}}{h}}{\partial x_{\beta}} + \frac{Q_{w\beta}}{h}\frac{\partial V_{d\alpha}^{(0)}}{\partial x_{\beta}} + V_{d\beta}^{(0)}\frac{\partial \frac{Q_{w\alpha}}{h}}{\partial x_{\beta}}\right)$$
$$\left. - \frac{1}{h}\frac{\partial}{\partial x_{\beta}}\int_{-h_o}^{\overline{\zeta}} V_{d\alpha}V_{d\beta}dz - \frac{1}{h}\frac{\partial}{\partial x_{\beta}}\left[V_{d\alpha}^{(0)}(\overline{\zeta})Q_{w\beta} + V_{d\beta}^{(0)}(\overline{\zeta})Q_{w\alpha}\right]\right\}. \tag{3.79}$$

The vertical velocity W is found by integrating the local continuity equation which results in

$$W = -\left[\left(\frac{\overline{Q}_{\gamma}}{h} + V_{d\gamma}^{(0)}(-h_o) - \frac{Q_{w\gamma}}{h}\right)\frac{\partial h_o}{\partial x_{\gamma}} + (h_o+z)\frac{\partial \frac{\overline{Q}_{\gamma}}{h}}{\partial x_{\gamma}} + \int_{-h_o}^{z}\frac{\partial V_{d\gamma}^{(0)}}{\partial x_{\gamma}} - \frac{\partial \frac{Q_{w\gamma}}{h}}{\partial x_{\gamma}}dz\right]. \tag{3.80}$$

Equations (3.78)-(3.80) are all in terms of $V_{d\alpha}^{(0)}$. Applying equation (3.48) in these equations reverts them back to the previous forms given by Putrevu and Svendsen (1999).

3.4 Simplifications for Use in SHORECIRC

Using (3.71), (3.76),(3.78),(3.79) and (3.80) in (3.45) results in equations in terms of depth-integrated properties that are solvable on a two-dimensional grid

rather than a three-dimensional grid. This section incorporates a few simplifications which we use to solve these equations within SC.

The previous versions of SC follow the scaling arguments for the relative sizes of the different components of the currents presented by Van Dongeren and Svendsen (1997) as follows

$$\tilde{V}_\alpha \gg V_{1\alpha} \tag{3.81}$$

and

$$V_{1\alpha} \sim -\frac{Q_{w\alpha}}{h}. \tag{3.82}$$

This says that the depth-averaged currents are much larger than the depth varying currents and the depth varying currents are the same order as the short-wave volume flux divided by the depth.

As a result of this scaling, all terms of $O(V_{1\alpha})^2$, $O(V_{1\alpha}\frac{Q_{w\alpha}}{h})$ and $O(\frac{Q_{w\alpha}}{h})^2$ are neglected in the forcing for $V_{1\alpha}^{(1)}$ which is the equivalent to the forcing for $V_{d\alpha}^{(1)}$ in equation (3.79). This includes all terms of $O(V_{1\alpha})$ and $O(\frac{Q_{w\alpha}}{h})$ in the equation for W, the equivalent of (3.80).

By using the alternate form for splitting V_α, different scaling arguments apply for the currents. Because $-\frac{Q_{w\alpha}}{h}$ is not a part of $V_{d\alpha}$, we use the following scaling arguments

$$\frac{\overline{Q}_\alpha}{h} \gg V_{d\alpha} \quad \text{and/or} \quad -\frac{Q_{w\alpha}}{h} \gg V_{d\alpha}. \tag{3.83}$$

This says that for the alternate method of splitting the current, either the depth-averaged current is much larger than the depth varying currents or the short-wave flux divided by the water depth is much larger than the depth varying currents.

As a result of (3.83), only terms of $O(V_{d\alpha})^2$ in (3.79) and terms of $O(V_{d\alpha})$ in (3.80) are neglected. This means terms of $O(V_{d\alpha}\frac{Q_{w\alpha}}{h})$ and $O(\frac{Q_{w\alpha}}{h})^2$ in the forcing $F_\alpha^{(1)}$ and terms of $O(\frac{Q_{w\alpha}}{h})$ in the vertical velocity W which were previously neglected

are included. Applying this scaling results in the following expressions for $F_\alpha^{(1)}$ and W,

$$\begin{aligned} F_\alpha^{(1)} = \; & -\Bigg\{ \left(\frac{\overline{Q}_\beta}{h} \frac{\partial V_{d\alpha}^{(0)}}{\partial x_\beta} + V_{d\beta}^{(0)} \frac{\partial \frac{\overline{Q}_\alpha}{h}}{\partial x_\beta} + W \frac{\partial V_{d\alpha}^{(0)}}{\partial z} \right) \\ & - \left(\frac{\overline{Q}_\beta}{h} \frac{\partial \frac{Q_{w\alpha}}{h}}{\partial x_\beta} + \frac{Q_{w\beta}}{h} \frac{\partial \frac{\overline{Q}_\alpha}{h}}{\partial x_\beta} - \frac{Q_{w\beta}}{h} \frac{\partial \frac{Q_{w\alpha}}{h}}{\partial x_\beta} + \frac{Q_{w\beta}}{h} \frac{\partial V_{d\alpha}^{(0)}}{\partial x_\beta} + V_{d\beta}^{(0)} \frac{\partial \frac{Q_{w\alpha}}{h}}{\partial x_\beta} \right) \\ & - \frac{1}{h} \frac{\partial}{\partial x_\beta} \left[V_{d\alpha}^{(0)}(\overline{\zeta}) Q_{w\beta} + V_{d\beta}^{(0)}(\overline{\zeta}) Q_{w\alpha} \right] \Bigg\} \end{aligned} \tag{3.84}$$

$$W = -\left[\left(\frac{\overline{Q}_\gamma}{h} - \frac{Q_{w\gamma}}{h} \right) \frac{\partial h_o}{\partial x_\gamma} + (h_o + z) \frac{\partial}{\partial x_\gamma} \left(\frac{\overline{Q}_\gamma}{h} - \frac{Q_{w\gamma}}{h} \right) \right]. \tag{3.85}$$

The second and third line of (3.84) and the $Q_{w\gamma}$ terms in (3.85) are the additional terms not included in previous versions of SC. Although these additional terms tend to be small inside the surf zone they have a important impact outside the surfzone which is examined in more detail in Chapter 5.

Inserting (3.84) and (3.85) into (3.78) results in the final expression for the depth integrals in the depth-integrated horizontal momentum balance which looks like

$$\int_{-h_o}^{\overline{\zeta}} V_{d\alpha}V_{d\beta}dz + V_{d\beta}(\overline{\zeta})Q_{w\alpha} + V_{d\alpha}(\overline{\zeta})Q_{w\beta} = M_{\alpha\beta} + A_{\alpha\beta\gamma}\frac{\overline{Q}_\gamma}{h} - h\left(D_{\gamma\beta}\frac{\partial\frac{\overline{Q}_\alpha}{h}}{\partial x_\gamma} + D_{\gamma\alpha}\frac{\partial\frac{\overline{Q}_\beta}{h}}{\partial x_\gamma} + B_{\alpha\beta}\frac{\partial\frac{\overline{Q}_\gamma}{h}}{\partial x_\gamma}\right) \quad (3.86)$$

where

$$A_{\alpha\beta\gamma} = -\left\{\int_{-h_o}^{\overline{\zeta}} \frac{1}{(\nu_t+\nu_s)}\left(\int_{-h_o}^{z}\frac{\partial V_{d\alpha}^{(0)}}{\partial x_\gamma} - \frac{\partial\frac{Q_{w\alpha}}{h}}{\partial x_\gamma} - \frac{\partial h_o}{\partial x_\gamma}\frac{\partial V_{d\alpha}^{(0)}}{\partial z}\right)\left(\int_{-h_o}^{z} V_{d\beta}^{(0)} - \frac{Q_{w\beta}}{h}dz'\right)dz + \int_{-h_o}^{\overline{\zeta}} \frac{1}{(\nu_t+\nu_s)}\left(\int_{-h_o}^{z}\frac{\partial V_{d\beta}^{(0)}}{\partial x_\gamma} - \frac{\partial\frac{Q_{w\beta}}{h}}{\partial x_\gamma} - \frac{\partial h_o}{\partial x_\gamma}\frac{\partial V_{d\beta}^{(0)}}{\partial z}\right)\left(\int_{-h_o}^{z} V_{d\alpha}^{(0)} - \frac{Q_{w\alpha}}{h}dz'\right)dz\right\} \quad (3.87)$$

$$B_{\alpha\beta} = -\frac{1}{h}\left\{\int_{-h_o}^{\overline{\zeta}} \frac{1}{(\nu_t+\nu_s)}\left(\int_{-h_o}^{z}(h_o+z')\frac{\partial V_{d\alpha}^{(0)}}{\partial z}dz'\right)\left(\int_{-h_o}^{z} V_{d\beta}^{(0)} - \frac{Q_{w\beta}}{h}dz'\right)dz + \int_{-h_o}^{\overline{\zeta}} \frac{1}{(\nu_t+\nu_s)}\left(\int_{-h_o}^{z}(h_o+z')\frac{\partial V_{d\beta}^{(0)}}{\partial z}dz'\right)\left(\int_{-h_o}^{z} V_{d\alpha}^{(0)} - \frac{Q_{w\alpha}}{h}dz'\right)dz\right\} \quad (3.88)$$

$$D_{\alpha\beta} = \frac{1}{h}\int_{-h_o}^{\overline{\zeta}} \frac{1}{(\nu_t+\nu_s)}\left(\int_{-h_o}^{z} V_{d\alpha}^{(0)} - \frac{Q_{w\alpha}}{h}dz'\right)\left(\int_{-h_o}^{z} V_{d\beta}^{(0)} - \frac{Q_{w\beta}}{h}dz'\right)dz \quad (3.89)$$

$$
\begin{aligned}
M_{\alpha\beta} &= \int_{-h_o}^{\overline{\zeta}} V_{d\alpha}^{(0)} V_{d\beta}^{(0)} dz + V_{d\beta}^{(0)}(\overline{\zeta}) Q_{w\alpha} + V_{d\alpha}^{(0)}(\overline{\zeta}) Q_{w\beta} \\
&+ \left\{ \int_{-h_o}^{\overline{\zeta}} \frac{1}{(\nu_t + \nu_s)} \left(\int_{-h_o}^{z} \left(V_{d\gamma}^{(0)} \frac{\partial \frac{Q_{w\alpha}}{h}}{\partial x_\gamma} + \frac{Q_{w\gamma}}{h} \frac{\partial V_{d\alpha}^{(0)}}{\partial x_\gamma} - \frac{Q_{w\gamma}}{h} \frac{\partial \frac{Q_{w\alpha}}{h}}{\partial x_\gamma} \right) dz' \right) \right. \\
&\qquad \left. \left(\int_{-h_o}^{z} V_{d\beta}^{(0)} - \frac{Q_{w\beta}}{h} dz' \right) dz \right. \\
&+ \left. \int_{-h_o}^{\overline{\zeta}} \frac{1}{(\nu_t + \nu_s)} \left(\int_{-h_o}^{z} \left(V_{d\gamma}^{(0)} \frac{\partial \frac{Q_{w\beta}}{h}}{\partial x_\gamma} + \frac{Q_{w\gamma}}{h} \frac{\partial V_{d\beta}^{(0)}}{\partial x_\gamma} - \frac{Q_{w\gamma}}{h} \frac{\partial \frac{Q_{w\beta}}{h}}{\partial x_\gamma} \right) dz' \right) \right. \\
&\qquad \left. \left(\int_{-h_o}^{z} V_{d\alpha}^{(0)} - \frac{Q_{w\alpha}}{h} dz' \right) dz \right\} \\
&- \frac{\partial h_o}{\partial x_\gamma} \left\{ \int_{-h_o}^{\overline{\zeta}} \frac{1}{(\nu_t + \nu_s)} \left(\int_{-h_o}^{z} \frac{Q_{w\gamma}}{h} \frac{\partial V_{d\alpha}^{(0)}}{\partial z} dz' \right) \left(\int_{-h_o}^{z} V_{d\beta}^{(0)} - \frac{Q_{w\beta}}{h} dz' \right) dz \right. \\
&+ \left. \int_{-h_o}^{\overline{\zeta}} \frac{1}{(\nu_t + \nu_s)} \left(\int_{-h_o}^{z} \frac{Q_{w\gamma}}{h} \frac{\partial V_{d\beta}^{(0)}}{\partial z} dz' \right) \left(\int_{-h_o}^{z} V_{d\alpha}^{(0)} - \frac{Q_{w\alpha}}{h} dz' \right) dz \right\} \\
&- \left\{ \int_{-h_o}^{\overline{\zeta}} \frac{1}{(\nu_t + \nu_s)} \left(\int_{-h_o}^{z} (h_o + z) \frac{\partial \frac{Q_{w\gamma}}{h}}{\partial x_\gamma} \frac{\partial V_{d\alpha}^{(0)}}{\partial z} dz' \right) \left(\int_{-h_o}^{z} V_{d\beta}^{(0)} - \frac{Q_{w\beta}}{h} dz' \right) dz \right. \\
&+ \left. \int_{-h_o}^{\overline{\zeta}} \frac{1}{(\nu_t + \nu_s)} \left(\int_{-h_o}^{z} (h_o + z) \frac{\partial \frac{Q_{w\gamma}}{h}}{\partial x_\gamma} \frac{\partial V_{d\beta}^{(0)}}{\partial z} dz' \right) \left(\int_{-h_o}^{z} V_{d\alpha}^{(0)} - \frac{Q_{w\alpha}}{h} dz' \right) dz \right\} \\
&+ \left\{ \int_{-h_o}^{\overline{\zeta}} \frac{1}{(\nu_t + \nu_s)} \left(\int_{-h_o}^{z} I_\alpha dz' \right) \left(\int_{-h_o}^{z} V_{d\beta}^{(0)} - \frac{Q_{w\beta}}{h} dz' \right) dz \right. \\
&\left. \int_{-h_o}^{\overline{\zeta}} \frac{1}{(\nu_t + \nu_s)} \left(\int_{-h_o}^{z} I_\beta dz' \right) \left(\int_{-h_o}^{z} V_{d\alpha}^{(0)} - \frac{Q_{w\alpha}}{h} dz' \right) dz \right\}
\end{aligned}
\tag{3.90}
$$

with I_α defined by

$$
I_\alpha = \frac{1}{h} \frac{\partial}{\partial x_\gamma} \left[V_{d\alpha}^{(0)}(\overline{\zeta}) Q_{w\gamma} + V_{d\gamma}^{(0)}(\overline{\zeta}) Q_{w\alpha} \right]. \tag{3.91}
$$

The form of the dispersive mixing coefficients $A_{\alpha\beta\gamma}$, $B_{\alpha\beta}$ and $D_{\alpha\beta}$ in terms of $V_{1\alpha}$ given by Putrevu and Svendsen (1999) and used in the previous versions of SC is recovered by using (3.48) in (3.87), (3.88) and (3.89). However, all but the first line in (3.90) for the dispersive mixing coefficient $M_{\alpha\beta}$ are terms created by the

alternate method for splitting the current not included in the previous versions of SC. In addition, the radiation stress has been modified as can be seen in (3.46).

The final depth-average horizontal momentum equation is

$$\frac{\partial \overline{Q}_\alpha}{\partial t} + \frac{\partial}{\partial x_\alpha}\left(\frac{\overline{Q}_\alpha \overline{Q}_\beta}{h} + A_{\alpha\beta\gamma}\frac{\overline{Q}_\gamma}{h}\right) + \frac{1}{\rho}\frac{\partial}{\partial x_\beta}\left[S'_{\alpha\beta} + \rho M_{\alpha\beta}\right] + gh\frac{\partial \overline{\zeta}}{\partial x_\alpha} + \frac{\tau^B_\alpha}{\rho}$$
$$-\frac{\partial}{\partial x_\beta}\left[\overline{\int_{-h_o}^{\zeta} T_{\alpha\beta} dz} + h\left(D_{\gamma\beta}\frac{\partial \frac{\overline{Q}_\alpha}{h}}{\partial x_\gamma} + D_{\gamma\alpha}\frac{\partial \frac{\overline{Q}_\beta}{h}}{\partial x_\gamma}\right)\right] - \frac{\partial}{\partial x_\beta}\left(hB_{\alpha\beta}\frac{\partial \frac{\overline{Q}_\gamma}{h}}{\partial x_\gamma}\right) = 0. \quad (3.92)$$

The alternate split for the current has not affected the momentum equation (3.92) or the continuity equation (3.22). The equation for $V^{(0)}_{d\alpha}$, (B.11), expressed in terms of depth-averaged properties as derived in Appendix B, is used in the preceding equations for application in SC.

3.5 Closure Models

This section discusses the closure submodels used when solving the governing equations in SC. A more thorough discussion on most of the submodels is found in Sancho and Svendsen (1997).

The short-wave forcing represents the time-averaged contribution from the short-waves to the momentum balance. The derivations of the equations make no assumptions as to how the short-waves are modeled.

Short Wave Model

The short wave model REF/DIF (Kirby and Dalrymple, 1994) is used as the wave driver accounting for the effects of bottom induced refraction-diffraction, current induced refraction and wave breaking dissipation by solving the parabolic equation initially developed by Kirby and Dalrymple (1983). The offshore wave height, direction and period is specified along the offshore boundary.

Wave current interaction is modeled by periodically recalculating the wave field based on the current field. The wave forcing is recalculated once every ten

short-wave periods which is short enough to prevent large changes in the wave field. Because the wave breaking is based on a depth limited breaking criteria, the ratio of wave height to depth for initiating breaking is reduced from 0.78 to 0.55 to prevent the steep waves around the rip current from becoming too large.

Radiation Stress

The radiation stress, which is the excess momentum due to the short-waves, is calculated with the following expressions,

$$S_{\alpha\beta} = e_{\alpha\beta} S_m + \delta_{\alpha\beta} S_p \tag{3.93}$$

where we use

$$e_{\alpha\beta} = \begin{bmatrix} \cos^2 \alpha_w & \sin \alpha_w \cos \alpha_w \\ \sin \alpha_w \cos \alpha_w & \sin^2 \alpha_w \end{bmatrix}. \tag{3.94}$$

We define α_w as the short-wave angle relative to the positive x-axis.

Outside the surfzone we choose to use linear theory to model the short-wave parameters. S_m and S_p are given by

$$S_m = \frac{1}{16} \rho \, g \, H^2 (1 + G) \tag{3.95}$$

$$S_p = \frac{1}{16} \rho \, g \, H^2 G \tag{3.96}$$

where G is

$$G = \frac{2kh}{\sinh 2kh}. \tag{3.97}$$

k is the short-wave number and H is the short-wave height.

Inside the surfzone we include the contribution of the roller to the momentum by using the formulation from Svendsen (1984b). Therefore S_m and S_p inside the surfzone are given by

$$S_m = \rho g H^2 \frac{c^2}{gh} \left[B_0 + \frac{A}{HL} \frac{h}{H} \right] = \rho g H^2 \frac{c^2}{gh} \left[B_0 + \frac{A}{H^2} \frac{h}{L} \right] \tag{3.98}$$

$$S_p = \frac{1}{2}\rho g H^2 B_0 \tag{3.99}$$

where L is the short-wave length, c is the short-wave celerity, A is the roller area and B_0 is the wave shape parameter defined by

$$B_0 = \frac{1}{T}\int_0^T \left(\frac{\eta}{H}\right)^2 dt. \tag{3.100}$$

Parameterizations of B_o is found in Hansen (1990) although we use the linear waves value of B_0=$\frac{1}{8}$. The formulation for the roller area is taken from Okaysu *et al.* (1986),

$$A = 0.06HL \tag{3.101}$$

When using the preceding equations to calculate the radiation stress it is apparent that a discontinuity results at the breaker line because the inclusion of the roller creates an immediate jump in radiation stress. The effect of the roller from (3.98) would be at its maximum at the breaker line and decreases toward the shoreline. Contrarily, Svendsen (1984a) found by comparisons with measurements that the radiation stress remains constant after breaking before decreasing toward the shoreline. The reason is that in nature, the wave breaking and the associated roller develop over some distance

In the model, this transition from outside the surfzone to inside is simulated by using a spline between the two regions which eliminates the sudden increase in radiation stress at the breaker line. The radiation stress from the seaward boundary up to the breaker line is determined. The length m of the transition between the breaker line and the region where the roller is fully developed is calculated based on the following empirical formula,

$$m = 0.25 h_b \left(-\frac{\partial h_o'}{\partial x}\right)^{-1.1} \tag{3.102}$$

where $\frac{\partial h_o'}{\partial x}$ is the average slope at the breaker line and h_b is the depth at the breaker line. The radiation stress from the end of the transition to the shoreline where the

roller is fully developed is determined. The radiation stress in the transition region is simulated with a spline fitting the radiation outside the breakers to the radiation stress with the fully developed roller.

Short-Wave Volume Flux

The short-wave volume flux outside the surfzone is given by

$$Q_{w\alpha} = B_0 \frac{gH^2}{c} \frac{k_\alpha}{k} \tag{3.103}$$

where k_α is the wave number vector in the direction x_α, $k_\alpha = k(\cos\alpha_w, \sin\alpha_w)$. Inside the surfzone the short-wave volume flux is from the formulation by Svendsen (1984b) given as

$$Q_{w\alpha} = \frac{gH^2}{c}\frac{c^2}{gh}(B_0 + \frac{A}{HL}\frac{h}{H})\frac{k_\alpha}{k} = \frac{gH^2}{c}\frac{c^2}{gh}(B_0 + \frac{A}{H^2}\frac{h}{L})\frac{k_\alpha}{k} \tag{3.104}$$

Once again, the transition outside the surfzone to inside the surfzone is simulated with a spline using (3.102).

Bottom Shear Stress

In nearshore flows, both the waves and currents create bottom shear stresses so SC needs to model the combined effect. We use the formulation for wave-averaged bottom shear stress for combined currents and waves given by Svendsen and Putrevu (1990) which is written as

$$\overline{\tau_\alpha^B} = \frac{1}{2}\rho f_{cw} u_0 (\beta_1 V_{b\alpha} + \beta_2 u_{0\alpha}). \tag{3.105}$$

where u_0 is the short-wave particle velocity amplitude evaluated at the bottom, f_{cw} is the friction factor and V_b is the current velocity at the bottom. For linear theory the weight factors for the current and wave motion β_1 and β_2 are given by

$$\beta_1 = \frac{\overline{[(\frac{V_b}{u_0})^2 + 2\frac{V_b}{u_0}\cos\theta\cos\mu + \cos^2\theta]^{1/2}}}{} \tag{3.106}$$

$$\beta_2 = \frac{}{\cos\theta\overline{[(\frac{V_b}{u_0})^2 + 2\frac{V_b}{u_0}\cos\theta\cos\mu + \cos^2\theta]^{1/2}}} \tag{3.107}$$

where μ is the angle between the short-waves and the currents at the bottom and θ is the short-wave phase $\theta = \omega t - \int \vec{k} \cdot d\vec{x}$ with ω being the short-wave frequency.

Steady Streaming

The bottom shear stress is applied at the top of the bottom boundary layer neglecting the effect of the bottom boundary layer. However, Putrevu and Svendsen (1993) find that the steady streaming induced by the oscillatory nature of the bottom boundary layer is important, particularly outside the surfzone. Therefore, the steady streaming stress τ^{SB} is included by using the formulation of Longuet-Higgins (1956),

$$\tau_\alpha^{SB} = \rho \frac{u_0 u_{0\alpha}}{c} \sqrt{\frac{\omega \nu_{tb}}{8}} \tag{3.108}$$

where ν_{tb} is the constant eddy viscosity in the boundary layer given by Svendsen *et al.* (1987) as

$$\nu_{tb} \simeq 0.08 f_{cw}^2 \left(\frac{H}{h}\right)^2 \frac{c}{k}. \tag{3.109}$$

Including the steady streaming stress modifies the bottom boundary condition in (3.62) as follows

$$(\nu_t + \nu_s) \frac{\partial V_{d\alpha}}{\partial z}\bigg|_{z=-h_o} = \frac{\tau_\alpha^B - \tau_\alpha^{SB}}{\rho}. \tag{3.110}$$

Turbulence

The wave-averaged subgrid stress is modeled using an eddy viscosity formulation given by (3.55) which is repeated here for convenience,

$$\overline{T_{\alpha\beta}} = \rho(\nu_t + \nu_s) \left(\frac{\partial V_\beta}{\partial x_\alpha} + \frac{\partial V_\alpha}{\partial x_\beta} \right). \tag{3.111}$$

The eddy viscosity has two components, ν_t represents the turbulence created by the bottom friction and the breaking waves and ν_s represents the turbulence created by the horizontal shear in the flow.

A detailed analysis on ν_t is given by Sancho and Svendsen (1997) and is only summarized here. The bottom induced turbulence is based on You (1994) and Coffey and Nielsen (1984). For the turbulence from breaking waves a modified Battjes (1975) model is utilized. The combined formulation is written as

$$\nu_t = C_1 \kappa \sqrt{\frac{f_w}{2}} u_0 h + Mh(\frac{D}{\rho})^{1/3} + \nu_{t,0} \tag{3.112}$$

where κ is the von Karman constant ($\kappa \simeq 0.4$), f_w is the friction factor, D is the energy dissipation in the breaking waves, $\nu_{t,0}$ is an empirical background eddy viscosity and C_1 and M are constant coefficients. It is apparent that the first term on the right hand side of (3.112) represents the bottom induced turbulence and the second terms represents the wave induced turbulence. Based on the experiments of Nadaoka and Kondoh (1982) and the estimates of Svendsen (1987) we typically use values for the constant coefficients of $M = 0.1$ and $C_1 = 0.2$.

The energy transport at turbulent scales is primarily accomplished by vortex stretching. Two-dimensional models, however, are not capable of vortex stretching unless an artificial viscosity is included. The dissipation from the artificial viscosity simulates the transfer of energy from the larger scales to the smaller scales. The eddy viscosity based on the horizontal shear in the flow (ν_s) models the dissipation from the eddies which are too small to be resolved by the numerical grid. We use the Smagorinsky eddy viscosity model, first introduced by Smagorinsky (1963), which is written as

$$\nu_s = (C_s \Delta)^2 \sqrt{2 e_{\alpha\beta} e_{\alpha\beta}} \tag{3.113}$$

where $e_{\alpha\beta}$ is given by

$$e_{\alpha\beta} = \frac{1}{2}\left(\frac{\partial V_\alpha}{\partial x_\beta} + \frac{\partial V_\beta}{\partial x_\alpha}\right). \tag{3.114}$$

C_s is the Smagorinsky coefficient and Δ is the characteristic length scale of the smallest resolvable eddy. Deardorff (1974) has an expression for Δ on an anisoptric grid which is given a rigorous basis by Scotti *et al.* (1993),

$$\Delta = \sqrt{\Delta x \Delta y}. \tag{3.115}$$

As with the mixing length scale in the traditional eddy viscosity formulation, the Smagorinsky coefficient C_s varies based on the flow. Rogallo and Moin (1984) summarize the findings from many applications of the Smagorinsky eddy viscosity and find that C_s varies in the range of $0.1 \leq C_s \leq 0.24$. However, these applications are for three-dimensional flows.

There are fewer documented applications for two-dimensional or depth-integrated flows. Madsen *et al.* (1988) find that for a depth-integrated flow model they need to use a large C_s in the range of $0.4 \leq C_s \leq 0.8$. Their model does not include bottom friction or any other form of dissipation to help stabilize the flow. They argue that for $\Delta x \leq h$, the eddy viscosity dominates over the bottom friction thereby requiring C_s to be larger than normal. Inside the surfzone we generally use $\Delta x \geq h$ which means that bottom friction dominates, consequently, the stability argument for the magnitude of C_s is not applicable.

In other two-dimensional studies, Kobayashi *et al.* (1984, 1985) find that they require much smaller values for C_s. They use $C_s \sim 0.1$ for most cases, although in the presence of mean shear they reduce it further to $C_s \sim 0.05$.

The Smagorinsky eddy viscosity is modeling the dissipation of energy from the subgrid scales. The size of the eddy viscosity is dependent on the scale of the grid. In this study, the grid in SC is sufficiently small to resolve the large and medium eddies. Intuitively, the dissipation from the subgrid eddies should be smaller than the turbulence generated by the breaking waves. On the other hand, in the rip current outside the breakers the subgrid dissipation may be larger than the turbulence created by the bottom boundary layer. Based on these arguments,

we use $0.1 \leq C_s \leq 0.25$ for all of the cases, producing physically acceptable levels of turbulence.

Chapter 4

NUMERICAL MODELING OF RIP CURRENT: 2DH PROPERTIES

This chapter presents the numerical modeling results from SHORECIRC for the depth-averaged flow properties of rip current systems. The preliminary work was previously presented by Haas *et al.* (1998) for a simplified version of the model with depth uniform currents. The two-dimensional horizontal (2DH) properties discussed in this chapter are obtained using the full model described in Chapter 3.

The first section outlines the situation modeled and discusses the mechanisms for the basic flow patterns in rip current systems. In addition, this section gives the values of the parameters used in the model.

The next section presents the time-averaged properties of the modeled results as well as discusses the reasons for using time-averaging. Comparisons between the model results and the experiments by Haller *et al.* (1997a,b) are given as well. The influence of the bottom stress is depicted in the following section. The effect on both the instantaneous and time-averaged flow patterns is included in this section.

The experiments in Chapter 2 demonstrate that the two rips in the wave basin behave differently. Section 4.4 notes that the rips behave differently in the model as well. The reasons leading to the differences between the rips are identified.

Section 4.5 discusses the importance of including wave and current interaction in rip current systems. The section illustrates the effect on both the wave field and

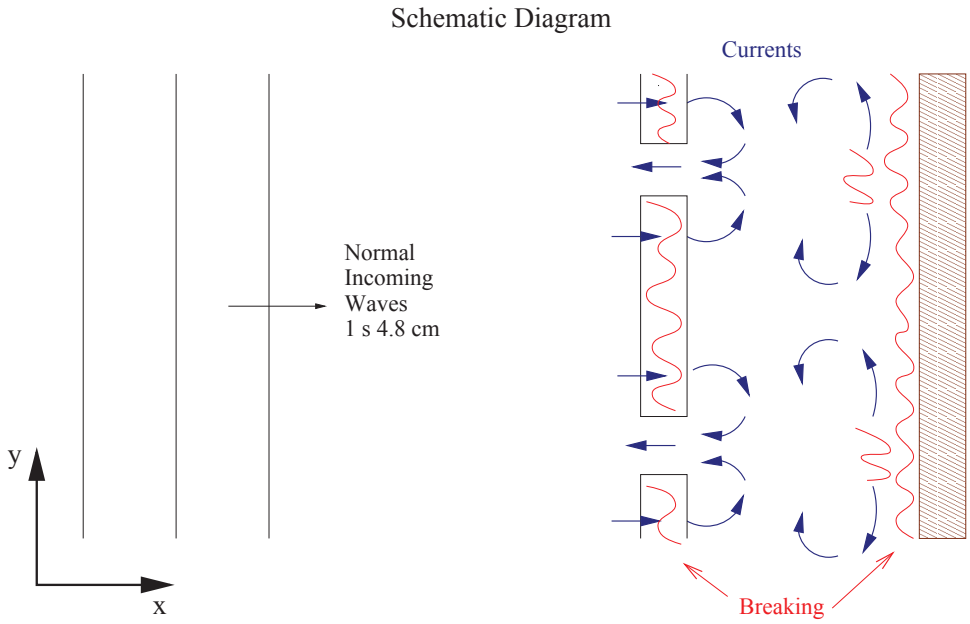

Figure 4.1: Schematic diagram of wave-averaged flow on a barred beach with rip channels.

the effect on the circulation patterns. The final section (4.6) presents the importance of including the 3D dispersive mixing terms for modeling rip current systems.

4.1 Introduction

Figure 4.1 shows a schematic diagram outlining the general flow patterns for the nearshore region of the basin. The short waves are normally incident with a period of 1 s and an offshore wave height of 4.8 cm. These waves propagate toward the shore and start breaking over the bars, as indicated in the figure, creating a setup in the mean water level. The waves are not breaking as much in the channels, therefore the mean water level is lower in the channels, which creates a longshore pressure gradient from the bars directed toward the channels. This pressure gradient is driving the currents toward the channels, creating the feeder currents for the rips.

Because the waves do not break as much in the channels, these waves are

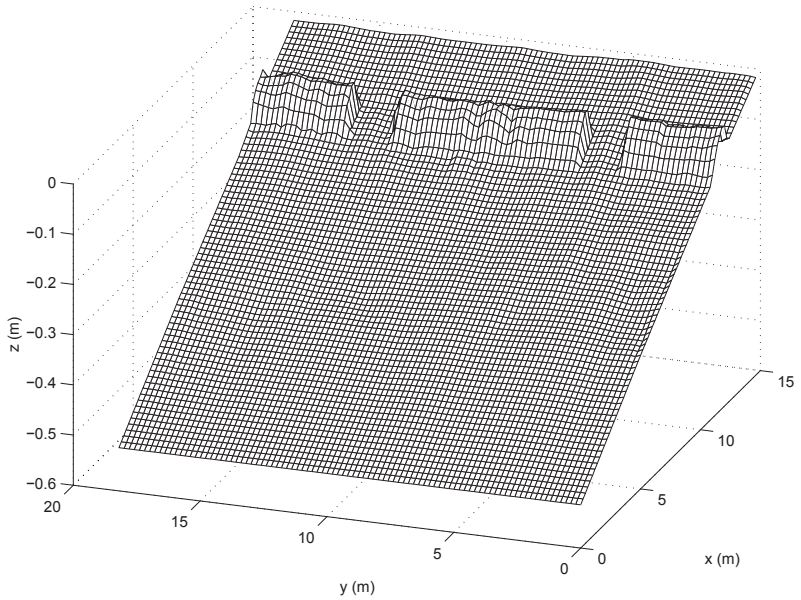

Figure 4.2: Topography interpolated from a survey of the CACR wave basin.

larger and therefore as they approach the shoreline break earlier than the waves behind the bar. This creates a larger setup, or a bump in the mean water level, close to the shoreline behind the channel. Therefore, a longshore pressure gradient drives flow away from the channels creating secondary or recirculation cells close to the shoreline. The circulation is highly dependent on the breaking pattern; if the waves do not break on the bar then there is no recirculation cells and the feeder currents for the rips are much smaller. Conversely if the waves also break strongly in the channel, the longshore surface gradients are reduced and so are the rips. This will be discussed further in Section 6.3.

The topography used in the model is taken from a detailed survey of the wave basin and is shown in Figure 4.2. The two rip channels were intended to be symmetric to each other although they clearly have some differences. The bars also exhibit longshore non-uniformities which has an impact on the circulation.

The model grid spacing is $\Delta x = 20$ cm and $\Delta y = 20$ cm, and the time step

is $\Delta t = 0.031490$ s corresponding to a Courant number of 0.5 at the largest depth. The model is run for 52,001 time steps or 1637.48 s, virtually identical to the length of the experimental runs. In addition, the time-averages in the model are done over the second half of the run, the same as in the experiments. The friction factor and eddy viscosity coefficients are as follows; $f_w = 0.01$, $C_1\kappa = 0.08$, $M = 0.1$ and $C_s = 0.15$.

4.2 Time-Averaged Properties

The measurements by Haller *et al.* (1997a,b) clearly indicate that rips are unstable. In order to compare measurements from separate experimental runs the data must be time-averaged. Although this does reduce the magnitude of the rip farther offshore, within the channel and behind the bar the general flow pattern is more or less unaffected. Furthermore, time-averaging allows for direct comparisons between the model and experimental data.

The unstable nature of rip currents is seen in Figure 4.3 which shows eight snapshots of computed velocity and vorticity. The rip is constantly meandering around shedding vortices. It is clear that a time-average is the only means for obtaining a true understanding of general circulation patterns for rip current systems. None the less, the time variations are not forgotten and are analyzed throughout this chapter.

The time-averaged wave height is shown as a three-dimensional mesh in Figure 4.4. The waves over the bars are breaking earlier than the waves in the channel although the waves in the channel are bigger because of the opposing rip current. Once the waves in the channel start breaking, they continue to break all the way to the shoreline. The waves over the bar, on the other hand, break on the bar and then reform in the trough region before beginning to break closer to the shoreline. The longshore variation in the wave height due to the irregularities in the topography is also evident.

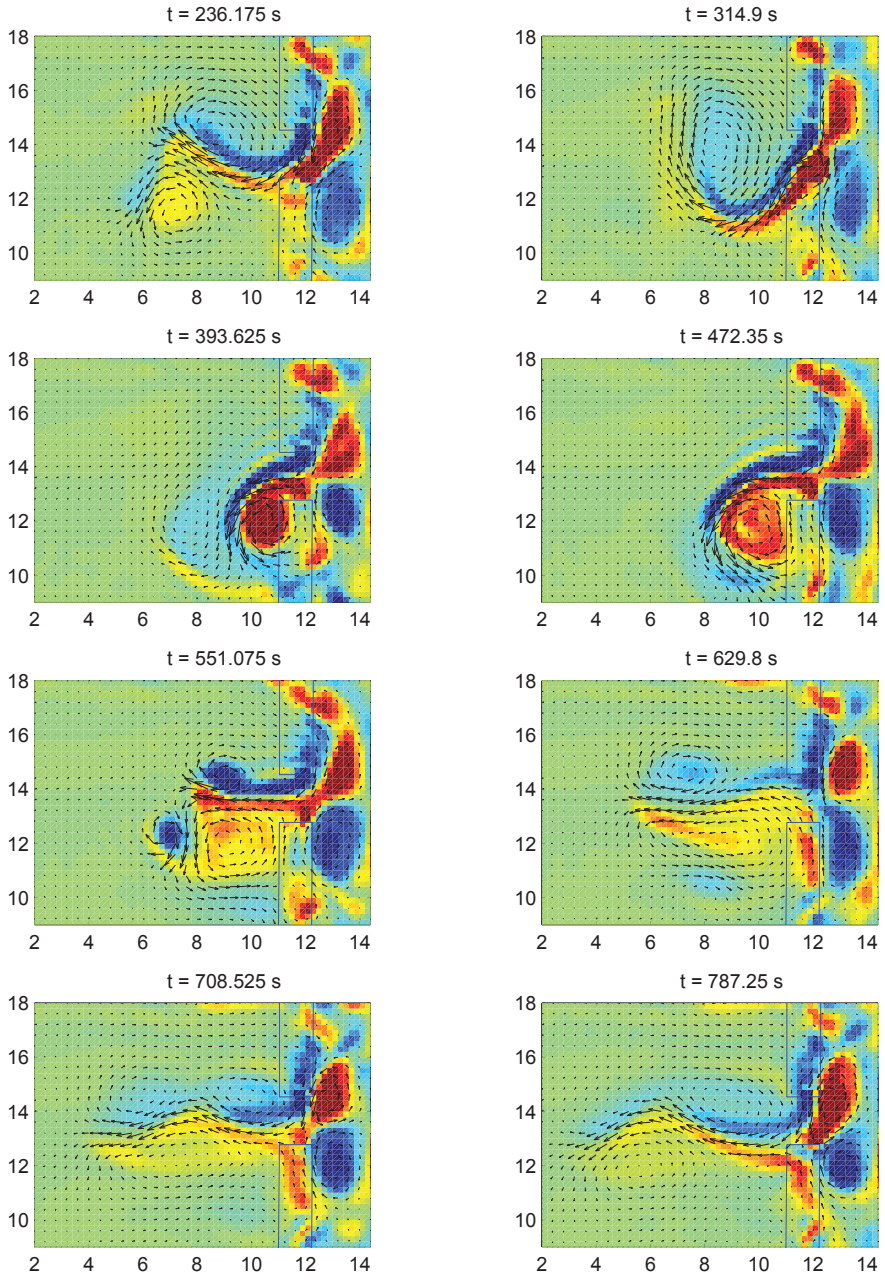

Figure 4.3: Instantaneous snapshots of vorticity and velocity vectors from the SC simulation. Only an excerpt of the entire computational domain is shown.

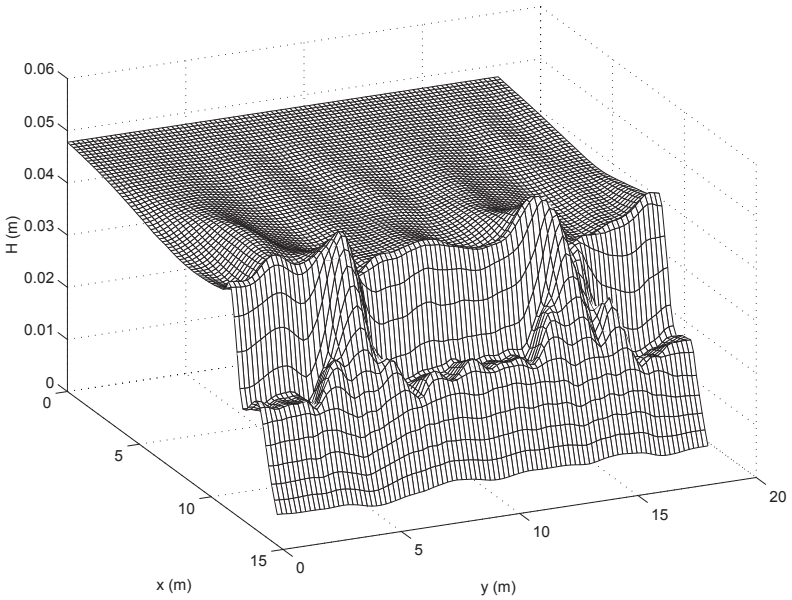

Figure 4.4: Time-averaged wave height from the SC simulation with wave current interaction. The shoreline is in the front of the figure.

The gradients in the radiation stresses created by the breaking wave pattern cause a setup in the water level. The time-averaged mean water level is shown in Figure 4.5. Because the basin is closed and the total mass must be conserved, the setup from the breaking waves is balanced by a small setdown in the offshore region. The breaking action over the bar causes a large setup which decreases toward the channels. The rip flowing offshore and turning toward the center of the basin creates a depression in the water level which is evident in the time-averaged water level. The more intense breaking behind the channel leads to an increase in water level close to the shoreline which decreases away from the channels.

Because the pressure is assumed to be hydrostatic, the variation in $\overline{\zeta}$ corresponds to the pressure gradient. The longshore pressure gradient driving the feeder currents for the rips is clearly evident in Figure 4.5. The longshore pressure gradient feeding the upper rip ($y = 13.6$ m) extends farther than the gradient feeding the

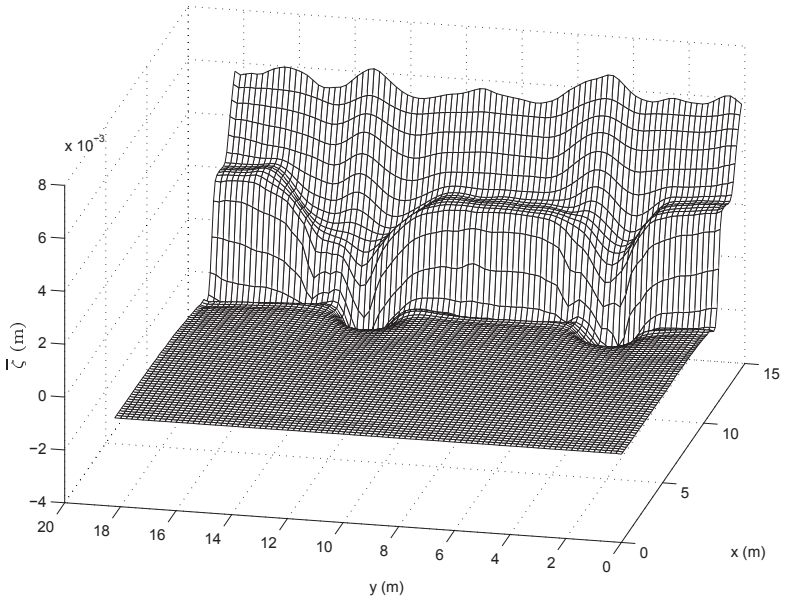

Figure 4.5: Time-averaged mean water level from the SC simulation. The shoreline is in the back of the figure.

lower rip ($y = 4.6$ m). The longshore pressure gradient close to the shoreline which drives the recirculation cells is also evident, albeit weaker than the gradients feeding the rips.

The time-averaged velocities from the experiments by Haller *et al.* (1997a,b) and the depth-integrated current $V_{m\alpha}$ from SC are displayed in Figure 4.6. The time-averaged flow pattern from SC looks similar to the measured flow field. The recirculation cells close to the shoreline have similar dimensions. The flow along the offshore edge of the central bar is parallel to the shore. The upper rip is biased toward the inside of the basin in both the measurements and the model results.

Direct comparisons between the experiments and model is possible for the time-averaged quantities. Figure 4.7 shows comparisons of the time-averaged short-wave height between Haller's laboratory data and the model along four longshore sections. The sections are (a) close to the shoreline, (b) in the trough behind the

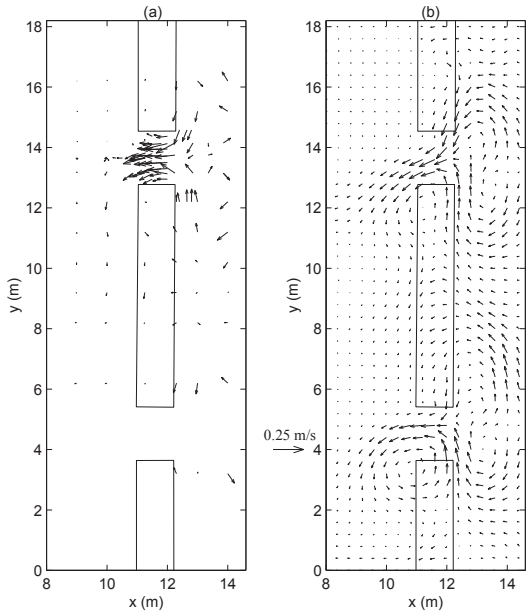

Figure 4.6: Time-averaged below-trough velocity ($V_{m\alpha}$) from (a) experimental data (Haller *et al.*, 1997a,b) and (b) the SC simulation.

bar, (c) on the seaward edge of the bar and (d) 1 m offshore of the bar. All four sections demonstrate excellent agreement between the model and measurements. The increase of the wave height across the channel is modeled well in (b).

Comparisons between the experimental data and the model results of the time-averaged mean water level are shown in Figure 4.8. This figure shows longshore sections from near the shoreline (a) to about 1 m seaward of the bar (d). The agreement for all four sections is quite good. In the trough region (b) the depression in $\overline{\zeta}$ behind the channel ($y \sim 13.6$ m) is modeled well. Near the shoreline in (a) the computed setup is slightly overpredicted, perhaps from the use of the wall shoreline boundary condition.

The time-averaged cross-shore velocity from the experimental measurements and the modeled time-averaged depth-integrated cross-shore currents from SC are compared in Figure 4.9. In general the agreement is fairly good for the four longshore

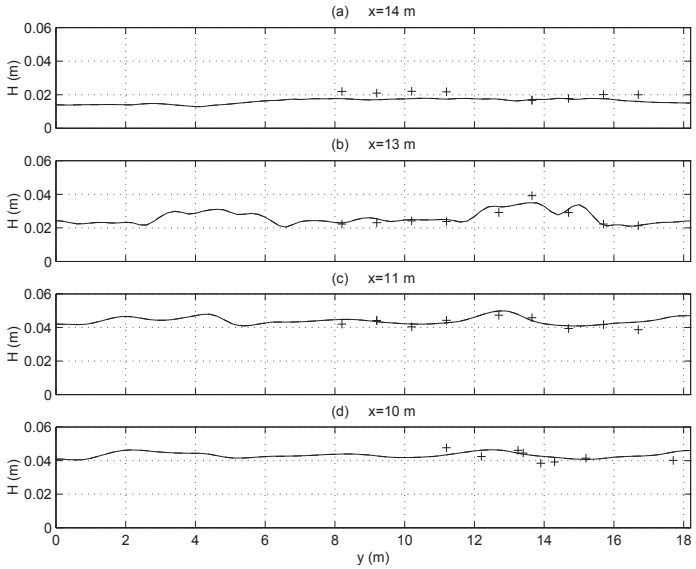

Figure 4.7: Comparison of time-averaged modeled wave height (-) to experimental data (+) (Haller *et al.*, 1997a,b) for (a) $x = 14$ m, (b) $x = 13$ m, (c) $x = 11$ m and (d) $x = 10$ m.

sections. Close to the shoreline in (a) the longshore variation is modeled well. In the trough, however, the cross-shore currents are not modeled as well. Along the offshore edge of the bar in (c) the currents are modeled accurately, the flow over the bar is nearly zero and the flow in the rip is quite large. The width and magnitude of the rip is reproduced nicely. The section farthest offshore (d) is also modeled fairly well, although the modeled currents show the offshore rip being larger than the measurements; however, as discussed in Chapter 2. This is possibly due to the measurements being lower in the water column which does not provide a true depth-average velocity.

Figure 4.10 shows the longshore velocity from the experimental measurements compared with the modeled time-averaged and depth-integrated longshore currents. Here, the currents are in good agreement. The modeled current is a little large in (a) and a little too small in (b). The offshore section (d) shows excellent agreement

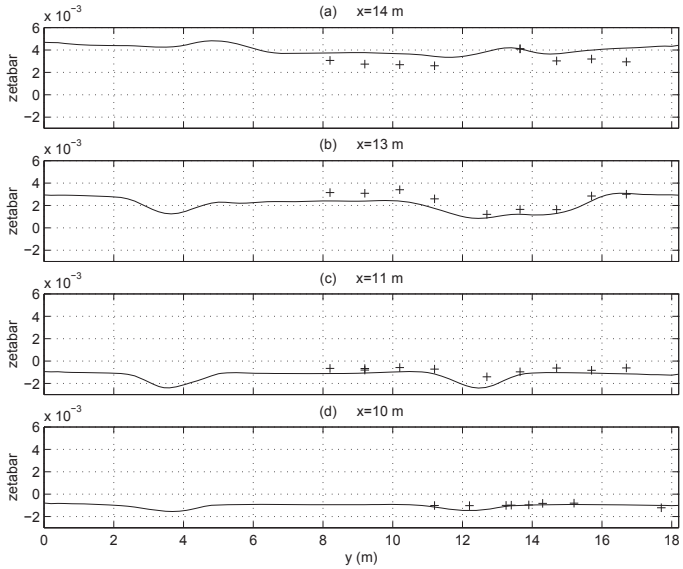

Figure 4.8: Comparison of time-averaged modeled mean water level (-) to experimental data (+) (Haller *et al.*, 1997a,b) for (a) $x = 14$ m, (b) $x = 13$ m, (c) $x = 11$ m and (d) $x = 10$ m.

demonstrating that the model does predict the correct bias of the rip current toward the inside of the basin.

The difficulties modeling the current in the trough region and close to the shoreline can be explained. Looking along $y = 13$ m in Figure 4.6b reveals that this section cuts fairly close to the center of the recirculation cells resulting in larger cross-shore currents and smaller longshore currents. The measurements, however, show that the cross-shore currents should be close to zero and the longshore currents are larger, signifying that the measurements are through the seaward edge of the recirculation cells. This indicates that the poor modeling along $y = 13$ m is a result of using the wall boundary condition at the shoreline which prevents the recirculation cells from shifting shoreward with the wave setup.

Rip currents are unstable flows as demonstrated by laboratory experiments and numerical simulations. In order to compare measurements from the laboratory

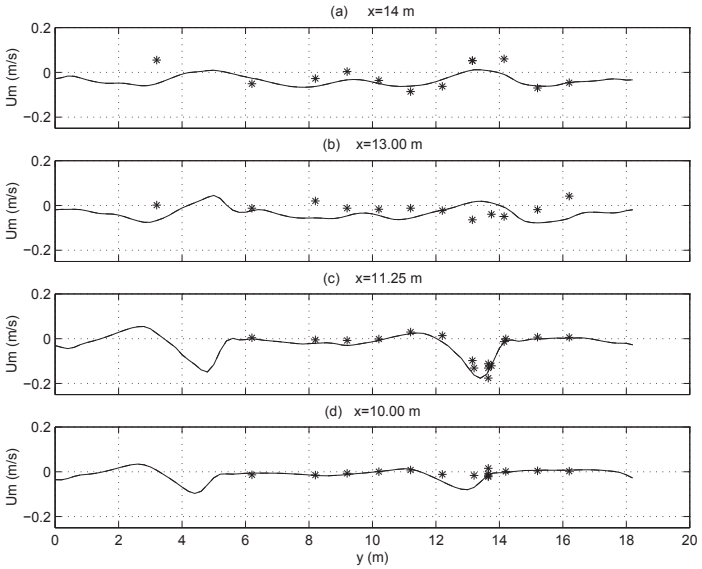

Figure 4.9: Comparison of time-averaged modeled cross-shore currents (-) to experimental data (+) (Haller *et al.*, 1997a,b) for (a) $x = 14$ m, (b) $x = 13$ m, (c) $x = 11.25$ m and (d) $x = 10$ m.

with the model results, a time-average is used. Comparisons between the model and experimental data of the wave height, mean water level and currents certify that SC successfully models rip current systems. Therefore, SC is used with confidence for further tests and analysis of rip currents.

4.3 Influence of the Bottom Stress

The influence of the bottom stress is ascertained by running SC with a higher bottom stress coefficient than the $f_w = 0.01$ used so far. This is accomplished by changing the bottom stress coefficient to $f_w = 0.025$ and holding all the other parameters constant. This allows for a direct comparison with the previous results where any changes are attributed to the increase in bottom stress.

As discussed in Haas *et al.* (1998), the bottom stress helps control the stability of the rip currents. Increasing the friction stabilizes the flow as seen in Figure 4.11.

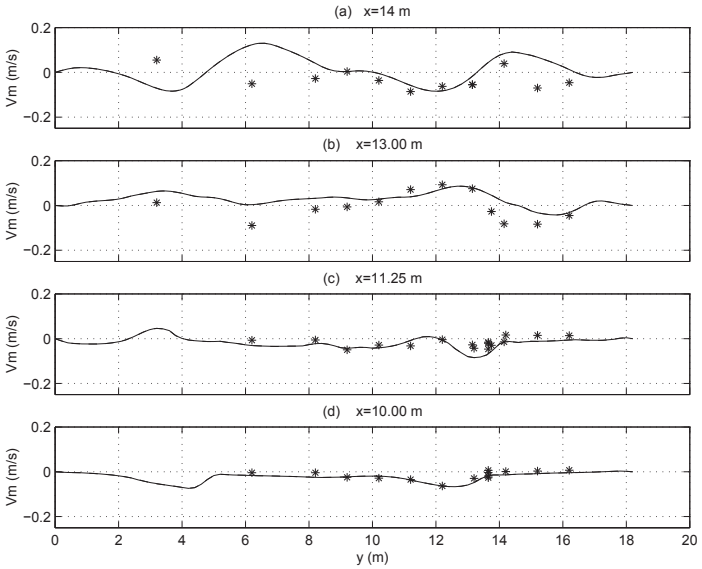

Figure 4.10: Comparison of time-averaged modeled longshore currents (-) to experimental data (+) (Haller *et al.*, 1997a,b) for (a) $x = 14$ m, (b) $x = 13$ m, (c) $x = 11.25$ m and (d) $x = 10$ m.

In this figure, eight snapshots of velocity and vorticity are displayed. Comparing it to Figure 4.3 reveals that the rip is much more stable with the larger bottom stress. The rip still meanders, but only at the seaward end, the flow in the channel is not moving as much.

Time-averaging the currents provides a clear picture of the alterations in the flow pattern produced by the increased friction factor. Figure 4.12 shows the time-averaged current vectors similar to Figure 4.6. In this figure it is apparent that the rip current flows much farther offshore, at least in the time-averaged sense. This is because the flow is much more stable leading to larger time-averaged currents, whereas before the current was so unstable that the rip was only at any given offshore location sporadically such that time-averaging removed the appearance of the rip.

Figure 4.13 shows longshore sections of the time-averaged depth-integrated cross-shore currents for model results with $f_w = 0.01$ and $f_w = 0.025$. Close to the

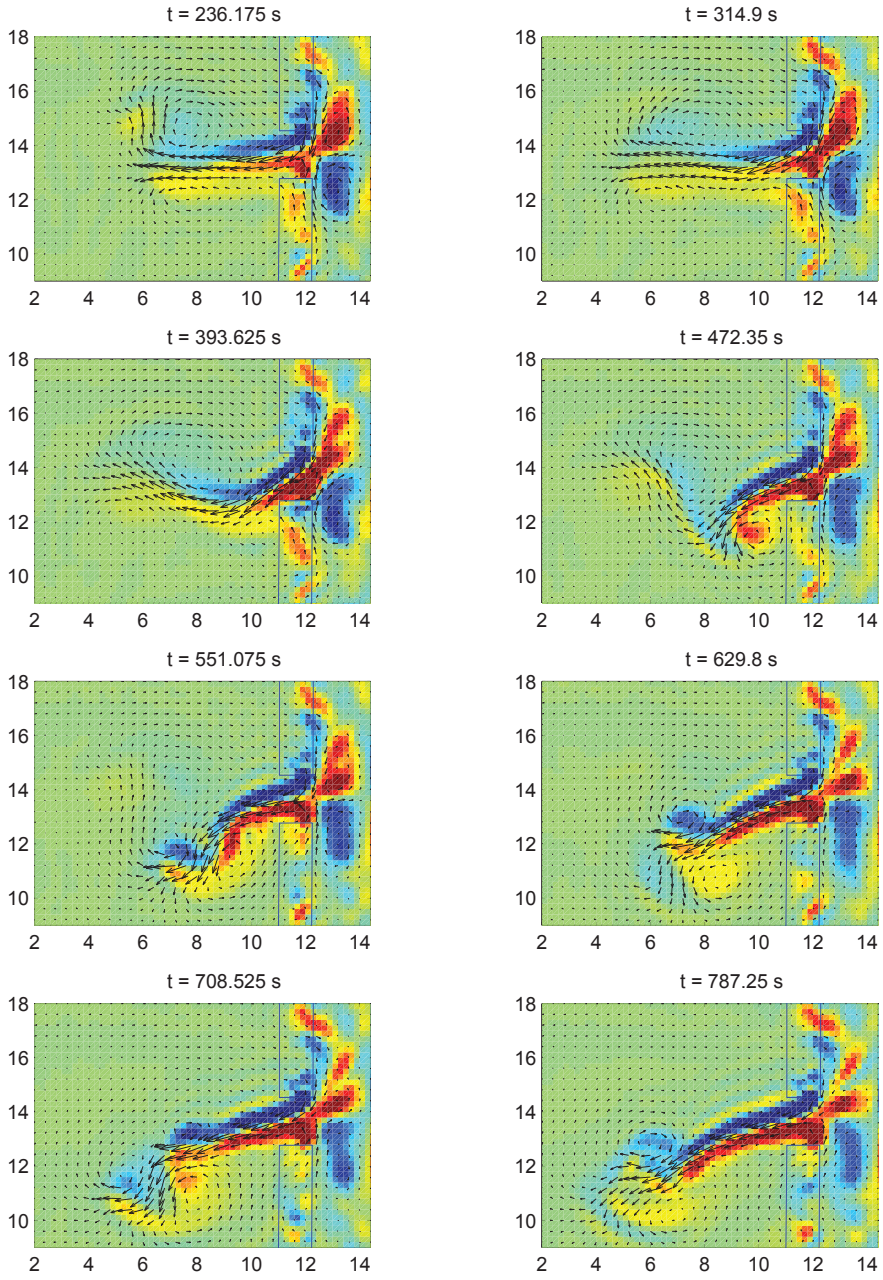

Figure 4.11: Instantaneous snapshots of vorticity and velocity vectors from the SC simulation with higher bottom stress ($f_w = 0.025$). Only an excerpt of the entire computational domain is shown. The rip is more stable than in Figure 4.3.

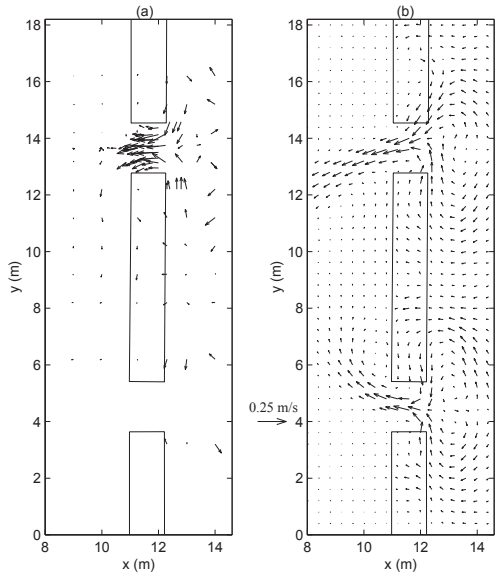

Figure 4.12: Time-averaged below-trough velocity ($V_{m\alpha}$) from (a) experimental data (Haller *et al.*, 1997a,b) and (b) the SC simulation with higher bottom stress ($f_w = 0.025$).

shoreline and in the trough region, (a) and (b), there is little difference between the currents for the two friction factors. In (c) at the seaward edge of the bar, the current over the bar remains small while the rip flow shifts slightly toward larger y for the higher friction factor. This is because the flow is more stable and does not turn as much toward the inside of the basin within the channel. For the section in (d) which is 1 m seaward of the bar, the velocity of the rip for the higher friction factor is much larger than the velocity for the lower friction factor. Even though the higher friction retards the flow, because the flow is more stable the rip meanders less producing a larger time average in the offshore region.

Finally, Figure 4.14 shows the the time-averaged depth-integrated longshore currents for model results with $f_w = 0.01$ and $f_w = 0.025$. Similar to the cross-shore currents, the longshore currents have few differences behind the bar and close to the shoreline in (a) and (b). However, the longshore current over and offshore of

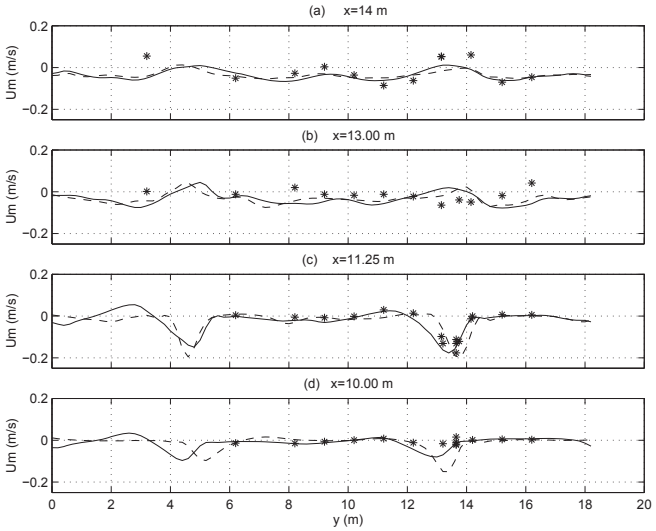

Figure 4.13: Comparison of time-averaged modeled cross-shore currents for (-) $f_w = 0.01$ and (- -) $f_w = 0.025$ to experimental data (+) (Haller *et al.*, 1997a,b) for (a) $x = 14$ m, (b) $x = 13$ m, (c) $x = 11.25$ m and (d) $x = 10$ m.

the bar in (c) and (d) is much weaker for the higher friction factor. The rip for the higher friction case is more or less flowing straight offshore because it is more stable resulting in a much smaller longshore current component.

Hence, it has been shown that the bottom stress contributes in the stability of rip current flows. Increasing the bottom friction leads to more stable flow patterns. Even though the increased friction results in lower instantaneous velocities, because the flow is more stable, the time-averaged rip current turns out to be larger.

4.4 Differences Between the Two Rips

The laboratory measurements from Test U outlined in Section 2.2.4 provide evidence that the two rip channels in the wave basin produce significantly different rip behavior. The lower rip ($y = 4.6$ m) is much weaker than the upper rip ($y = 13.6$ m). The fluctuations in the lower rip are smaller than the upper rip producing less

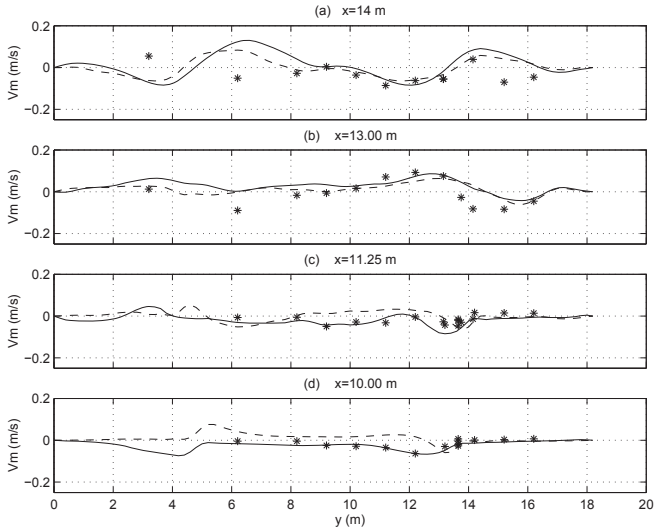

Figure 4.14: Comparison of time-averaged modeled longshore currents for (-) $f_w = 0.01$ and (- -) $f_w = 0.025$ to experimental data (+) (Haller *et al.*, 1997a,b) for (a) $x = 14$ m, (b) $x = 13$ m, (c) $x = 11.25$ m and (d) $x = 10$ m.

energy in the lower frequencies of the spectrum. This section establishes the behavior of the two rips in the simulations by SC and analyzes the reasons for the difference between the two rips.

Figure 4.15 shows computed time series of the cross-shore volume flux Q_x for each rip at three cross-shore locations. It is immediately obvious from the larger fluxes that the rip is much stronger in the upper channel. In addition, the fluctuations are larger and more frequent for the upper rip.

The energy spectra of the cross-shore volume flux in each channel at three cross-shore locations are shown in Figure 4.16. Similar to the spectra of the laboratory measurements shown in Figure 2.42, the energy in the upper rip is larger than the energy in the lower rip. Similar to the measurements, in (c) closer to the shoreline, the differences between the energy in the two rips are minor. Overall, the simulations by SC produces rip flow in the upper channel which is much stronger

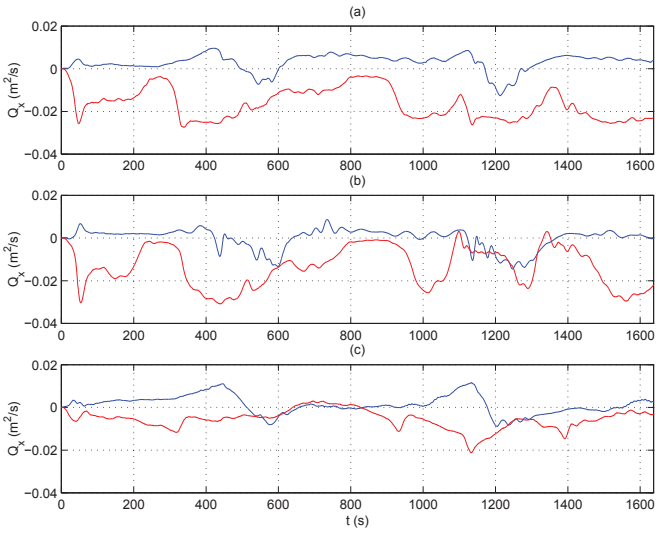

Figure 4.15: Time series of Q_x inside each rip ((blue) $y = 4.6$ and (red) $y = 13.6$ m) from SC simulations for (a) $x = 10.8$ m, (b) $x = 11.6$ m and (c) $x = 12.2$ m.

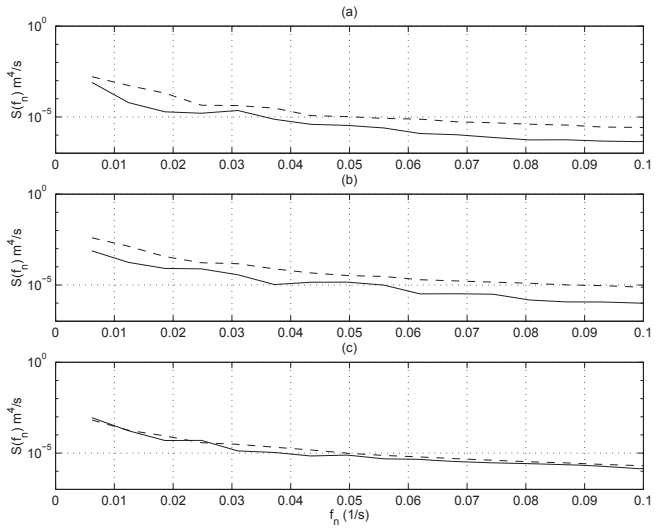

Figure 4.16: Energy spectra (20 degrees of freedom) for the cross-shore volume flux in each rip ((-) $y = 4.6$ and (- -) $y = 13.6$) from SC simulations for (a) $x = 10.8$, (b) $x = 11.4$ and (c) $x = 12.20$.

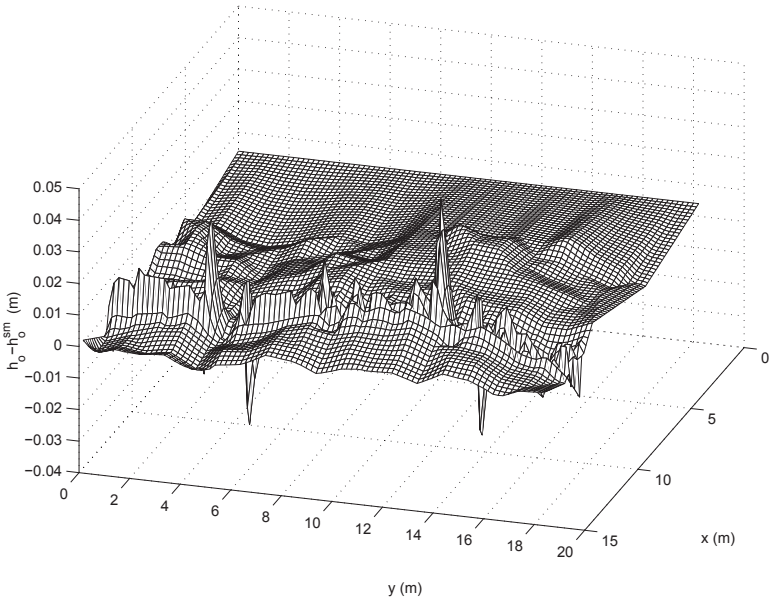

Figure 4.17: Three-dimensional mesh of the difference between h_o and h_o^{sm}.

and has larger fluctuations than the rip flow in the lower channel. These striking differences in rips are in agreement with the laboratory measurements in Section 2.2.4.

When the model is run with the idealized topography the two rips behave similarly. This leaves only one feature of the wave basin used in SC which influences the flow pattern accounting for the differences between the rip flow in the two channels, the topography. An inspection of the topography in Figure 4.2 reveals that many irregularities exist. The pattern of these variations is made clearer by subtracting the idealized symmetric design topography h_o^{sm} from the actual still water depth h_o. A three-dimensional view of the resulting difference in depth is shown in Figure 4.17. Positive values represent deeper depths and negative values represent shallower depths.

The large spikes on either side of the two channels signify that the channels are not exactly centered where they are supposed to be. Both channels are shifted

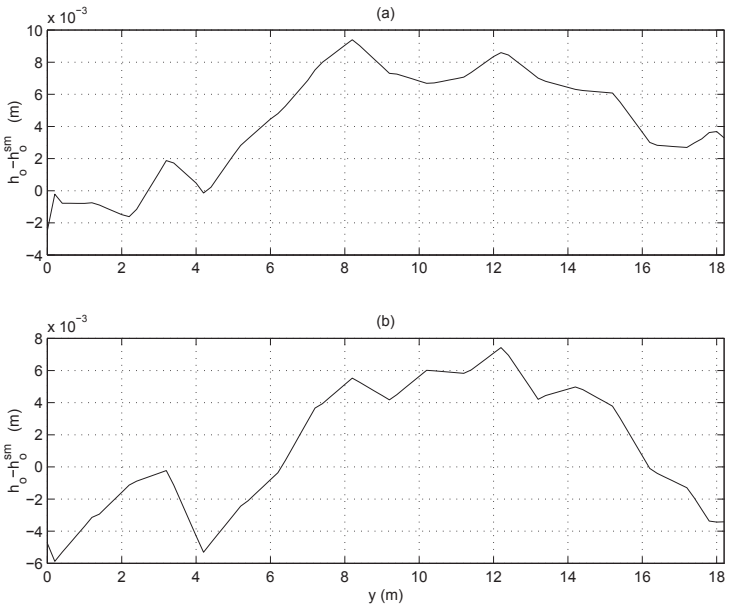

Figure 4.18: Longshore section of the difference between h_o and h_o^{sm} for (a) $x = 9$ m and (b) $x = 13$ m.

in the same direction. A closer look reveals that the depth for the upper half of the basin, $y > 9$ m, is larger than the depth in the lower half. It is possible that this deeper depth accounts for the difference in the rip flows.

A more detailed look at the depth variations is offered in Figure 4.18. This figure shows longshore sections of the depth variation offshore of the bar at $x = 9$ m and shoreward of the bar at $x = 13$ m. Along both sections the depth is larger for $y > 7$ m than for $y < 7$ m. This depth variations forces more feeder currents to flow toward the upper channel creating more flow in that rip. Looking back at Figure 4.6b confirms that more flow in the trough region behind the bar is feeding the upper rip. In fact, some of the flow from the recirculation cell behind the lower channel ($y = 4.6$ m) is going past the center line and feeding the upper rip ($y = 13.6$ m). Because the upper channel has more feeder currents, the flux in that rip is larger leading to more instabilities which account for the larger fluctuations in the

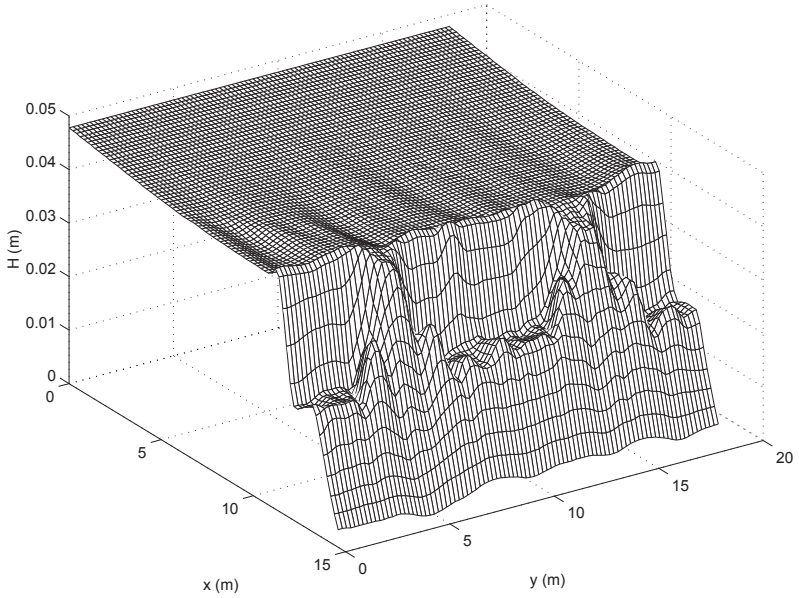

Figure 4.19: Time-averaged wave from the SC simulation without wave current interaction.

time series in both the laboratory measurements and the SC simulations.

4.5 Significance of Wave Current Interaction

When encountering opposing currents, waves increase in height and shorten in length thereby causing them to become steeper. In Chapter 2, visual observations during the laboratory experiments of the waves in the presence of rip currents indicate that the current has an effect on the waves. This section discusses the effect of the wave current interaction by looking at the wave and current patterns using SC without wave current interaction and comparing this with the previous results in Section 4.2 which include wave current interaction.

The time-averaged wave heights from the SC simulation without wave current interaction is shown in Figure 4.19. The waves are calculated without any currents and are held constant throughout the entire simulation. Comparing this figure

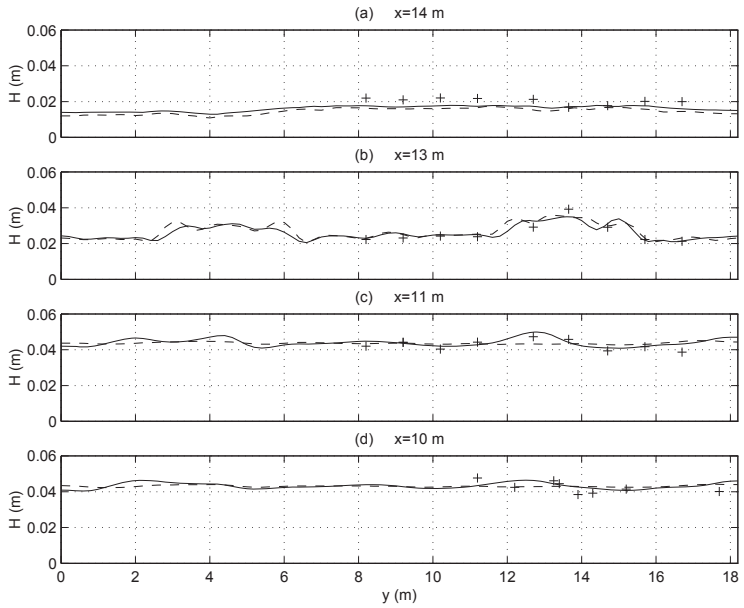

Figure 4.20: Comparison of time-averaged modeled wave height (-) with wave current interaction and (- -) without wave current interaction to experimental data (+) (Haller *et al.*, 1997a,b) for (a) $x = 14$ m, (b) $x = 13$ m, (c) $x = 11$ m and (d) $x = 10$ m.

with Figure 4.4 identifies the importance of including wave current interaction in the model simulations. In Figure 4.4 each rip creates larger wave heights in their immediate vicinity whereas in Figure 4.19 the waves offshore of the bar remain fairly longshore uniform.

A detailed comparison of the wave height with the experimental data is shown in Figure 4.20. This figure shows four longshore sections of the wave height with and without wave current interaction. Close to the shoreline in (a), the wave heights for both simulations are similar because the cross-shore currents here are weak. Similarly, the wave heights in the trough region behind the bar (b) are equivalent. The wave heights with wave current interaction on the seaward edge of the bar (c), however, are larger in the rip region ($11.8 < y < 13.8$ m). This is true 1 m offshore of the bar in (d) as well.

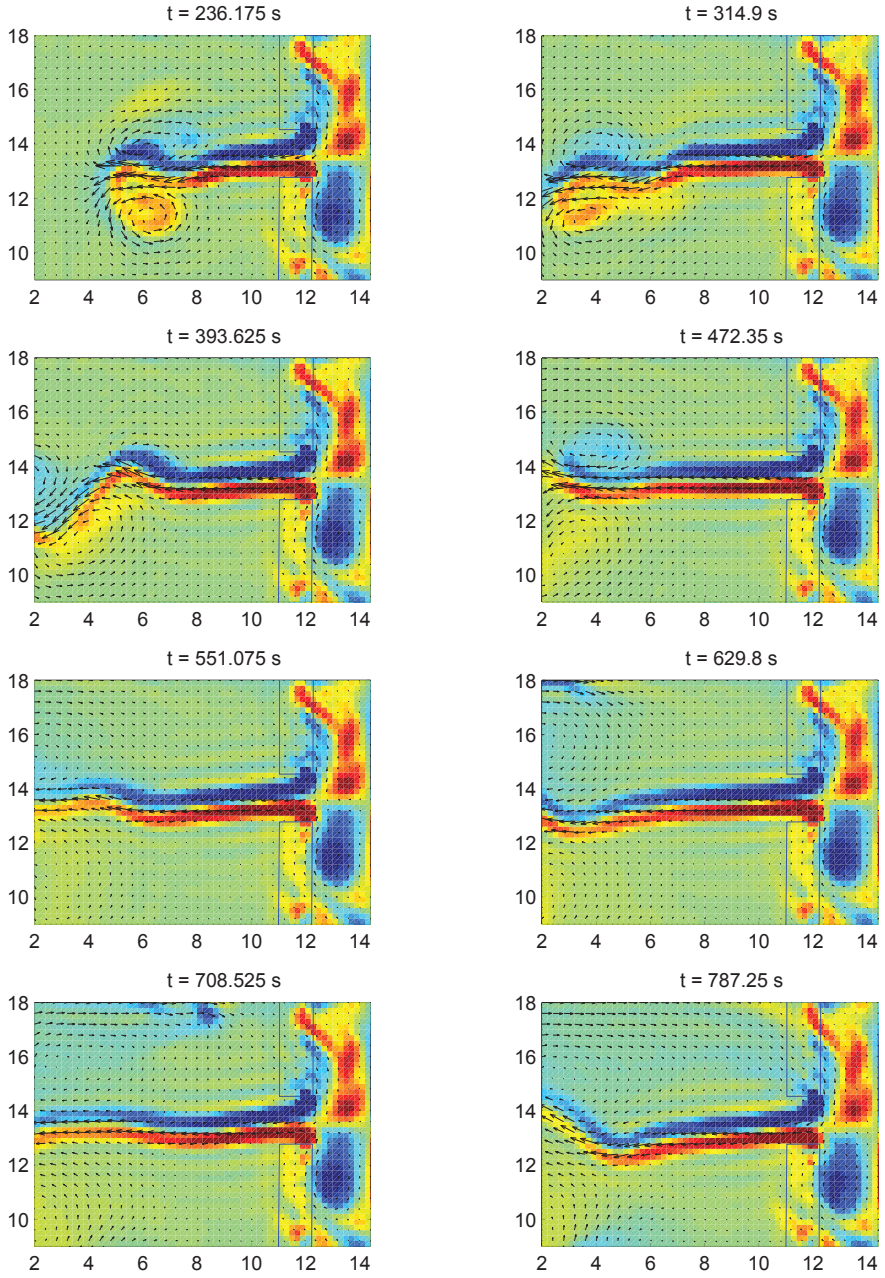

Figure 4.21: Instantaneous snapshots of vorticity and velocity vectors from SC without wave current interaction showing the rip current extending far offshore. Only an excerpt of the entire computational domain is shown.

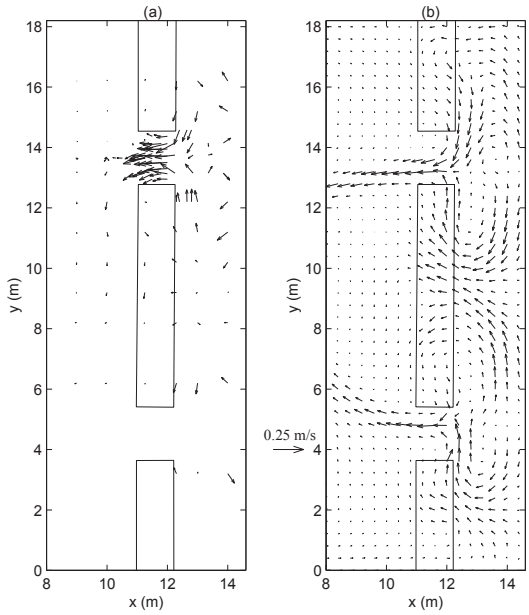

Figure 4.22: Time-averaged below-trough velocity ($V_{m\alpha}$) from (a) experimental data (Haller *et al.*, 1997a,b) and (b) SC without wave current interaction.

The difference in wave height with and without wave current interaction translates into different forcing for the currents. The resulting currents are significantly different than the currents with the wave current interaction. Figure 4.21 shows eight snapshots of vorticity and velocity vectors from the SC simulation without wave current interactions. Clearly, the rip extends much farther offshore than it does for the simulations with wave current interaction in Figure 4.3. The rip current is still unstable as evident by the meandering of the rip head.

Figure 4.22 shows the time-averaged current $V_{m\alpha}$ for the SC simulation without wave current interaction. The rip flows much farther offshore in this figure than it does in Figure 4.6 for the SC simulation with wave current interaction. The impact on the circulation pattern of the wave current interaction is that it prevents the rip from flowing as far offshore.

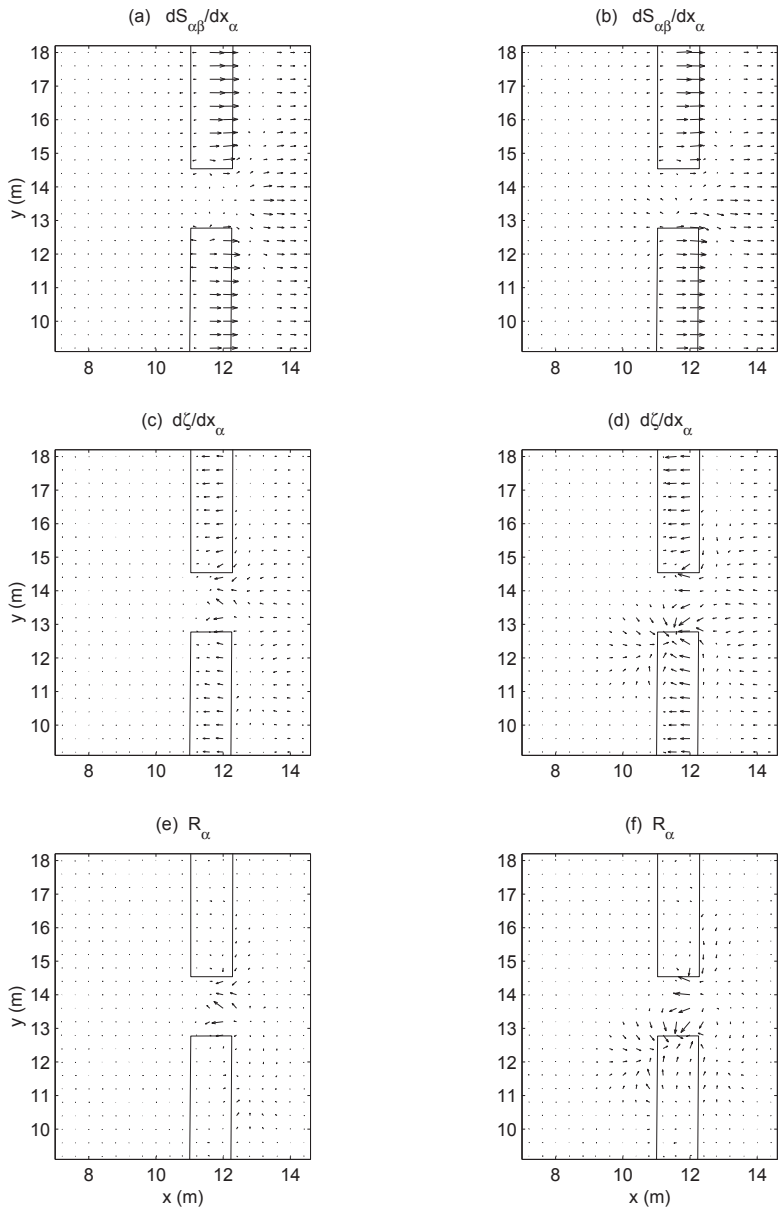

Figure 4.23: Vectors of ((a) and (b)) radiation stress, ((c) and (d)) pressure gradient and ((e) and (f)) forcing residual where the left column ((a), (c) and (e)) is without wave current interaction and the right column ((b), (d) and (f)) is with wave current interaction.

The reason for the rip being prevented from flowing farther offshore by the wave current interaction is seen in Figure 4.23. This figure shows the time-averaged radiation stress forcing, pressure gradient and forcing residual (R_α). The left column is for the simulation without wave current interaction corresponding to the time-averaged currents in Figure 4.22 and the right column is for the simulation with wave current interaction corresponding to the time-averaged currents in Figure 4.6. The forcing residual is defined as the summation of the radiation stress and the pressure gradient,

$$R_\alpha = -\frac{1}{\rho}\frac{\partial S_{\alpha\beta}}{\partial x_\beta} - gh\frac{\partial \overline{\zeta}}{\partial x_\alpha} \tag{4.1}$$

which represents the local forcing available for driving currents. More details about the forcing residual is given in Chapter 6.

The radiation stress forcing just offshore of the channel in (a) is negligible whereas the forcing in (b) is larger and directed offshore because of the increasing wave height due to the opposing current. The pressure gradient is large and directed offshore in the shoreward half of the channel in (c) as well as in (d). However in (d), there is a large pressure gradient directed shoreward on the lower offshore edge of the channel. This pressure gradient is from the depression of the water surface where the rip shoots out of the channel and turns toward the middle of the basin (or the bottom of the figure). The forcing residual in the shoreward part of the channel in (e) and (f) is large and directed offshore. This is the forcing which drives the rip current offshore. For the simulation with wave current interaction in (f) there is also a forcing residual offshore of the channel. This is the forcing which prevents the rip from flowing far offshore.

The wave current interaction modifies the wave field by increasing the waves in the presence of the opposing current. These modified waves result in radiation stress forcing offshore from the channel which cause a depression in the water level. The resulting pressure gradient is sufficient to prevent the rip current from flowing

straight offshore. Therefore, in order to accurately model rip currents, the wave current interaction must be included in the modeling system.

4.6 Significance of 3D Dispersive Mixing

The advantage of using SC over other types of nearshore circulation models is that it includes the effect of the vertical variation of the currents. This results in dispersive mixing like terms as seen in Section 3.3. The significance of these terms is established in this section by showing the results of SC simulations without including them.

When doing computations for depth uniform currents all the dispersive mixing terms are exactly zero. The only mixing in the model comes from the turbulent mixing due to the wave breaking, bottom friction and the shear in the flow. Figure 4.24 shows eight snapshots of the vorticity and current vectors from the SC simulation for depth uniform currents. It is obvious that the currents are much more unstable in this figure than for the simulation with depth varying currents in Figure 4.3. The eddies which are created and shed by the rip drift around the domain and take a long time to dissipate. The rip in the simulation with the 3D dispersive mixing also generates eddies, however, these eddies are dissipated much more rapidly.

Figure 4.25 shows the time-averaged velocity vectors from the simulation for depth uniform currents. Because of the highly unstable nature of the flow without the 3D dispersive mixing mechanism, the rip in this figure is much broader than the rip in Figure 4.6. Also, the rip meanders to both sides such that the time-average does not appear to be biased to any particular side. Inspecting the flow over the center bar reveals that there is a significant return current over this bar. Eddies which are generated in the trough region and not dissipated pass over the center of the bar resulting in the net flow seaward.

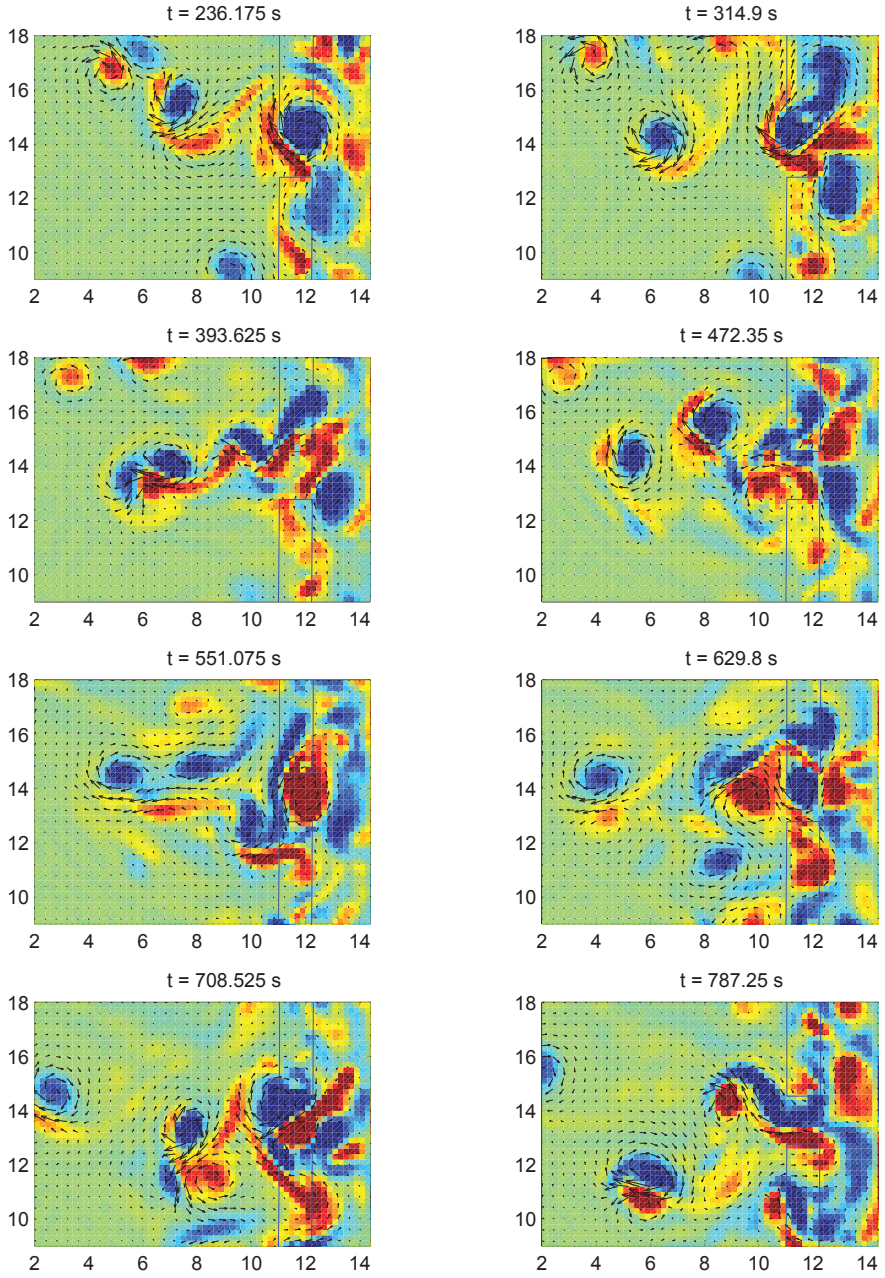

Figure 4.24: Instantaneous snapshots of vorticity and velocity vectors from the SC simulation without 3D dispersive mixing. Only an excerpt of the entire computational domain is shown. Comparison with Figure 4.3 show that the flow is much more unstable with depth uniform currents.

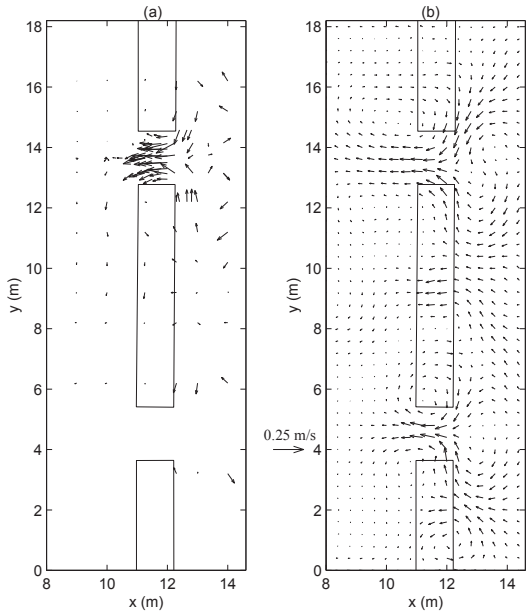

Figure 4.25: Time-averaged below-trough velocity ($V_{m\alpha}$) from (a) experimental data (Haller *et al.*, 1997a,b) and (b) the SC simulation without 3D dispersive mixing.

Hence, the flow patterns for the SC simulations using depth uniform currents are significantly different than the flow patterns for the depth varying currents. The flow is much more unstable without the dispersive mixing mechanism. Eddies generated by the rip currents are dispersed much slower and tend to fill the domain. The 3D dispersive mixing is the dominant mixing mechanism for rip current systems making it imperative to include it when simulating rip currents.

Chapter 5

NUMERICAL MODELING OF RIP CURRENT: 3D PROPERTIES

The experimental measurements from Chapter 2 indicate that the depth variation of rip currents transform from depth uniform inside the channel to depth varying outside the surfzone. As the rip flows offshore the velocity near the surface becomes much larger than the velocity lower in the water column.

This chapter uses the numerical nearshore circulation model SHORECIRC (SC) to identify the mechanisms for creating the depth variation in rip currents outside the surfzone. In addition, the structure of the depth variations is examined throughout the rip current system.

The first section looks at the vertical structure of the rip currents by analyzing a rip current on an idealized topography. Using the idealized topography simplifies the rip current analysis immensely by producing a symmetric rip current. The terms governing the vertical variation of currents is scaled to determine the relative importance of each term. In addition, the idealized topography is used in SC to model the rip currents numerically.

The second section utilizes the actual topography from the basin allowing for direct comparisons between the measurements and numerical model results. This section compares the mechanisms for creating the depth variations on the real topography with the idealized rip case.

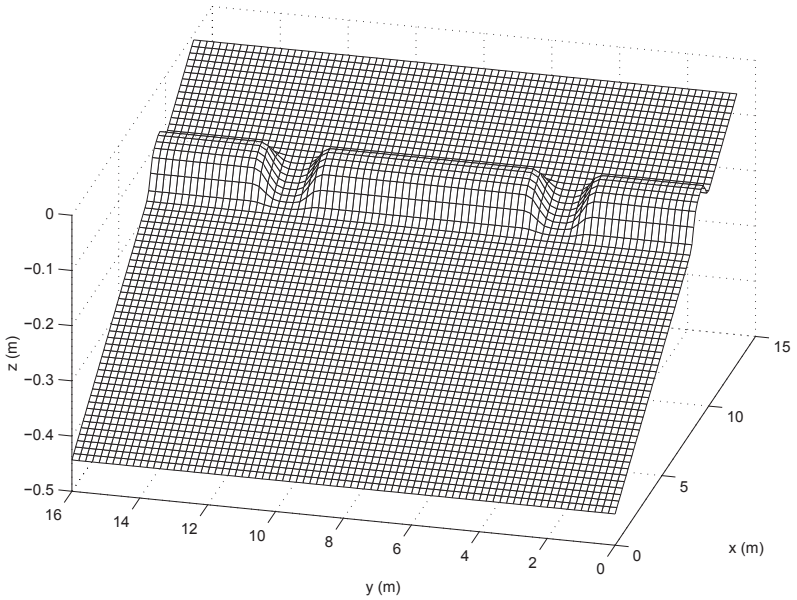

Figure 5.1: Idealized topography which is symmetric about the centerline of beach and symmetric about the centerline of each channel.

5.1 Idealized Topography

Rip current circulation systems are complex, therefore, in order to simplify the analysis an idealized rip current is used. The real topography is used in Section 5.2 and the comparisons with the experimental data are given which demonstrate the validity of using SC to model the vertical variations of rip currents. The idealized topography for this case is shown in Figure 5.1. The topography is symmetric about the center of the domain as well as symmetric around the centerline of each rip channel. This topography produces two symmetric rip currents.

In addition, to simplify the analysis further, the simulation is run for a short enough period of time that the rip current remains stable. The resulting stable rip currents are symmetric about their centerline reducing the forcing terms for the vertical profiles to much simpler forms.

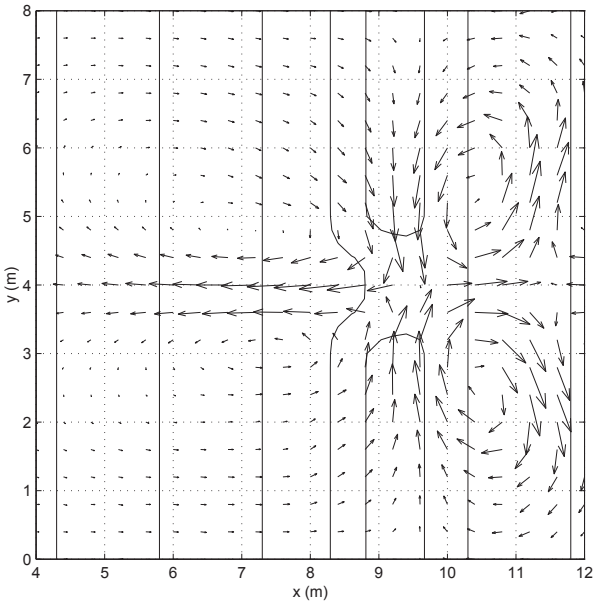

Figure 5.2: Vector plot of $V_{m\alpha}$ from the SC simulations with the idealized topography contours shown. Only one rip channel is shown.

5.1.1 Overall Structure of the Current Profiles

The results from running SC with the idealized topography are presented in this subsection. Here, we focus on the overall structure of the current profiles throughout the entire circulation system and the next subsection describes the mechanisms for the vertical variations.

Figure 5.2 shows vectors of the depth-average velocity $V_{m\alpha}$ along with contours of the depth. Note that this is a snapshot of one rip channel and not the entire computational domain. The rip channel is centered at $x = 9$ and $y = 4$ m. The rip flows offshore, essentially symmetric about $y = 4$ m, before diverging around $x = 6.5$ m.

Figure 5.3 shows the cross-shore evolution of the vertical variation of V_x across the bar (a) and through the rip current (b). On top of the bar ($x = 9$ m) in Figure 5.3a, the vertical profile looks similar to the shape of the undertow profile inside

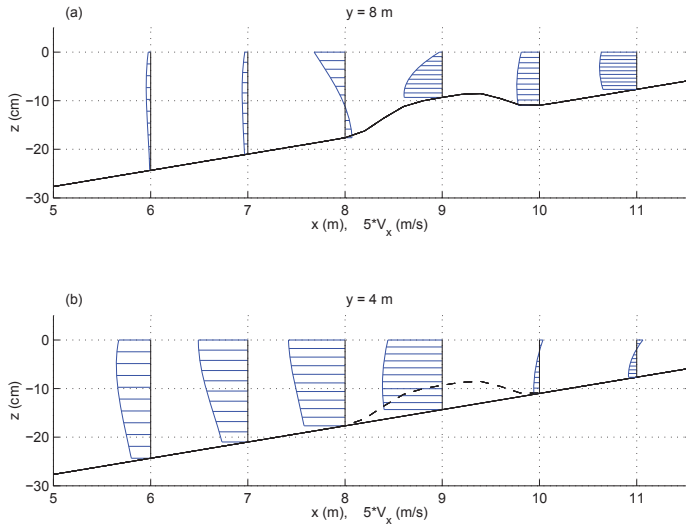

Figure 5.3: SC simulations on the idealized topography of the vertical profiles of V_x over the bar (a) and through the rip channel (b). The dashed line represents the location of the bar.

the surfzone given by Putrevu and Svendsen (1993). The undertow profile in the surfzone is characterized by strong depth variations with weak offshore or shoreward velocity near the surface. The forcing for the velocity profile inside the surfzone is dominated locally by the breaking waves. On the other hand, the profiles farther offshore ($x \leq 7$ m) have little local wave forcing because the waves are only shoaling and not breaking. These profiles are characterized by little vertical structure and have a similar variation to the profiles outside the surfzone in Putrevu and Svendsen (1993).

The vertical variations of the rip currents in Figure 5.3b demonstrate much different characteristics. Inside the channel ($x = 9$ m) the current is strong and virtually depth uniform. As the rip flows offshore, the velocity remains large near the surface and decreases lower in the water column. Outside the surfzone, the waves in the rip are refracting around the strong opposing current which creates forcing which is stronger than the forcing by waves passing over the bar. The

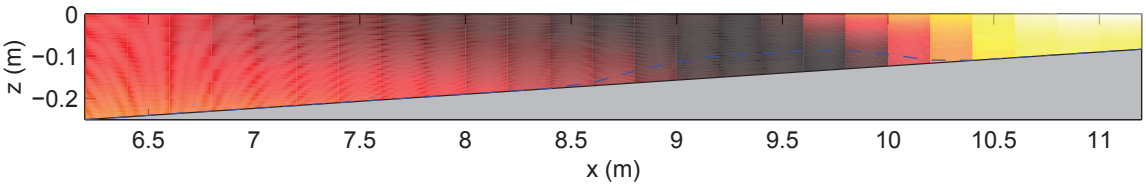

Figure 5.4: Color contour plot of V_x through the rip channel from the SC simulation on the idealized topography. Darker colors represent offshore velocity, lighter colors represent onshore velocity.

profiles offshore of the channel are qualitatively similar to the profiles found in the measurements in Chapter 2. Note that the profiles at $x = 10$ and 11 m are both at nodal locations where there is very little current.

Figure 5.4 provides a continuous picture of the vertical structure of the rip current. This figure shows a color contour plot of the cross-shore currents through the center of the rip. The darker color represents strong offshore velocities and the lighter color represents onshore velocities. The gray area is the bottom topography and the dashed blue line represents the location of the bar. The currents well inside the surfzone ($x \geq 9.5$) have larger velocities nearer the bottom than at the top, similar to undertow, as indicated by the lighter color above the darker color. Through the channel ($8.5 \leq x \leq 9.5$) the current is fairly depth uniform. Offshore from the channel ($x \leq 8.5$) the darker color is above the lighter color indicating that the larger velocities are near the surface.

The previous figures have all been two dimensional representations of the current. The advantage of using SC is that it provides three-dimensional current variations. The three-dimensional variation of the rip current can be seen in Figure 5.5 for the flow pattern shown in Figure 5.2. Numerous vertical profiles of the currents are drawn throughout the rip current system. The section through the channel is from the middle of the rip current. The sections on either side show the

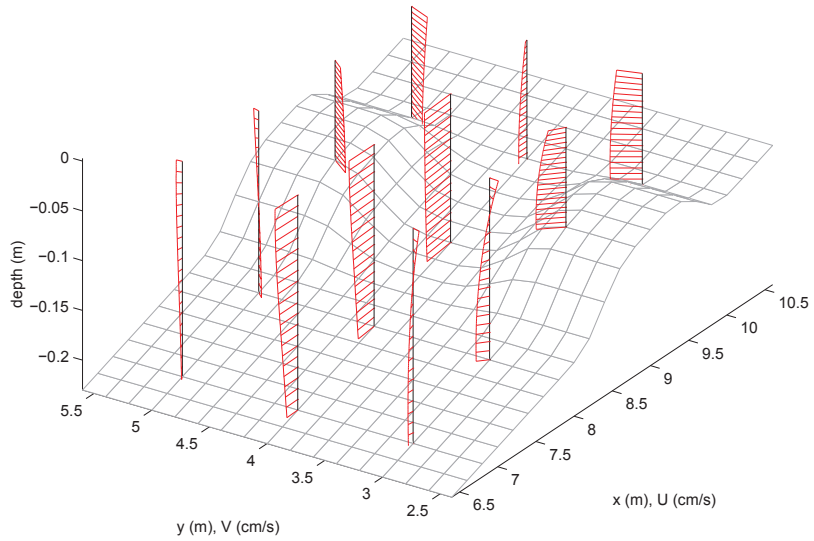

Figure 5.5: SC modeled vertical profiles of V_α for the idealized topography.

feeder currents behind and over the bars. Note that in order to reduce the clutter in the figure the profiles are only plotted at a few computational points.

The profiles of the rip currents show the same depth varying trend offshore of the channel. Interestingly, the rip feeder currents are not just behind the bar but also flow over the top of the bar. The vertical variations of these feeder currents are similar to the variation of undertow, reduced velocity near the surface, because the forcing is primarily from the breaking waves.

Immediately offshore of the bar, $x = 8$ m, the feeder currents are weak with the velocity near the surface flowing away from the rip and the current over the majority of the depth flowing toward the rip. Farther offshore of the bar, $x = 7$ m, the currents alongside the rip are no longer feeding the rip but flowing parallel near the bottom and away from the rip near the surface. In the horizontal flow patterns shown in Figure 5.2 it is evident that as the rip flows offshore, it becomes narrower at first ($7 < x < 9$ m) but then becomes wider as it begins to diverge ($x < 7$ m).

In Figure 5.5, the flow near the surface along the sides of the rip begins diverging immediately offshore of the channel even though the depth integrated current is still feeding the rip.

5.1.2 Scaling Analysis of the Current Profiles

The previous subsection demonstrated the depth variation of the currents in the rip current circulation system. Performing a scaling analysis on the magnitudes of the terms governing the vertical profiles of the current can provide insight as to which terms are important for the rip current. The scaling analysis by Putrevu and Svendsen (1999) was based on the magnitudes of the terms inside the surfzone. Here, the scaling incorporates the different magnitudes of the terms inside and outside the surfzone as well as distinctions inside and outside the rip current.

Based on the solutions for $V_{d\alpha}^{(0)}$, equations (B.9) and(B.10), and $V_{d\alpha}^{(1)}$, equation (B.19) in Appendix B the depth varying current is proportional to the following,

$$\begin{aligned} V_{dx} \sim \quad & \frac{F_x}{\nu_t} + \frac{\tau_x^B}{\rho h \nu_t} - \frac{Q_x}{\rho h \nu_t}\left(\frac{\partial V_{dx}}{\partial x} - \frac{\partial \frac{Q_{wx}}{h}}{\partial x}\right) - \frac{Q_y}{\rho h \nu_t}\left(\frac{\partial V_{dx}}{\partial y} - \frac{\partial \frac{Q_{wx}}{h}}{\partial y}\right) \\ & -\frac{1}{\nu_t}\left(V_{dx} - \frac{Q_{wx}}{h}\right)\frac{\partial \frac{Q_x}{h}}{\partial x} - \frac{1}{\nu_t}\left(V_{dy} - \frac{Q_{wy}}{h}\right)\frac{\partial \frac{Q_y}{h}}{\partial y} - \frac{W}{\nu_t}\frac{\partial V_{dx}}{\partial z} \\ & +\frac{Q_{wx}}{h\nu_t}\frac{\partial \frac{Q_{wx}}{h}}{\partial x} + \frac{Q_{wy}}{h\nu_t}\frac{\partial \frac{Q_{wx}}{h}}{\partial y} - \frac{Q_{wx}}{h\nu_t}\frac{\partial V_{dx}}{\partial x} - \frac{Q_{wy}}{h\nu_t}\frac{\partial V_{dx}}{\partial y} - \frac{V_{dx}}{\nu_t}\frac{\partial \frac{Q_{wx}}{h}}{\partial x} - \frac{V_{dy}}{\nu_t}\frac{\partial \frac{Q_{wx}}{h}}{\partial y} \\ & -\frac{1}{h\nu_t}\frac{\partial}{\partial x}\left[2V_{dx}Q_{wx}\right] - \frac{1}{h\nu_t}\frac{\partial}{\partial y}\left[V_{dx}Q_{wy} + V_{dy}Q_{wx}\right]. \end{aligned} \tag{5.1}$$

Because of the symmetry in the rip current the following simplifications for the current profile along the centerline of the rip are made,

$$Q_y = 0 \tag{5.2}$$

$$Q_{wy} = 0 \tag{5.3}$$

$$V_{dy} = 0 \tag{5.4}$$

$$\frac{\partial V_{dx}}{\partial y} = 0 \tag{5.5}$$

$$\frac{\partial Q_{wx}}{\partial y} = 0. \tag{5.6}$$

Using equations (5.2)-(5.6), equation (5.1) is transformed to

$$\begin{aligned} V_{dx} \sim \; & \frac{F_x}{\nu_t} + \frac{\tau_x^B}{\rho h \nu_t} - \frac{Q_x}{h\nu_t}\frac{\partial V_{dx}}{\partial x} + \frac{Q_x}{h\nu_t}\frac{\partial \frac{Q_{wx}}{h}}{\partial x} - \frac{1}{\nu_t}V_{dx}\frac{\partial \frac{Q_x}{h}}{\partial x} + \frac{Q_{wx}}{h\nu_t}\frac{\partial \frac{Q_x}{h}}{\partial x} \\ & -\frac{W}{\nu_t}\frac{\partial V_{dx}}{\partial z} + \frac{Q_{wx}}{h\nu_t}\frac{\partial \frac{Q_{wx}}{h}}{\partial x} - \frac{Q_{wx}}{h\nu_t}\frac{\partial V_{dx}}{\partial x} - \frac{V_{dx}}{\nu_t}\frac{\partial \frac{Q_{wx}}{h}}{\partial x} \\ & -\frac{2}{h\nu_t}V_{dx}\frac{\partial Q_{wx}}{\partial x} - \frac{2}{h\nu_t}Q_{wx}\frac{\partial V_{dx}}{\partial x} - \frac{1}{h\nu_t}Q_{wx}\frac{\partial V_{dy}}{\partial y} - \frac{1}{h\nu_t}V_{dx}\frac{\partial Q_{wy}}{\partial y}. \end{aligned} \tag{5.7}$$

A scaling analysis differentiating between the size of the terms inside and outside the surfzone and rip current is used to compare the relative sizes of each term in (5.7) by introducing the following non-dimensional variables,

$$\begin{aligned} & x = Lx^*, \;\; y = \mu L y^*, \;\; z = h_b z^*, \;\; h = h_b h^*, \\ & F_x = \frac{\gamma\delta c_b^2}{L}F_x^*, \;\; \tau_x^B = (\kappa+\delta) f_w \rho c_b^2 \tau_x^{B*}, \;\; Q_\alpha = \kappa c_b h_b Q_\alpha^*, \;\; W = (\kappa+\delta)\frac{h_b}{L}c_b W^*, \\ & V_{d\alpha} = \epsilon c_b V_{d\alpha}^*, \;\; Q_{wx} = \delta c_b h_b Q_{wx}^*, \;\; Q_{wy} = \mu\delta c_b h_b Q_{wx}^*, \;\; \nu_t = \gamma h_b c_b \nu_t^* \end{aligned} \tag{5.8}$$

where the starred quantities are non-dimensional and are expected to be order 1. L (~ 100 m) is the typical horizontal length scale, h_b (~ 1 m) is the vertical scale and $c_b = \sqrt{g h_b}$ is the wave celerity. The six non-dimensional parameters $(\mu, \gamma, \delta, \epsilon, \kappa, f_w)$ are chosen to represent the physical quantities in terms of the chosen scales.

- μ is the ratio of the longshore to the cross-shore horizontal scales which as a value of 0.1 in the rip and 1 outside the rip.
- γ is the parameter for the variations due to short-wave breaking which has a value of 1 inside the surfzone and 0.1 outside the surfzone.
- δ is the relative size of the short-wave motion and has a value of 0.1.
- ϵ is the relative size of the depth varying currents and has a value of 0.1 in the surfzone or the rip and a value of 0.01 outside the surfzone.

- κ is the relative size of the depth-averaged currents and has a value of 0.1.
- f_w is the friction factor with a value of 0.01.

Introducing the preceding scaling into the right-hand-side of (5.7) results in the following expression,

$$\begin{aligned}
&\gamma\delta\frac{F_x^*}{\nu_t^*}+\frac{(\kappa+\delta)f_wL}{h_b}\frac{\tau_x^{B*}}{h^*\nu_t^*}\\
&-\kappa\epsilon\frac{Q_x^*}{h^*\nu_t^*}\frac{\partial V_{dx}^*}{\partial x}+\kappa\delta\frac{Q_x^*}{h^*\nu_t^*}\frac{\partial\frac{Q_{wx}^*}{h^*}}{\partial x}\\
&-\kappa\epsilon\frac{1}{\nu_t^*}V_{dx}^*\frac{\partial\frac{Q_x^*}{h}}{\partial x}+\kappa\delta\frac{Q_{wx}^*}{h^*}\frac{\partial\frac{Q_x^*}{h}}{\partial x}\\
&-(\kappa+\delta)\epsilon\frac{W^*}{\nu_t^*}\frac{\partial V_{dx}^*}{\partial z}+\delta^2\frac{Q_{wx}^*}{h^*\nu_t^*}\frac{\partial\frac{Q_{wx}^*}{h^*}}{\partial x}\\
&-\delta\epsilon\frac{Q_{wx}^*}{h^*\nu_t^*}\frac{\partial V_{dx}^*}{\partial x}-\delta\epsilon\frac{V_{dx}^*}{\nu_t^*}\frac{\partial\frac{Q_{wx}^*}{h^*}}{\partial x}\\
&-\delta\epsilon\frac{2}{h^*\nu_t^*}V_{dx}^*\frac{\partial Q_{wx}^*}{\partial x}-\delta\epsilon\frac{2}{h^*\nu_t^*}Q_{wx}^*\frac{\partial V_{dx}^*}{\partial x}\\
&-\frac{\delta\epsilon}{\mu}\frac{1}{h^*\nu_t^*}Q_{wx}^*\frac{\partial V_{dy}^*}{\partial y}-\delta\epsilon\frac{1}{h^*\nu_t^*}V_{dx}^*\frac{\partial Q_{wy}^*}{\partial y}.
\end{aligned}\tag{5.9}$$

Based on the definitions of the scales, $\frac{f_wL}{h_b}$ is always $O(1)$. In addition, the terms of magnitude $\kappa\epsilon$, $\kappa\delta$, $(\kappa+\delta)\epsilon$, δ^2 and $\delta\epsilon$ in (5.9) are always an order of magnitude smaller than the other terms.

Using the scaling for the non-dimensional parameters in (5.9) for the rip current outside the surfzone results in $(\kappa+\delta)=O(0.1)$ and $\frac{\delta\epsilon}{\mu}=O(0.1)$ while the rest of the terms are $O(0.01)$. Reverting back to dimensional variables, the depth varying current in the rip current outside the surfzone is proportional to

$$V_{dx}\sim\frac{\tau_x^B}{h\nu_t}-\frac{1}{h\nu_t}Q_{wx}\frac{\partial V_{dy}}{\partial y}.\tag{5.10}$$

The first term represents effect of the shear stress causing the velocity profile to lag at the bottom and increase near the surface. The second term represents the nonlinear effect of wave current interaction on the vertical variation of the current.

The experiments with a plane jet in shallow water by Giger *et al.* (1991) and Dracos *et al.* (1992) did not include any waves so there was no wave current interaction which may be one of the reasons why there was no depth variation in the measurements. This term results from the longshore velocity near the surface along the sides of the rip flowing away from the rip as seen in Figure 5.5. This diverging longshore current advects the shoreward oriented cross-shore momentum from the short waves away from the rip current.

Using the scaling for the non-dimensional parameters in (5.9) for the rip current inside the channel (inside the surfzone) results in $(\kappa + \delta) = O(0.1)$, $\frac{\delta\epsilon}{\mu} = O(0.1)$ and $\gamma\delta = O(0.1)$ while the rest of the terms are $O(0.01)$. In dimensional variables this gives

$$V_{dx} \sim \frac{F_x}{\nu_t} + \frac{\tau_x^B}{h\nu_t} - \frac{1}{h\nu_t} Q_{wx} \frac{\partial V_{dy}}{\partial y}. \tag{5.11}$$

There is an additional term that includes the short-wave forcing. This forcing term is shoreward oriented and tends to be larger near the surface than at the bottom. The net effect is that this term decreases the offshore velocity near the surface, resulting in the nearly depth uniform velocity profile in the rip channel.

The scaling for the non-dimensional parameters in (5.9) for the current away from the channel inside the surfzone results in $(\kappa + \delta) = O(0.1)$ and $\gamma\delta = O(0.1)$ while the rest of the terms are $O(0.01)$. Here the vertical variation is proportional to

$$V_{dx} \sim \frac{F_x}{\nu_t} + \frac{\tau_x^B}{h\nu_t}. \tag{5.12}$$

The contribution from the convective term is no longer present because the longshore variations are small. This is similar to the scaling for the classical one-dimensional undertow profile resulting from the balance between the depth uniform pressure gradient and the depth varying radiation stress. Because the radiation stresses are

larger near the surface than at the bottom, the offshore flow near the surface is reduced relative to the offshore flow at the bottom.

Finally, the scaling for the non-dimensional parameters in (5.9) for the current away from the channel outside the surfzone results in $(\kappa + \delta) = O(0.1)$ while the rest of the terms are $O(0.01)$ or smaller. The vertical variation of the current is proportional to

$$V_{dx} \sim \frac{\tau_x^B}{h\nu_t}. \tag{5.13}$$

In this region the undertow depth variation is the result of the bottom stress causing the velocity to lag at the bottom. The profile is nearly linear with little curvature similar to the profiles discussed in Putrevu and Svendsen (1993).

The scaling analysis for the vertical variation of the currents reveals that the convective term representing the non-linear interaction between the waves and currents is important in the rip current. This scaling is for an idealized rip where due to the narrow nature of rip currents only the longshore gradient are large. However, when rip becomes unstable and meanders, the other convective terms may increase in magnitude when the cross-shore gradients are locally as large as the longshore gradients. The scaling does reproduce the correct forcing for the one-dimensional undertow profile inside and outside the surfzone.

5.1.3 Components of the Current Profiles

This subsection identifies the mechanisms for creating the depth variations from the SC results. The current is split, using (3.42), into a depth uniform component ($V_{m\alpha}$) and a depth varying term ($V_{d\alpha}$). Because we are examining the vertical variation of the currents, the depth uniform term is not of interest but examining the components of $V_{d\alpha}$ does help to identify the mechanisms for the depth variations.

The depth varying velocity is split again, using (3.68), into a term forced by the local conditions ($V_{d\alpha}^{(0)}$) and a term forced by non-local conditions ($V_{d\alpha}^{(1)}$). The

solutions for these two current terms are given by (B.3) and (B.28). The solution for $V_{d\alpha}^{(0)}$ contains the following two terms

- $V_{d\alpha}^{(0,0)}$ matches the shear stress above the bottom boundary layer.
- $V_{d\alpha}^{(0,1)}$ is forced by $F_{\alpha}^{(0)}$, the short-wave forcing as given by (B.2).

The solution for $V_{d\alpha}^{(1)}$ contains the following six terms

- $V_{d\alpha}^{(1,a)}$ is forced by $\frac{\overline{Q}_\beta}{h}\frac{\partial V_{d\alpha}^{(0)}}{\partial x_\beta} - \frac{\overline{Q}_\beta}{h}\frac{\partial \frac{Q_{w\alpha}}{h}}{\partial x_\beta}$
- $V_{d\alpha}^{(1,b)}$ is forced by $V_{d\beta}^{(0)}\frac{\partial \frac{\overline{Q}_\alpha}{h}}{\partial x_\beta} - \frac{Q_{w\beta}}{h}\frac{\partial \frac{\overline{Q}_\alpha}{h}}{\partial x_\beta}$
- $V_{d\alpha}^{(1,d)}$ is forced by $\frac{Q_{w\beta}}{h}\frac{\partial \frac{Q_{w\alpha}}{h}}{\partial x_\beta} + \frac{Q_{w\beta}}{h}\frac{\partial V_{d\alpha}^{(0)}}{\partial x_\beta} + V_{d\beta}^{(0)}\frac{\partial \frac{Q_{w\alpha}}{h}}{\partial x_\beta}$
- $V_{d\alpha}^{(1,e)}$ is forced by $-\frac{1}{h}\frac{\partial}{\partial x_\gamma}\left[V_{d\alpha}^{(0)}(h)Q_{w\gamma} + V_{d\gamma}^{(0)}(h)Q_{w\alpha}\right]$
- $V_{d\alpha}^{(1,w)}$ is forced by $W\frac{\partial V_{d\alpha}^{(0)}}{\partial \xi}$
- $V_{d\alpha}^{(1,c)}$ satisfies the boundary condition of no net depth integrated flow.

Examining the relative size for each of the previous eight terms will establish the corresponding mechanism for the depth variations in the rip currents.

Figure 5.6 shows the eight components for U_d in the rip at a location offshore of the bar ($x = 7$, $y = 4$ m) where negative currents indicate offshore flow. The depth is nondimensionalized by the still water depth. Seven of the components are depth varying terms and the last component $U_d^{(1,c)}$ is depth uniform. $U_d^{(1,c)}$ shifts the total $U_d^{(1)}$ velocity such that the depth integral is 0, consequently, $U_d^{(1,c)}$ is not discussed further.

Several of the terms are contributing to the increased velocity at the surface as seen in the total velocity profile shown in Figure 5.3b. $U_d^{(0,0)}$ has a profile which tilts forward. The drag from the friction causes the velocity to lag at the bottom. Because the integrated flow must remain 0, the drag at the bottom causes the

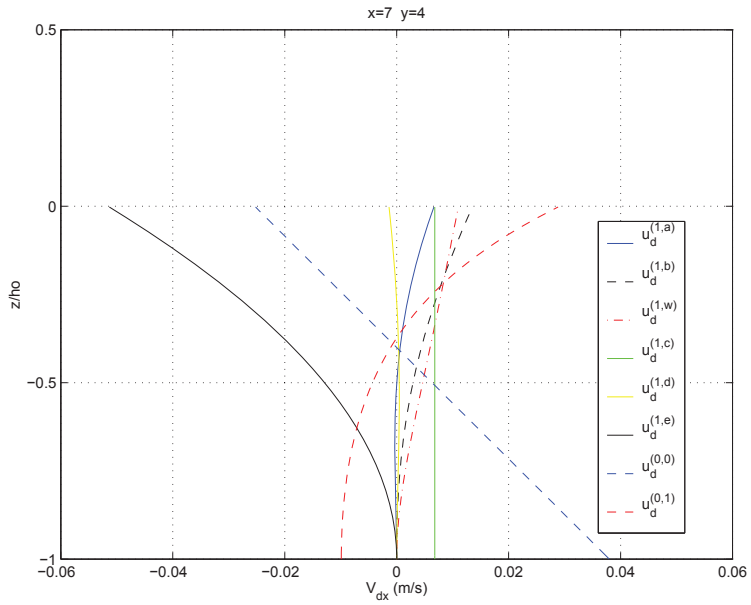

Figure 5.6: Vertical variation of the components of U_d offshore the rip channel $(x = 7, y = 4)$ from the SC simulations on the idealized topography.

velocity at the surface to increase. Another term which has a large contribution to the offshore velocity at the surface is $U_d^{(1,e)}$. This is the term representing the wave current interaction found to be large by the scaling analysis in the previous section and is one of the terms created by the utilization of the alternate velocity split. Similar to the scaling analysis in the previous subsection, the results from SC indicate that the bottom stress and the convective acceleration term $U_d^{(1,e)}$ have the largest contributions to the vertical variation of the rip current outside the surfzone.

The other additional term created by the new velocity split is $U_d^{(1,d)}$. This term has a minimal increase in the offshore velocity near the surface. Overall this term has a negligible contribution to the velocity profile. The remaining terms decrease the offshore velocity near the surface. The largest of these terms is $U_d^{(0,1)}$ which is the term forced by the local short-waves.

The components for the velocity profile inside the rip channel ($x = 9$, $y = 4$

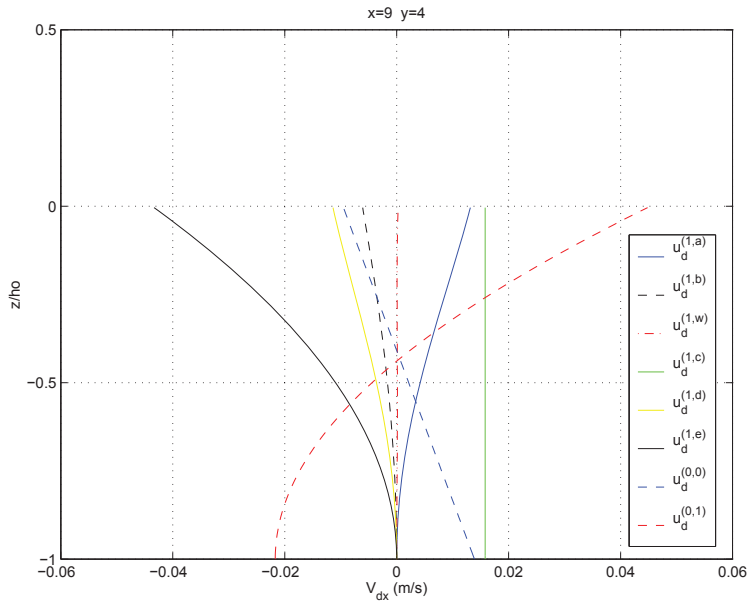

Figure 5.7: Vertical variation of the components of U_d in the rip channel ($x = 9, y = 4$) from the SC simulations on the idealized topography.

m) are shown in Figure 5.7. At this location the total current profile, as seen in Figure 5.3b, is virtually depth uniform. The term from the bottom stress ($U_d^{(0,0)}$) has been reduced substantially. On the other hand, $U_d^{(1,e)}$ has only been reduced slightly but is balanced by an increase in $U_d^{(0,1)}$ resulting from the short-wave forcing being much larger due to the presence of the breaking waves at this location. The term $U_d^{(1,b)}$ now contributes towards the offshore flow near the surface, albeit a small contribution. The relative sizes of the other terms have increased as well, except for $U_d^{(1,w)}$ which has virtually no contribution to the velocity profile.

The primary terms governing the velocity profile for the rip inside the surfzone are the bottom stress, the short-wave forcing and the convective acceleration. This is in agreement with the scaling arguments from the previous subsection.

Figure 5.8 shows the components for the velocity profile in the center of the basin offshore from the bar ($x = 7$, $y = 8$ m). The current profile seen in Figure 5.3a

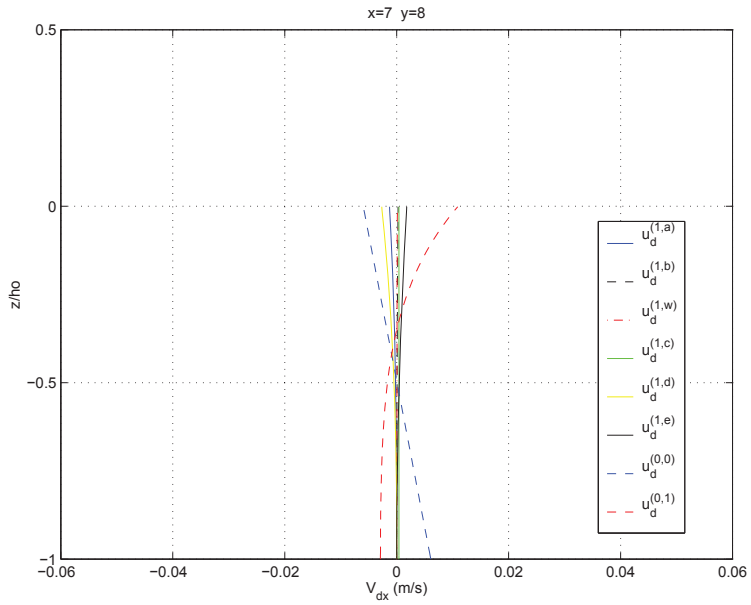

Figure 5.8: Vertical variation of the components of U_d offshore of the bar ($x = 7, y = 8$) from the SC simulations on the idealized topography.

shows a weak, nearly uniform profile which tilts slightly offshore. At this location only the two terms from $U_d^{(0)}$ have significant contributions to the profile. The bottom stress term ($U_d^{(0,0)}$) is small but does tilt forward due to the presence of an undertow returning the local short-wave volume flux. The shoaling of the short-waves create little forcing for the term $U_d^{(0,1)}$ which produces the slight shoreward velocity near the surface. The net result is a velocity with minimal tilt forward as seen in Figure 5.3a.

The scaling arguments of the previous subsection determined that the bottom friction dominates the vertical profiles outside the surfzone. Figure 5.8 confirms that, although, the short-wave forcing also provides a non-negligible contribution.

Finally, Figure 5.9 shows the components for the velocity profile over the bar in the center of the basin ($x = 9$, $y = 8$ m). The vertical profile shown in Figure 5.3a has strong depth variations with the velocity near the surface weaker than the

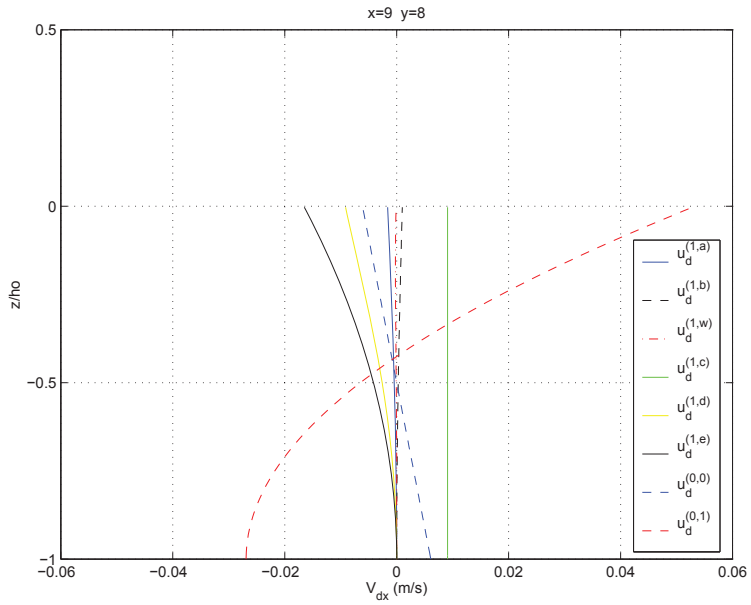

Figure 5.9: Vertical variation of the components of U_d over the bar $(x = 9, y = 8)$ from the SC simulations on the idealized topography.

velocity in the lower half of the water column. At this location the forward tilt from the bottom stress is still small, although, because of the breaking waves, the short-wave forcing is quite large creating a large depth variation for $U_d^{(0,1)}$. The other terms from the $U_d^{(1)}$ terms are larger than in Figure 5.8 but are still small relative to $U_d^{(0,1)}$. As seen from the scaling arguments bottom friction is significant inside the surfzone although the short-wave forcing is the most dominate term.

There are substantial differences between the mechanisms governing the vertical profiles in the rip and the profiles in the center of the basin. The center of the basin behaves similarly to one-dimensional undertow and is dominated by the local forcing terms in $V_{d\alpha}^{(0)}$. On the other hand, the profiles in the rip currents still have significant contributions from $V_{d\alpha}^{(0)}$ but the contributions from the non-local forcing in $V_{d\alpha}^{(1)}$ is as large or larger.

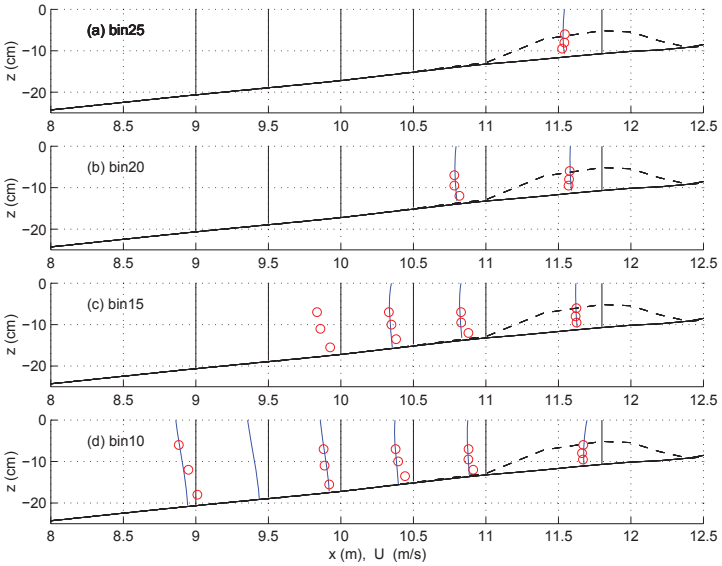

Figure 5.10: Comparisons of bin-averaged vertical profiles of the current with measurements from Test R. The solid lines are SC profiles and the circles are measurements.

5.2 Real Topography

The vertical profiles of symmetric rip current have been successfully modeled for the idealized topography. This section presents the modeling of the rip currents on real topography without preventing the rips from becoming unstable and validates the use of the model with comparisons to the experimental data. The topography and wave conditions for the experiments in the CACR wave basin are used in SC to model the rip currents. The details about the topography and methodology are given in Chapter 4.

5.2.1 Overall Structure of the Current Profiles

The modeling is done for the conditions of Test R from Chapter 2 which corresponds to Test B from Haller and Dalrymple (1999). This allows for direct comparisons between vertical profiles calculated by the numerical model and the

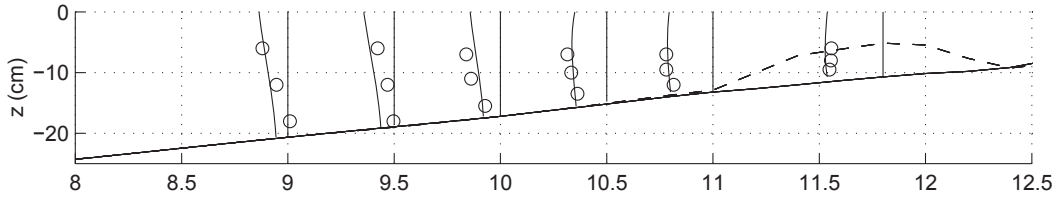

Figure 5.11: Maximum averaged current profiles from the SC simulation on the real topography and the measurements from Test R.

experimental measurements. Because the velocity measurements in the experiments are not repeatable in the instantaneous sense, averaging must be done to facilitate direct comparisons. A simple time-average is ineffective because it suppresses the rip signal due to the sporadic nature of the rip, therefore, the bin averaging method from Chapter 2 is utilized.

Velocity profiles are calculated from time series of the coefficients for $V_{d\alpha}$, given in Appendix B, at the same locations as the experimental measurements. The current is sorted into the bins based on the velocity at the same depth as the measurement from the gage closest to the surface. This is the identical sorting method used on the experimental measurements, allowing direct comparisons. The current is averaged to produce vertical profiles in each bin for all of the cross-shore locations.

The bin-averaged profiles and measurements are shown in Figure 5.10. The modeled profiles are quite similar to the measurements, fairly depth uniform in the channel and stronger depth variations offshore with increased velocity near the surface. In addition, the modeled profiles appear in nearly all of the same bins as the measurements at each location. This is an indication that the relative strength of the modeled rip current is similar to the strength of the actual rip current in the basin.

Inside the channel the modeled currents and measurements are in excellent

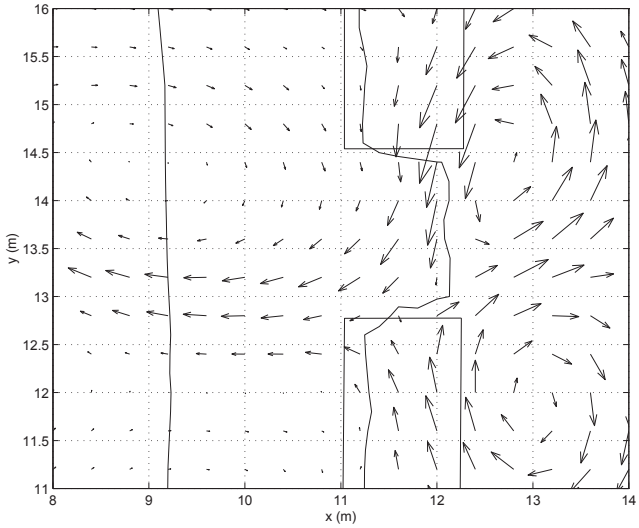

Figure 5.12: Instantaneous snapshot at $t = 771$ s of $V_{m\alpha}$ vectors and topography contours from the SC simulations with the real topography. Only one rip current is shown and the three-dimensional profiles are shown in Figures 5.13 and 5.14.

agreement. Farther offshore the agreement is good at the upper and mid-depth locations. In bin10 at the farthest location offshore, the velocity close to the surface is in good agreement but the velocity at the bottom is slightly over predicted. In general, this trend holds true and the velocity near the bottom is slightly over predicted for most locations outside the surfzone.

Another method for comparing the current profiles is to calculate maximum averaged profiles using the method from Chapter 2. The profiles at a given location that are within 3 cm/s of the maximum offshore velocity at the same depth where the measurement closest to the surface was taken are grouped together and averaged. The comparisons of the maximum averaged profiles between the SC simulation and the experimental measurements are shown in Figure 5.11. The maximum velocities at each location are well predicted. In addition the depth variation is qualitatively similar with slight over prediction of near bottom velocities for $x \leq 9$.

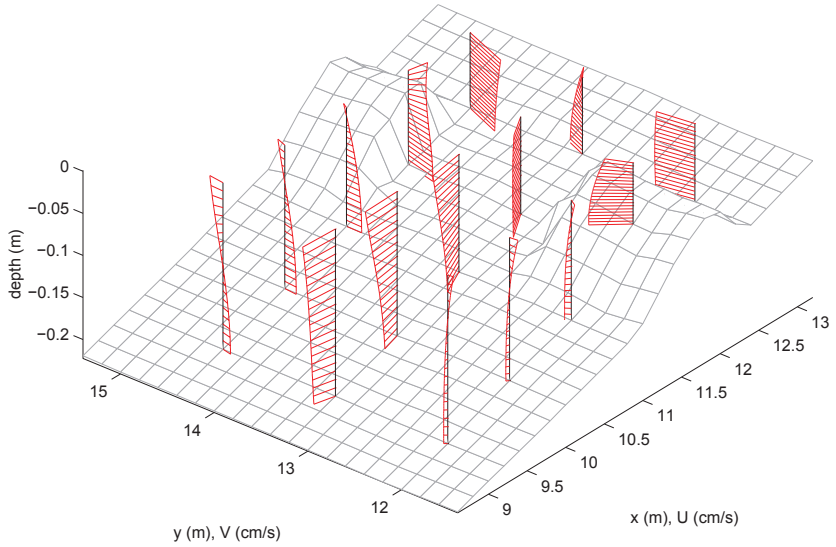

Figure 5.13: Instantaneous snapshot at $t = 771$ s of the 3D variation of V_α from the SC simulations with the real topography for the flow pattern shown in Figure 5.12. The middle row of profiles is along the centerline of the rip.

The advantage of using a numerical model is that the model provides the currents over the entire domain. Figure 5.12 provides an instantaneous vector plot of the depth-averaged velocity $V_{m\alpha}$ at $t = 771$ s when a strong rip is flowing offshore. The rip is not flowing through the center of the channel, rather it is flowing out of the side of the channel. Note that this figure only shows an excerpt of the entire computational domain and in order to reduce clutter the vectors are only plotted at a few computational points.

Figure 5.13 shows the computed results for three-dimensional variation of the currents in and around the channel. The center row of profiles shows the depth variation of the current through the center of the rip current. The two row of profiles on the sides show the feeder currents. This figure is remarkably similar to the three-dimensional flow pattern for the idealized topography in Figure 5.5. The rip shows

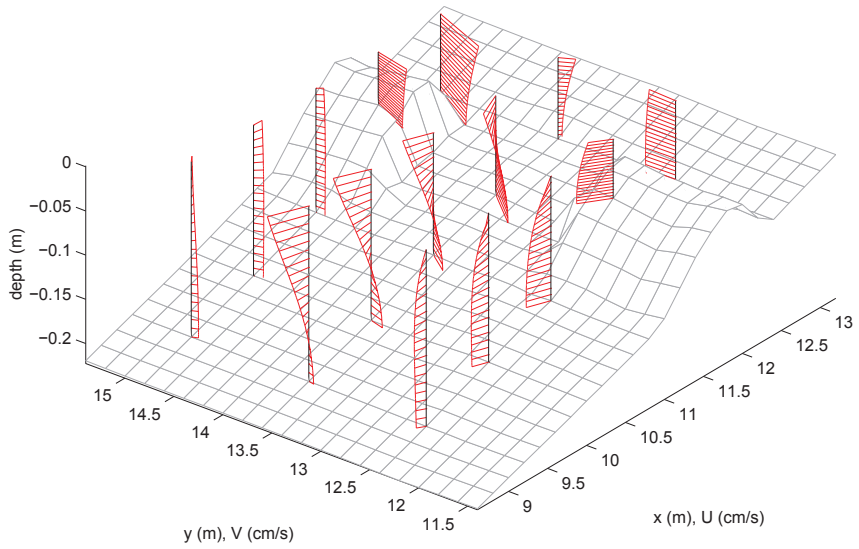

Figure 5.14: Instantaneous snapshot of the 3D variation of V_α from the SC simulations with the real topography for the flow pattern shown in Figure 5.12. The middle row of profiles is along the edge of the rip.

the same depth variations, larger velocity at the surface than the bottom as the rip flows offshore. The feeder currents behind and over the bar have little depth variation. The profiles along the edge of the rip offshore of the bar have currents at the surface flowing away from the rip. Even though the depth integrated currents along $y = 14.4$ m are feeding the rip, the velocity at the surface is flowing away from the rip. This is the mechanism for the velocity component $V_{dx}^{(1,e)}$ discussed in the previous section that increases the offshore velocity near the surface in the rip.

Figure 5.14 shows different three-dimensional profiles from the rip current at the same instant as Figure 5.13. The center row of profiles is along the edge of the rip current. The large longshore current flowing away from the rip is evident in the upper part of the water column. The cross-shore component of the current also has large depth variations, the velocity at the bottom is weak for the offshore profiles,

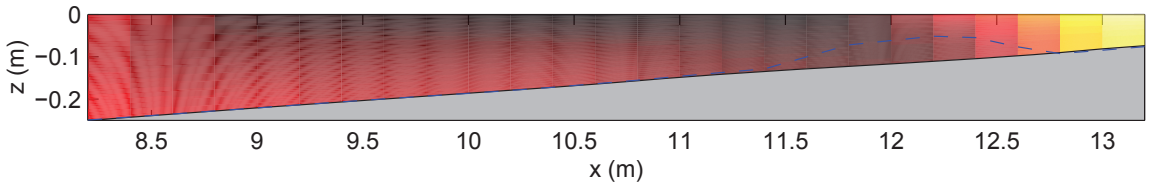

Figure 5.15: Color contour plot of V_x through the center of the rip ($y = 13.2$) at $t = 771$ s from the SC simulations with the real topography for the flow pattern shown in Figure 5.12. Darker colors represent offshore velocity, lighter colors represent shoreward velocity and the dashed line represents the position of the bar.

yet the velocity near the surface is still strongly offshore. Similar to Figure 5.13, the feeder currents behind and over the bar are fairly depth uniform.

Figure 5.15 shows a two-dimensional color contour plot of the vertical variation of the current through the center of the rip for $t = 771$ s from the SC simulation. The darker colors show the large offshore velocity of the rip current and the lighter colors represent the shoreward velocity. Inside the channel the rip current has nearly depth uniform velocity. Farther offshore the velocity closer to the surface is larger than the velocity below, indicated by the darker color in the upper part of the water column. The variation of the currents for the basin topography are similar to the variation of the currents for the idealized topography, Figure 5.4, which validates the use of the idealized rip for analyzing the depth variations of the rip currents.

The time evolution of the vertical variations of currents from the SC simulations are shown in Figures 5.16 to 5.19. Each of these figures show eight three-dimensional snapshots of the vertical variation of the current during a burst of the rip current. These figures are similar to the three-dimensional plots of the measurements shown in Figures 2.15 and 2.16.

Figure 5.16 shows the currents at $x = 9, y = 13.6$ m which is 2 m offshore from the bar. This figure is for the same location as the measurements in Figure

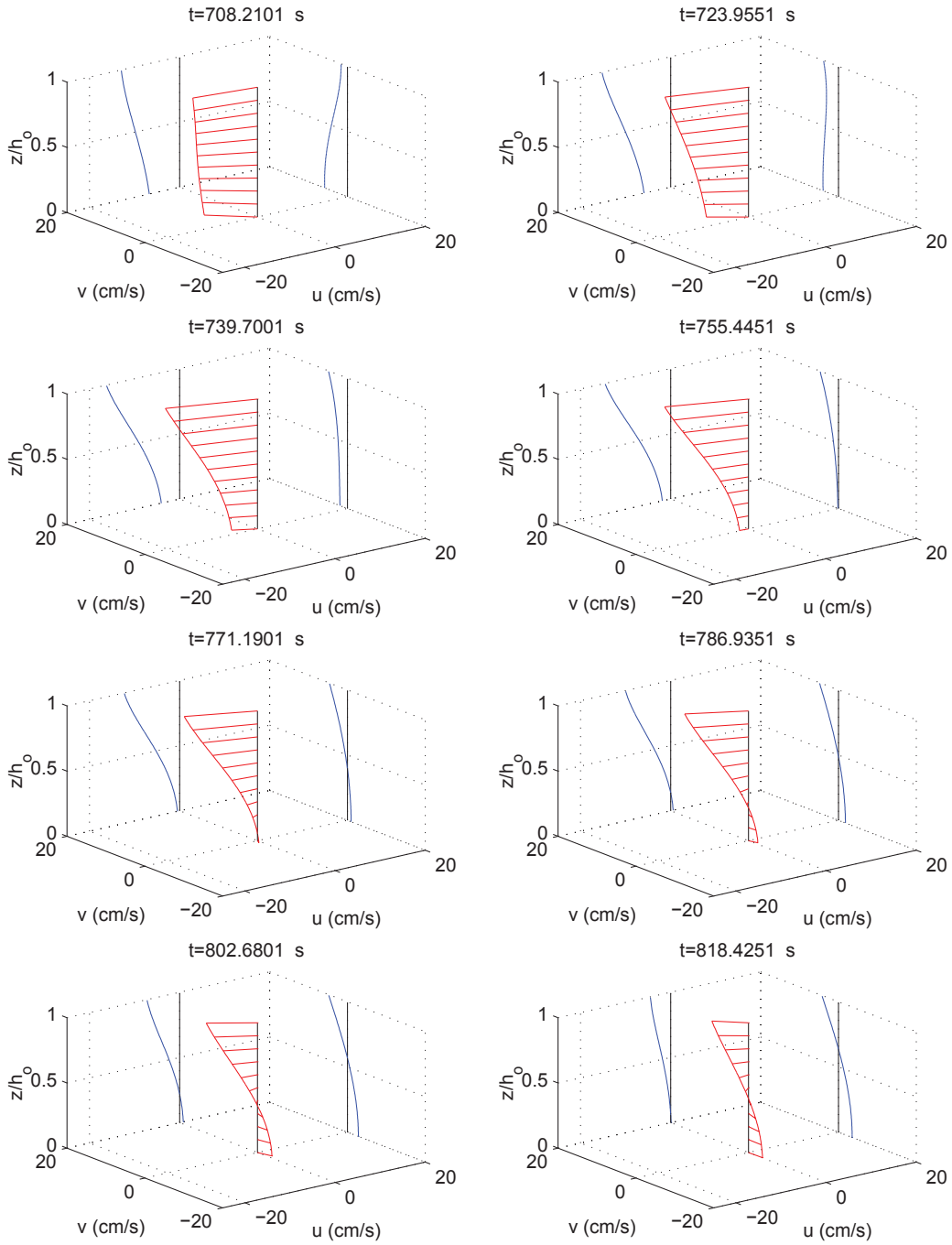

Figure 5.16: Snapshots in time of the vertical variation of V_α 2 m offshore of the rip channel ($x = 9$, $y = 13.6$ m) from the SC simulation on the real topography.

2.15. Initially there is little depth variation but as the burst of rip velocity grows, the depth variation becomes significant. The velocity at the surface is much larger than the velocity at the bottom. In the later stages, the velocity at the bottom becomes slightly shoreward even though the velocity in the upper part of the water column is offshore. The vertical variations of the rip in this figure are qualitatively similar to the vertical variation of the rip current from the measurements in Figure 2.15.

Figure 5.17 shows the snapshots of the vertical variations of current at $x = 10, y = 13.6$ m which is 1 m seaward of the bar. At this location depth variations of the current are much weaker than in Figure 5.16 which is 1 m farther seaward. The velocity in the upper part of the water column is still larger than the velocity near the bottom although the profile does tend to tilt shoreward near the surface.

Figure 5.18 shows the time evolution of the profiles for the location at $x = 11, y = 13.6$ which is in the channel at the seaward edge of the bar. The cross-shore profiles are nearly depth uniform throughout the entire rip burst. Even the longshore currents are virtually depth uniform.

Finally, Figure 5.19 shows the vertical profiles for the rip in the middle of the channel at $x = 11.8, y = 13.6$. The cross-shore profiles show slight curvature reducing the velocity near the surface. The longshore currents are only slightly weaker than the cross-shore currents indicating that the rip is not flowing straight offshore but at a small angle through the channel.

5.2.2 Components of the Current Profiles

The mechanisms for creating the depth variation of the rip currents are established by examining the components for the velocity profile $V_{d\alpha}$. Because the rip current is unstable in the wave basin, time series of the components show how the depth variation of the rip current evolves over time.

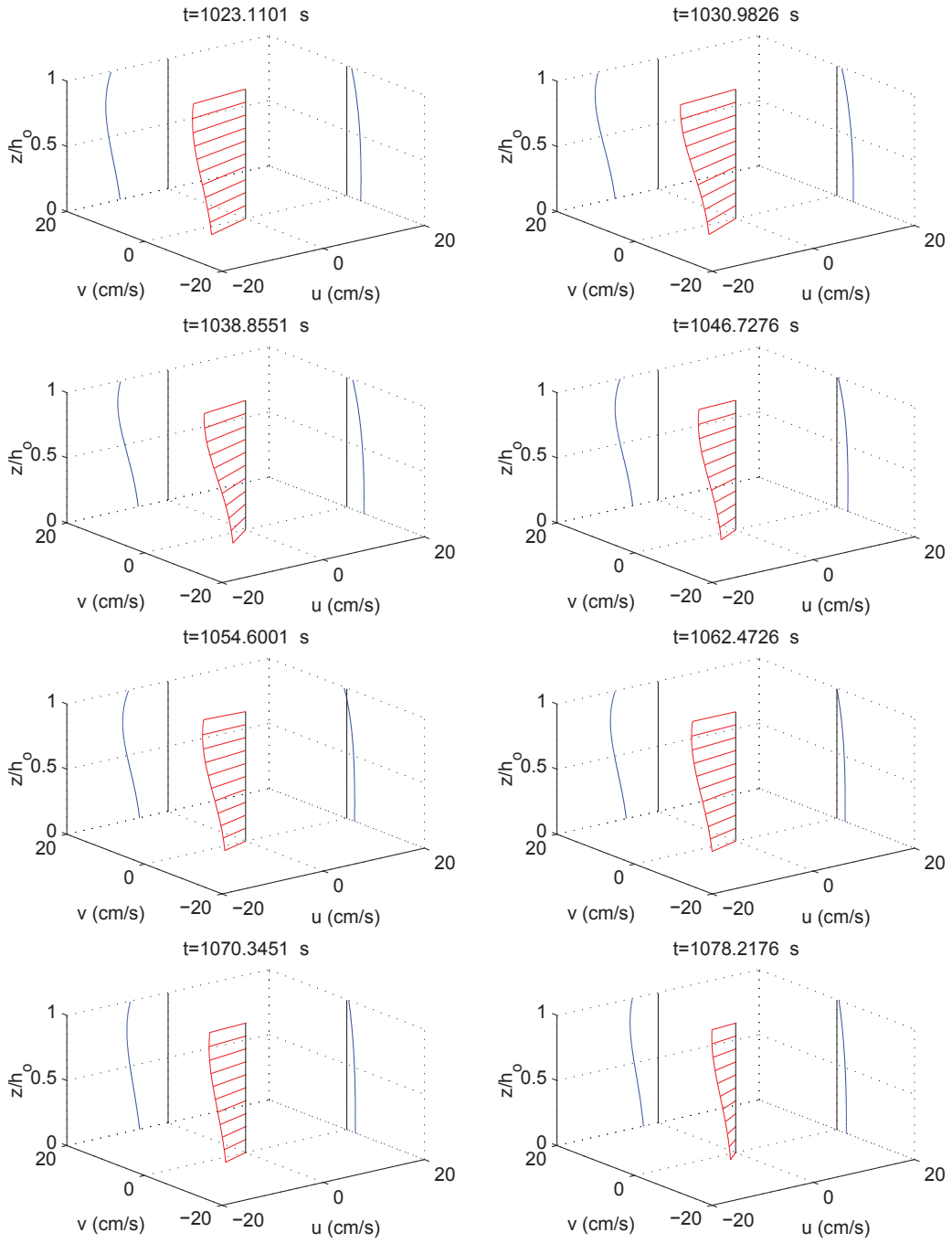

Figure 5.17: Snapshots in time of the vertical variation of V_α 1 m offshore of the rip ($x = 10$, $y = 13.6$ m) from the SC simulation on the real topography.

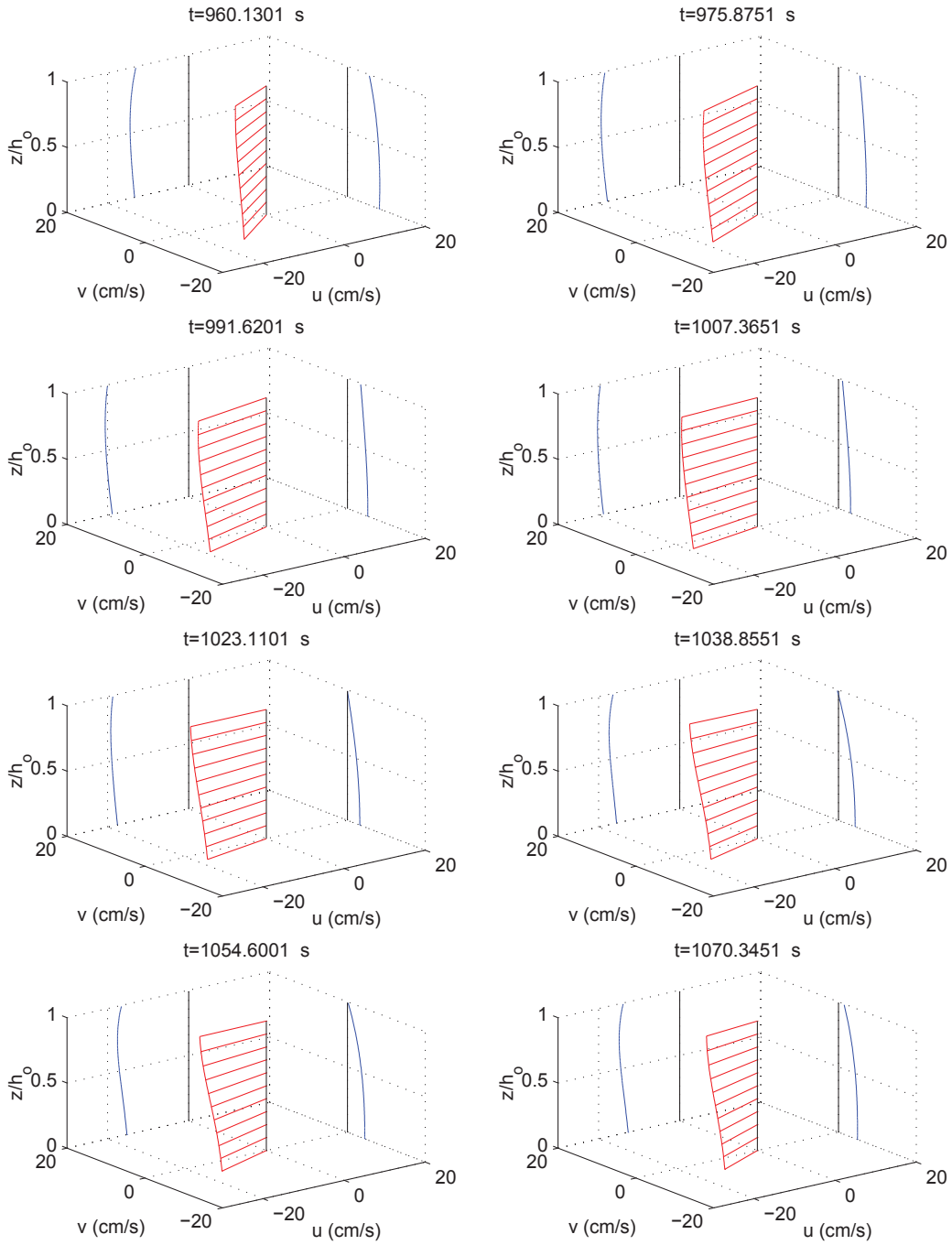

Figure 5.18: Snapshots in time of the vertical variation of V_α at the offshore edge of the channel ($x = 11$, $y = 13.6$ m) from the SC simulation on the real topography.

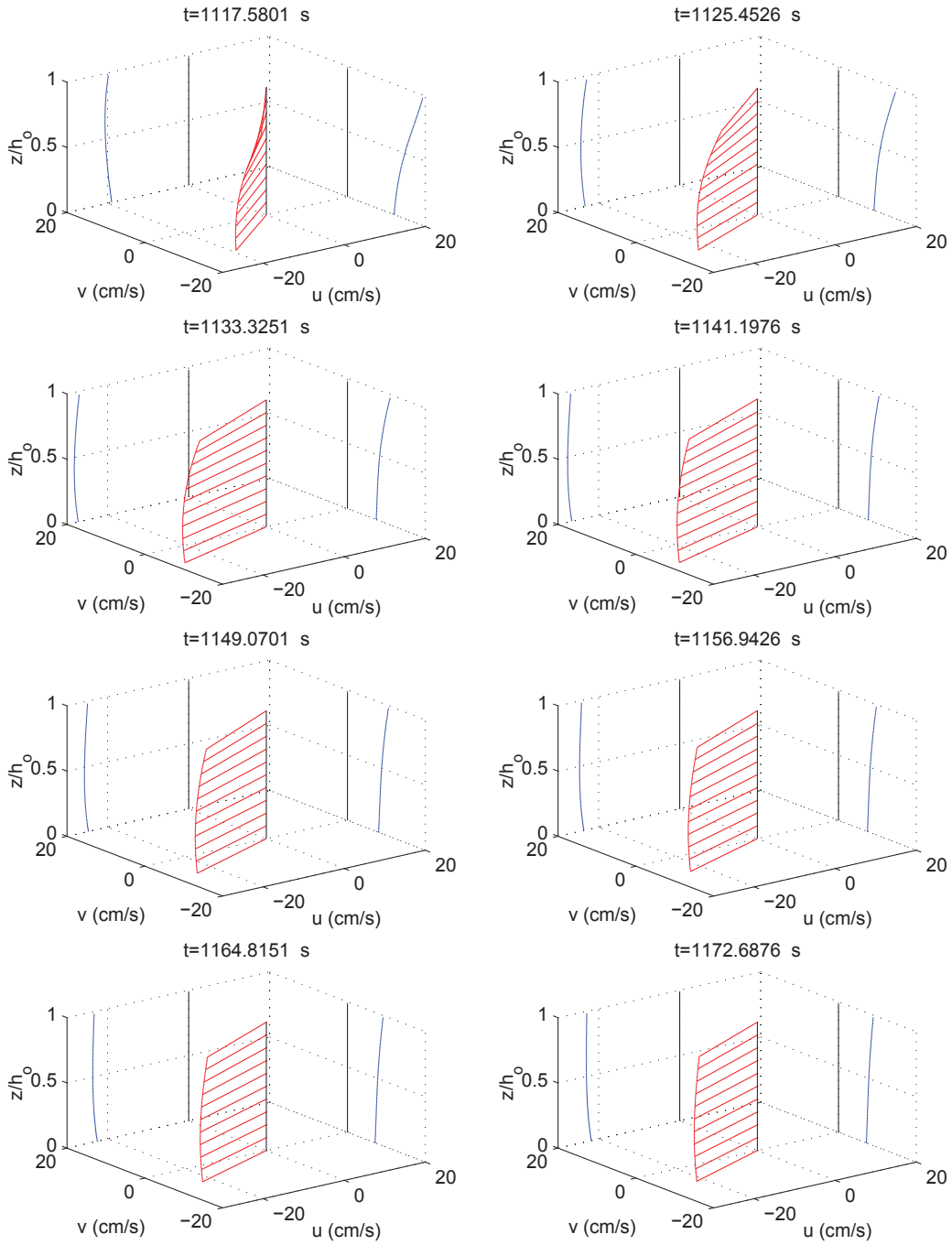

Figure 5.19: Snapshots in time of the vertical variation of V_α in the rip channel ($x = 11.8$, $y = 13.6$ m) from the SC simulation on the real topography.

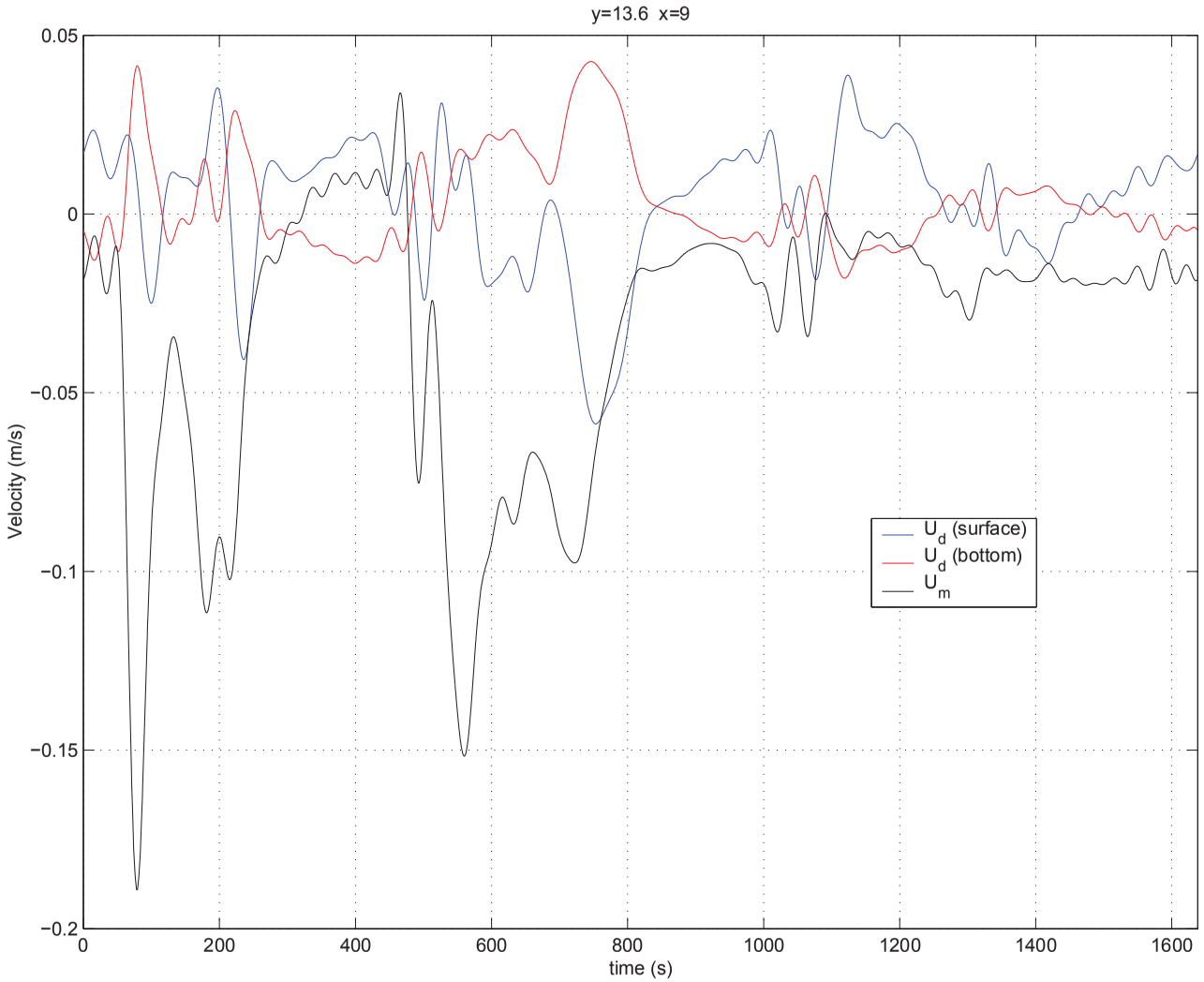

Figure 5.20: Time series from the SC simulation on the real topography of U_m, U_d at the surface and U_d at the bottom 2 m offshore of the channel ($x = 9, y = 13.6$ m).

The rip current tends to have large velocities at the surface and small velocities near the bottom, therefore, the easiest way to present the time variation of the profiles is to show the difference in the velocity at the surface from the velocity at the bottom. Figure 5.20 shows time series for the velocity U_d at the surface and the bottom located at $x = 9, y = 13.6$ m. In addition the depth averaged velocity U_m is included in this figure to indicate when the rip is present at this location. Note that the velocities at the surface and bottom are not the actual velocity but are the depth varying component.

U_m in Figure 5.20 indicates that only a few sporadic rip events occurs. The longest rip event occurs between $t = 500$ and 800 seconds. The velocity at the surface tends to be offshore (negative) during the rip while the velocity at the bottom tends to be onshore (positive). This variation produces the profiles with the larger velocity at the top than the bottom. The difference between the surface and bottom velocities is as large as 10 cm/s.

The time series for each component of the difference in the top and bottom velocity is shown in Figure 5.21 for the location at $x = 9, y = 13.6$ m. Only five of the components for $U_d^{(1)}$ are included because the term $U_d^{(1,c)}$ is depth uniform and provides no contribution to the difference between surface and bottom velocity. During the rip event between $t = 500$ and 800 seconds the two largest terms producing the offshore velocity are $U_d^{(0,0)}$ and $U_d^{(1,e)}$. These are the same two terms which are found to dominate the offshore rip current profile for the idealized topography.

In the latter part of this rip burst the term $U_d^{(1,b)}$ produces a large offshore current. This term is negligible for the rip current on the idealized topography. As seen from equation B.33 $U_d^{(1,b)}$ is proportional to

$$U_d^{(1,b)} \sim U_d \frac{\partial \frac{Q_x}{h}}{\partial x} + V_d \frac{\partial \frac{Q_x}{h}}{\partial y} - \frac{Q_{wx}}{h} \frac{\partial \frac{Q_x}{h}}{\partial x} - \frac{Q_{wy}}{h} \frac{\partial \frac{Q_x}{h}}{\partial y}. \tag{5.14}$$

Due to the symmetry of the rip on the ideal topography the second and fourth terms on the right-hand-side of (5.14) are neglected for the idealized rip. The remaining

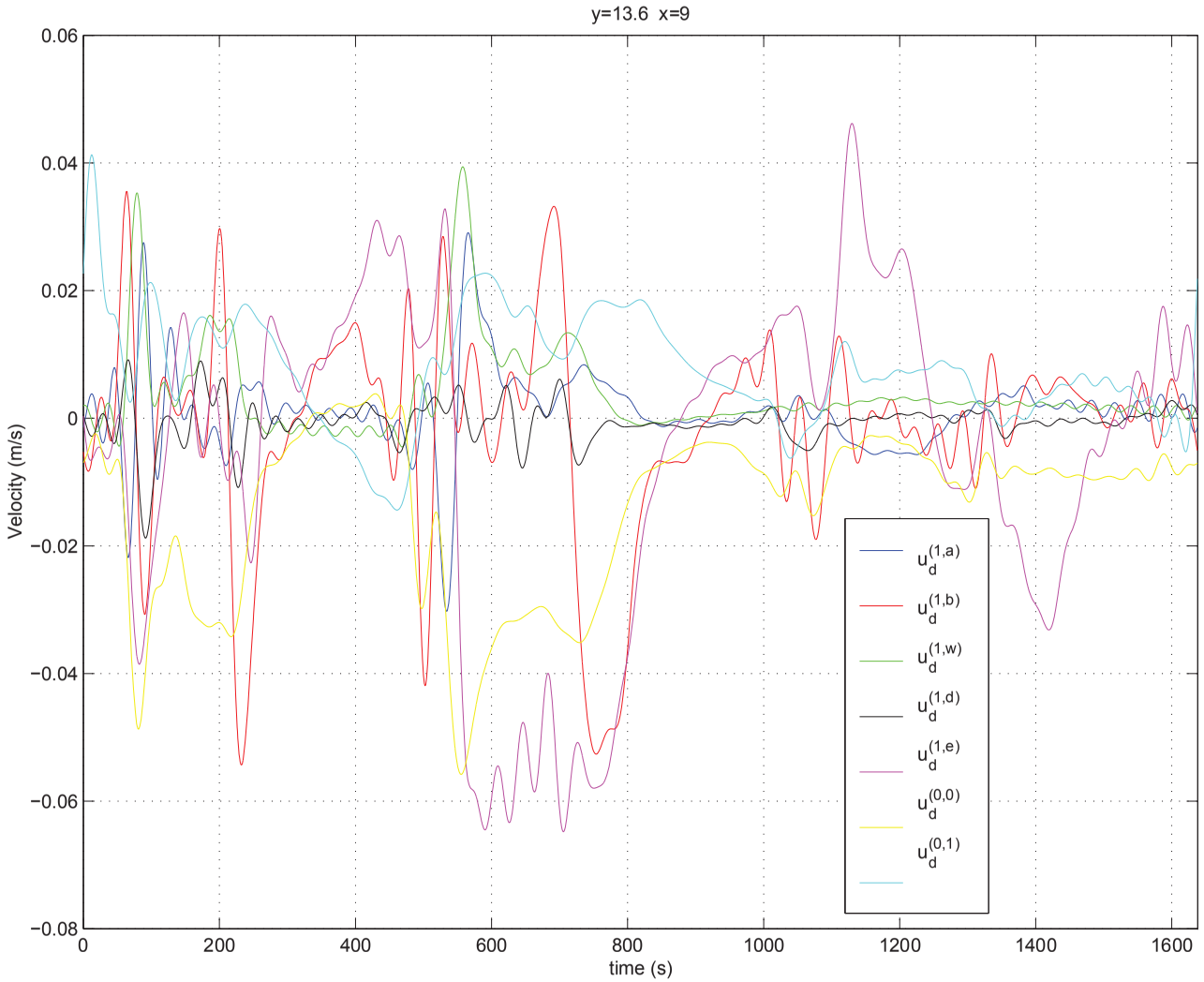

Figure 5.21: Time series from the SC simulation on the real topography of the components of difference between U_d and the surface and U_d at the bottom 2 m offshore of the channel ($x = 9, y = 13.6$ m).

terms are small for the symmetric rip because the cross-shore variation of the rip current is weak which makes $\frac{\partial \frac{Q_x}{h}}{\partial x}$ small. On the basin topography the rip is not symmetric, which means that the second and fourth term of (5.14) are not negligible. At the end of the burst between $t = 500$ and 800 seconds in Figure 5.21 the rip is flowing at an angle which causes the $\frac{\partial}{\partial y}$ and V_d terms to become large. This makes $U_d^{(1,b)}$ as large as $U_d^{(1,e)}$ at the end of this burst.

Figure 5.22 shows time series of the U_d velocity at the surface and at the bottom as well as the time series of U_m for a location at $x = 10, y = 13.6$ m situated 1 m shoreward of the previous location. In this figure there is an additional rip event after $t = 1000$ seconds, but in general, the rip is sporadic. The difference between the surface and bottom velocities are much smaller, the surface is only around 7 cm/s larger than the bottom during the rip event around $t = 700$ s.

The components for the difference in the top and bottom depth varying velocity U_d at this location are shown in Figure 5.23. Similar to Figure 5.21 the two largest components increasing the velocity at the surface are $U_d^{(0,0)}$ and $U_d^{(1,e)}$. As before $U_d^{(1,b)}$ increases the rip velocity at the surface during the end of the burst between $t = 600$ and 800 seconds, although, $U_d^{(1,b)}$ has a weaker contribution of only 3.5 cm/s.

The time series for the surface and bottom components of U_d along with U_m for the location at the offshore edge of the channel ($x = 11, y = 13.6$ m) are shown in Figure 5.24. The rip occurrences are much more frequent as evident from the multiple large peaks of U_m. The difference between the velocity at the surface and the bottom is much weaker. The velocity at the surface alternates between onshore and offshore, tending to be offshore during most rip bursts. The maximum difference between the top and bottom velocity is only a few cm/s.

Figure 5.25 shows the components for the difference between the top and bottom velocity U_d for the location at the offshore edge of the channel. The largest

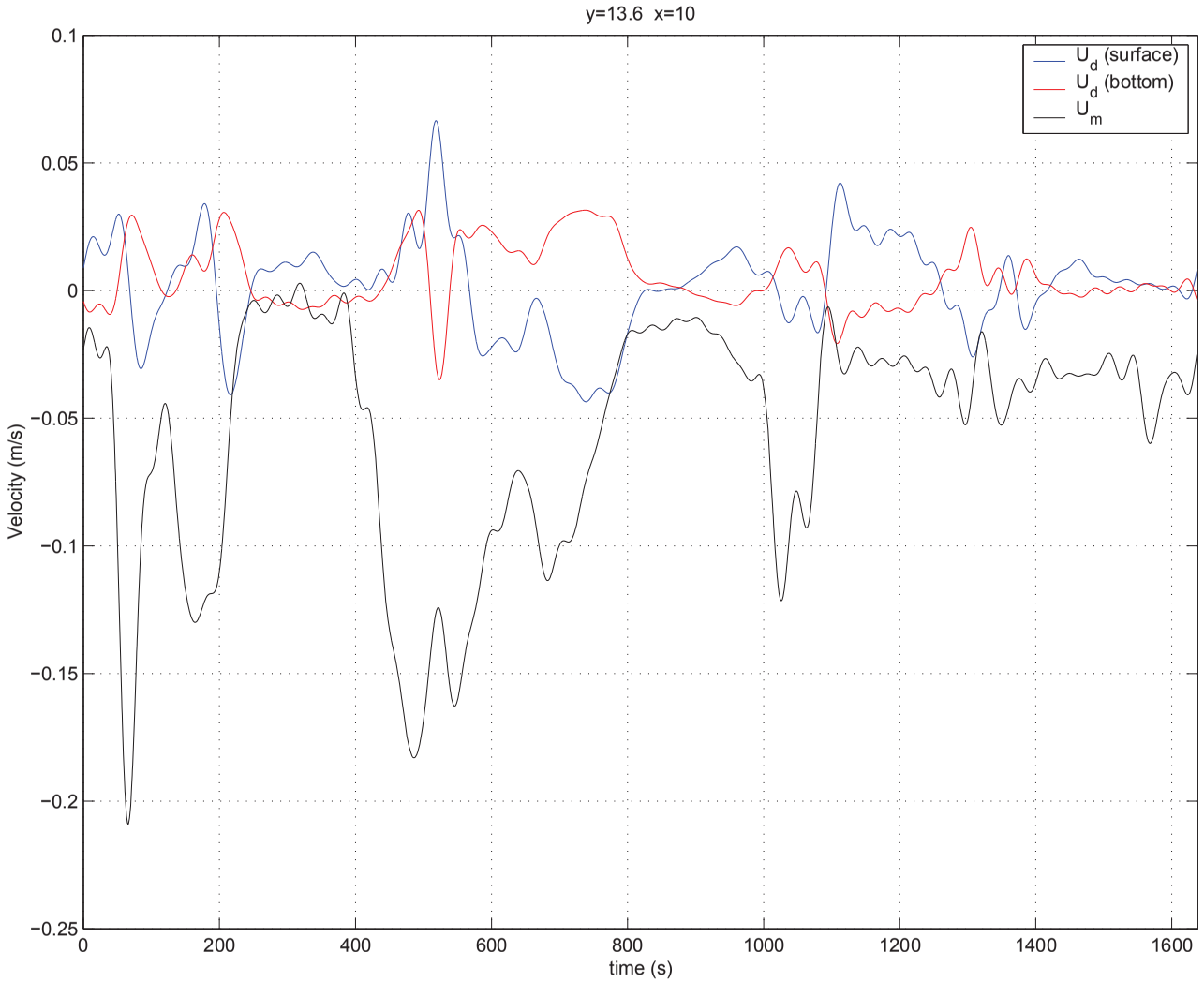

Figure 5.22: Time series from the SC simulation on the real topography of U_m, U_d at the surface and U_d at the bottom 1 m offshore of the channel ($x = 10, y = 13.6$ m).

Figure 5.23: Time series from the SC simulation on the real topography of the components of difference between U_d and the surface and U_d at the bottom 1 m offshore of the channel ($x = 10, y = 13.6$ m).

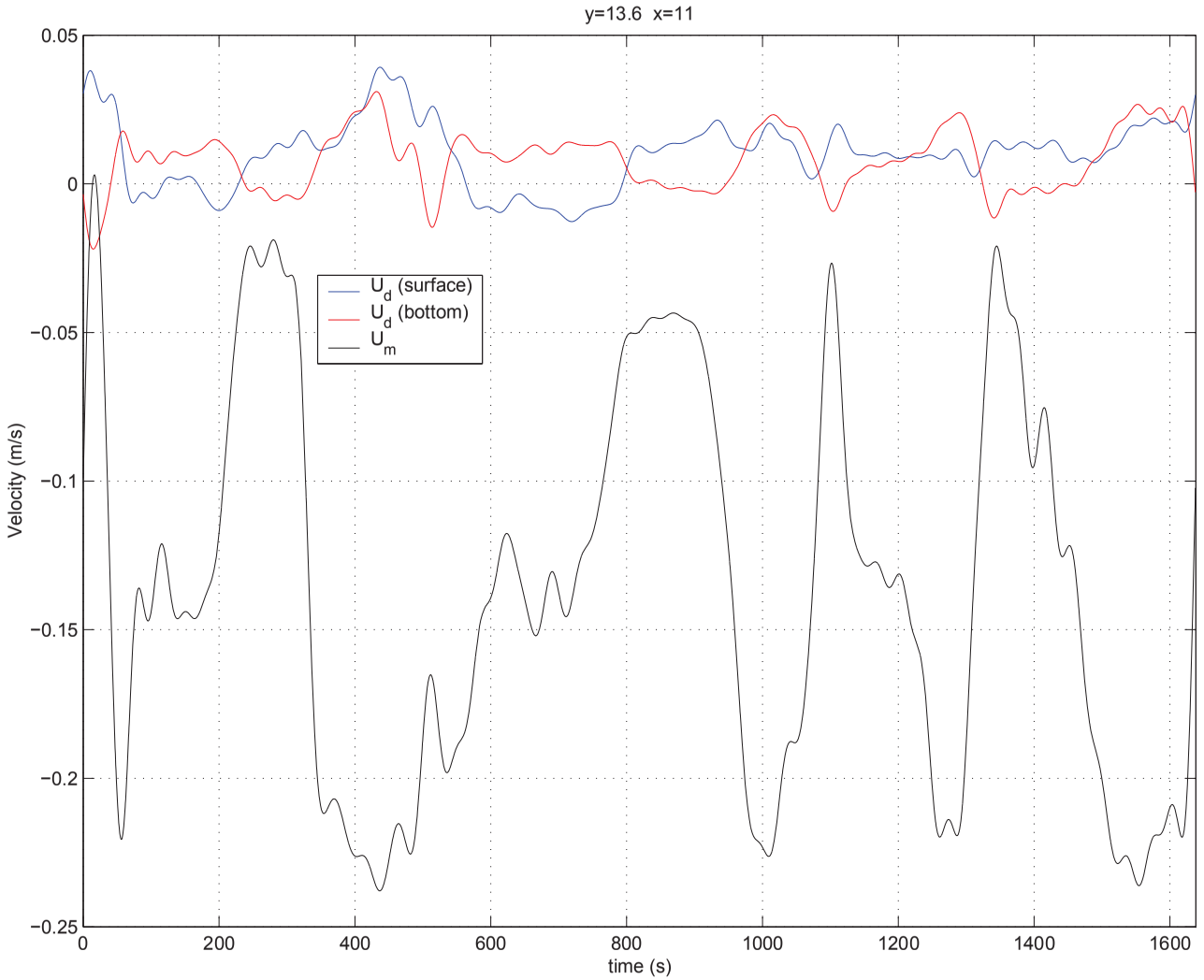

Figure 5.24: Time series from the SC simulation on the real topography of U_m, U_d at the surface and U_d at the bottom at the offshore edge of the channel ($x = 11, y = 13.6$ m).

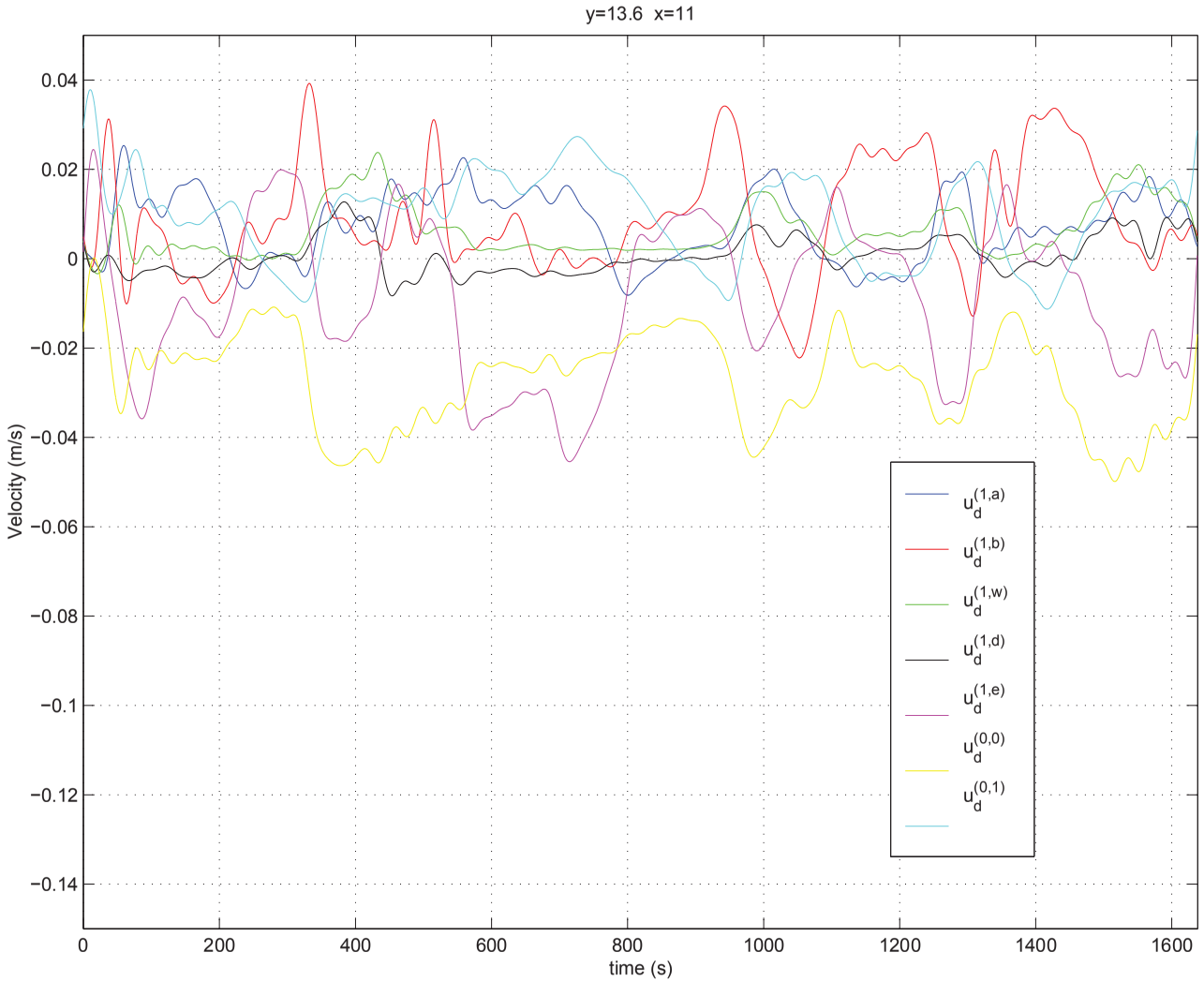

Figure 5.25: Time series from the SC simulation on the real topography of the components of difference between U_d and the surface and U_d at the bottom at the offshore edge of the channel ($x = 11, y = 13.6$ m).

offshore components are still $U_d^{(0,0)}$ and $U_d^{(1,e)}$ although they are much smaller than before. In addition, the shoreward contribution from the short-wave forcing ($U_d^{(0,1)}$) has increased. The net result is the weak depth variation seen in Figure 5.24.

Finally, the time series of the depth-averaged velocity (U_m) and the depth varying velocity (U_d) at the surface and bottom is shown in Figure 5.26 for a location in the middle of the rip channel at $x = 11.8, y = 13.6$ m. The rip is nearly continuously present, the only exception is during the middle of the time series around $t = 800$ seconds. The difference between the surface velocity and the bottom velocity is small. During some of the rip events, the bottom velocity tends to have a larger offshore component than the top velocity.

Figure 5.27 shows the time series for each component contributing to the difference between the surface and bottom velocities. The largest component is the shoreward velocity $U_d^{(0,1)}$ which is forced by the wave breaking occurring inside the channel. The bottom stress still contributes a significant offshore component via $U_d^{(0,0)}$, but the term $U_d^{(1,e)}$ has become relatively small. Because the rip is moving from side to side in the channel the currents at this location are actually changing back and forth between rip currents and feeder currents. The feeder currents flow at an angle relative to the cross-shore direction while the rip tends to flow straight offshore. This change in direction causes the terms $U_d^{(1,a)}$ and $U_d^{(1,b)}$ to fluctuate although the current at the surface is still dominated by $U_d^{(0,1)}$.

In general, inside the surfzone the vertical variations of the currents are governed by the forcing from the short-waves, although, in the rip channel, bottom friction and convective terms contribute. The short-wave forcing reduces the offshore velocity at the surface while the bottom stress tends to increase the offshore velocity at the surface. The vertical profile of the rip inside the surfzone tends to be close to depth uniform with slightly decreased velocity near the surface.

As the rip flows offshore out of the surfzone, the role of the forcing from the

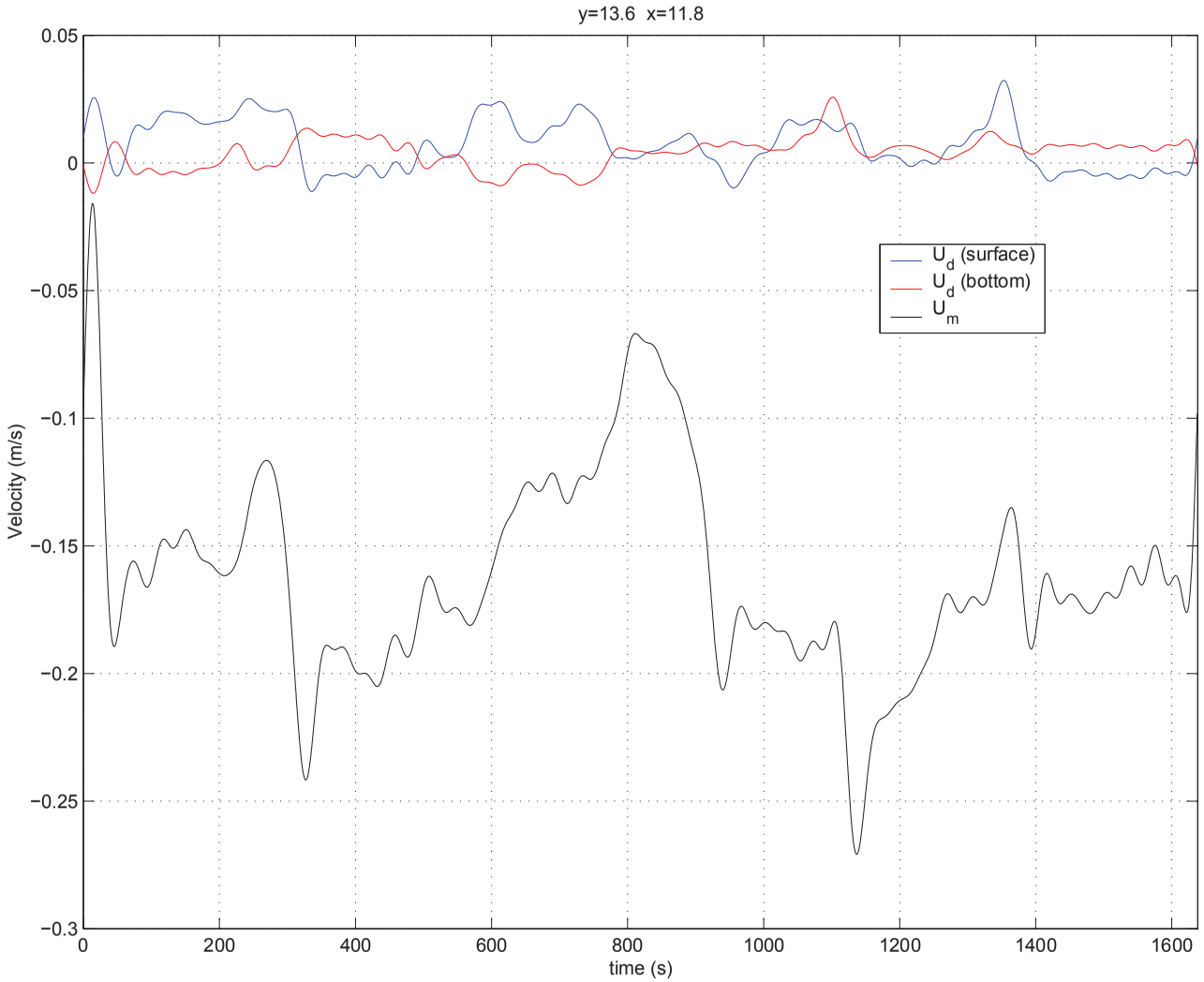

Figure 5.26: Time series from the SC simulation on the real topography of U_m, U_d at the surface and U_d at the bottom in the channel ($x = 11.8, y = 13.6$ m).

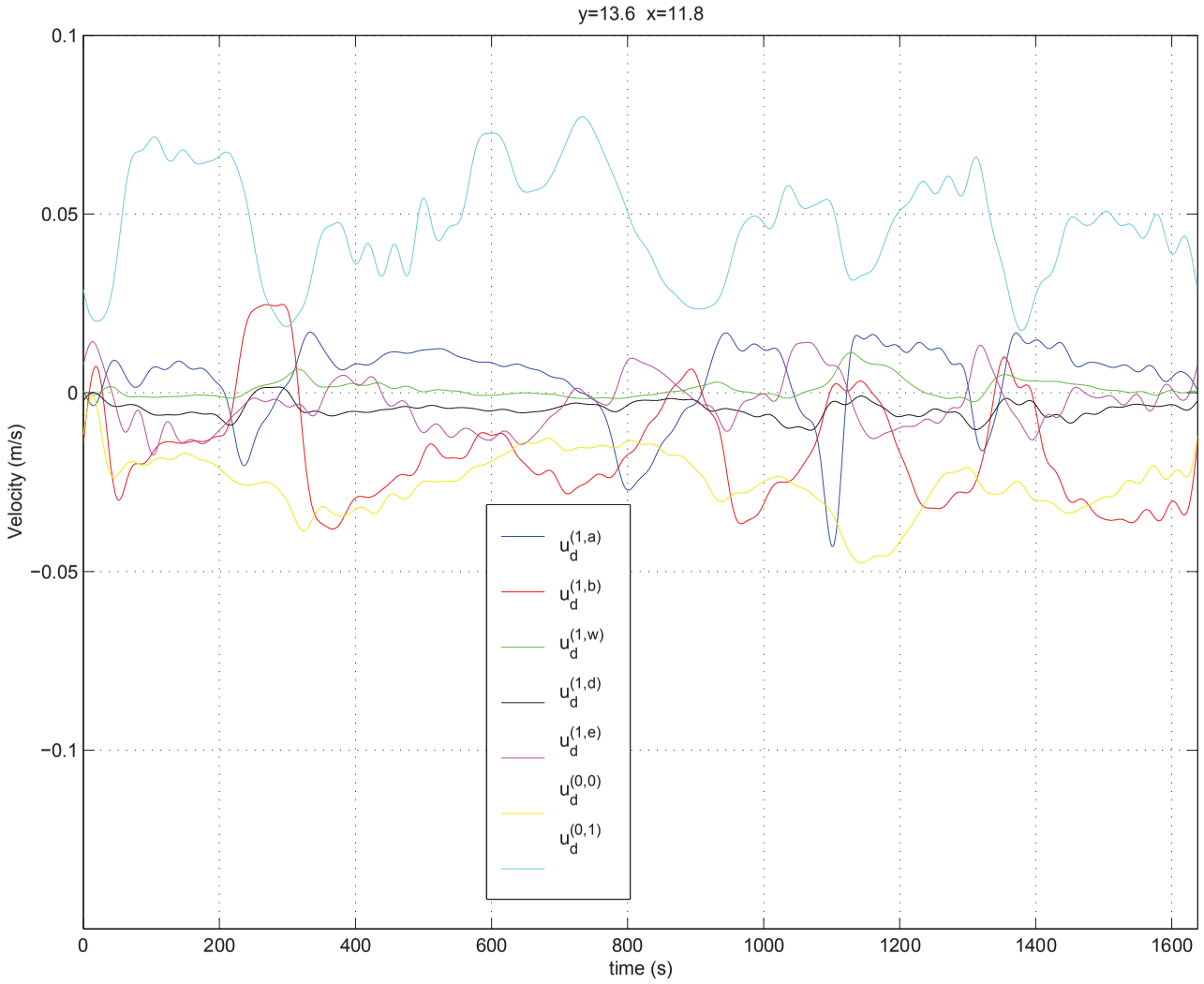

Figure 5.27: Time series from the SC simulation on the real topography of the components of difference between U_d and the surface and U_d at the bottom in the channel ($x = 11.8, y = 13.6$ m).

short-waves is reduced. Bottom friction and the convective accelerations govern the vertical profiles outside the surfzone. The narrow nature of the rip currents creates large gradients across the flow which leads to the importance of the convective accelerations. These terms tend to cause an increase in the velocity near the surface and decrease the velocity near the bottom producing vertical profiles similar to the experimental measurements.

Chapter 6

ANALYZING RIP CURRENT SYSTEMS

The previous chapters establish the ability of SHORECIRC to model rip currents on beaches with bars and channels. The beauty of numerical models is that many hydrodynamic conditions can easily be studied. In this chapter we use SHORECIRC to analyze rip current systems on varying topographies and wave conditions.

The first section provides a general overview of the conditions modeled including the parameterization of the geometry. In addition, a discussion of the general features of the circulation patterns is included.

The next section analyzes the effect of different topographies on the circulation, specifically, the rip channel spacing and the distance between the bar and shoreline are varied. Detailed discussions of the flow patterns as well as the momentum balances are presented.

The final section presents the analysis of the influence of the wave field on the circulation where the wave angle and breaking pattern are varied. Again, the flow patterns and momentum balances are discussed in detail.

6.1 General Overview

Figure 6.1 shows an example of the topography used for the simulations. The longshore bar is located on a flat bottom with two rip channels and is followed by a quadratic beach. The topography is chosen such that the geometry is easily varied without changing the depth over the bar. The depth of the flat portion is always 15

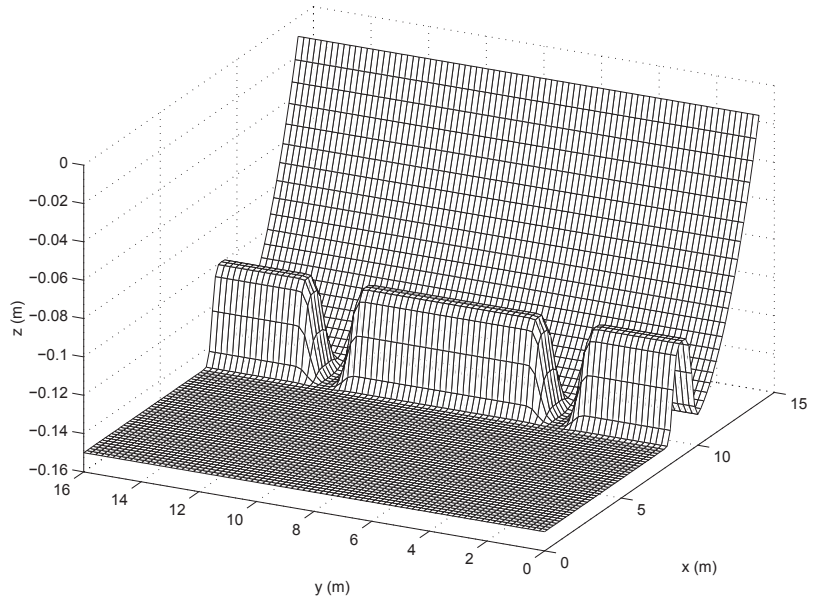

Figure 6.1: Topography used in numerical calculations.

cm and the depth over the bar is 10 cm. This topography is similar to the beach topography considered by Dalrymple (1978).

The definitions for the geometry parameters are seen in Figure 6.2 where L_c is the width of the rip channel, L_B is the spacing between rip channels and L_s is the distance from the peak of the bar to the shoreline. Two nondimensional parameters are used to characterize the geometry; L_B/L_c is the relative distance between channels and L_s/L_c is the relative distance of the bar from the shoreline.

Table 6.1 lists the values of all the parameters used for the twelve runs in the study. Four values of $\frac{L_B}{L_c}$ and three values of $\frac{L_s}{L_c}$ are utilized by changing L_B and L_s while L_c is held constant. These twelve runs represent cases where the rip channel spacing ranges from close to far apart. The wave input is identical for each case where the offshore wave height is 7 cm and the wave period is 1 second. In addition, the friction factor and eddy viscosity coefficients are held constant ($f_w = 0.015$, $C_1\kappa = 0.1$, $M = 0.1$ and $C_s = 0.25$).

Table 6.1: Values of the topography parameters L_c, L_B and L_s and two nondimensional parameters L_B/L_c andL_s/L_c used for the geometry study.

Run	L_c (m)	L_B (m)	L_s (m)	L_B/L_c	L_s/L_c
1	2	8	4	4	2
2	2	8	5	4	2.5
5	2	12	4	6	2
6	2	12	5	6	2.5
9	2	16	4	8	2
10	2	16	5	8	2.5
13	2	24	4	12	2
14	2	24	5	12	2.5
17	2	8	3	4	1.5
18	2	12	3	6	1.5
19	2	16	3	8	1.5
20	2	24	3	12	1.5

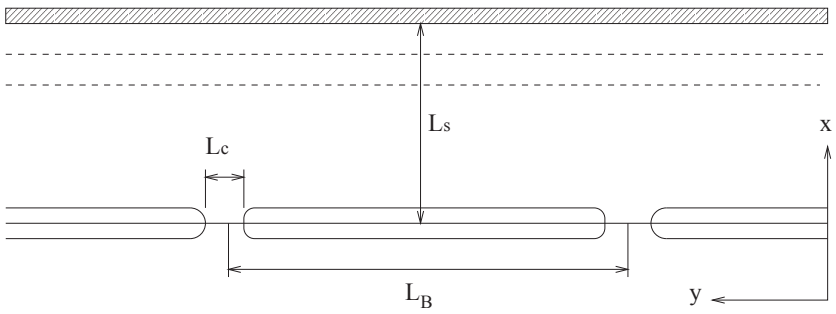

Figure 6.2: Definition sketch of topography parameters.

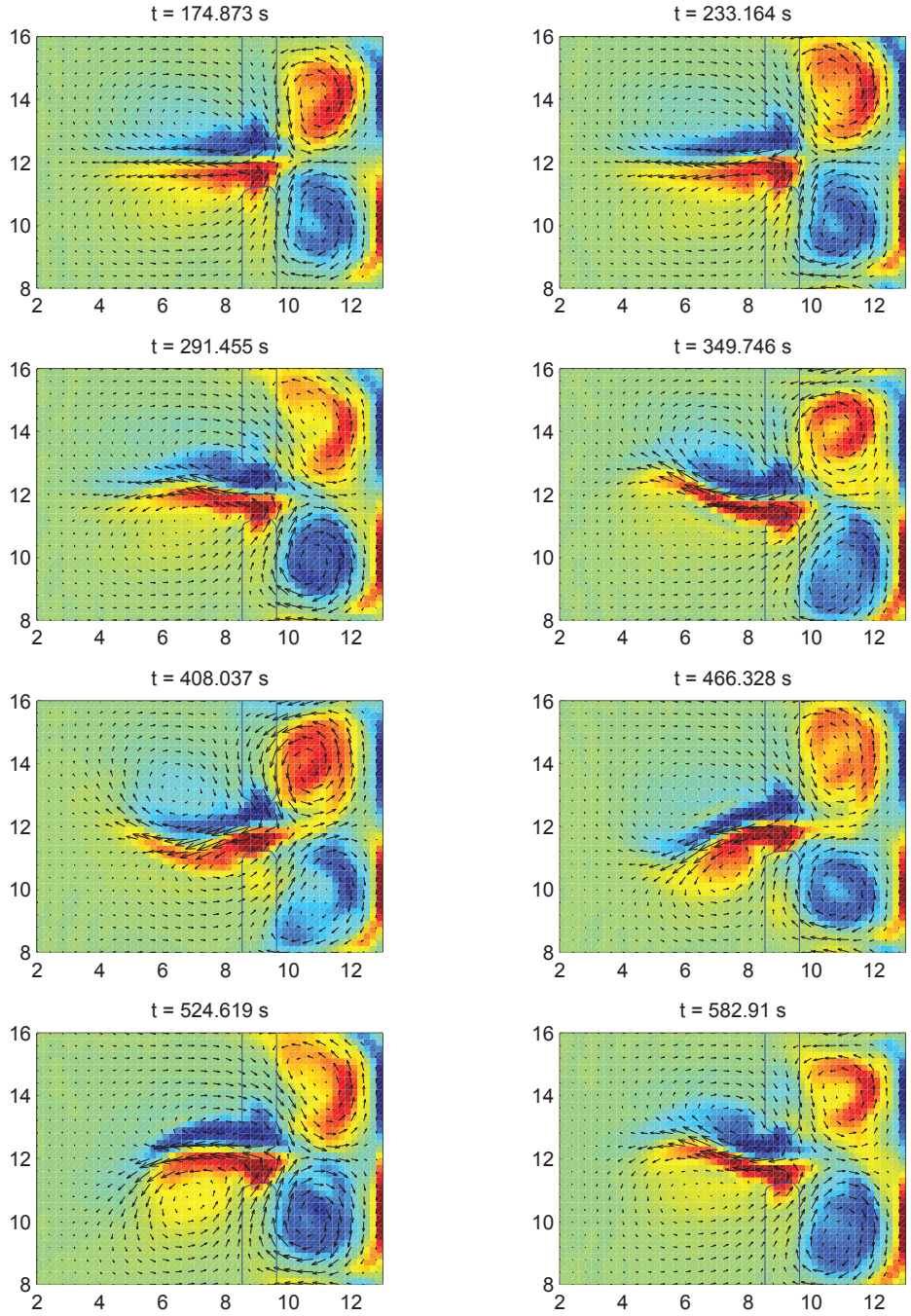

Figure 6.3: Instantaneous snapshots of vorticity and velocity vectors showing the unstable nature of rip currents on the idealized topography. Only an excerpt of the entire computational domain is shown.

Even for idealized smoothed topographies, rip currents are unstable as seen in Figure 6.3. The series of instantaneous snapshots of vorticity and velocity vectors show the time variation of the rip current where it is flopping slightly from side to side. The unstable motion of the rip current on the idealized topography is much weaker than on the wave basin topography. In Chapter 2, simulations on the wave basin topography show that time-averaging eliminates the rip signal offshore of the bar, however, the weaker instabilities on the idealized topography create less meandering of the rip which only reduces the time-averaged current offshore. Because the interest of this study is in the rip channel, over and behind the bar, the time-average is a viable tool.

Results of time-averaging the current are seen in Figure 6.4 which shows the velocity vectors of $V_{m\alpha}$ and depth contours. The topography for this figure is from case 10 in Table 6.1 where the channel spacing is relatively large. The two rip currents are evident in the channels and appear to be symmetric to one another. Between the bar and the shoreline in the trough region, recirculation cells are evident behind each channel; these cells are providing the feeder currents for the rips. In the middle of the domain far away from either rip channel the current is flowing straight offshore as one-dimensional undertow.

The time-averaged mean water level ($\overline{\zeta}$) is shown in Figure 6.5 for case 10 from Table 6.1. The water level shows a slight setdown before the larger setup due to wave breaking. The water level in the channel is lower than the water level over the bar which provides the pressure gradient to drive the feeder currents towards the rip channel. However, the setup close to the shoreline behind the channel is larger than the setup behind the bar, providing the driving force for the recirculation cells. In the center region between the channels the setup is constant with no longshore variations.

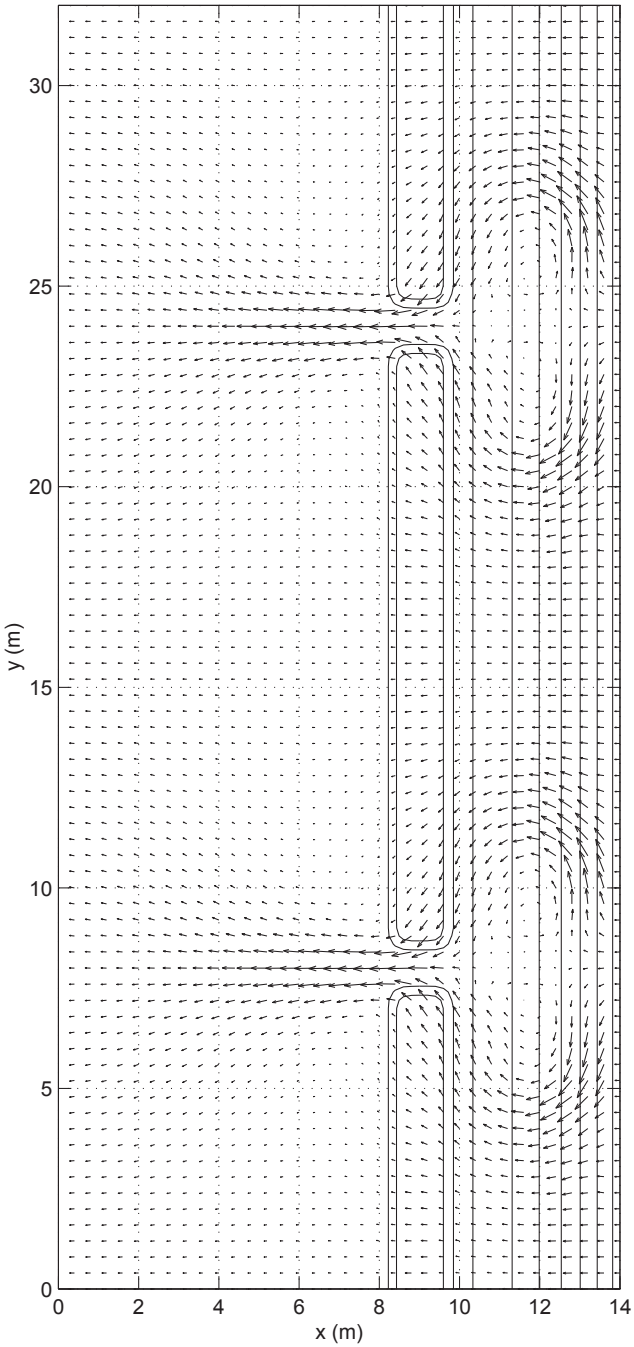

Figure 6.4: Time-averaged depth integrated current vectors for the entire computational domain.

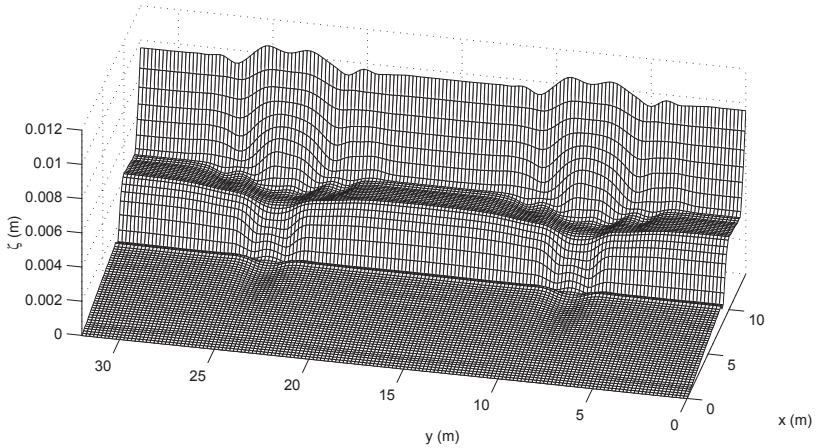

Figure 6.5: Time-averaged mean water level for the entire computational domain.

6.2 Varying the Topography

This sections establishes the effect of varying the geometry of the topography, specifically the rip spacing and bar location, on the flow in rip current systems.

6.2.1 Analysis of the Flow Patterns

Taking into account continuity for the entire domain, the net shoreward volume flux carried by the short waves must be balanced by the seaward current. Hansen and Svendsen (1986) point out that part of the seaward volume flux passes over the bar as undertow, especially when the channel spacing becomes large.

In order to analyze the return flow in the rip versus the return flow over the bar, consider the following definitions,

$$I_r = \int_{rip} U_m h dy \tag{6.1}$$

and

$$I_w = \int_{bar} Q_w dy. \tag{6.2}$$

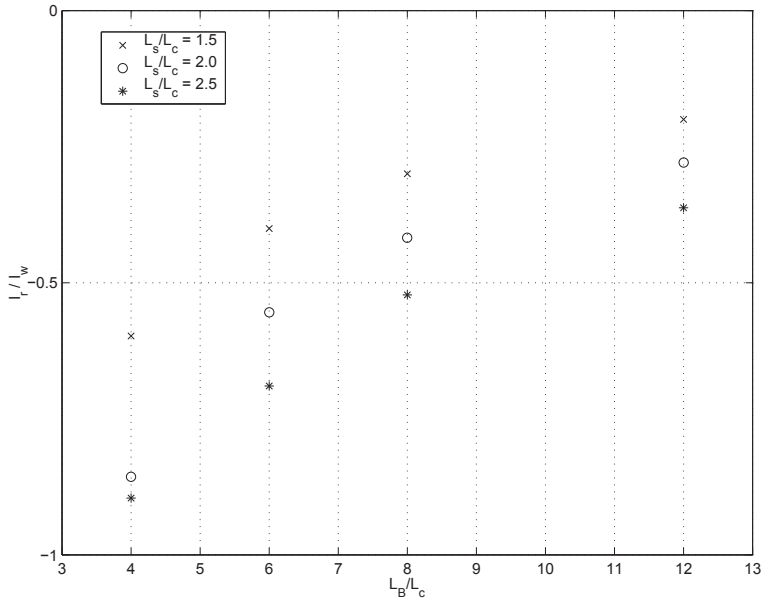

Figure 6.6: Ratio of I_r/I_w as a function of L_B/L_c for three values of L_s/L_c illustrating the point that closer channel spacing increases the percentage of the shoreward flux returned by the rip currents.

I_r is the total seaward volume flux in the rip current and I_w is the total shoreward short-wave volume flux passing over the bar and channel. These volumes are calculated at $x = 8$ m which is slightly offshore of the bar where the rip flow is maximized.

Figure 6.6 illustrates the effect of varying the relative channel spacing and the position of the shoreline on the percentage of the total seaward volume flux in the rip current. The value of I_r/I_w varies between 0, where none of the seaward flux is in the rip, and -1, where all of the seaward flux is in the rip. The negative value of I_r results from the seaward flux being defined as negative.

Clearly, for smaller rip channel spacing the percentage of seaward volume flux in the rip is higher than for large rip spacing. The smallest channel spacing of $L_B/L_c = 4$ shows that around 90% of the seaward volume flux is returned in the

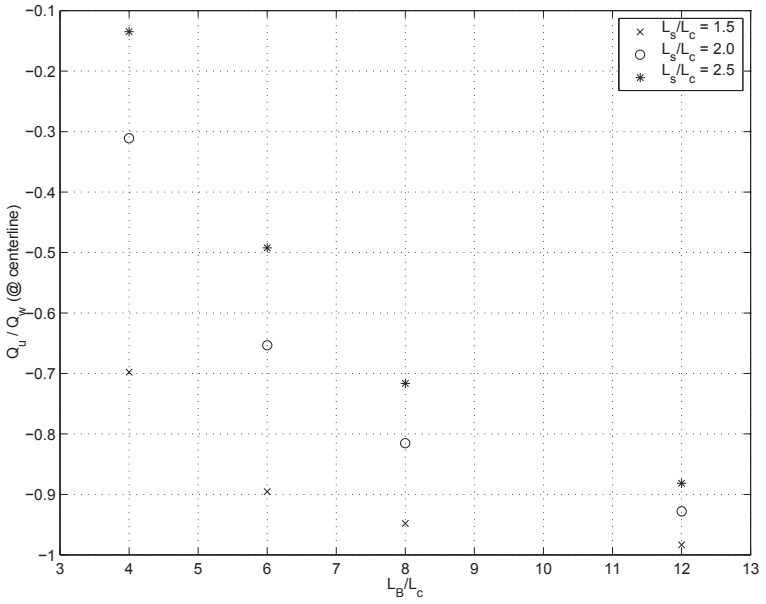

Figure 6.7: Ratio of Q_u/Q_w at the centerline of the bar as a function of L_B/L_c for three values of L_s/L_c demonstrating that small rip spacing and close proximity of the bar to the shoreline decrease the return flow over the centerline of the bar.

rip current. On the other hand, the large channel spacing, $L_B/L_c = 12$, only has 25% of the seaward flux contained in the rip channel. Regardless of the rip spacing, some of the seaward flux must be returned over the bar as undertow.

The relative flux in the rip is also sensitive to the position of the bar to the shoreline. When the bar is closer to the shoreline the percentage of seaward volume flux in the rip is decreased. The seaward flux for $L_B/L_c = 4$ is decreased to 60% for smallest relative bar position, $L_s/L_c = 1.5$. The effect of the position of the bar relative to the shoreline on the relative strength of the rip is decreased as the channel spacing increases.

In addition to examining the flow in the rip itself, the volume flux over the

bar is analyzed. To that end, we define the following,

$$Q_u = U_m h \tag{6.3}$$

where Q_u is volume flux of the undertow. Using this definition, Figure 6.7 shows the relative strength of the undertow Q_u/Q_w at the centerline of the middle bar for different values of L_B/L_c and L_s/L_c. Q_u/Q_w varies from 0 for no undertow to -1 for all the short-wave volume flux being returned as undertow.

The undertow over the bar is strongly dependent on the relative rip spacing. When the channels are close together the undertow over the mid-line bar is less than 15% of the incoming volume flux for $L_s/L_c = 2.5$. However, as the channel spacing increases the undertow over the bar increases to nearly 90% for a spacing $L_B/L_c = 12$.

In addition, the undertow is sensitive to the position of the bar relative to the shoreline. When the bar is closer to the shoreline, more flow is returned over the bar as undertow. For example, in Figure 6.7 when $L_B/L_c = 4$ and $L_s/L_c = 2.5$, approximately 15% of the short-wave volume flux is returned as undertow over the bar. Whereas, when $L_s/L_c = 1.5$, the bar is close to the shoreline, the undertow is increased to 70%. The sensitivity of the undertow to the shoreline position is reduced as the channel spacing increases.

6.2.1.1 Varying Rip Spacing

The effect of the relative rip spacing, L_B/L_c, for a constant shoreline location is shown in Figure 6.8. The four plots of depth-averaged current ($V_{m\alpha}$) vectors and streamlines are for different relative channel spacings, $L_B/L_c = 4, 6, 8, 12$, while the position of the bar relative to the shoreline is held constant at $L_s/L_c = 2.5$. In (a), immediately offshore of the bar for $6 < x < 8$ the undertow is nearly non-existent, because virtually all of the seaward flux is contained in the rip. However, as the channel spacing increases, (c) and (d), the undertow over the bar is increased. The

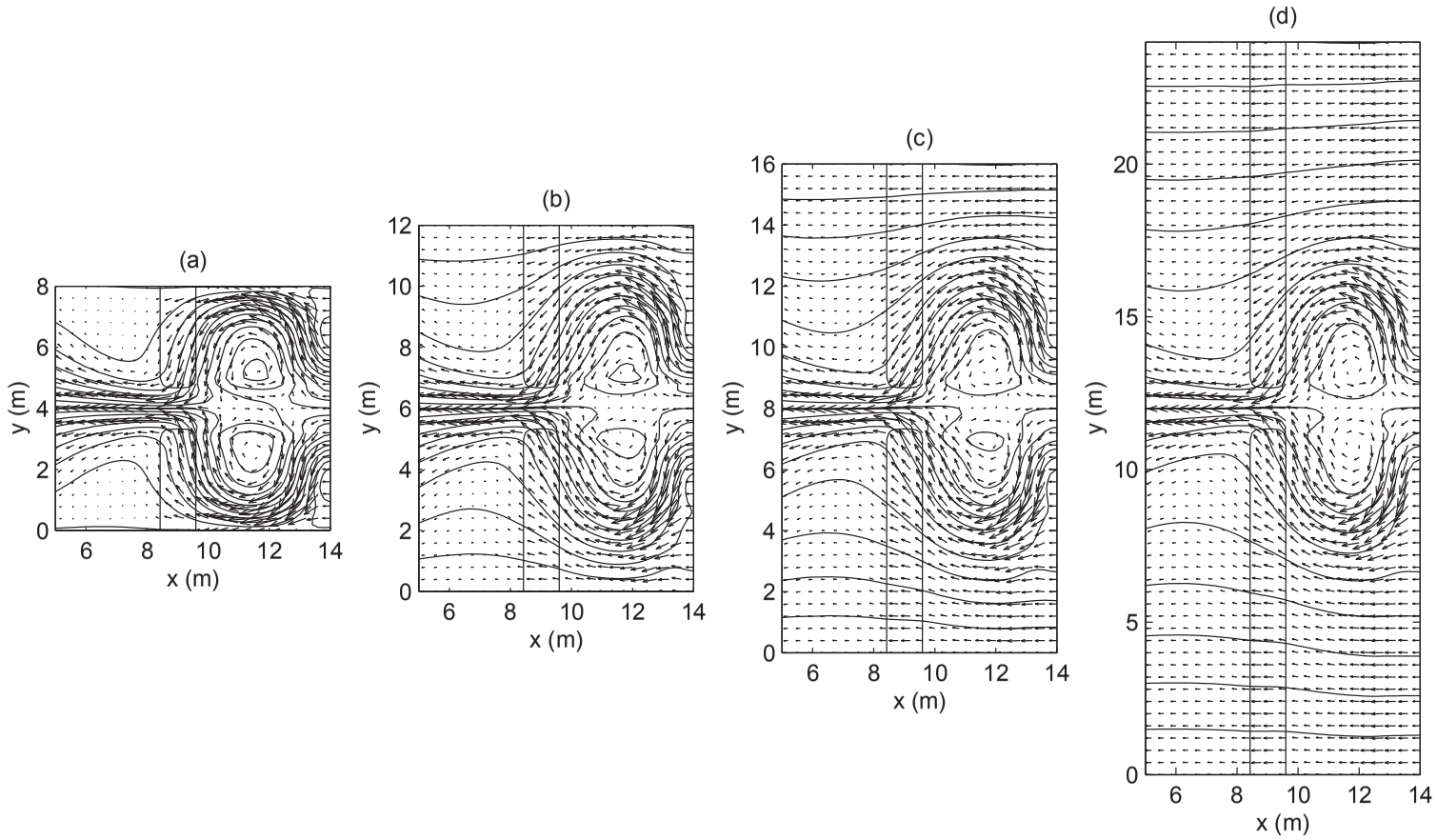

Figure 6.8: Vectors and streamlines of the depth integrated current $V_{m\alpha}$ for $L_s/L_c = 2.5$ where (a) $L_B/L_c = 4$, (b) $L_B/L_c = 6$, (c) $L_B/L_c = 8$ and (d) $L_B/L_c = 12$ showing the pinching of the currents for small rip spacings and 1D undertow far away from the rips for the large spacings.

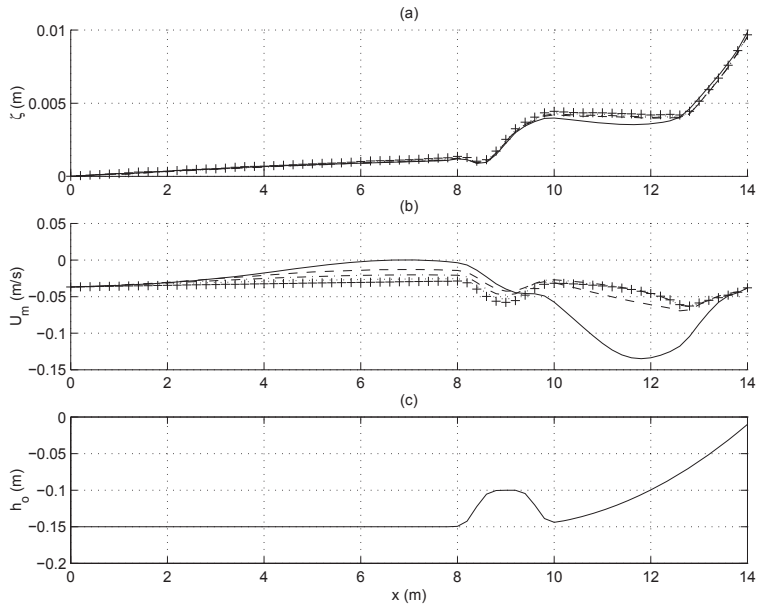

Figure 6.9: Cross-shore sections of (a) setup (ζ), (b) cross-shore velocity (U_m) and (c) the still water depth where (+) is for no channels, (-) $L_B/L_c = 4$, (- -) $L_B/L_c = 6$, (-.) $L_B/L_c = 8$ and $(\cdots)$ $L_B/L_c = 12$ showing the deviation from the 1D undertow.

flow over the bar close to the side boundaries, which represent the symmetry line between neighboring rips, closely resembles one-dimensional cross-shore flow.

The similarity of the flow over the mid-line of the bar and one-dimensional undertow is better illustrated in Figure 6.9. This figure shows cross-shore sections of (a) the setup and (b) the undertow for different rip channel spacings compared to a longshore uniform beach with no channels. In (b) it is evident that the closer the rip channel spacing is, the more the undertow deviates from the classical one-dimensional undertow. The undertow for $L_B/L_c = 4$ has a large offshore component shoreward of the bar, which is part of the recirculation cells, and has no velocity seaward of the bar because most of the return flow is contained within the rip. The undertow for the larger values of L_B/L_c are similar to the classical undertow.

Even with the large deviations in velocity, the setup shows little variation

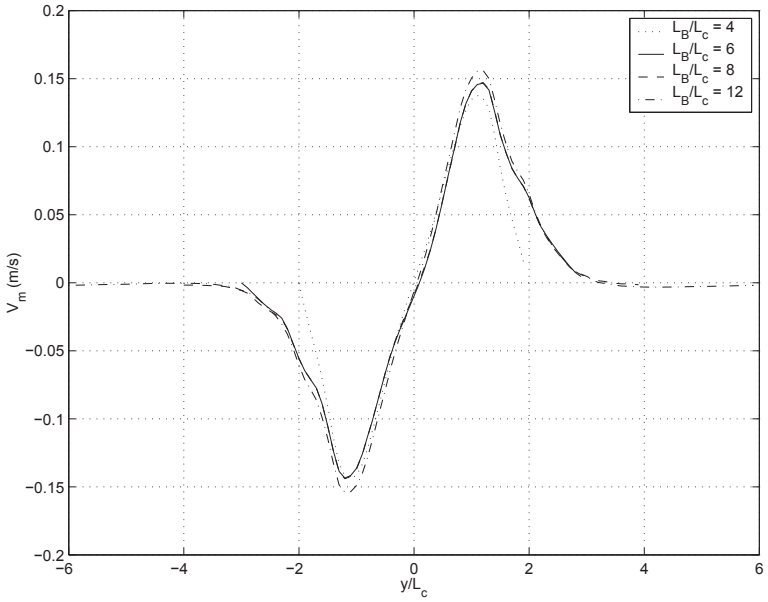

Figure 6.10: Variation of V_m as a function of y/L_c for $x = 13$ m, 1 m seaward of the shoreline. Only the smallest rip spacing pinches the size of the recirculation cells.

for the different rip spacings. This confirms the findings by Hansen and Svendsen (1986) who found that the setup has small variations for varying currents over the bar. Sancho *et al.* (1999) found that small variations in longshore conditions can contribute to large dynamic effects on the currents. The small variation in the setup for $L_B/L_c = 4$ in Figure 6.9 leads to substantially different current patterns as seen in Figure 6.8.

The recirculation cells behind the bar in Figure 6.8a fill the entire trough region and are squeezed by the sides. The increased rip spacing in (b) allows for larger recirculation cells. However, increasing the rip spacing further, in (c) and (d), does not lead to larger recirculation cells. The size of the circulation cells is not governed by the spacing between rips unless the rips are close enough to pinch the cells.

Figure 6.10 shows the longshore variation of the depth-averaged longshore current V_m, 1 m seaward of the shoreline for the four values of L_B/L_c. The curves are plotted for one of the rips where the boundaries, representing the symmetry lines, have differing end points because of the varying rip spacings. Because the longshore velocity approaches 0 between the rips, these curves reveal the size of the recirculation cells. The three largest rip spacings produce recirculation cells remarkably similar in size, only the smallest rip spacing has a reduced recirculation cell.

Figure 6.11 shows the vectors and streamlines for the total volume flux Q_α for the same four geometries in Figure 6.8. The recirculation cells between the bar and the shoreline appear to be isolated from the rip with no exchange of flow. This is just an illusion, the circulation cells do exchange flow with the rip which is illustrated by examining Figures 6.8 and 6.11 together. The circulation is as follows: the short waves transport water shoreward above the trough level into the recirculation cells, and the currents, which are essentially below trough, return the water seaward through the rip current. The net result is the appearance of closed circulation loops in Figure 6.11 but in reality, there is a continuous exchange of water between the rip and recirculation cells as seen when considering Figure 6.8 as well.

The large vortices of flow feeding the rip over the bar are evident in Figure 6.11 as well. The water flows over the bar, turns, feeds the rip, then flows out the channel and returns once again over the bar. Contrary to the recirculation cells behind the bar, these vortices grow with increasing rip channel spacing. There is flow feeding the rip over nearly the entire length of the bar between rips, albeit a small flow farther away from the rip.

The longshore extent of the feeder currents is established by integrating the

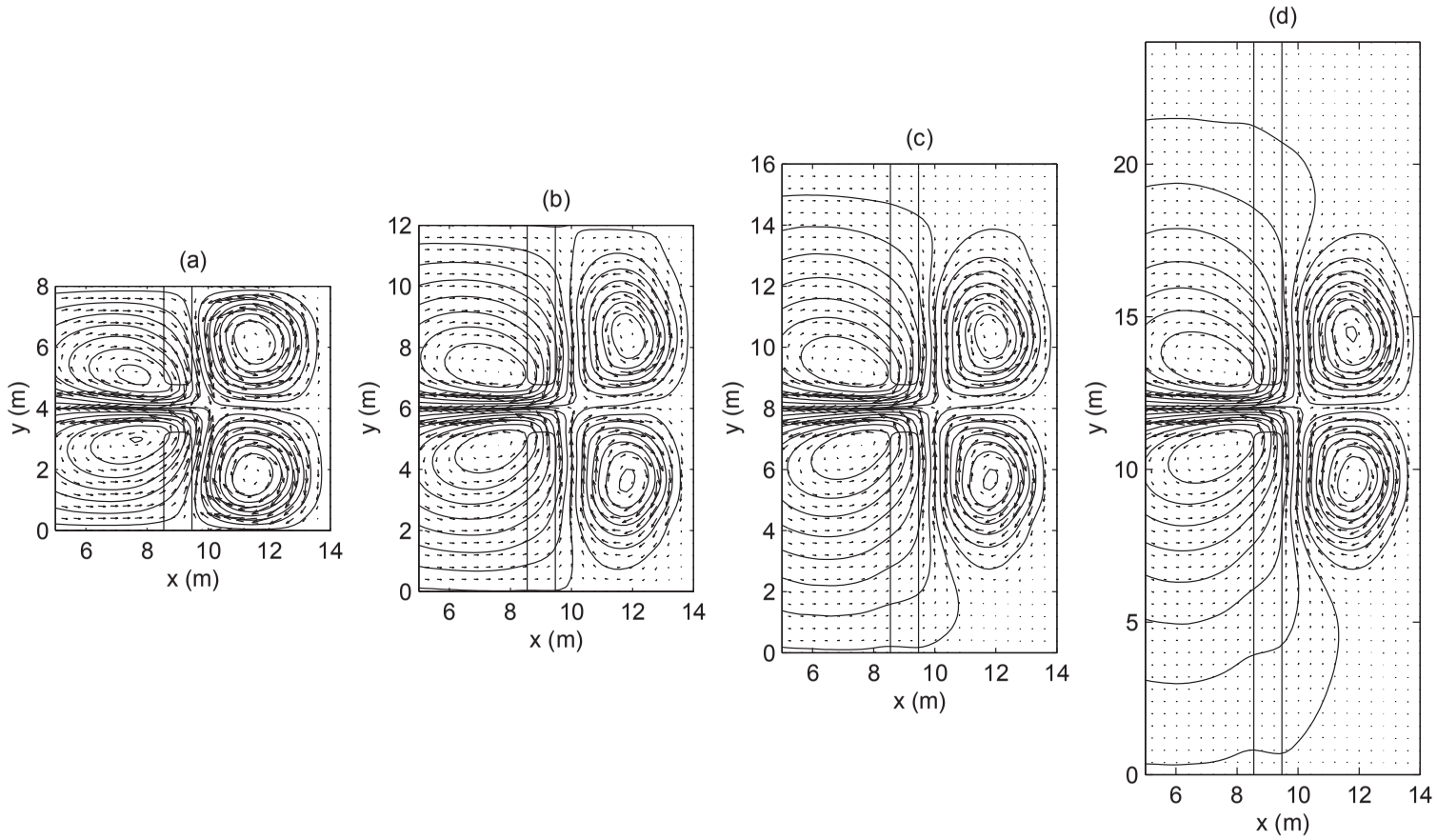

Figure 6.11: Vectors and streamlines of the total volume flux Q_α for $L_s/L_c = 2.5$ where (a) $L_B/L_c = 4$, (b) $L_B/L_c = 6$, (c) $L_B/L_c = 8$ and (d) $L_B/L_c = 12$. The small rip spacing pinches the recirculation cells and the large spacing allows the feeder currents to grow.

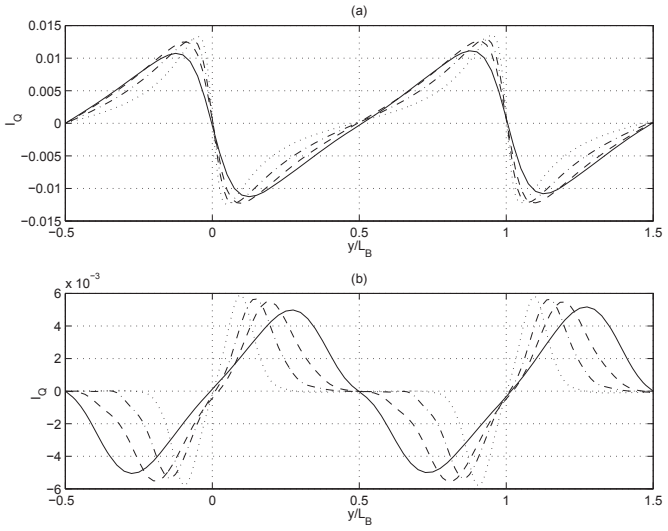

Figure 6.12: Variation of I_Q as a function of y/L_B for (a) $x = 8$ m and (b) $x = 13$ m with (-) $L_B/L_c = 4$, (- -) $L_B/L_c = 6$, (-.) $L_B/L_c = 8$ and $(\cdots)$ $L_B/L_c = 12$. The feeder cells grow with increasing rip spacing and the recirculation cells do not grow.

total cross-shore flux across the width of the rip current system for a given cross-shore position. We define the quantity I_Q as

$$I_Q = \int_{y_o}^{y} Q_x dy \tag{6.4}$$

where y_o is the lower longshore boundary at the symmetry line. Figure 6.12 demonstrates the variation of I_Q along the (a) rip feeder vortices and (b) the recirculation cells for the four values of L_B/L_c. Increasing I_Q indicates shoreward volume flux and decreasing I_Q indicates seaward flux.

In (a), I_Q increases until boundary of the rip, then decreases, passing 0 at the rip symmetry line, until it reaches a minimum and then increases, passing 0 at the bar symmetry line, repeating the pattern for the next rip. Clearly, the maximums and minimums represent the relative strength of the rip current and the curve flattens when the total volume flux is small. The curve begins to flatten

slightly as the distance between the rips is increased. Although, for the largest rip spacing the feeder currents between the two rips are still significant. In addition, the strength of the rip only decreases slightly for the shorter rip spacing. The width of the feeder current circulation cells grows with increased rip spacing.

On the other hand, close to the shoreline in the recirculation cells in (b), I_Q has much more variation for varying L_B/L_c. Increasing the rip spacing causes it to flatten between recirculation cells quickly. This indicates that the size of the cells do not grow with increased rip spacing. The dynamics of the recirculation cells are apparently different from the feeder current vortices.

6.2.1.2 Varying Bar Distance from the Shoreline

This subsection examines how the position of the bar relative to the shoreline affects the flow in rip current systems by varying L_s/L_c while holding L_B/L_c constant.

Figure 6.13 shows the velocity vectors and streamlines of the below trough current for three different bar locations and two rip spacings. Reviewing (a), (c) and (e) ($L_B/L_c = 4$) reveals that the undertow is strongly dependent on the location of the bar relative to the shoreline. For example, in (a) the undertow offshore of the bar remains large, even close to the symmetry line at the top, while in (e) the undertow is virtually non-existent offshore of the bar outside of the rip. Decreasing the distance from the bar to the shoreline increases the flow returning to sea as undertow over the bar. In addition, in (b), (d) and (f) ($L_B/L_c = 6$), the longshore width of the recirculation cells grows with increasing spacing between the bar and shoreline.

Similar to Figure 6.10, Figure 6.14 establishes the width of the recirculation cells by showing the variation of V_m 1 m seaward of the shoreline for three different L_s/L_c. Significant differences between the width of the recirculation cells exist. When the bar is closer to the shoreline, the extent as well as the magnitude of the

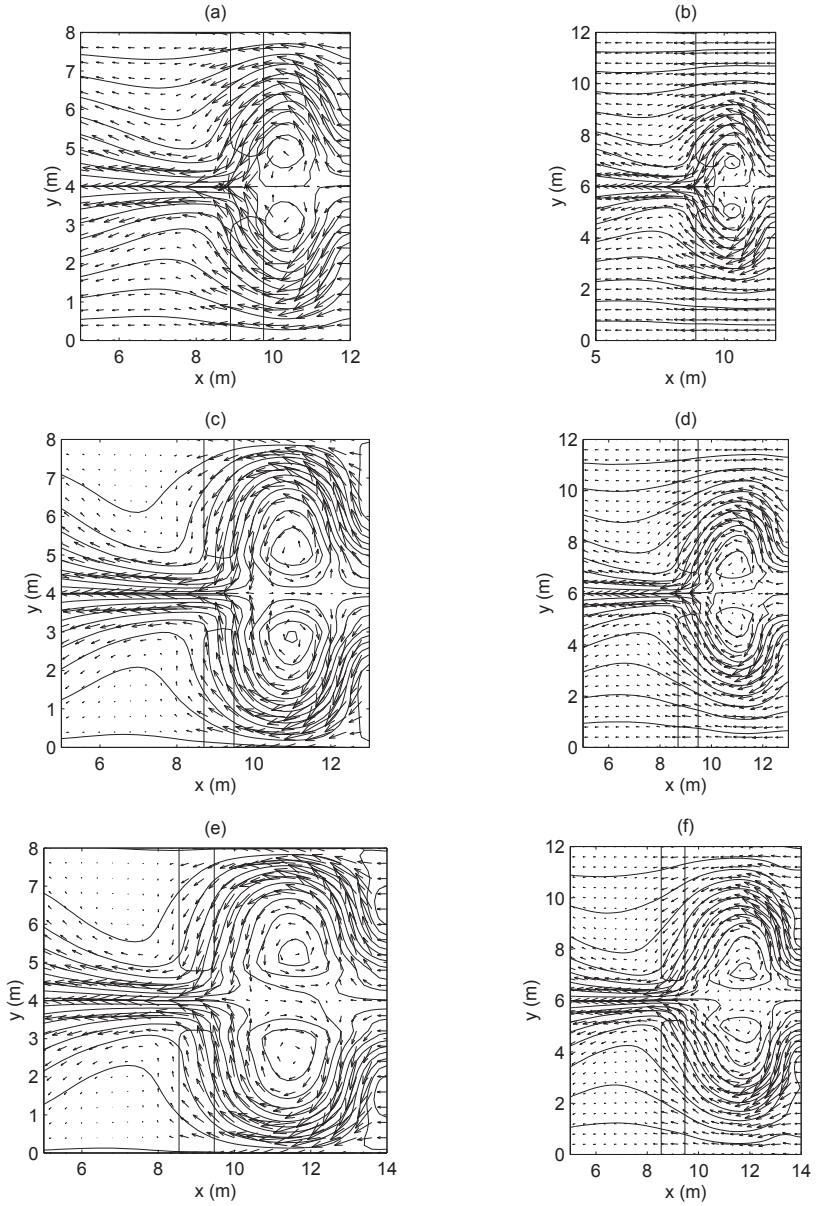

Figure 6.13: Vectors and streamlines of the depth integrated current $V_{m\alpha}$ for the top row ((a) and (b)) $L_s/L_c = 1.5$, the middle row ((c) and (d)) $L_s/L_c = 2.0$ and the bottom row ((e) and (f)) $L_s/L_c = 2.5$. The left column ((a), (c) and (e)) is for $L_B/L_c = 4$ and the right column ((b), (d) and (f)) is for $L_B/L_c = 6$. Increasing the distance between the bar and shoreline increases the width of the recirculation cells.

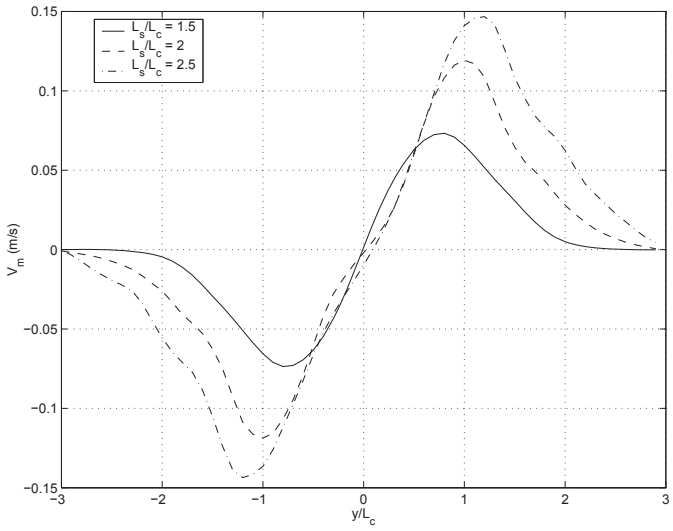

Figure 6.14: Variation of V_m as a function of y/L_c 1 m seaward of the shoreline showing that increasing the distance between the bar and shoreline increases the recirculation cells.

nonzero V_m is reduced. Whereas the relative channel spacing has little influence on the width of the recirculation cells, the position of the bar relative to the shoreline has a profound effect on the circulation.

Figure 6.15 shows the vectors and streamlines of the total volume flux Q_α for the same six geometries shown in Figure 6.13. The recirculation patterns again appear to be closed loops and increase in size with increasing L_s/L_c. On the other hand, the size of the feeder vortices appears to only increase slightly with when increasing the distance of the bar relative to the shoreline.

The variation of I_Q is shown in Figure 6.16 along (a) the outer edge of the bar and (b) 1 m seaward of the shoreline for three different values of L_s/L_c. The extent of the circulation cells are increased for larger L_s/L_c. In addition, the strength of the rip current is extremely sensitive to the position of the bar; the closer the shoreline is to the bar the weaker the rip current. The smaller circulation cells produce less feeder currents to feed the rip and more flow returns to sea over the bar as seen in

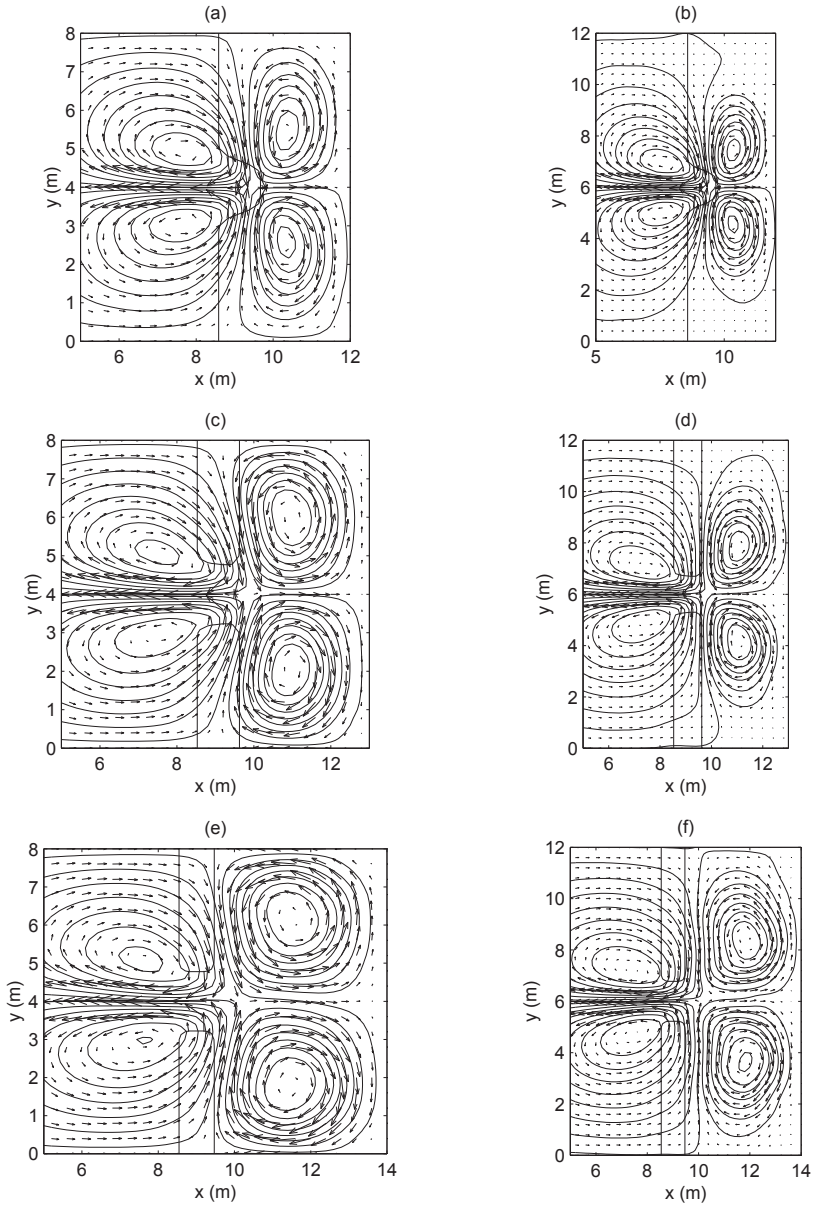

Figure 6.15: Vectors and streamlines of the total volume flux Q_α for the top row ((a) and (b)) $L_s/L_c = 1.5$, the middle row ((c) and (d)) $L_s/L_c = 2.0$ and the bottom row ((e) and (f)) $L_s/L_c = 2.5$. The left column ((a), (c) and (e)) is for $L_B/L_c = 4$ and the right column ((b), (d) and (f)) is for $L_B/L_c = 6$. The width of the cells feeding the rips are not dependent on the distance between the shoreline and the bar.

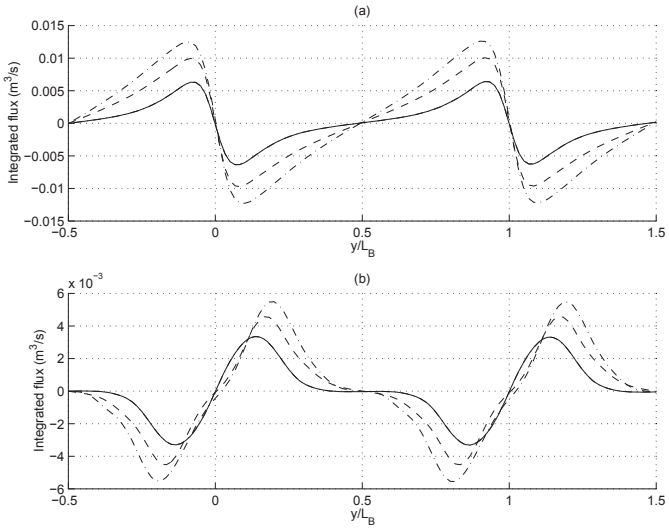

Figure 6.16: Variation of I_Q as a function of y/L_B for (a) $x = 8$ m and (b) 1 m seaward of the shoreline with (-) $L_s/L_c = 1.5$, (- -) $L_s/L_c = 2.0$, (-.) and $L_s/L_c = 2.5$ demonstrating the dependence of the flow in the rip on the position of the bar relative to the shoreline.

Figure 6.13.

6.2.1.3 Relative Strength of the Rip Current

The previous subsection analyzes how the overall circulation pattern is related to the geometry, especially the relationship between the undertow over the bar and the rip flow in the channel. This section analyzes the absolute volume flux in the rip I_r. To aid in the analysis, define the short-wave volume flux within the rip as

$$I_{wr} = \int_{rip} Q_w dy. \tag{6.5}$$

This quantity, unlike the total short-wave volume flux I_w, does not change much with rip spacing. The ratio I_r/I_{rw} is a measure of the absolute volume flux in the rip and can be considered an amplification factor since the extent which this ratio exceeds 1 indicates the amount of water outside the channel that the rip collects.

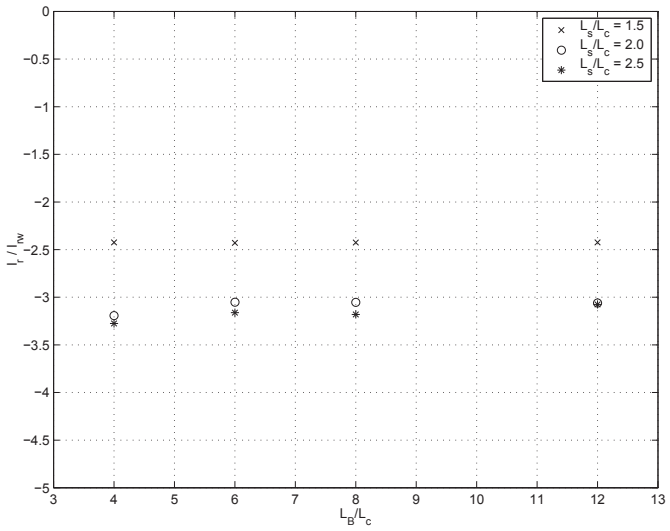

Figure 6.17: Ratio of I_r/I_{rw} as a function of L_B/L_c for three values of L_s/L_c indicating the independence of the relative strength of the rip to the channel spacing.

Amazingly, as shown in Figure 6.17, the absolute volume flux contained in the rip does not vary with rip spacing. Even though the circulation pattern feeding the rip grew significantly with increasing L_B/L_c, the total flux within the rip is unaffected. Similar to the previous findings, decreasing L_s/L_c reduces the total discharge of the rip.

Similarly, Figure 6.18 shows the depth-averaged velocity in the rip is independent of the rip spacing as well. Not surprisingly, decreasing the distance between the bar and the shoreline reduces the velocity in the rip slightly.

Remarkably, the channel spacing does not control the flow in the rip. However, the spacing of the channels does control the amount of flow return as undertow over the bar. Because the total flow in the rip remains constant for a given bar and shoreline position, increasing the channel spacing only increases the flow returning as undertow over the bar.

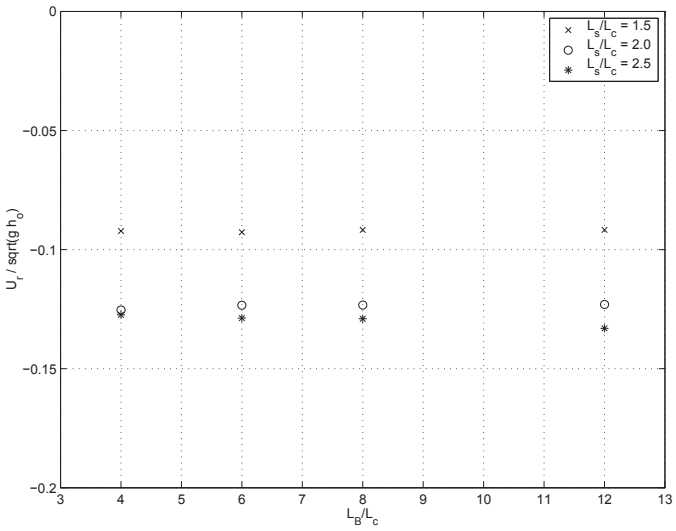

Figure 6.18: Cross-shore velocity U_r at the center of the rip normalized by $\sqrt{gh}$ as a function of L_B/L_c for three values of L_s/L_c showing the independence of the relative velocity of the rip to the channel spacing.

6.2.2 Analysis of the Forcing and Momentum Balances

Thus far, the analysis has been focusing on the flow patterns associated with different geometries. This section examines the forcing for the rip current systems and the associated momentum balances.

The two main driving forces for nearshore circulation are the gradients of the radiation stress $S_{\alpha\beta}$ and the pressure, represented by the mean water level $\overline{\zeta}$. On a long straight beach these two forces nearly balance each other in the cross-shore direction leaving around 5% of the radiation stress to balance the bottom stress from the undertow (Svendsen and Hansen, 1988). In the longshore direction there is no pressure gradient so the small gradient in the radiation stress is balanced by the bottom stress from the longshore current. The mixing terms from the 3D dispersion and turbulence only redistribute the currents and do not actively drive them.

Complex rip current systems are primarily driven by the gradients in the

radiation stress and the pressure as well. However, due to the presence of the channels, longshore variations in the forcing drives the rip currents. The two driving forces can be summed vectorially to give a "residual forcing" R_α

$$R_\alpha = -\frac{1}{\rho}\frac{\partial S_{\alpha\beta}}{\partial x_\beta} - gh\frac{\partial \overline{\zeta}}{\partial x_\alpha} \tag{6.6}$$

which represents the local forcing available to drive the currents.

6.2.2.1 Varying Rip Spacing

The radiation stress forcing for various values of L_B/L_c is shown in Figure 6.19 for the flow patterns described by Figures 6.13 and 6.15. Because the waves are normally incident there is only cross-shore forcing, except around the channel where the wave diffraction creates some longshore forcing. The strongest forcing occurs over the bar where the breaking is the most intense. Along the shoreline there is stronger forcing behind the channel because the waves passing through the channel have weaker dissipation before reaching the shoreline than the waves passing over the bar. The longshore extent of the increased forcing along the shoreline is independent of the rip spacing.

Figure 6.20 shows the pressure forcing for the same four geometries. Similar to the radiation stress, the pressure has primarily cross-shore forcing except in the region close to the channel. The largest pressure gradient is over the bar where the radiation stress gradient is the largest. Along the shoreline, similar to the radiation stress, the pressure gradient is larger behind the channel, with the longshore extent of this increased forcing also independent of rip spacing. However, inside the channel there is a large pressure gradient forcing flow offshore which is unbalanced by the radiation stress.

The forcing residual R_α for these geometries is shown in Figure 6.21. R_α is largest in the channel where the pressure gradient is not balanced by the radiation stress. This is interpreted to be the driving force for the rip current. In the trough

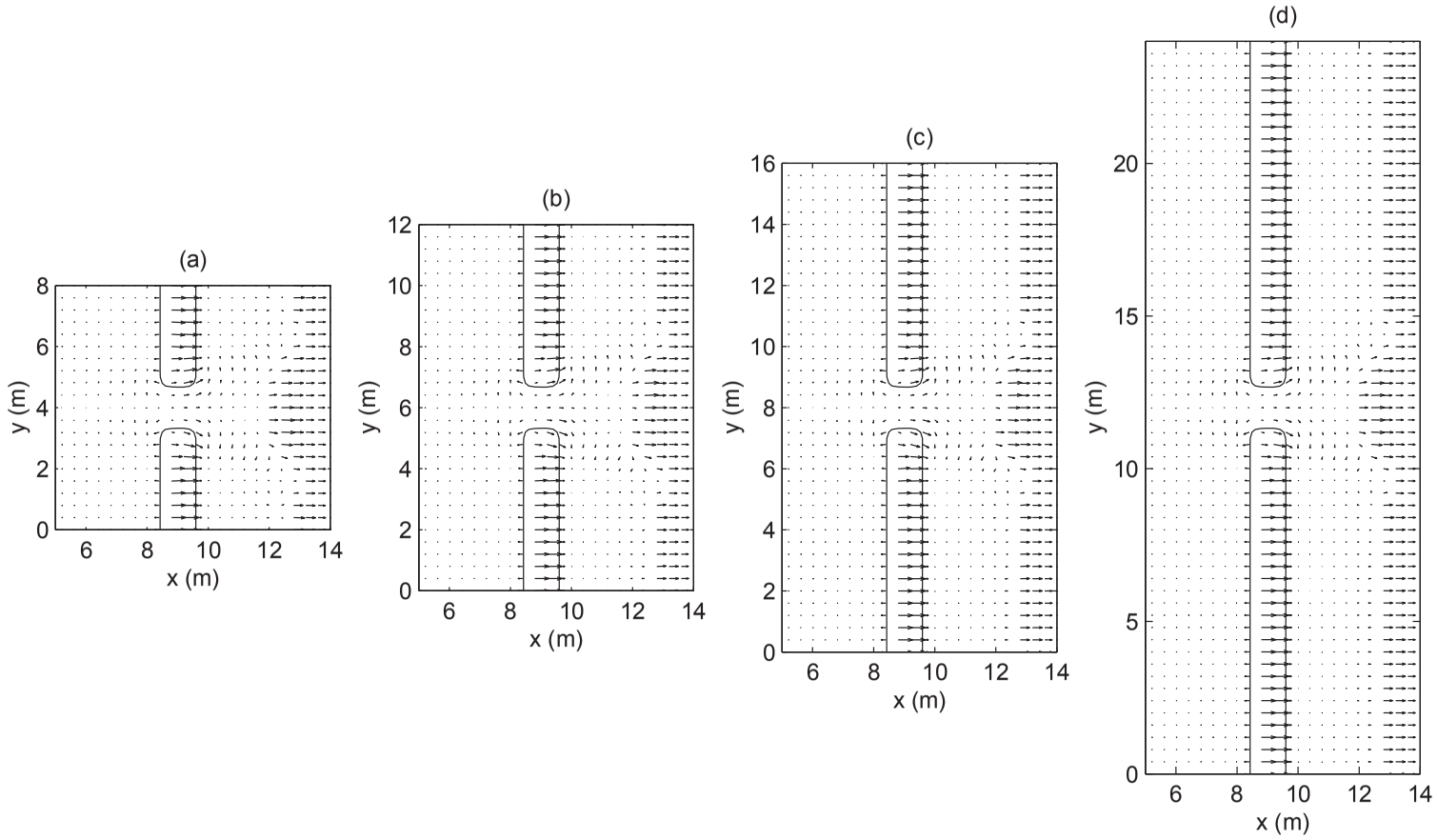

Figure 6.19: The effect of rip spacing on the radiation stress forcing for $L_s/L_c = 2.5$ where (a) $L_B/L_c = 4$, (b) $L_B/L_c = 6$, (c) $L_B/L_c = 8$ and (d) $L_B/L_c = 12$. $L_s/L_c = 2.5$.

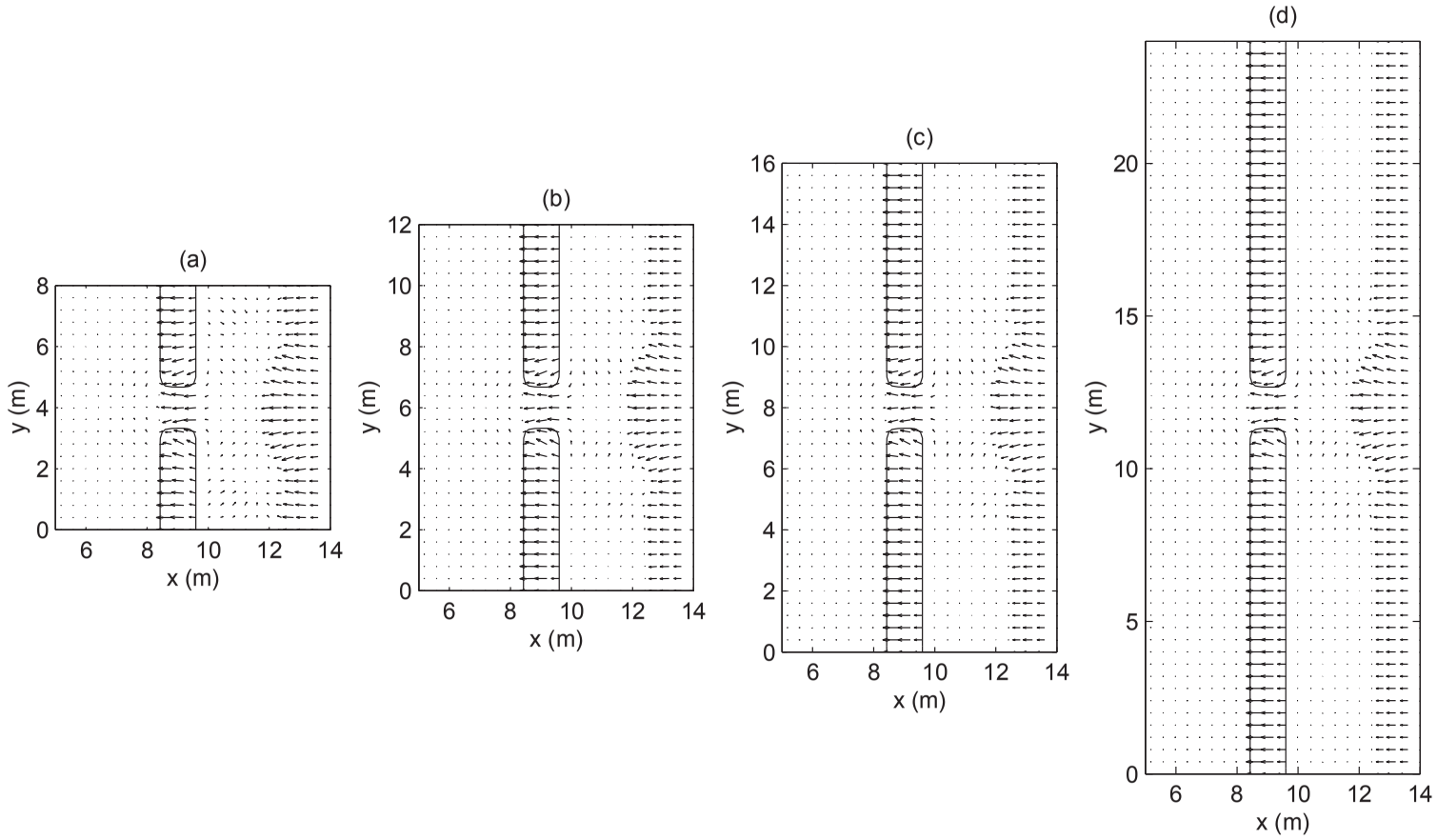

Figure 6.20: The effect of rip spacing on the pressure gradient for $L_s/L_c = 2.5$ where (a) $L_B/L_c = 4$, (b) $L_B/L_c = 6$, (c) $L_B/L_c = 8$ and (d) $L_B/L_c = 12$. $L_s/L_c = 2.5$.

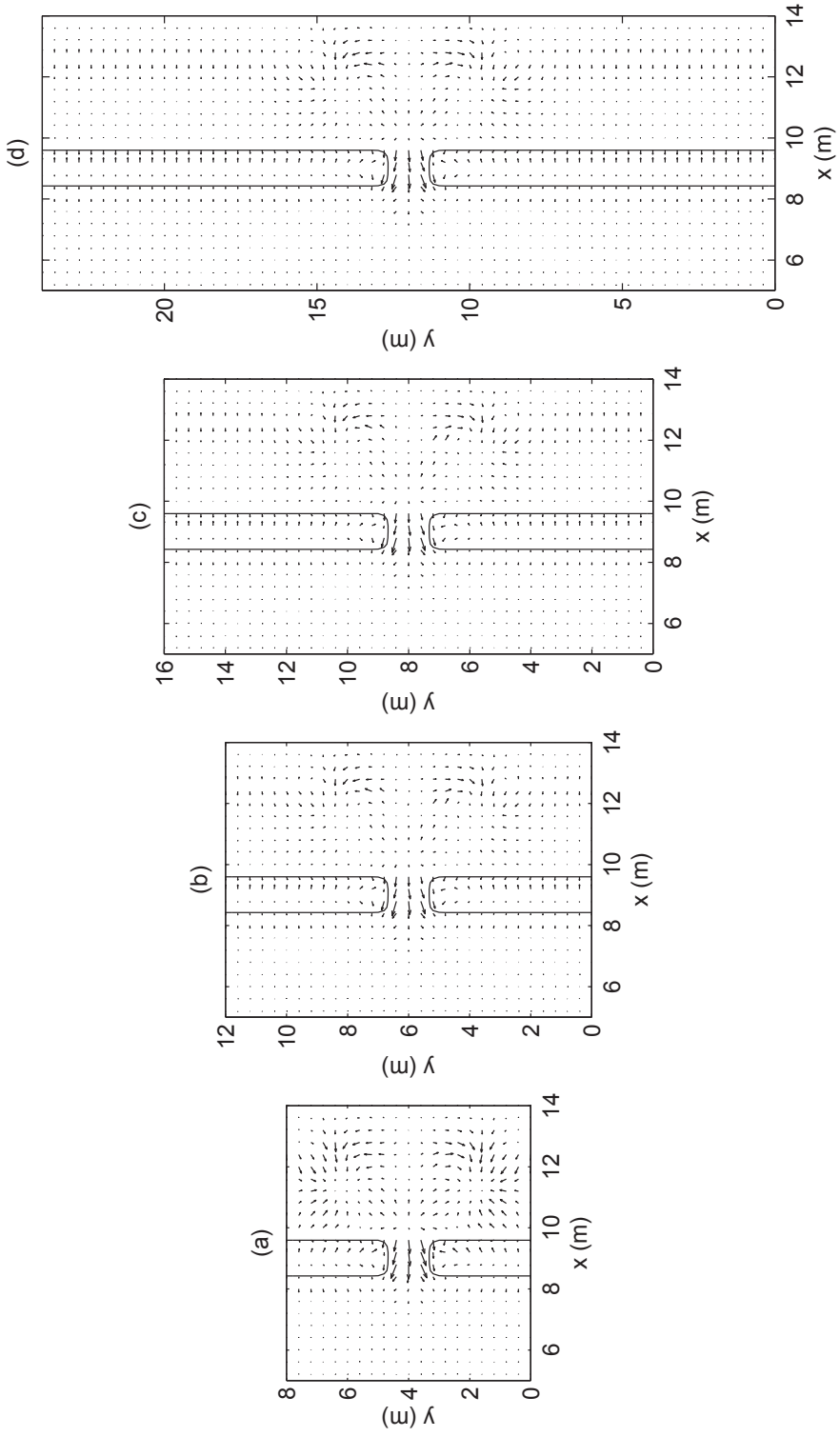

Figure 6.21: The effect of rip spacing on the residual forcing R_α for $L_s/L_c = 2.5$ where (a) $L_B/L_c = 4$, (b) $L_B/L_c = 6$, (c) $L_B/L_c = 8$ and (d) $L_B/L_c = 12$. $L_s/L_c = 2.5$.

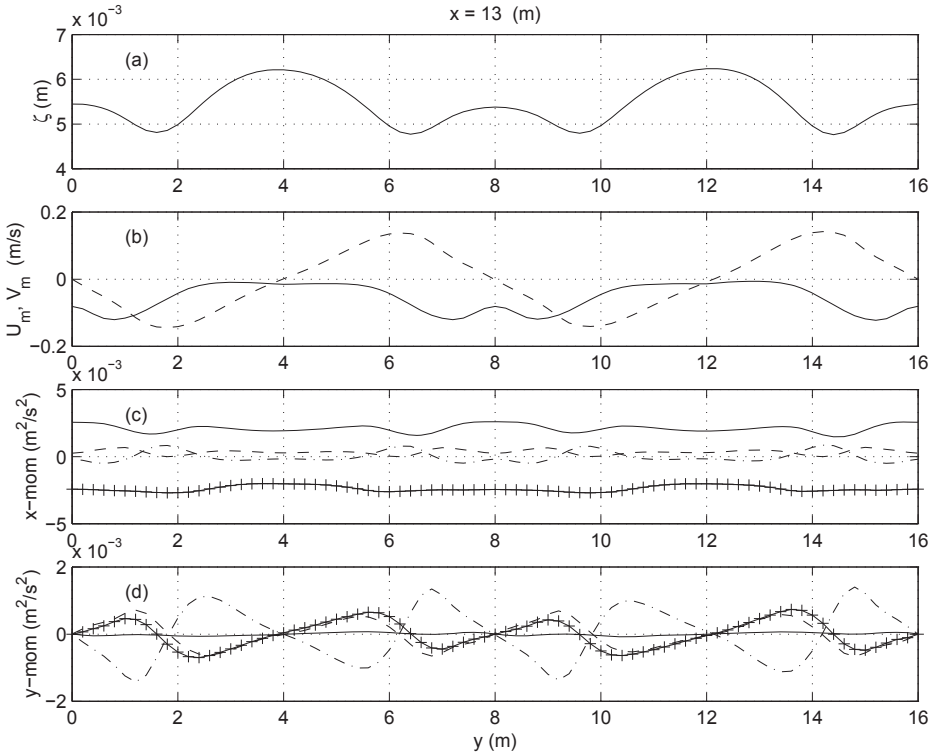

Figure 6.22: The longshore variation 1 m seaward of the shoreline ($x = 13$ m) for $L_B/L_c = 4$ of (a) ζ, (b) (-) U_m and (- -) V_m, (c) cross-shore momentum balance with (-) $\frac{\partial S_{x\beta}}{\partial x_\beta}$, (- -) $\frac{\partial Q_x^2}{\partial x}$, (-.) $\frac{\partial Q_x Q_y}{\partial y}$ and (+) $\frac{\partial \overline{\zeta}}{\partial x}$ and (d) longshore momentum with (-) $\frac{\partial S_{y\beta}}{\partial x_\beta}$, (-.) $\frac{\partial Q_y^2}{\partial y}$, (- -) $\frac{\partial Q_x Q_y}{\partial x}$ and (+) $\frac{\partial \overline{\zeta}}{\partial y}$. The channels are centered about $y = 4$ m and $y = 12$ m.

region behind the bar, local residuals exist providing the driving force for the recirculation cells. The large setup behind the channel creates a longshore pressure gradient, which is not balanced by any radiation stress, and hence is driving the flow outwards. An adverse pressure gradient causes the flow to decelerate and turn away from the shoreline as seen in the flow patterns in Figure 6.13. As the flow approaches the bar, the longshore pressure gradient drives the flow toward the channel and into the rip.

The nonlinear convective forces play an important role in the rip and trough region. Figure 6.22 shows the balance of the relevant momentum terms for the flow pattern shown in Figure 6.13a of (c) the cross-shore and (d) the longshore direction near the shoreline at $x = 13$ m. The cross-shore balance is essentially between the radiation stresses and the pressure gradient with the nonlinear terms being rather small. The longshore momentum balance, however, is primarily between the pressure gradient and the convective terms while the radiation stresses are negligible. The convective terms result from deceleration and turning of the flow away from the large setup behind the rip channel.

The mean water level variation in (a) shows the large setup behind the rip channels, $y = 4$ and 12 m, which decreases in the longshore direction before increasing between the channels. The flow accelerates in the longshore direction away from the setup behind the channel. The small increase of the setup between the rip channels cause the flow to decelerate and turn offshore.

Figure 6.23 shows the momentum balances for the same situation just shoreward of the bar at $x = 10$ m. Behind the channel the primary cross-shore momentum balance is between the radiation stresses and the pressure gradient as the convective terms balance each other. On the other hand, away from the channel the radiation stresses are small and the balance is between the pressure gradient and the convective accelerations. This balance results in the seaward flow decelerating and turning towards the channels.

All the terms are important for the longshore momentum balance behind the channels whereas behind the bar the radiation stress forcing is negligible. The variation in the mean water level in (a) clearly leads to the pressure gradient which drives the flow from behind the bar towards the channels. The convective terms represent the accelerating and decelerating flow from the bar to the channel.

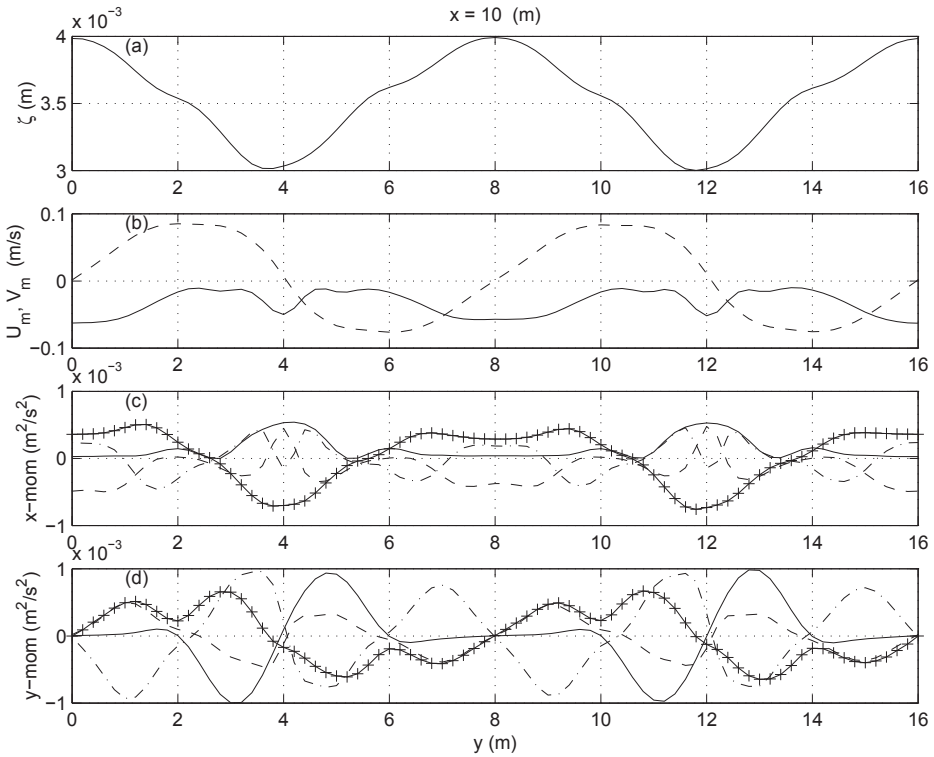

Figure 6.23: The longshore variation on the lee side of the bar ($x = 10$ m) for $L_B/L_c = 4$ of (a) ζ, (b) (-) U_m and (- -) V_m, (c) cross-shore momentum balance with (-) $\frac{\partial S_{x\beta}}{\partial x_\beta}$, (- -) $\frac{\partial Q_x^2}{\partial x}$, (-.) $\frac{\partial Q_x Q_y}{\partial y}$ and (+) $\frac{\partial \overline{\zeta}}{\partial x}$ and (d) longshore momentum with (-) $\frac{\partial S_{y\beta}}{\partial x_\beta}$, (-.) $\frac{\partial Q_y^2}{\partial y}$, (- -) $\frac{\partial Q_x Q_y}{\partial x}$ and (+) $\frac{\partial \overline{\zeta}}{\partial y}$. The channels are centered about $y = 4$ m and $y = 12$ m.

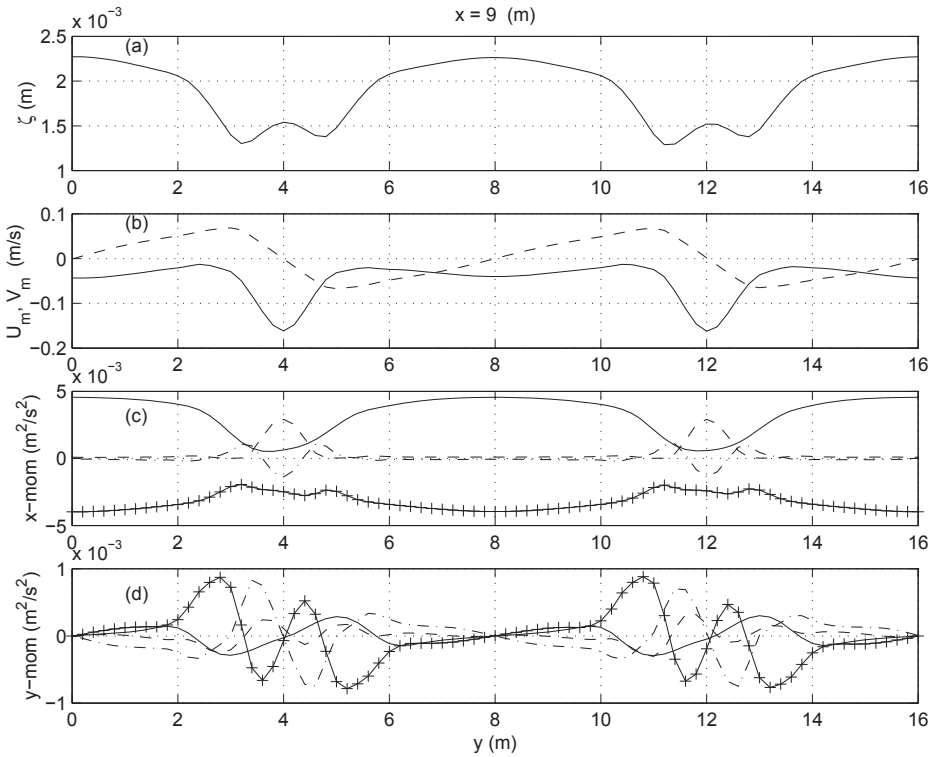

Figure 6.24: The longshore variation on the crest of the bar ($x = 9$ m) for $L_B/L_c = 4$ of (a) ζ, (b) (-) U_m and (- -) V_m, (c) cross-shore momentum balance with (-) $\frac{\partial S_{x\beta}}{\partial x_\beta}$, (- -) $\frac{\partial Q_x^2}{\partial x}$, (-.) $\frac{\partial Q_x Q_y}{\partial y}$ and (+) $\frac{\partial \overline{\zeta}}{\partial x}$ and (d) longshore momentum with (-) $\frac{\partial S_{y\beta}}{\partial x_\beta}$, (-.) $\frac{\partial Q_y^2}{\partial y}$, (- -) $\frac{\partial Q_x Q_y}{\partial x}$ and (+) $\frac{\partial \overline{\zeta}}{\partial y}$. The channels are centered about $y = 4$ m and $y = 12$ m.

Similar longshore sections on the crest of the bar ($x = 9$ m) are shown in Figure 6.24. Here the cross-shore momentum is a simple balance between the pressure and radiation stress over the bar and between the pressure and the convective terms in the channel. The radiation stresses are large over the bar due to the short-wave breaking but in the channel, they are virtually zero. The convective terms represent the turning of the flow from the feeder currents to the rip and the accelerating of the flow seawards out the channel. The acceleration of the flow in the rip is driven by the large pressure gradient in the channel.

The longshore momentum balance looks more complicated with all terms contributing to the balance. The pressure gradient is best understood by examining the mean water variation in (a). The setup is largest over the bar and decreases toward the channel, however, the water level is increased slightly in the center of the rips. The decrease in $\overline{\zeta}$ from the bar to the channel drives the feeder currents and is balanced by the acceleration terms. In the rip channel, the feeder currents decelerate rapidly and turn, leading to large convective terms which are balanced by the adverse pressure gradient.

The influence of the rip spacing on the momentum balance is established by Figures 6.25 to 6.27. These figures show the momentum balances for the larger channel spacing $L_B/L_c = 8$ with the flow patterns shown in Figure 6.13c. The cross-shore momentum balance in the recirculation cells close to the shoreline in Figure 6.25 is similar to the balance in Figure 6.22. Although, between the channels for the larger rip spacing the balance essentially becomes longshore uniform. Similarly, the longshore balance in the recirculation cells is essentially unchanged while between the rips there is no longshore momentum.

Figures 6.26 and 6.27 and shows the momentum balances for $L_B/L_c = 8$, 1 m shoreward of and on the crest of the bar, respectively. In both of these figures the nonlinear terms are only important in the immediate vicinity of the channel.

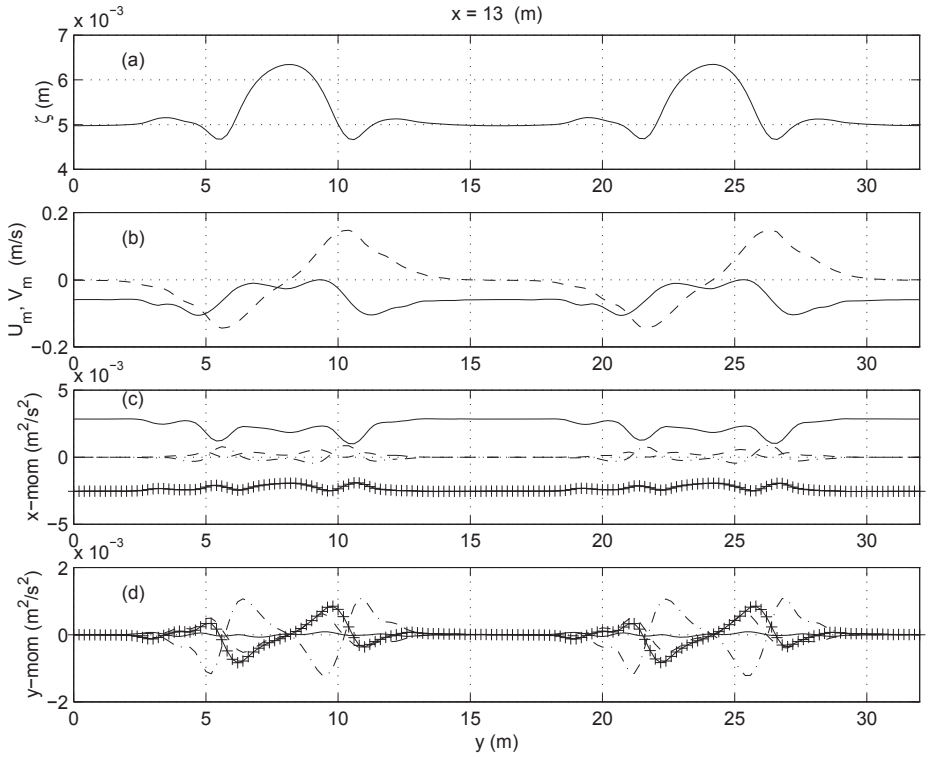

Figure 6.25: The longshore variation 1 m seaward of the shoreline ($x = 13$ m) for $L_B/L_c = 8$ of (a) ζ, (b) (-) U_m and (- -) V_m, (c) cross-shore momentum balance with (-) $\frac{\partial S_{x\beta}}{\partial x_\beta}$, (- -) $\frac{\partial Q_x^2}{\partial x}$, (-.) $\frac{\partial Q_x Q_y}{\partial y}$ and (+) $\frac{\partial \overline{\zeta}}{\partial x}$ and (d) longshore momentum with (-) $\frac{\partial S_{y\beta}}{\partial x_\beta}$, (-.) $\frac{\partial Q_y^2}{\partial y}$, (- -) $\frac{\partial Q_x Q_y}{\partial x}$ and (+) $\frac{\partial \overline{\zeta}}{\partial y}$. The channels are centered about $y = 8$ m and $y = 24$ m.

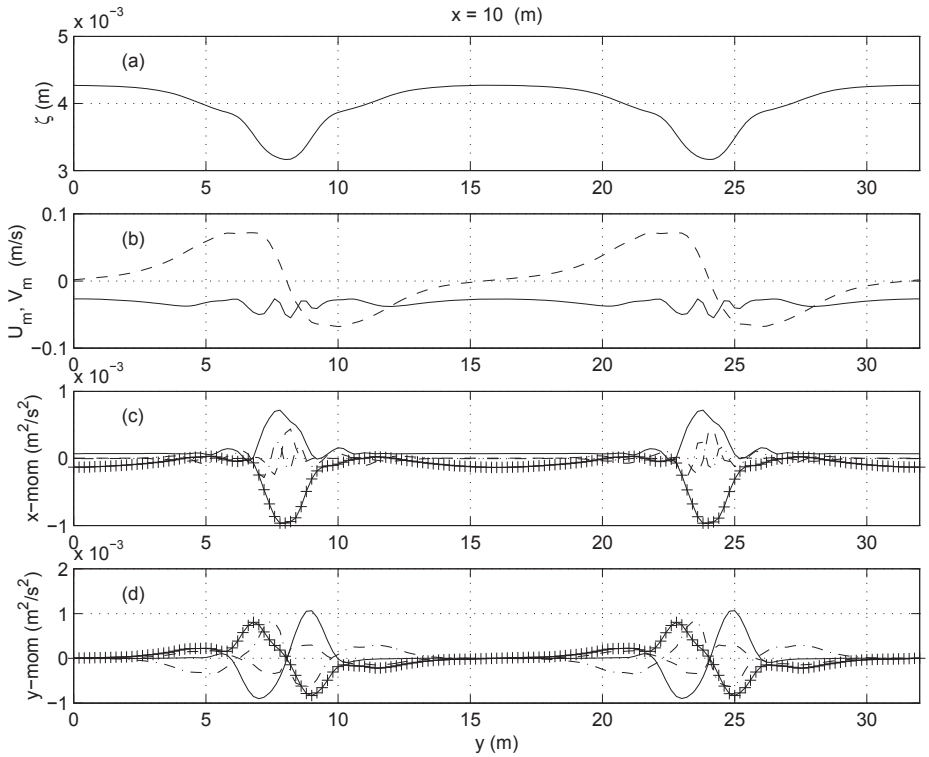

Figure 6.26: The longshore variation on the lee side of the bar ($x = 10$ m) for $L_B/L_c = 8$ of (a) ζ, (b) (-) U_m and (- -) V_m, (c) cross-shore momentum balance with (-) $\frac{\partial S_{x\beta}}{\partial x_\beta}$, (- -) $\frac{\partial Q_x^2}{\partial x}$, (-.) $\frac{\partial Q_x Q_y}{\partial y}$ and (+) $\frac{\partial \overline{\zeta}}{\partial x}$ and (d) longshore momentum with (-) $\frac{\partial S_{y\beta}}{\partial x_\beta}$, (-.) $\frac{\partial Q_y^2}{\partial y}$, (- -) $\frac{\partial Q_x Q_y}{\partial x}$ and (+) $\frac{\partial \overline{\zeta}}{\partial y}$. The channels are centered about $y = 8$ m and $y = 24$ m.

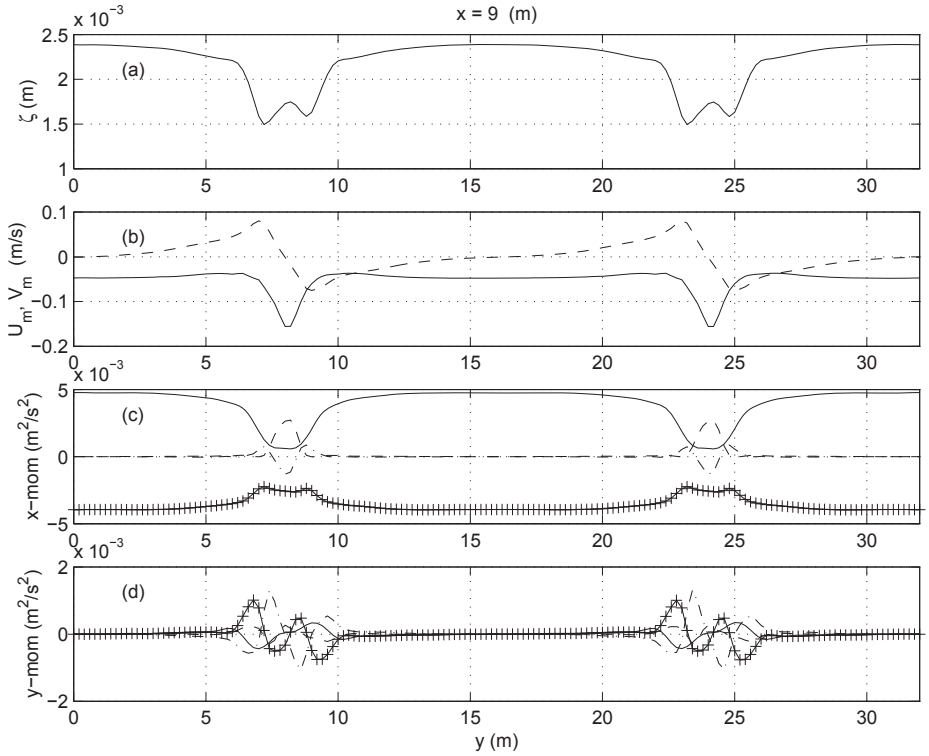

Figure 6.27: The longshore variation on the crest of the bar ($x = 9$ m) for $L_B/L_c = 8$ of (a) ζ, (b) (-) U_m and (- -) V_m, (c) cross-shore momentum balance with (-) $\frac{\partial S_{x\beta}}{\partial x_\beta}$, (- -) $\frac{\partial Q_x^2}{\partial x}$, (-.) $\frac{\partial Q_x Q_y}{\partial y}$ and (+) $\frac{\partial \overline{\zeta}}{\partial x}$ and (d) longshore momentum with (-) $\frac{\partial S_{y\beta}}{\partial x_\beta}$, (-.) $\frac{\partial Q_y^2}{\partial y}$, (- -) $\frac{\partial Q_x Q_y}{\partial x}$ and (+) $\frac{\partial \overline{\zeta}}{\partial y}$. The channels are centered about $y = 8$ m and $y = 24$ m.

Farther away from the channel the balance is strictly between the pressure gradient and the radiation stress in the cross-shore. The rip channels only have a local effect on the overall momentum of the nearshore circulation.

The effect of the rip channel spacing is summarized as follows:

- The channel spacing has little influence on the total flow in the rip current.
- The spacing controls the amount of flow passing over the bar as undertow.

- Once the channel spacing is sufficiently large, it has no influence on the size of the recirculation cells.

Therefore, we conclude that channel spacing has little local effect on the flow in and around the rip currents. The spacing only affects the large scale flow properties such as the percentage of flow passing over the bar as undertow.

6.2.2.2 Varying Bar Distance from the Shoreline

Figure 6.28 shows vectors of the radiation stress forcing for the flow conditions shown in Figure 6.13 and 6.15. The radiation stress over the bar is similar for all cases, however, the cross-shore width of the reduced forcing from the non-breaking waves between the bar and the shoreline is shrunk for smaller L_s/L_c. Behind the channel, for $L_s/L_c = 1.5$ shown in (a) and (b), the radiation stress forcing becomes large because the waves begin breaking in the decreasing depth due to the proximity of the shoreline. The longshore variation in the short-wave forcing is much smaller when the shoreline is closer to the bar.

The pressure gradient vectors are shown in Figure 6.29 for the same six geometries. When $L_s/L_c = 1.5$, (a) and (b), the longshore pressure gradient is much smaller than when $L_s/L_c = 2.5$, (e) and (f). This is a direct result of the smaller longshore variations of the radiation stress forcing. The pressure gradient in the seaward half of the channel is still unbalanced by the radiation stress, thereby driving the rip current offshore.

Finally, in Figure 6.30 the forcing residual R_α is shown. The forcing for the rip current in the channel remains similar for all shoreline positions. However, the forcing for the circulation in the trough behind the bar is weakened when the shoreline is closer to the bar. The strength of the recirculation cells is very sensitive to the location of the bar relative to the shoreline.

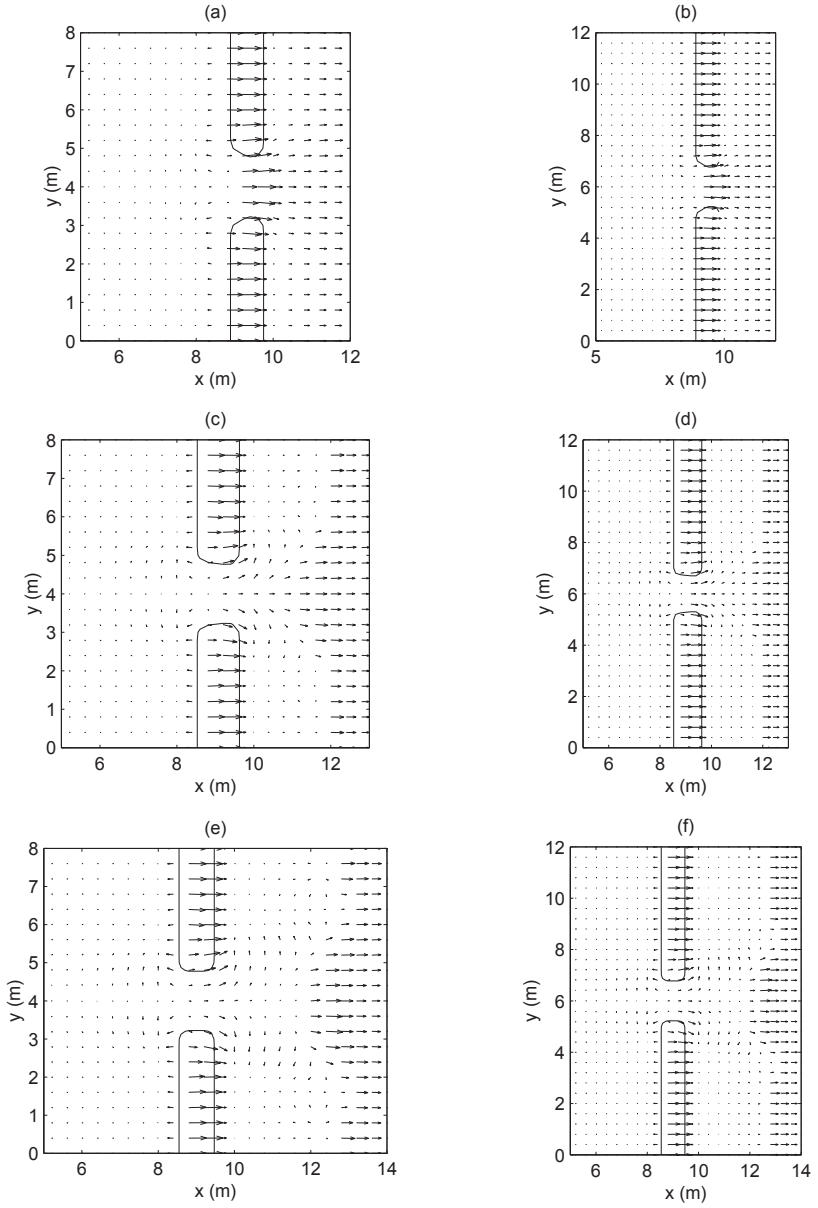

Figure 6.28: The effect of L_s/L_c on the radiation stress forcing with the top row ((a) and (b)) $L_s/L_c = 1.5$, the middle row ((c) and (d)) $L_s/L_c = 2.0$ and the bottom row ((e) and (f)) $L_s/L_c = 2.5$. The left column ((a), (c) and (e)) is for $L_B/L_c = 4$ and the right column ((b), (d) and (f)) is for $L_B/L_c = 6$.

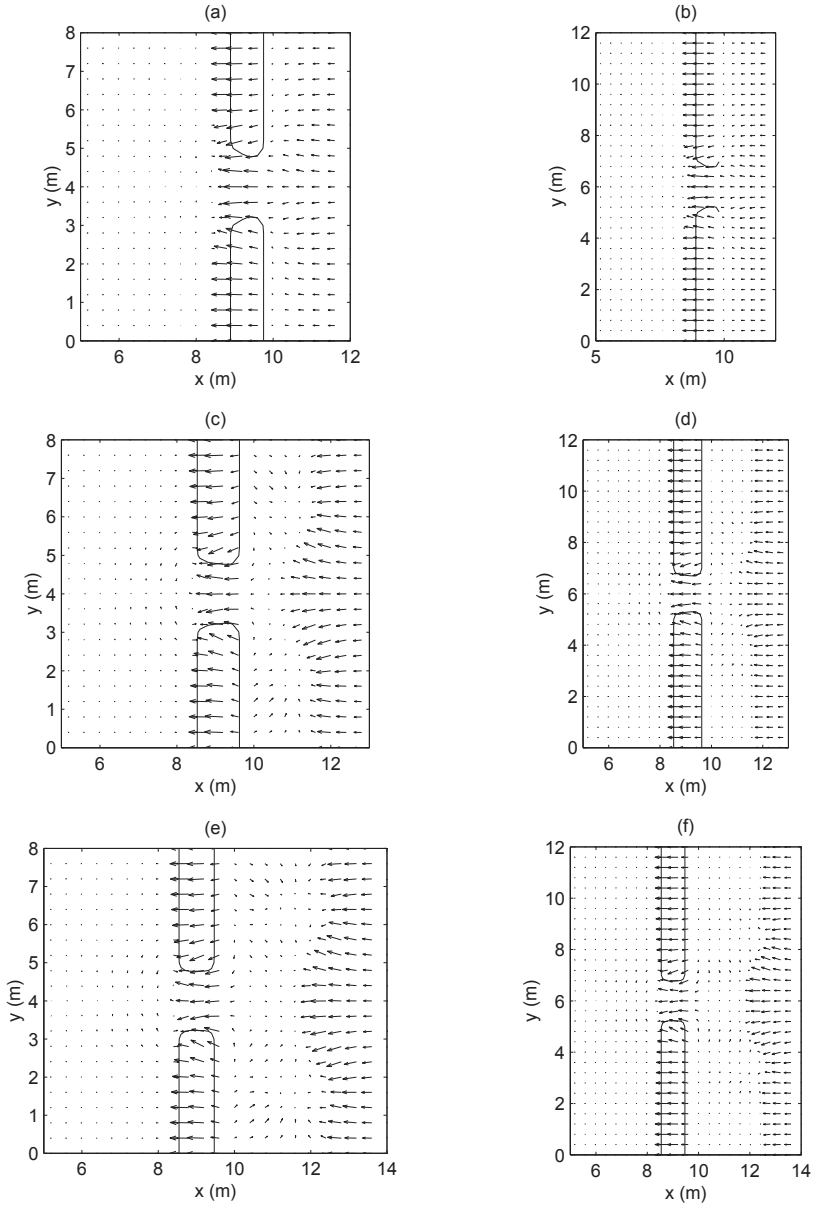

Figure 6.29: The effect of L_s/L_c on the pressure gradient with the top row ((a) and (b)) $L_s/L_c = 1.5$, the middle row ((c) and (d)) $L_s/L_c = 2.0$ and the bottom row ((e) and (f)) $L_s/L_c = 2.5$. The left column ((a), (c) and (e)) is for $L_B/L_c = 4$ and the right column ((b), (d) and (f)) is for $L_B/L_c = 6$.

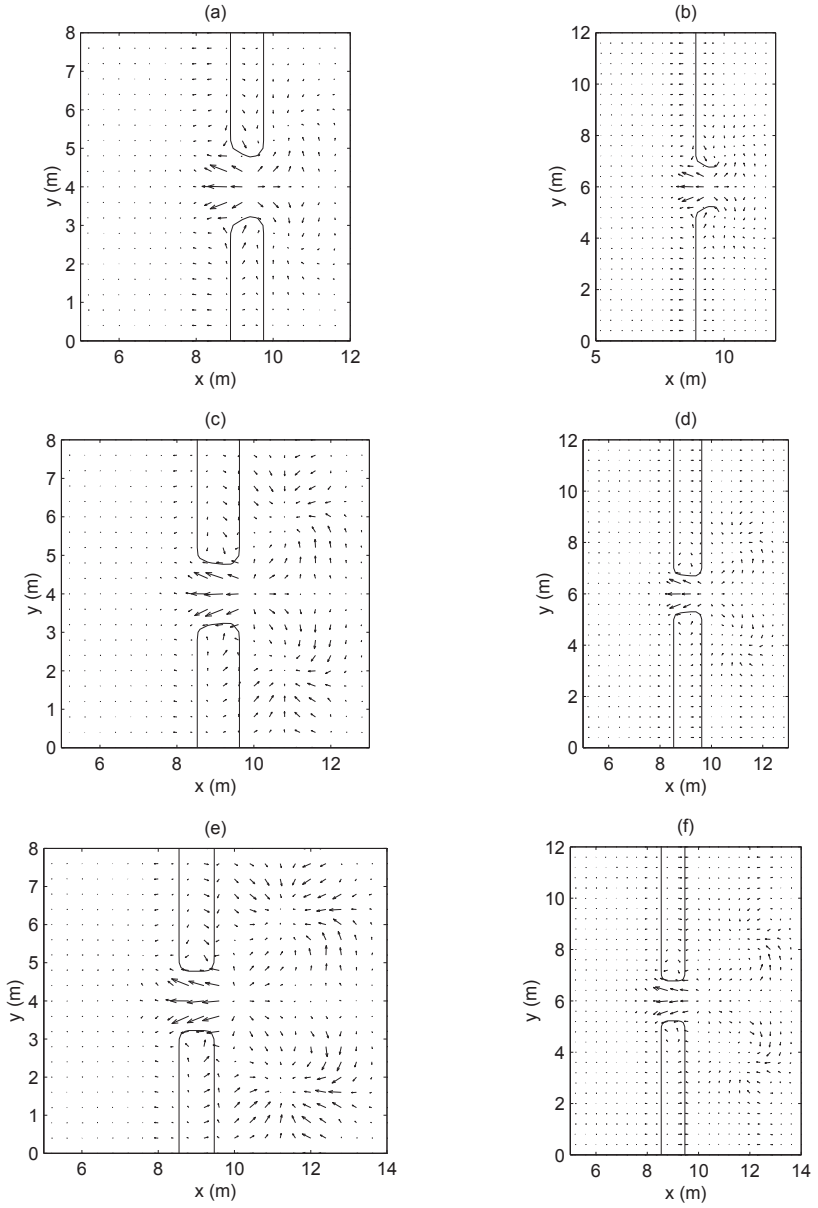

Figure 6.30: The effect of L_s/L_c on the residual forcing R_α with the top row ((a) and (b)) $L_s/L_c = 1.5$, the middle row ((c) and (d)) $L_s/L_c = 2.0$ and the bottom row ((e) and (f)) $L_s/L_c = 2.5$. The left column ((a), (c) and (e)) is for $L_B/L_c = 4$ and the right column ((b), (d) and (f)) is for $L_B/L_c = 6$.

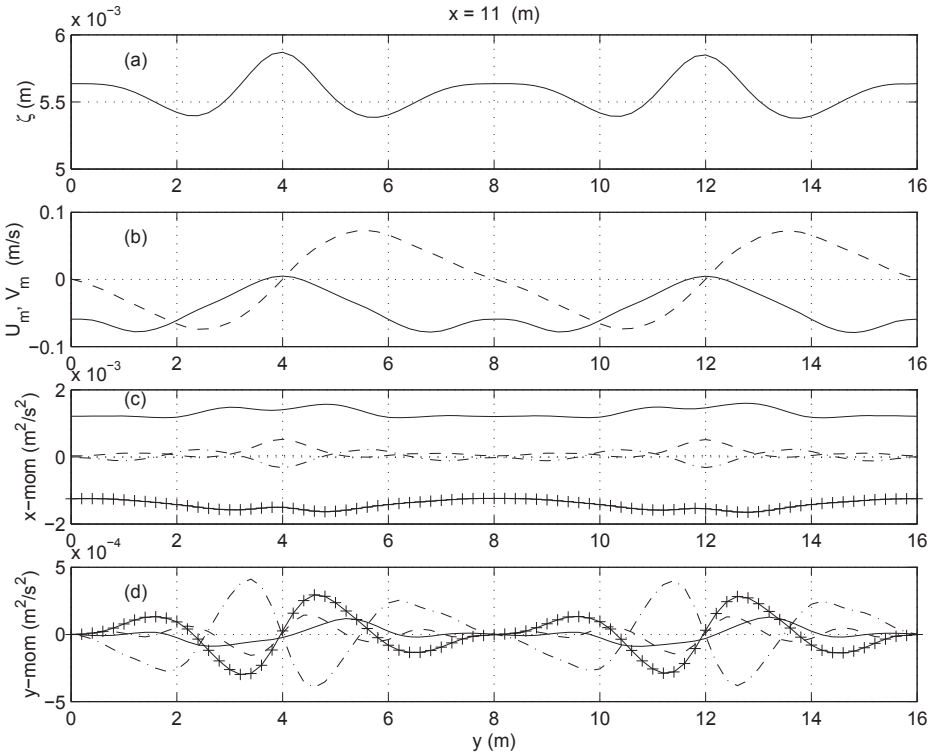

Figure 6.31: The longshore variation 1 m seaward of the shoreline ($x = 11$ m) for $L_B/L_c = 4$ and $L_s/L_c = 1.5$ of (a) ζ, (b) (-) U_m and (- -) V_m, (c) cross-shore momentum balance with (-) $\frac{\partial S_{x\beta}}{\partial x_\beta}$, (- -) $\frac{\partial Q_x^2}{\partial x}$, (-.) $\frac{\partial Q_x Q_y}{\partial y}$ and (+) $\frac{\partial \overline{\zeta}}{\partial x}$ and (d) longshore momentum with (-) $\frac{\partial S_{y\beta}}{\partial x_\beta}$, (-.) $\frac{\partial Q_y^2}{\partial y}$, (- -) $\frac{\partial Q_x Q_y}{\partial x}$ and (+) $\frac{\partial \overline{\zeta}}{\partial y}$. The channels are centered about $y = 4$ m and $y = 12$ m. The effect of the position of the bar relative to the shoreline is seen by comparing with Figure 6.22

Figure 6.31 shows the longshore variation of the setup, velocities and momentum balances at $x = 11$ m, 1 m seaward of the shoreline for $L_s/L_c = 1.5$. A direct comparison can be made with Figure 6.22 where the bar is located farther from the shoreline ($L_s/L_c = 2.5$). Inspection of the setup and currents reveals that the water level is lower and the longshore velocity is reduced for the closer shoreline. The cross-shore momentum balance is still between the pressure and radiation stress although both are much smaller. The longshore momentum balance is similar in shape although the magnitudes are smaller. As a result of the reduced forcing, the convective terms and the longshore pressure gradient do not extend quite as far out from the channels.

Similarly, Figure 6.32 is for a section over the crest of the bar. The setup over the bar is virtually the same as in Figure 6.24 because the forcing is nearly identical. The cross-shore velocity, however, is larger over the bar and smaller in the rip current. This is a direct result of the extra flow passing over the bar as undertow reducing the flow in the rip. Because of the reduced flow in the rip, the cross-shore convective terms in the channel are also reduced. The longshore momentum balance is nearly unchanged because the longshore variation of the forcing is virtually the same.

The impact of the shoreline being closer to the channel is best summarized by the following sequence:

1. When the bar is close to the shoreline, as seen in Figure 6.13a, some of the flow in the recirculation cells do not turn and feed the rip but passes over the bar.

2. Because more flow is passing over the bar as undertow for the reduced distance between the bar and shoreline, the flow in the rip is reduced.

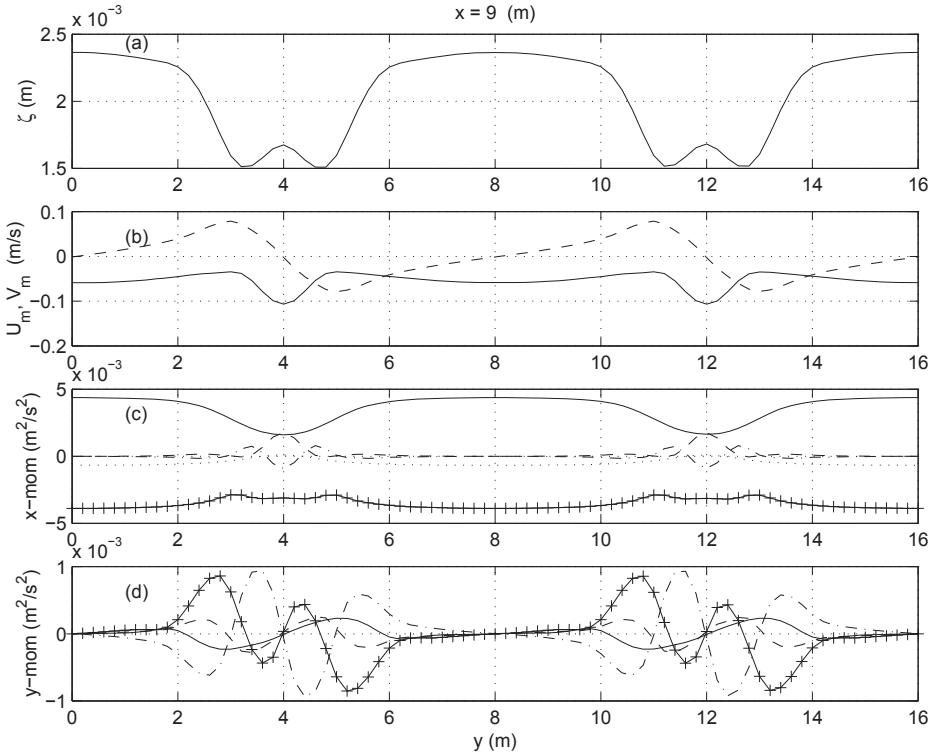

Figure 6.32: The longshore variation on the crest of the bar ($x = 9$ m) for $L_B/L_c = 4$ and $L_s/L_c = 1.5$ of (a) ζ, (b) (-) U_m and (- -) V_m, (c) cross-shore momentum balance with (-) $\frac{\partial S_{x\beta}}{\partial x_\beta}$, (- -) $\frac{\partial Q_x^2}{\partial x}$, (-.) $\frac{\partial Q_x Q_y}{\partial y}$ and (+) $\frac{\partial \overline{\zeta}}{\partial x}$ and (d) longshore momentum with (-) $\frac{\partial S_{y\beta}}{\partial x_\beta}$, (-.) $\frac{\partial Q_y^2}{\partial y}$, (- -) $\frac{\partial Q_x Q_y}{\partial x}$ and (+) $\frac{\partial \overline{\zeta}}{\partial y}$. The channels are centered about $y = 4$ m and $y = 12$ m. The effect of the position of the bar relative to the shoreline is seen by comparing with Figure 6.24

3. Smaller currents in the rip mean less current diffraction resulting in smaller wave heights in the channel.

4. Smaller waves produce reduced forcing and less setup behind the channel at the shoreline.

5. Less setup behind the channel means a smaller longshore pressure gradient and therefore reduced driving forces for the recirculation cells.

6. Reduced driving forcing leads to less flow in the recirculation cells thereby reducing the inertia which must be overcome to turn the flow away from the shoreline.

7. Less inertia means the flow in the recirculation cells turn over a shorter distance resulting in smaller recirculation cells.

It is seen that the proximity of the bar relative to the shoreline affects the local forcing, hence, the flow in the rip and the recirculation cells are affected.

6.3 Varying Wave Conditions

The previous sections establish the influence of the topography on rip current systems. On a real coastline the wave conditions vary, therefore, this section looks at the effect of different wave conditions on the circulation, specifically, changes in the breaking pattern and short-wave angles.

If the waves break in the rip channel, large cross-shore gradients of radiation stress are created there, which reduce the residual forcing and hence the driving force for the rip currents. Similarly, if the waves do not break over the bar or in the channel (for example, during high tide the increased water level decreases the breaking over the bar) the longshore variation and therefore the residual forcing is reduced. Rip current flow patterns are also sensitive to the wave angle; larger angles drive more longshore current which significantly alters the circulation.

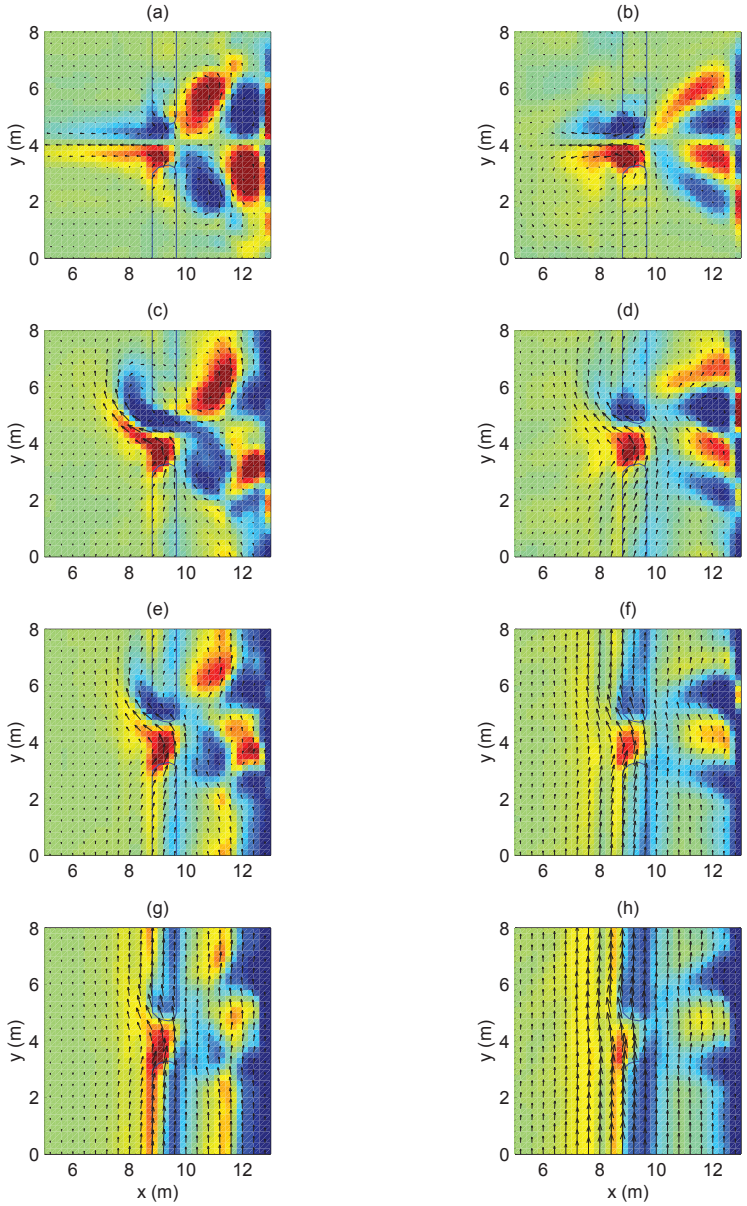

Figure 6.33: Vorticity and velocity vectors for different offshore wave angles: (a) and (b) $\theta = 0$, (c) and (d) $\theta = 5$, (e) and (f) $\theta = 10$, (g) and (h) $\theta = 20$. The left column shows cases with no breaking in the channel and the right column shows cases with breaking in the channel.

Figure 6.33 shows rip currents on a sloping beach with a longshore bar and rip channel for different incident wave angles and with and without breaking in the channel. When the waves break in the channels, the right column, the longshore pressure gradient is reduced which greatly reduces the strength of the circulation in the trough between the bar and shoreline. Hence the feeder currents for the rip are reduced, leading to a decrease in the strength of the rip current.

The effect from obliquely incident waves is clear when comparing the rows in Figure 6.33. As the angle of incidence for the short waves increases, a longshore current is formed, which for small angles turn the rips in the downstream direction, and for large angles may have sufficient inertia to pass over the rip channel and suppress the rip current completely [(f), (g), and (h) in the figure].

Vectors of the radiation stress forcing are shown in Figure 6.34. When the waves are not breaking in the channel, (a), (c), (e) and (g), the gradient of the radiation stress is weak inside the entrance of the channel. Although, in (a), the radiation stress forcing is stronger in the back half of the channel because the rip is stronger for the normal incident waves than for the oblique incident waves leading to larger waves which break earlier on the sloping beach. In contrast, the radiation stress forcing when the waves are breaking in the channel is only slightly reduced in the channel compared to the breaking over the bar due to the greater depth in the channel. The angle of the waves is represented the angle of the radiation stress.

Figure 6.35 shows the pressure gradient vectors for the same cases. For normally incident waves, (a) and (b), the pressure gradient is nearly uniform between the bar and channel. For the incident angle cases without breaking in the channel, the cross-shore pressure gradient is progressively weaker for larger angles of incidence. This pressure gradient is the driving force for the rip current and the weaker gradients lead to weaker rips. Contrarily, when the waves break in the channel, the pressure gradient is nearly the same over the bar and in the channel, and is

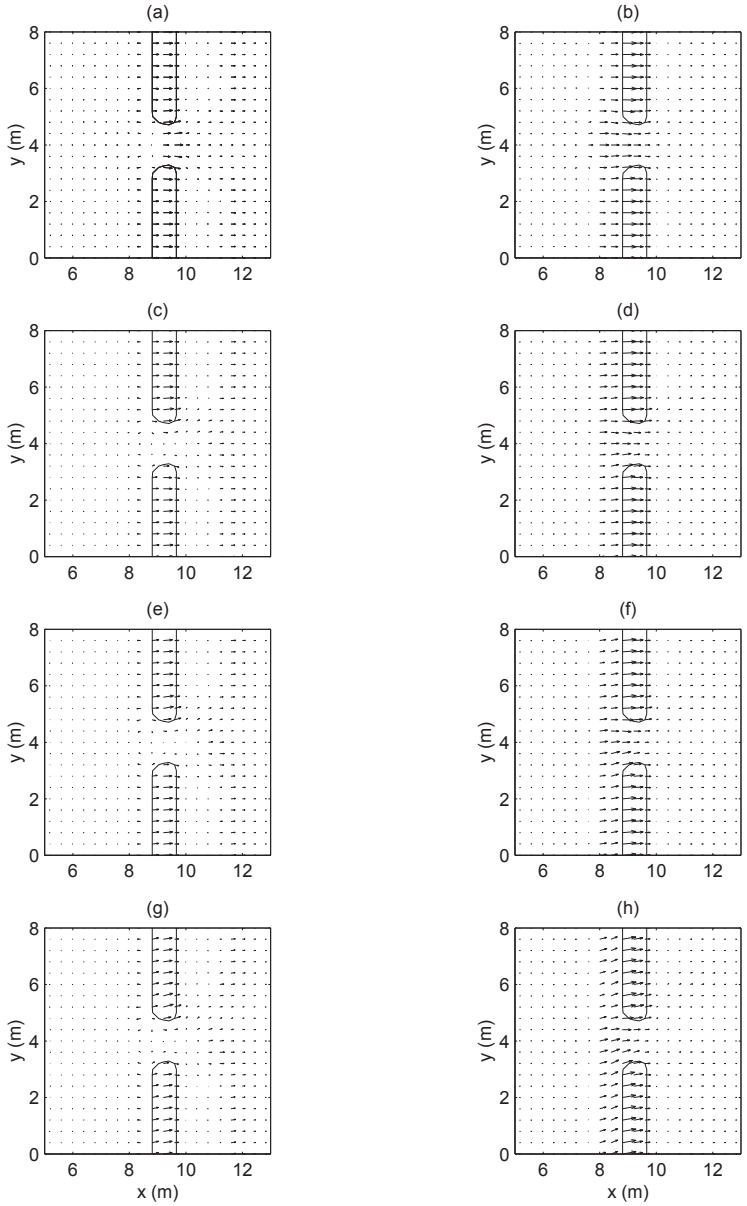

Figure 6.34: The radiation stress forcing for the flow conditions in Figure 6.33: (a) and (b) $\theta = 0$, (c) and (d) $\theta = 5$, (e) and (f) $\theta = 10$, (g) and (h) $\theta = 20$. The left column shows cases with no breaking in the channel and the right column shows cases with breaking in the channel.

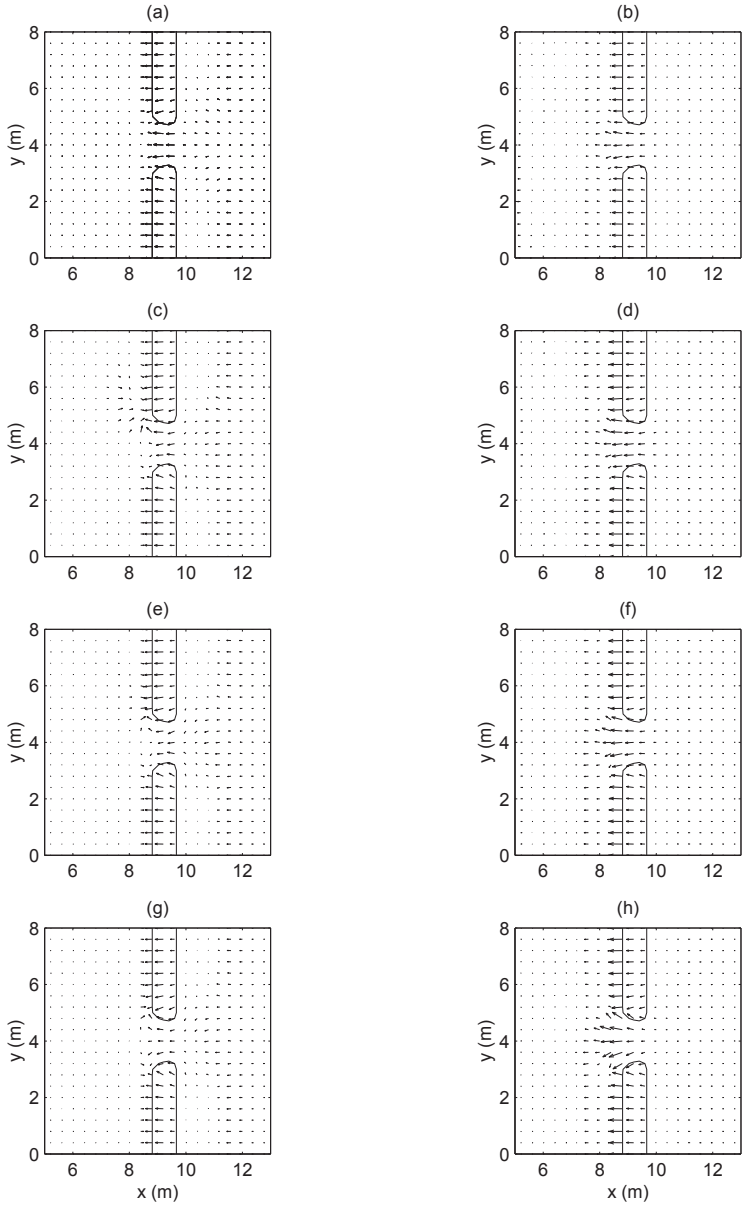

Figure 6.35: The pressure gradient for the flow conditions in Figure 6.33: (a) and (b) $\theta = 0$, (c) and (d) $\theta = 5$, (e) and (f) $\theta = 10$, (g) and (h) $\theta = 20$. The left column shows cases with no breaking in the channel and the right column shows cases with breaking in the channel.

non-existent behind the bar.

Figure 6.36 shows the forcing residual R_α for the eight cases.

The case with normally incident waves without breaking in the channel (a) has large forcing in the channel for the rip currents as well as forcing behind the bar for the recirculation cells. On the other hand, the case with normally incident waves breaking in the channel only has weak forcing in the channel and none behind the bar.

For the cases with wave angles of 5 and 10 degrees and no breaking in the channel, (c) and (e), the residual in the channel is large and non-symmetric. Inspection of (d) and (f) reveals that the when the waves break in the channel, the residual forcing has weaker longshore variations, although the forcing in the channel is still larger than the forcing over the bar.

The forcing for the largest wave angle (f) and (g) show similar trends. However, reviewing Figure 6.33 reveals that the stronger longshore currents contain nearly enough inertia to overcome the local cross-shore forcing in the channel resulting in only the slightest deviation from longshore uniform currents.

Figures 6.37 and 6.38 show the longshore variations of the setup, velocities and the momentum balances for sections across the crest of the bars from the simulations with $\theta = 5$ and $\theta = 20$ respectively. The longshore velocity for the small angle (dashed line in Figure 6.37b) changes sign across the channel because it is feeding the rip. The longshore velocity for the large angle (dashed line in Figure 6.38b), however, is much stronger and does not change sign and is essentially acting as longshore current. The cross-shore current for the small angle (solid line in Figure 6.37b) shows a strong offshore rip while the cross-shore current for the larger angle (solid line in Figure 6.38b) shows a weak rip.

The cross-shore momentum balances for the two wave angles are virtually identical. The only difference is that the inertial term $\frac{\partial Q_x^2}{\partial x}$ is much weaker for the

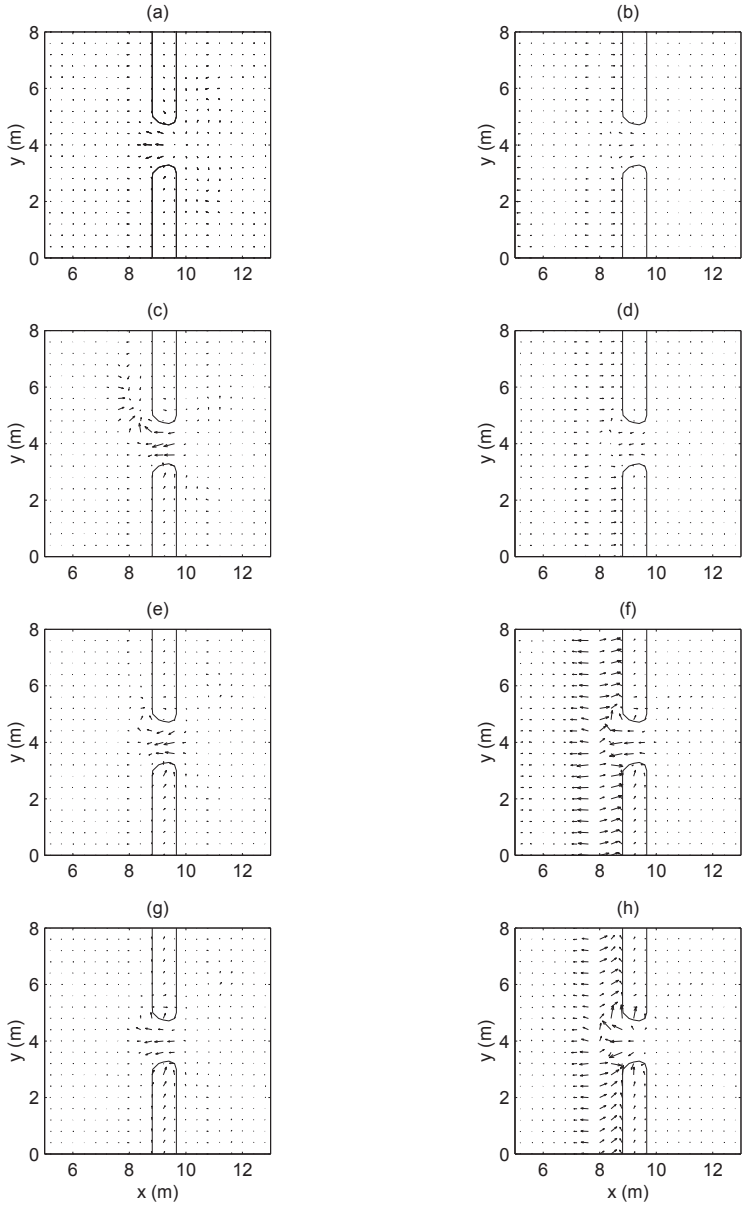

Figure 6.36: The forcing residual R_α for the flow conditions in Figure 6.33: (a) and (b) $\theta = 0$, (c) and (d) $\theta = 5$, (e) and (f) $\theta = 10$, (g) and (h) $\theta = 20$. The left column shows cases with no breaking in the channel and the right column shows cases with breaking in the channel.

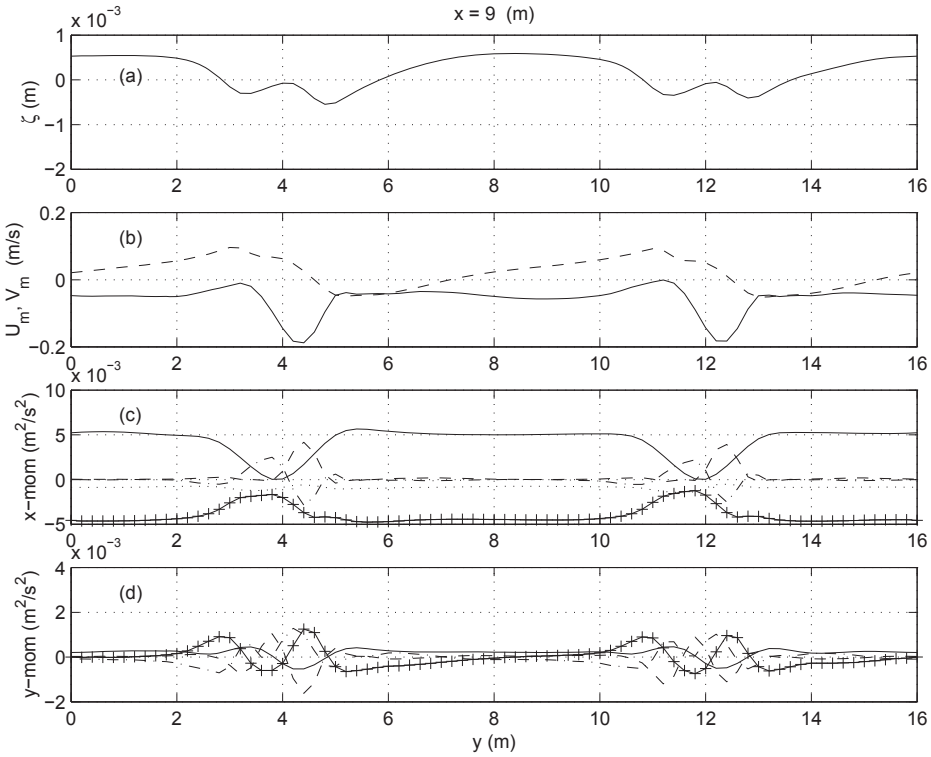

Figure 6.37: The longshore variation on the crest of the bar ($x = 9$ m) for the offshore $\theta = 5$ of (a) ζ, (b) (-) U_m and (- -) V_m, (c) cross-shore momentum balance with (-) $\frac{\partial S_{x\beta}}{\partial x_\beta}$, (- -) $\frac{\partial Q_x^2}{\partial x}$, (-.) $\frac{\partial Q_x Q_y}{\partial y}$ and (+) $\frac{\partial \overline{\zeta}}{\partial x}$ and (d) longshore momentum with (-) $\frac{\partial S_{y\beta}}{\partial x_\beta}$, (-.) $\frac{\partial Q_y^2}{\partial y}$, (- -) $\frac{\partial Q_x Q_y}{\partial x}$ and (+) $\frac{\partial \overline{\zeta}}{\partial y}$. The channels are centered about $y = 4$ m and $y = 12$ m.

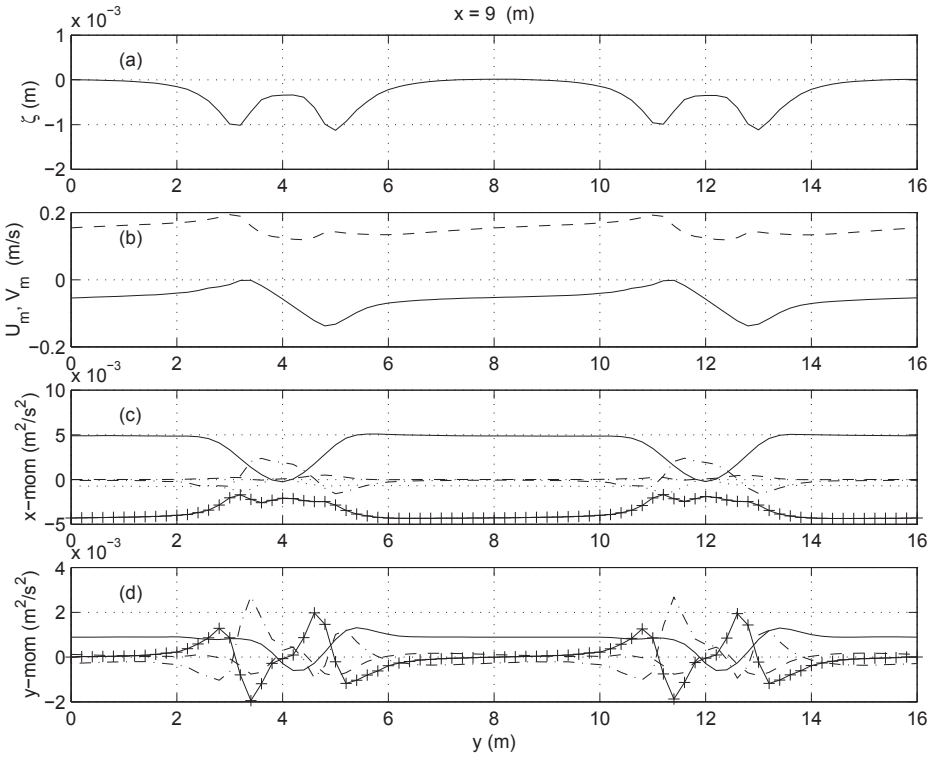

Figure 6.38: The longshore variation on the crest of the bar ($x = 9$ m) for the offshore $\theta = 20$ of (a) ζ, (b) (-) U_m and (- -) V_m, (c) cross-shore momentum balance with (-) $\frac{\partial S_{x\beta}}{\partial x_\beta}$, (- -) $\frac{\partial Q_x^2}{\partial x}$, (-.) $\frac{\partial Q_x Q_y}{\partial y}$ and (+) $\frac{\partial \overline{\zeta}}{\partial x}$ and (d) longshore momentum with (-) $\frac{\partial S_{y\beta}}{\partial x_\beta}$, (-.) $\frac{\partial Q_y^2}{\partial y}$, (- -) $\frac{\partial Q_x Q_y}{\partial x}$ and (+) $\frac{\partial \overline{\zeta}}{\partial y}$. The channels are centered about $y = 4$ m and $y = 12$ m.

larger wave angle (dashed line in Figure 6.38c) because the weaker rip has little cross-shore acceleration. In the longshore momentum balance, the radiation stress is much larger for the larger angle (solid line in Figure 6.38d) which is not balanced by the longshore pressure gradient (pluses) resulting in a longshore current. Because of the larger longshore current, the inertial term $\frac{\partial Q_y^2}{\partial y}$ (dash dot) is larger in Figure 6.38d. The longshore pressure gradient is not sufficient to reverse the flow for the large wave angle case, therefore, only flow from the upstream side of the channel feeds the rip. The longshore pressure gradient for the small wave angle case (pluses in Figure 6.37d) is sufficient to reverse the weaker flow, hence the change in direction for the longshore current. The rip for the smaller wave simulation is fed from both directions although the feeder currents on the upstream side are larger and the rip turns in the downstream direction.

Figures 6.39 and 6.40 show the longshore variations of the setup, velocities and the momentum balances for sections 1 m offshore of the bars from the simulations with $\theta = 5$ and $\theta = 20$ respectively. It is immediately obvious that the flow for the larger wave angle case (Figure 6.40) is much more longshore uniform than the flow for the smaller wave angle case (Figure 6.39). The setdown in the Figure 6.40a shows little longshore variation whereas the setdown in Figure 6.39a has strong variations from the rips. The current for the small wave angle in Figure 6.39b shows strong longshore and cross-shore currents localized near the rips only. In contrast, the current for the large wave angle case shown in Figure 6.40b has strong but nearly uniform longshore currents and weak offshore currents near the channels.

The cross-shore and longshore momentum balances for the small wave angle case (Figure 6.39)c and d) show large inertial terms from the turning of the rip current in the downstream direction. The momentum balances for the large angle case in Figure 6.40)c and d shows virtually no inertial terms because there is only

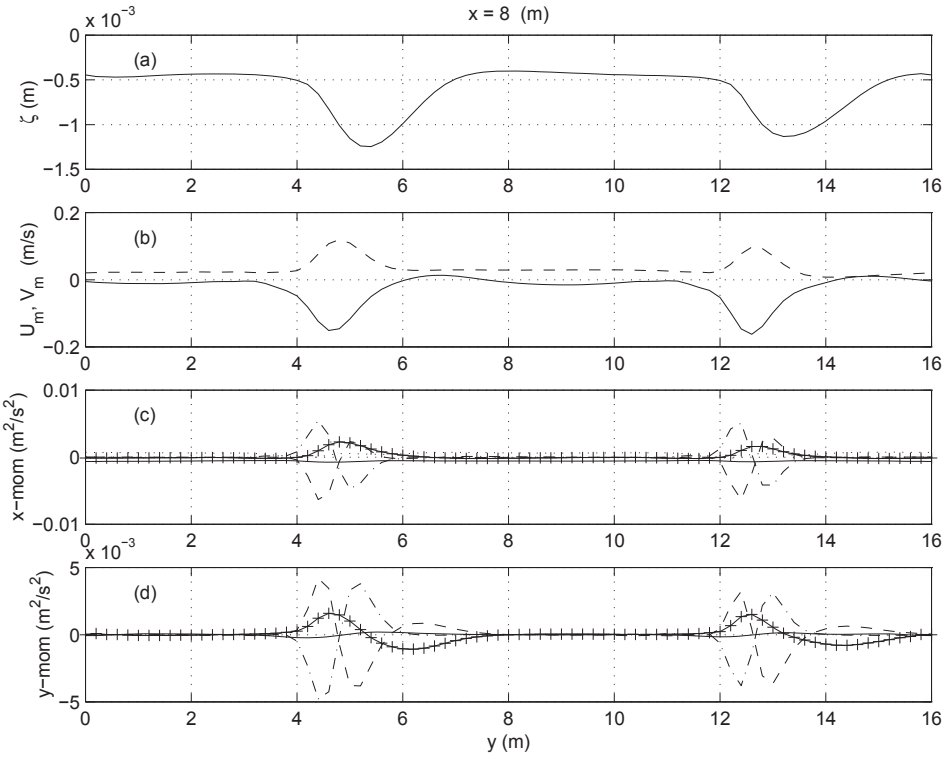

Figure 6.39: The longshore variation 1 m offshore of the bar ($x = 10$ m) for the offshore $\theta = 5$ of (a) ζ, (b) (-) U_m and (- -) V_m, (c) cross-shore momentum balance with (-) $\frac{\partial S_{x\beta}}{\partial x_\beta}$, (- -) $\frac{\partial Q_x^2}{\partial x}$, (-.) $\frac{\partial Q_x Q_y}{\partial y}$ and (+) $\frac{\partial \overline{\zeta}}{\partial x}$ and (d) longshore momentum with (-) $\frac{\partial S_{y\beta}}{\partial x_\beta}$, (-.) $\frac{\partial Q_y^2}{\partial y}$, (- -) $\frac{\partial Q_x Q_y}{\partial x}$ and (+) $\frac{\partial \overline{\zeta}}{\partial y}$. The channels are centered about $y = 4$ m and $y = 12$ m.

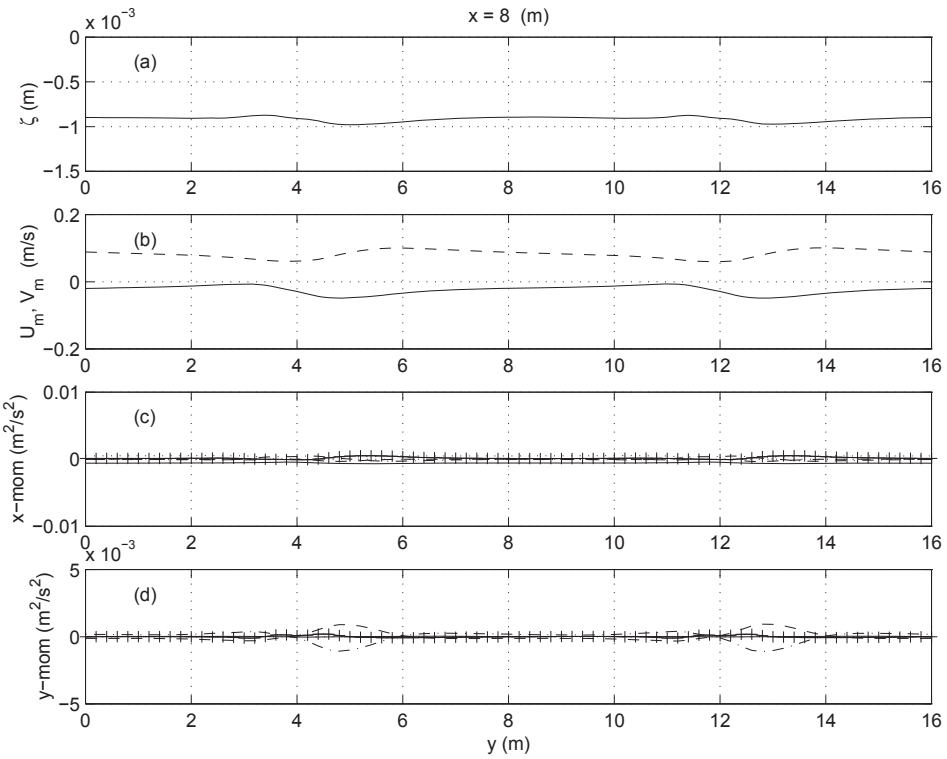

Figure 6.40: The longshore variation 1 m offshore of the bar ($x = 10$ m) for the offshore $\theta = 20$ of (a) ζ, (b) (-) U_m and (- -) V_m, (c) cross-shore momentum balance with (-) $\frac{\partial S_{x\beta}}{\partial x_\beta}$, (- -) $\frac{\partial Q_x^2}{\partial x}$, (-.) $\frac{\partial Q_x Q_y}{\partial y}$ and (+) $\frac{\partial \overline{\zeta}}{\partial x}$ and (d) longshore momentum with (-) $\frac{\partial S_{y\beta}}{\partial x_\beta}$, (-.) $\frac{\partial Q_y^2}{\partial y}$, (- -) $\frac{\partial Q_x Q_y}{\partial x}$ and (+) $\frac{\partial \overline{\zeta}}{\partial y}$. The channels are centered about $y = 4$ m and $y = 12$ m.

a weak rip current. In addition the longshore variation of the setup for the small wave angle case leads to a significant longshore pressure gradient whereas the large wave angle case has no pressure gradients.

In conclusion, the wave field has a pronounced effect on the dynamics of the rip currents, specifically the wave angle and the breaking pattern. Because the rip currents respond primarily to local forcing, changes in the wave field (which changes the local forcing) produce significantly different rips. Rip currents should be expected to be strongest for nearly normal incident waves and nonuniform breaking between the bar and channel.

Chapter 7

CONCLUSIONS

Rip currents are some of the most exciting and dangerous phenomena occurring in the nearshore region. As demonstrated by the literature review in the first chapter, there is much about rip currents which remains unknown. This thesis has analyzed the dynamics of rip current systems using both laboratory experiments and numerical modeling.

The experiments presented in Chapter 2 were an extension of the experiments by Haller and Dalrymple (1999) and primarily showed the depth structure of rip currents. Inside the channel where the waves are breaking, the rip current is nearly depth-uniform. Offshore of the channel, however, the rip current has strong depth variations, with strong seaward velocities in the upper half of the water column and weak seaward or landward velocities near the bottom. The depth variations are shown to be sensitive to the total volume flux in the rip. The rips with larger fluxes resulting from bigger waves show less depth variation than the rips with smaller fluxes.

In addition, the experiments showed that the rip behavior in the two channels was different. The channel where most of the measurements were taken has more frequent and stronger rip flow than the other channel. The measurements do not indicate that rip currents in the two channels are interacting with each other, they appear to be behaving independently.

The derivation of the numerical nearshore circulation model SHORECIRC (SC) was presented in Chapter 3. The primary change between the present version

and the previous versions is the choice made for splitting the currents. By splitting the currents into depth-averaged and depth varying components using the present method, additional terms are included in the dispersive mixing coefficients which turn out to be important when modeling rip currents. This chapter also included discussions about the closure submodels used in SC. The Smagorinksy eddy viscosity model has been added to SC to model the subgrid stresses.

The model SC is applied for the rip currents case in the wave basin from the experiments in Chapter 4. The time-averaged flow properties from the model were compared with the time-averaged measurements from Haller *et al.* (1997a,b). Good agreement between the model and laboratory data was achieved. The sensitivity of the model to the physical mechanisms was analyzed.

It was found that the bottom stress affects the stability of the rip current. Higher bottom stress leads to more stable flow where the rip current meandered less and fewer eddies were generated. Even though the higher friction reduced the magnitude of the instantaneous velocity, because the flow was more stable the time-averaged velocity of the rip current was increased.

Similar to the experiments, the flow in the two channels was found to behave differently in the model. The rip in the upper channel where the vast majority of measurements were taken was more energetic than the lower channel. The reason for this was attributed to the longshore variation in the topography. The depth between the bar and the shoreline is deeper on the upper half of the basin. This increased depth results in more flow feeding the upper rip current.

Wave current interaction was found to be important in rip current systems. Visual observations during the laboratory experiments indicated that the wave heights were increased in the presence of the rip. The modeled wave heights showed increases in wave height in the channels where the rip current was present. The wave current interaction creates forcing which prevents the rip currents from

flowing as far offshore.

The importance of the dispersive mixing mechanism from the vertical variation of the currents was demonstrated. The flow patterns are much more stable when this mechanism is included. The model runs with depth uniform currents were less stable and the generated eddies were dispersed slower and tended to fill the domain.

The vertical variations of rip currents as modeled by SC was presented in Chapter 5. The rip current profiles were shown to be in good agreement with the laboratory measurements. The vertical variation of one-dimensional undertow is generally governed by the short-wave forcing and bottom stress inside the surfzone but only the bottom stress outside the surfzone. In the rip current, however, the vertical variation of the current is also controlled by the convective accelerations. The interaction of the currents and the waves, which was neglected in previous versions of SC, turns out to play an important role in the vertical variation of the rip currents outside the breakers.

Finally, a study on the effects from varying topography and wave conditions was presented in Chapter 6. The flow in the rip currents was found to be insensitive to the channel spacing. The undertow passing over the bar, however, was found to be sensitive to the channel spacing. When the channels were closer, a higher percentage of the total shoreward flux from the short waves was returned by the rip currents rather than the undertow over the bar. The distance between the bar and the shoreline was found to have a profound impact on the flow in the rip current. When the shoreline was closer to the bar, less flow was returned by the rip currents.

It turns out that the flow in the rip currents and the recirculation cells close to the shoreline are only affected by changes in the local forcing. The position of the shoreline relative to the bar changes the local forcing while the rip spacing does not. On the other hand, the percentage of the flow passing over the bar is controlled

by the geometry of the whole system including the channel spacing.

The wave field was found to have a pronounced effect on the dynamics of rip current systems. Waves with an incident angle create a longshore current in the nearshore. When this current becomes sufficiently large, the flow has enough inertia to pass the channel without producing a rip current. In addition, when the waves break in the channel, the longshore variation in the setup which drives the rip current is much weaker, thereby creating weaker rip currents. Changes in the wave field effect the local forcing for the rips, hence the effect on the rip currents.

Although this study on rip currents has been extensive, there is always room for improvements and additional work. Additional measurements of rip currents are always beneficial. Future experiments should include additional gages measuring more than one profile simultaneously. In addition, the depth variation of the turbulence should be determined, especially in the rip current outside the breakers. Further comparisons between the flow in the two rip channels can be made by running the experiment for a longer time period. The one feature this study lacked was comparisons with field measurements of rip currents. If high quality field measurements can be obtained, comparisons between them and SC would be extremely beneficial.

Now that the SC model has been verified to simulate rip currents well, more analysis should be done for different conditions. The influence of wave conditions such as random waves should be tested. In addition, more geometries could be studied with alternate bar configurations. A good test would be to study the circulation on a wider, shallower bar with rip channels. Another important upgrade to SC would be in incorporate a sediment transport model into it so that the morphology of rip current systems could be studied.

Appendix A

LOCATION OF GAGES FOR THE EXPERIMENTS

Table A.1: Location of ADV's for Test R where x and y are the horizontal locations of the gage array, z_0, z_1 and z_2 is the depth below the still water level for each gage and h_o is the still water depth. Note that tests 16 and 18 where discarded because of poor wave conditions

Run	x (m)	y (m)	z_0 (cm)	z_1 (cm)	z_2 (cm)	h_o (cm)
1	11.75	14	10.5	6.5	8.5	11
2	11	14	11.5	6.5	9	14
3	10.5	14	13	6.5	9.5	15.5
4	10	14	15	6.5	11	17.5
5	10	13.6	15	6.5	10.5	17.5
6	10.5	13.6	13	6.5	9.5	15.5
7	11	13.6	11.5	6.5	9	13.5
8	11.75	13.6	9	5.5	7.5	11
9	11.75	13.2	9.5	6	8	11.5
10	11	13.2	12	6	9	13.5
11	10.5	13.2	13.5	6	9.5	15.5
12	10	13.2	16	5.5	10.5	18
13	9	13.2	19	5.5	12.5	21
14	9.5	13.2	17.5	5.5	13	19.5
15	9.5	13.6	17.5	5.5	11.5	19.5
17	9	13.6	17.5	5.5	11.5	20.5
19	9	14	17.5	5.5	11.5	21
20	9.5	14	16.5	6.5	11.5	19.5

Table A.2: Location of ADV's for Test S where x and y are the horizontal locations of the gage array, z_0, z_1 and z_2 is the depth below the still water level for each gage and h_o is the still water depth.

Run	x (m)	y (m)	z_0 (cm)	z_1 (cm)	z_2 (cm)	h_o (cm)
1	9	13.6	19	4	12	21
2	9	13.6	13.5	3.5	8	21
3	9.2	13.6	13.5	3.5	7.5	20
4	9.2	13.6	17.5	3	11	20
5	9.4	13.6	17.5	3.5	10.5	19.5
6	9.4	13.6	14.5	3	7	19.5
7	9.6	13.6	17	3	10.5	19
8	9.6	13.6	14	3	7	19
9	9.8	13.6	16.5	3	10	18.5
10	9.8	13.6	13.5	3	6.5	18.5
11	10	13.6	15	3	9.5	17.5
12	10	13.6	12	3	6	17.5
13	10.2	13.6	13.5	3	9	17
14	10.2	13.6	11	3	6	17
15	10.4	13.6	13	3	8	16
16	10.4	13.6	10.5	3	5.5	16
17	10.6	13.6	13	3	7.5	15.25
18	10.6	13.6	10	3	6	15.25
19	10.8	13.6	11.5	3	7.5	14.5
20	10.8	13.6	9.5	3.5	5.5	14.5
21	11	13.6	11.5	3.5	7.5	14
22	11	13.6	9.5	3.5	5.5	14
23	11.2	13.6	10.5	3.5	7	13
24	11.2	13.6	8.5	3.5	5.5	13
25	11.4	13.6	10	3.5	7	12.25
26	11.4	13.6	8.5	3.5	5	12.25
27	11.6	13.6	8.5	3.5	6	11.5
28	11.8	13.6	8.5	3.5	6	11
29	12	13.6	7.5	3.5	5.5	10.5
30	12.2	13.6	7	3.5	5	9.5

Table A.3: Location of ADV's for Test T where x and y are the horizontal locations of the gage array, z_0, z_1 and z_2 are the depths below the still water level for each gage and h_o is the still water depth.

Run	x (m)	y (m)	z_0 (cm)	z_1 (cm)	z_2 (cm)	h_o (cm)
2	11.5	13.6	8.5	4.5	6.5	12
3	11	13.6	10	4.5	7	13.5
4	10.5	13.6	11.5	4.5	8	15
5	10	13.6	14	4.5	9.5	17.5
6	9.5	13.6	15.5	4.5	10	19
7	9	13.6	17	4.5	10.5	20.5

Table A.4: Location of ADV's for Test U where x and y are the horizontal locations of each gage, z is the depth below the still water level for each gage and h is the still water depth.

		Gage #					Gage #		
Run		1	2	3	Run		1	2	3
1	x(m)	12.9	11.35	11.35	2	x (m)	12.9	11.35	11.35
	y (m)	9.2	13.6	4.6		y (m)	9.2	13.6	4.6
	z (cm)	4.5	5.5	5.5		z (cm)	3	5.5	5.5
	h (cm)	7	12.5	12		h (cm)	7	12.5	12
3	x(m)	12.45	10.85	10.85	4	x (m)	13.85	12.25	12.25
	y (m)	9.2	13.6	4.6		y (m)	9.2	13.6	4.6
	z (cm)	4	5.5	5.5		z (cm)	2.5	4	4
	h (cm)	9	14	13.5		h (cm)	4	9.5	9

Table A.5: Location of wave gages for Test R where x and y are the horizontal locations of each gage. All coordinates are in meters. Note that gages 3-5 are excluded.

Run	x_1	x_2	x_{6-10}	y_1	y_2	y_6	y_7	y_8	y_9	y_{10}
1	6	11.45	12.35	16.2	13.8	13.4	13.2	12.05	11.2	9.2
2	6	10.75	12.35	16.2	13.8	13.4	13.2	12.05	11.2	9.2
3	6	10.2	12.35	16.2	13.8	13.4	13.2	12.05	11.2	9.2
4	6	9.8	12.35	16.2	13.8	13.4	13.2	12.05	11.2	9.2
5	6	11	12.35	16.2	13.4	13.4	13.2	12.05	11.2	9.2
6	6	10.25	12.35	16.2	13.4	13.4	13.2	12.05	11.2	9.2
7	6	10.75	12.35	16.2	13.4	13.4	13.2	12.05	11.2	9.2
8	6	11.5	12.35	16.2	13.4	13.4	13.2	12.05	11.2	9.2
9	6	11.5	12.35	16.2	13	13.4	13.2	12.05	11.2	9.2
10	6	10.75	12.35	16.2	13	13.4	13.2	12.05	11.2	9.2
11	6	10.25	12.35	16.2	13	13.4	13.2	12.05	11.2	9.2
12	6	9.75	12.35	16.2	13	13.4	13.2	12.05	11.2	9.2
13	6	8.75	12.35	16.2	13	13.4	13.2	12.05	11.2	9.2
14	6	9.25	12.35	16.2	13	13.4	13.2	12.05	11.2	9.2
15	6	9.25	12.35	16.2	13.4	13.4	13.2	12.05	11.2	9.2
17	6	8.75	12.35	16.2	13.4	13.4	13.2	12.05	11.2	9.2
19	6	8.75	12.35	16.2	13.8	13.4	13.2	12.05	11.2	9.2
20	6	9.25	12.35	16.2	13.8	13.4	13.2	12.05	11.2	9.2

Table A.6: Location of wave gages for Test S where x and y are the horizontal locations of each gage. All coordinates are in meters. Note that gage 5 is excluded.

Run	x_1	x_2	x_{3-10}	y_1	y_2	y_3	y_4	y_6	y_7	y_8	y_9	y_{10}
1 - 2	6	8.8	10.8	16.2	13.4	15.15	14.30	13.35	13.15	12	11.15	9.2
3 - 4	6	9	10.8	16.2	13.4	15.15	14.30	13.35	13.15	12	11.15	9.2
5 - 6	6	9.2	10.8	16.2	13.4	15.15	14.30	13.35	13.15	12	11.15	9.2
7 - 8	6	9.4	10.8	16.2	13.4	15.15	14.30	13.35	13.15	12	11.15	9.2
9 - 12	6	9.6	10.8	16.2	13.4	15.15	14.30	13.35	13.15	12	11.15	9.2
13 - 16	6	10	n/a	16.2	13.4	n/a	n/a	n/a	n/a	n/a	n/a	n/a
17 - 18	6	10.4	n/a	16.2	13.4	n/a	n/a	n/a	n/a	n/a	n/a	n/a
19 - 22	6	10.6	n/a	16.2	13.4	n/a	n/a	n/a	n/a	n/a	n/a	n/a
23 - 26	6	11	n/a	16.2	13.4	n/a	n/a	n/a	n/a	n/a	n/a	n/a
27 - 28	6	11.4	n/a	16.2	13.4	n/a	n/a	n/a	n/a	n/a	n/a	n/a
29 - 30	6	11.8	n/a	16.2	13.4	n/a	n/a	n/a	n/a	n/a	n/a	n/a

Table A.7: Location of wave gages for Test T where x and y are the horizontal locations of each gage. All coordinates are in meters. Note that run 1 and 14 are discarded and gage 6 is excluded.

Run	x_1	x_2	x_{3-10}	y_1	y_2	y_3	y_4	y_5	y_7	y_8	y_9	y_{10}
2	6	11	12.65	16.2	13.4	15.2	14.35	13.8	12.45	n/a	11.2	9.2
3	6	10.5	12.65	16.2	13.4	15.2	14.35	13.8	12.45	n/a	11.2	9.2
4	6	10.25	12.65	16.2	13.4	15.2	14.35	13.8	12.45	n/a	11.2	9.2
5	6	9.5	12.65	16.2	13.4	15.2	14.35	13.8	12.45	n/a	11.2	9.2
6	6	8.8	12.65	16.2	13.4	15.2	14.35	13.8	12.45	n/a	11.2	9.2
7	6	8.8	12.65	16.2	13.4	15.2	14.35	13.8	12.45	n/a	11.2	9.2
8	6	9	9	16.2	15.2	14.1	13.8	13.2	12.4	11.2	9.2	n/a
9	6	9.5	9.5	16.2	15.2	14.1	13.8	13.2	12.4	11.2	9.2	n/a
10	6	10	10	16.2	15.2	14.1	13.8	13.2	12.4	11.2	9.2	n/a
11	6	10.5	10.5	16.2	15.2	14.1	13.8	13.2	12.4	11.2	9.2	n/a
12	6	11	11	16.2	15.2	14.1	13.8	13.2	12.4	11.2	9.2	n/a
13	6	11.5	11.5	16.2	15.2	14.1	13.8	13.2	12.4	11.2	9.2	n/a
15	6	12.5	12.5	16.2	15.2	14.1	13.8	13.2	12.4	11.2	9.2	n/a
16	6	13	13	16.2	15.2	14.1	13.8	13.2	12.4	11.2	9.2	n/a

Table A.8: Location of wave gages for Test U where x and y are the horizontal locations of each gage. All coordinates are in meters. Note gage 6 is excluded

Run	x_1	x_{2-9}	y_1	y_2	y_3	y_4	y_5	y_7	y_8	y_9
1	6	11.5	16.2	16.4	13.4	10.8	9.1	7.4	4.8	1.8
2	6	11.5	16.2	16.4	13.4	10.8	9.1	7.4	4.8	1.8
3	6	11	16.2	16.4	13.4	10.8	9.1	7.4	4.8	1.8
4	6	12.35	16.2	16.4	13.4	10.8	9.1	7.4	4.8	1.8

Appendix B

CALCULATION OF THE VERTICAL PROFILES

This appendix outlines the derivation of the coefficients for $V_{d\alpha}^{(0)}$ and $V_{d\alpha}^{(1)}$. The coefficients for $V_{d\alpha}^{(0)}$ are required for the calculation of the 3-D dispersive mixing terms given by (3.87) - (3.90). The effect of $V_{d\alpha}^{(1)}$ is implicitly included in the 3-D dispersive mixing terms, therefore it does not need to be explicitly determined for solving the horizontal momentum equations. In the previous versions of SHORECIRC (SC) $V_{d\alpha}^{(1)}$ was never explicity modeled. On the other hand, when analyzing the vertical structure of the current, the vertical variation of $V_{d\alpha}^{(1)}$ does need to be calculated and is presented here for the first time.

Solution for $V_{d\alpha}^{(0)}$

The derivation for $V_{d\alpha}^{(0)}$ begins with (3.71) which is written again here for convenience,

$$\begin{aligned} V_{d\alpha}^{(0)} = \; & \frac{\tau_\alpha^B}{\rho}\left(\int_{-h_o}^{z}\frac{dz'}{(\nu_t+\nu_s)} - \frac{1}{h}\int_{-h_o}^{\overline{\zeta}}\int_{-h_o}^{z}\frac{dz'}{(\nu_t+\nu_s)}dz\right) \\ & - \int_{-h_o}^{z}\frac{1}{(\nu_t+\nu_s)}\int_{-h_o}^{z'}F_\alpha^{(0)}dz'dz \\ & + \frac{1}{h}\int_{-h_o}^{\overline{\zeta}}\int_{-h_o}^{z}\frac{1}{(\nu_t+\nu_s)}\int_{-h_o}^{z'}F_\alpha^{(0)}dz''dz'dz \end{aligned} \tag{B.1}$$

with $F_\alpha^{(0)}$ given by

$$F_\alpha^{(0)} = \left\{\frac{1}{\rho h}\frac{\partial S'_{\alpha\beta}}{\partial x_\beta} + \frac{\tau_\alpha^B}{\rho h} - f_\alpha\right\}. \tag{B.2}$$

In parallel with the splitting of $V_{1\alpha}^{(0)}$ in Putrevu and Svendsen (1999), we break the solution for $V_{d\alpha}^{(0)}$ into two parts,

$$V_{d\alpha}^{(0)} = V_{d\alpha}^{(0,0)} + V_{d\alpha}^{(0,1)} \tag{B.3}$$

where

$$V_{d\alpha}^{(0,0)} = \frac{\tau_\alpha^B}{\rho}\left(\int_{-h_o}^{z}\frac{dz'}{(\nu_t+\nu_s)} - \frac{1}{h}\int_{-h_o}^{\overline{\zeta}}\int_{-h_o}^{z}\frac{dz'}{(\nu_t+\nu_s)}dz\right) \tag{B.4}$$

$$V_{d\alpha}^{(0,1)} = -\int_{-h_o}^{z}\frac{1}{(\nu_t+\nu_s)}\int_{-h_o}^{z'}F_\alpha^{(0)}dz'dz + \frac{1}{h}\int_{-h_o}^{\overline{\zeta}}\int_{-h_o}^{z}\frac{1}{(\nu_t+\nu_s)}\int_{-h_o}^{z'}F_\alpha^{(0)}dz''dz'dz. \tag{B.5}$$

$V_{d\alpha}^{(0,0)}$ is the component of $V_{d\alpha}^{(0)}$ which satisfies the boundary conditions given by (3.62) and is similar to the velocity component given by Putrevu and Svendsen (1999) equation (34). $V_{d\alpha}^{(0,1)}$ is the component which is forced by $F_\alpha^{(0)}$ and is similar to $V_{s\alpha}^{(0)}$) given by equation (38) in Putrevu and Svendsen (1999).

In order to simplify the solution we use the transformation for the vertical coordinate as used by both Van Dongeren and Svendsen (1997) and Putrevu and Svendsen (1999)

$$\xi = z + h_o \tag{B.6}$$

which has the properties of

$$\frac{\partial}{\partial z} = \frac{\partial}{\partial \xi} \tag{B.7}$$

$$\frac{\partial}{\partial x_\alpha}(f(x_\alpha, z)) = \frac{\partial}{\partial x_\alpha}(f(x_\alpha,\xi)) + \frac{\partial h_o}{\partial x_\alpha}\frac{\partial}{\partial \xi}(f(x_\alpha,\xi)) \tag{B.8}$$

where f is a function.

As in earlier versions we assume the eddy viscosity is constant over depth and get the expression for $V_{d\alpha}^{(0,0)}$ written as

$$V_{d\alpha}^{(0,0)} = \frac{\tau_\alpha^B}{\rho(\nu_t+\nu_s)}\left[\xi - \frac{h}{2}\right]. \tag{B.9}$$

We also continue to assume that $F_\alpha^{(0)}$ is depth independent, which amounts to using long wave theory to find f_α, to get the expression for $V_{d\alpha}^{(0,1)}$ given as

$$V_{d\alpha}^{(0,1)} = -\frac{F_\alpha^{(0)}}{(\nu_t + \nu_s)}\left(\frac{\xi^2}{2} - \frac{h^2}{6}\right). \tag{B.10}$$

The final result for $V_{d\alpha}^{(0)}$, which is used for calculating the 3-D dispersive mixing coefficients, is written as

$$V_{d\alpha}^{(0)} = d_{1\alpha}\xi^2 + e_{1\alpha}\xi + (f_{1\alpha} + f_{2\alpha}) \tag{B.11}$$

where

$$d_{1\alpha} = -\frac{F_\alpha^{(0)}}{2(\nu_t + \nu_s)} \tag{B.12}$$

$$e_{1\alpha} = \frac{\tau_\alpha^B}{\rho(\nu_t + \nu_s)} \tag{B.13}$$

$$f_{1\alpha} = -\frac{h}{2}\frac{\tau_\alpha^B}{\rho(\nu_t + \nu_s)} \tag{B.14}$$

$$f_{2\alpha} = \frac{h^2 F_\alpha^{(0)}}{6(\nu_t + \nu_s)}. \tag{B.15}$$

The equation for $V_{d\alpha}^{(0)}$ (B.11) corresponds to equation (2.76) for $V_{1\alpha}^{(0)}$ in Van Dongeren and Svendsen (1997). The coefficients for $V_{d\alpha}^{(0)}$ are equivalent to the coefficients for $V_{1\alpha}^{(0)}$ given by Equations (2.77)-(2.79) in Van Dongeren and Svendsen (1997) with the following relationships

$$d_{1\alpha} = b_1 \tag{B.16}$$

$$e_{1\alpha} = b_2 \tag{B.17}$$

$$f_{1\alpha} + f_{2\alpha} = b_3 + \frac{Q_{w\alpha}}{h} \tag{B.18}$$

(B.18) accounts for the difference between $V_{d\alpha}^{(0)}$ and $V_{1\alpha}^{(0)}$ given by (3.48).

Solution for $V_{d\alpha}^{(1)}$

The previous versions of SC do not solve for $V_{d\alpha}^{(1)}$, therefore the rest of this appendix

presents derivations. The solution for $V_{d\alpha}^{(1)}$ begins with (3.74) which is written as follows after applying the vertical coordinate transformation (B.6)

$$\begin{aligned} V_{d\alpha}^{(1)} = & -\int_0^\xi \frac{1}{(\nu_t+\nu_s)} \int_0^{\xi'} F_\alpha^{(1)} d\xi' d\xi \\ & + \frac{1}{h}\int_0^h \int_0^\xi \frac{1}{(\nu_t+\nu_s)} \int_0^{\xi'} F_\alpha^{(1)} d\xi'' d\xi' d\xi \end{aligned} \tag{B.19}$$

where $F_\alpha^{(1)}$ is given by

$$\begin{aligned} F_\alpha^{(1)} = & -\left\{ \left(\frac{\overline{Q}_\beta}{h} \frac{\partial V_{d\alpha}^{(0)}}{\partial x_\beta} + V_{d\beta}^{(0)} \frac{\partial \frac{\overline{Q}_\alpha}{h}}{\partial x_\beta} + W \frac{\partial V_{d\alpha}^{(0)}}{\partial \xi} \right) \right. \\ & - \left(\frac{\overline{Q}_\beta}{h} \frac{\partial \frac{Q_{w\alpha}}{h}}{\partial x_\beta} + \frac{Q_{w\beta}}{h} \frac{\partial \frac{\overline{Q}_\alpha}{h}}{\partial x_\beta} - \frac{Q_{w\beta}}{h} \frac{\partial \frac{Q_{w\alpha}}{h}}{\partial x_\beta} + \frac{Q_{w\beta}}{h} \frac{\partial V_{d\alpha}^{(0)}}{\partial x_\beta} + V_{d\beta}^{(0)} \frac{\partial \frac{Q_{w\alpha}}{h}}{\partial x_\beta} \right) \\ & \left. - \frac{1}{h} \frac{\partial}{\partial x_\gamma} \left[V_{d\alpha}^{(0)}(h) Q_{w\gamma} + V_{d\gamma}^{(0)}(h) Q_{w\alpha} \right] \right\} \end{aligned} \tag{B.20}$$

with the vertical velocity given by

$$W = -\left[\left(\frac{\overline{Q}_\gamma}{h} - \frac{Q_{w\gamma}}{h} \right) \frac{\partial h_o}{\partial x_\gamma} + \xi \frac{\partial}{\partial x_\gamma} \left(\frac{\overline{Q}_\gamma}{h} - \frac{Q_{w\gamma}}{h} \right) \right]. \tag{B.21}$$

Next we insert the expression for $V_{d\alpha}^{(0)}$, (B.11), into (B.20) and (B.21). Writing the results term by term gives the following,

$$\begin{aligned} \frac{\overline{Q}_\beta}{h} \left(\frac{\partial V_{d\alpha}^{(0)}}{\partial x_\beta} - \frac{\partial \frac{Q_{w\alpha}}{h}}{\partial x_\beta} \right) = & \frac{\overline{Q}_\beta}{h} \left[\frac{\partial d_{1\alpha}}{\partial x_\beta} \xi^2 + \left(\frac{\partial e_{1\alpha}}{\partial x_\beta} + 2 d_{1\alpha} \frac{\partial h_o}{\partial x_\beta} \right) \xi \right. \\ & \left. + \left(\frac{\partial (f_{1\alpha} + f_{2\alpha})}{\partial x_\beta} + e_{1\alpha} \frac{\partial h_o}{\partial x_\beta} - \frac{\partial \frac{Q_{w\alpha}}{h}}{\partial x_\beta} \right) \right] \end{aligned} \tag{B.22}$$

$$\left(V_{d\beta}^{(0)} - \frac{Q_{w\beta}}{h} \right) \frac{\partial \frac{\overline{Q}_\alpha}{h}}{\partial x_\beta} = \frac{\partial \frac{\overline{Q}_\alpha}{h}}{\partial x_\beta} \left[d_{1\beta} \xi^2 + e_{1\beta} \xi + \left(f_{1\beta} + f_{2\beta} - \frac{Q_{w\beta}}{h} \right) \right] \tag{B.23}$$

$$\begin{aligned} W \frac{\partial V_{d\alpha}^{(0)}}{\partial \xi} = & -2 d_{1\alpha} \frac{\partial}{\partial x_\gamma} \left(\frac{\overline{Q}_\gamma}{h} - \frac{Q_{w\gamma}}{h} \right) \xi^2 \\ & - \left[e_{1\alpha} \frac{\partial}{\partial x_\gamma} \left(\frac{\overline{Q}_\gamma}{h} - \frac{Q_{w\gamma}}{h} \right) + 2 d_{1\alpha} \frac{\partial h_o}{\partial x_\gamma} \left(\frac{\overline{Q}_\gamma}{h} - \frac{Q_{w\gamma}}{h} \right) \right] \xi \\ & - d_{1\alpha} \frac{\partial h_o}{\partial x_\gamma} \left(\frac{\overline{Q}_\gamma}{h} - \frac{Q_{w\gamma}}{h} \right) \end{aligned} \tag{B.24}$$

$$\frac{Q_{w\beta}}{h}\frac{\partial V_{d\alpha}^{(0)}}{\partial x_\beta} + V_{d\beta}^{(0)}\frac{\partial \frac{Q_{w\alpha}}{h}}{\partial x_\beta} + \frac{Q_{w\beta}}{h}\frac{\partial \frac{Q_{w\alpha}}{h}}{\partial x_\beta} = \left[\frac{Q_{w\beta}}{h}\frac{\partial d_{1\alpha}}{\partial x_\beta} + d_{1\beta}\frac{\partial \frac{Q_{w\alpha}}{h}}{\partial x_\beta}\right]\xi^2$$
$$+\left[\frac{Q_{w\beta}}{h}\left(\frac{\partial e_{1\alpha}}{\partial x_\beta} + 2\frac{\partial h_o}{\partial x_\beta}d_{1\alpha}\right) + e_{1\beta}\frac{\partial \frac{Q_{w\alpha}}{h}}{\partial x_\beta}\right]\xi$$
$$+\left[\frac{Q_{w\beta}}{h}\left(\frac{\partial(f_{1\alpha}+f_{2\alpha})}{\partial x_\beta} + \frac{\partial h_o}{\partial x_\beta}e_{1\alpha}\right) + \left(f_{1\beta}+f_{2\beta}-\frac{Q_{w\beta}}{h}\right)\frac{\partial \frac{Q_{w\alpha}}{h}}{\partial x_\beta}\right] \tag{B.25}$$

$$\frac{1}{h}\frac{\partial}{\partial x_\gamma}\left[V_{d\alpha}^{(0)}(h)Q_{w\gamma} + V_{d\gamma}^{(0)}(h)Q_{w\alpha}\right] = \frac{1}{h}\,\frac{\partial I_{\alpha\gamma}}{\partial x_\gamma} \tag{B.26}$$

where

$$I_{\alpha\gamma} = Q_{w\alpha}(d_{1\beta}h^2 + e_{1\beta}h + f_{1\beta} + f_{2\beta}) + Q_{w\beta}(d_{1\alpha}h^2 + e_{1\alpha}h + f_{1\alpha} + f_{2\alpha}). \tag{B.27}$$

Substituting (B.22) - (B.27) into (B.19) and performing the integrations results in the following expression for $V_{d\alpha}^{(1)}$,

$$V_{d\alpha}^{(1)} = V_{d\alpha}^{(1,a)} + V_{d\alpha}^{(1,b)} + V_{d\alpha}^{(1,w)} + V_{d\alpha}^{(1,d)} + V_{d\alpha}^{(1,e)} + V_{d\alpha}^{(1,c)} \tag{B.28}$$

where the velocity component $V_{d\alpha}^{(1,a)}$ is given by

$$V_{d\alpha}^{(1,a)} = V_{d\alpha}^{(1,a,4)}\xi^4 + V_{d\alpha}^{(1,a,3)}\xi^3 + V_{d\alpha}^{(1,a,2)}\xi^2 \tag{B.29}$$

$$V_{d\alpha}^{(1,a,4)} = \frac{1}{12(\nu_t+\nu_s)}\frac{\overline{Q}_\beta}{h}\left(\frac{\partial d_{1\alpha}}{\partial x_\beta}\right) \tag{B.30}$$

$$V_{d\alpha}^{(1,a,3)} = \frac{1}{6(\nu_t+\nu_s)}\frac{\overline{Q}_\beta}{h}\left(\frac{\partial e_{1\alpha}}{\partial x_\beta} + 2d_{1\alpha}\frac{\partial h_o}{\partial x_\beta}\right) \tag{B.31}$$

$$V_{d\alpha}^{(1,a,2)} = \frac{1}{2(\nu_t+\nu_s)}\frac{\overline{Q}_\beta}{h}\left(\frac{\partial(f_{1\alpha}+f_{2\alpha}}{\partial x_\beta}) + e_{1\alpha}\frac{\partial h_o}{\partial x_\beta} - \frac{\partial \frac{Q_{w\alpha}}{h}}{\partial x_\beta}\right) \tag{B.32}$$

the velocity component $V_{d\alpha}^{(1,b)}$ is given by

$$V_{d\alpha}^{(1,b)} = V_{d\alpha}^{(1,b,4)}\xi^4 + V_{d\alpha}^{(1,b,3)}\xi^3 + V_{d\alpha}^{(1,b,2)}\xi^2 \tag{B.33}$$

$$V_{d\alpha}^{(1,b,4)} = \frac{1}{12(\nu_t+\nu_s)}\frac{\partial \frac{\overline{Q}_\alpha}{h}}{\partial x_\beta}d_{1\beta} \tag{B.34}$$

$$V_{d\alpha}^{(1,b,3)} = \frac{1}{6(\nu_t+\nu_s)}\frac{\partial \frac{\overline{Q}_\alpha}{h}}{\partial x_\beta}e_{1\beta} \tag{B.35}$$

$$V_{d\alpha}^{(1,b,2)} = \frac{1}{2(\nu_t+\nu_s)}\frac{\partial \frac{\overline{Q}_\alpha}{h}}{\partial x_\beta}\left(f_{1\beta}+f_{2\beta}-\frac{Q_{w\beta}}{h}\right) \tag{B.36}$$

the velocity component $V_{d\alpha}^{(1,w)}$ is given by

$$V_{d\alpha}^{(1,w)} = V_{d\alpha}^{(1,w,4)}\xi^4 + V_{d\alpha}^{(1,w,3)}\xi^3 + V_{d\alpha}^{(1,w,2)}\xi^2 \tag{B.37}$$

$$V_{d\alpha}^{(1,w,4)} = -\frac{1}{6(\nu_t+\nu_s)} d_{1\alpha}\frac{\partial}{\partial x_\gamma}\left(\frac{\overline{Q}_\gamma}{h} - \frac{Q_{w\gamma}}{h}\right) \tag{B.38}$$

$$\begin{aligned} V_{d\alpha}^{(1,w,3)} = & -\frac{1}{6(\nu_t+\nu_s)}\left[e_{1\alpha}\frac{\partial}{\partial x_\gamma}\left(\frac{\overline{Q}_\gamma}{h} - \frac{Q_{w\gamma}}{h}\right)\right. \\ & \left. +2d_{1\alpha}\frac{\partial h_o}{\partial x_\gamma}\left(\frac{\overline{Q}_\gamma}{h} - \frac{Q_{w\gamma}}{h}\right)\right] \end{aligned} \tag{B.39}$$

$$V_{d\alpha}^{(1,w,2)} = -\frac{1}{2(\nu_t+\nu_s)}\left[e_{1\alpha}\frac{\partial h_o}{\partial x_\gamma}\left(\frac{\overline{Q}_\gamma}{h} - \frac{Q_{w\gamma}}{h}\right)\right] \tag{B.40}$$

the velocity component $V_{d\alpha}^{(1,d)}$ is given by

$$V_{d\alpha}^{(1,d)} = V_{d\alpha}^{(1,d,4)}\xi^4 + V_{d\alpha}^{(1,d,3)}\xi^3 + V_{d\alpha}^{(1,d,2)}\xi^2 \tag{B.41}$$

$$V_{d\alpha}^{(1,d,4)} = \frac{1}{12(\nu_t+\nu_s)}\left[\frac{Q_{w\beta}}{h}\frac{\partial d_{1\alpha}}{\partial x_\beta} + d_{1\beta}\frac{\partial \frac{Q_{w\alpha}}{h}}{\partial x_\beta}\right] \tag{B.42}$$

$$V_{d\alpha}^{(1,d,3)} = \frac{1}{6(\nu_t+\nu_s)}\left[\frac{Q_{w\beta}}{h}\left(\frac{\partial e_{1\alpha}}{\partial x_\beta} + 2\frac{\partial h_o}{\partial x_\beta}d_{1\alpha}\right) + e_{1\beta}\frac{\partial \frac{Q_{w\alpha}}{h}}{\partial x_\beta}\right] \tag{B.43}$$

$$\begin{aligned} V_{d\alpha}^{(1,d,2)} = & \frac{1}{2(\nu_t+\nu_s)}\left[\frac{Q_{w\beta}}{h}\left(\frac{\partial(f_{1\alpha}+f_{2\alpha})}{\partial x_\beta} + \frac{\partial h_o}{\partial x_\beta}e_{1\alpha}\right)\right. \\ & \left. + \left(f_{1\beta} + f_{2\beta} - \frac{Q_{w\beta}}{h}\right)\frac{\partial \frac{Q_{w\alpha}}{h}}{\partial x_\beta}\right] \end{aligned} \tag{B.44}$$

the velocity component $V_{d\alpha}^{(1,e)}$ is given by

$$V_{d\alpha}^{(1,e)} = V_{d\alpha}^{(1,e,2)}\xi^2 \tag{B.45}$$

$$V_{d\alpha}^{(1,e,2)} = \frac{1}{2(\nu_t+\nu_s)}\frac{1}{h}\frac{\partial I_{\alpha\gamma}}{\partial x_\gamma} \tag{B.46}$$

and the velocity component $V_{d\alpha}^{(1,c)}$ is given by

$$\begin{aligned} V_{d\alpha}^{(1,c)} = & \left[V_{d\alpha}^{(1,a,4)} + V_{d\alpha}^{(1,b,4)} + V_{d\alpha}^{(1,w,4)} + V_{d\alpha}^{(1,d,4)}\right]\frac{h^4}{5} \\ & \left[V_{d\alpha}^{(1,a,3)} + V_{d\alpha}^{(1,b,3)} + V_{d\alpha}^{(1,w,3)} + V_{d\alpha}^{(1,d,3)}\right]\frac{h^3}{4} \\ & \left[V_{d\alpha}^{(1,a,2)} + V_{d\alpha}^{(1,b,2)} + V_{d\alpha}^{(1,w,2)} + V_{d\alpha}^{(1,d,2)} + V_{d\alpha}^{(1,e,2)}\right]\frac{h^2}{3}. \end{aligned} \tag{B.47}$$

Bibliography

Aagaard, T., Greenwood, B., and Nielsen, J. (1997). Mean currents and sediment transport in a rip channel. *Journal of Marine Geology*, **140**, 25–45.

Arthur, R. S. (1962). A note on the dynamics of rip currents. *J. Geophys. Res.*, **67**, 2777–2779.

Battjes, J. A. (1975). Modelling of turbulence in the surfzone. In *Proceedings of the Symposium on Modelling Techniques*, pages 1050–1061. ASCE.

Bowen, A. J. (1969a). The generation of longshore currents on a plane beach. *Journal of Marine Research*, **27**, 206–215.

Bowen, A. J. (1969b). Rip currents. 1. Theoretical investigations. *J. Geophys. Res.*, **74**, 5467–5478.

Bowen, A. J. and Inman, D. L. (1969). Rip currents. 2. Laboratory and field observations. *J. Geophys. Res.*, **74**, 5479–5490.

Bowman, D., Arad, D., Rosen, S., Kit, E., Goldbery, R., and Slavicz, A. (1988a). Flow characteristics along the rip current system under low-energy conditions. *Marine Geology*, **82**, 149–167.

Bowman, D., Rosen, D. S., Kit, E., Arad, E., and Slavicz, A. (1988b). Flow characteristics at the rip current neck under low energy conditions. *Journal of Marine Geology*, **79**, 41–54.

Bowman, D., Birkenfeld, H., and Rosen, D. S. (1992). The longshore flow component in low-energy rip channels: The Mediterranean, Israel. *Journal of Marine Geology*, **108**, 259–274.

Brander, R. W. (1999). Field observations on the morphodynamic evolution of a low-energy rip current system. *Journal of Marine Geology*, **157**, 199–217.

Brant, I. (1925). The "Undertow". *Science*, **62**, 30–31.

Briand, M. G. and Kamphuis, J. W. (1993). Waves and currents on natural beaches: A quasi 3-D numerical model. *Coastal Engineering*, **20**, 101–134.

Chandramohan, P., Kumar, V. S., and Jena, B. K. (1997). Rip current zones along beaches in Goa west coast of India. *J. of Waterway, Port, Coastal and Ocean Engng.*, **123**, 322–328.

Chen, Q., Dalrymple, R. A., Kirby, J. T., Kennedy, A. B., and Haller, M. C. (1999). Boussinesq modeling of a rip current system. *J. Geophys. Res.*, **104**, 20617–20637.

Chen, Q., Kirby, J. T., Dalrymple, R. A., Kennedy, A. B., Thornton, E., and Shi, F. (2000). Boussinesq modeling of waves and longshore currents under field conditions. In *Proc. 27th Coastal Engineering Conference*, Sydney. ASCE.

Coffey, F. C. and Nielsen, P. (1984). Aspects of wave current boundary layer flows. In *Proc. 19th Coastal Engineering Conference*, volume 3, pages 2232–2245, Houston. ASCE.

Cook, D. O. (1970). The occurence and geological work of rip currents off Southern California. *Journal of Marine Geology*, **9**, 173–186.

Craig, W. (1925). The "Undertow". *Science*, **62**, 30.

Dally, W. R. and Dean, R. G. (1984). Suspended sediment transport and beach profile evaluation. *J. of Waterway, Port, Coastal and Ocean Engng.*, **110**, 15–33.

Dalrymple, R. (1989). Directional wavemaker theory with sidewall reflection. *J. Hydr. Res*, **27**, 23–34.

Dalrymple, R. A. (1975). A mechanism for rip current generation on an open coast. *J. Geophys. Res.*, **80**, 3485–3487.

Dalrymple, R. A. (1978). Rip currents and their causes. In *Proc. 14th Coastal Engineering Conference*, pages 1414–1427.

Dalrymple, R. A. and Lozano, C. J. (1978). Wave-current interaction models for rip currents. *J. Geophys. Res.*, **83**, 6063–6071.

Davis, W. M. (1925a). The undertow myth. *Science*, **61**, 206–208.

Davis, W. M. (1925b). The "Undertow". *Science*, **62**, 33.

De Vriend, H. J. and Stive, M. J. F. (1987). Quasi-3D modelling of nearshore currents. *Coastal Engineering*, **11**, 565–601.

Deardorff, J. W. (1974). A numerical study of three-dimensional turbulent channel flow at large Reynolds numbers. *J. Fluid Mech.*, **41**, 453–480.

Deigaard, R. (1990). The formation of rip channels on a barred coast. Technical Report 72, Technical University of Denmark.

Deigaard, R., Drønen, N., Fredsøe, J., Jensen, J. H., and Jørgensen, M. P. (1999). A morphological stability analysis for a long straight coast. *Coastal Engng.*, **36**, 171–195.

Dette, H.-H., Peters, K., and Spignat, F. (1995). About rip currents at a mesotidal coastal. In *Coastal Dynamics'95*, pages 477–488, Gdansk. ASCE.

Dracos, T., Giger, M., and Jirka, G. H. (1992). Plane turbulent jets in a bounded fluid layer. *Journal of Fluid Mechanics*, **241**, 587–614.

Drønen, N., Karunarathna, H., Fredsøe, J., Sumer, B. M., and Deigaard, R. (1999). The circulation over a longshore bar with rip channels. In *Coastal Sediments*, pages 576–587.

Dyhr-Nielsen, M. and Sørensen, T. (1970). Same sand transport phenomena on coasts with bars. In *Proc. 12th Coastal Engineering Conference*, pages 855–866. ASCE.

Ebersole, B. A. and Dalrymple, R. A. (1980). Numerical modeling of nearshore circulation. In *Proc. 17th Coastal Engineering Conference*, pages 2710–2725. ASCE.

Evans, O. F. (1938). The undertow. *Science*, **88**, 279–281.

Garcez Faria, A. F., Thornton, E. B., and Stanton, T. P. (1995). A quasi-3D model of longshore currents. In *Coastal Dynamics'95*, pages 389–400, Gdansk. ASCE.

Garcez Faria, A. F., Thornton, E. B., and Stanton, T. C. L. T. P. (2000). Undertow over a barred beach. *J. Geophys. Res.*, **105**, 16999–17011.

Giger, M., Dracos, T., and Jirka, G. H. (1991). Entrainment and mixing in plane turbulent jets in shallow water. *Journal of Hydraulic Research*, **29**, 615–641.

Greenwood, B. and Osborne, P. D. (1990). Vertical and horizontal structure in cross-shore flows: An example of undertow and wave set-up on a barred beach. *Coastal Engineering*, **14**, 543–580.

Guza, R. T. and Thornton, E. B. (1985). Velocity moments in the nearshore. *J. of Waterway, Port, Coastal and Ocean Engng.*, **111**, 235–256.

Haas, K. A., Svendsen, I. A., and Haller, M. (1998). Numerical modeling of nearshore circulation on a barred beach with rip channels. In *Proc. 26th Coastal Engineering Conference*, volume 1, pages 801–814, Copenhagen. ASCE.

Haas, K. A., Svendsen, I. A., and Zhao, Q. (2000). 3D modeling of rip currents. In *Proc. 27th Coastal Engineering Conference*, Sydney. ASCE.

Haller, M. and Dalrymple, R. A. (1999). Rip current dynamics and nearshore circulation. (Ph. D. Dissertation), Res. Report CACR-99-05, Center for Applied Coastal Research, Univ. of Delaware.

Haller, M., Dalrymple, R., and Svendsen, I. A. (1997a). Rip channels and nearshore circulation: Experiments. In *Proceedings Coastal Dynamics*, pages 594–603.

Haller, M., Dalrymple, R., and Svendsen, I. A. (1997b). Experimental modeling of a rip current system. In *Proceedings of the Third International Symposium on Ocean Wave Measurement and Analysis*.

Haller, M. C., Dalrymple, R. A., and Svendsen, I. A. (2000). Experiments on rip currents and nearshore circulation: Data report. Technical Report CACR-00-04, Center for Applied Coastal Research, Univ. of Delaware.

Hamm, L. (1992). Directional nearshore wave propagation over a rip channel: an experiment. In *Proc. 23rd Coastal Engineering Conference*, volume 1, pages 226–239, Venice. ASCE.

Hansen, J. and Svendsen, I. A. (1986). Experimental investigation of the wave and current motion over a longshore bar. In *Proc. 20th Coastal Engineering Conference*, pages 1166–1179.

Hansen, J. B. (1990). Periodic waves in the surf zone: analysis of experimental data. *Coastal Engng.*, **14**, 19–41.

Hino, M. (1974). Theory and formation of rip-current and cuspidal coast. In *Proc. 12th Coastal Engineering Conference*, pages 901–919.

Hite, M. P. (1925). The "Undertow". *Science*, **62**, 31–33.

Huntley, D. A. and Short, A. D. (1992). On the spacing between observed rip currents. *Coastal Engineering*, **17**, 211–225.

Huntley, D. A., Hendry, M. D., Haines, J., and Greenridge, B. (1988). Waves and rip currents on a Caribbean pocket beach, jamaica. *Journal of Coastal Research*, **4**, 69–79.

Jones, W. C. (1925). The undertow myth. *Science*, **61**, 444.

Kirby, J. and Dalrymple, R. (1994). Combined refraction/diffraction model ref/dif 1, version 2.5. Technical Report CACR-94-22, Center for Applied Coastal Research, Univ. of Delaware.

Kirby, J. T. and Dalrymple, R. A. (1983). A parabolic equation for the combined refraction-diffraction of stokes waves by mildly varying topography. *Journal of Fluid Mechanics*, **136**, 453–466.

Kobayashi, T., Kano, M., and Ishihara, T. (1984). Prediction of turbulent-flow in two-dimensional channel with turbulence promoters. 2. Numerical prediction by large eddy simulation. *Bulletin of JSME*, **27**, 1893–1898.

Kobayashi, T., Kano, M., and Ishihara, T. (1985). Prediction of turbulent-flow in two-dimensional channel with turbulence promoters. 3. Improvements of large eddy simulation and formation of streaklines. *Bulletin of JSME*, **28**, 2948–2953.

LeBlond, P. H. and Tang, C. L. (1974). On energy coupling between waves and rip currents. *J. Geophys. Res.*, **79**(6), 811–816.

Lesieur, M. and Métais, O. (1996). New trends in large-eddy simulations of turbulence. *Annu. Rev. Fluid Mech.*, **28**, 45–82.

Longuet-Higgins, M. S. (1956). The mechanics of the boundary-layer near the bottom in a progressive wave. In *Proc. 6th Coastal Engineering Conference*, volume 1, pages 184–193, Miami. ASCE.

Longuet-Higgins, M. S. (1970a). Longshore currents generated by obliquely incident sea waves,1. *J. Geophys. Res.*, **75**, 6778–6789.

Longuet-Higgins, M. S. (1970b). Longshore currents generated by obliquely incident sea waves, 2. *J. Geophys. Res.*, **75**, 6790–6801.

Longuet-Higgins, M. S. and Stewart, R. W. (1962). Radiation stress and mass transport in gravity waves with applications to 'surf-beats'. *Journal of Fluid Mechanics*, **8**, 565–583.

Longuet-Higgins, M. S. and Stewart, R. W. (1964). Radiation stress in water waves, a physical discussion with application. *Deep Sea Research*, **11**, 529–563.

Madsen, P. A., Rugbjerg, M., and Warren, I. (1988). Subgrid modelling in depth integrated flows. In *Proc. 21st Coastal Engineering Conference*, pages 505–511.

Madsen, P. A., Sørensen, O. R., and Schäffer, H. A. (1997a). Surf zone dynamics simulated by a Boussinesq type model. Part I. Model description and cross-shore motion of regular waves. *Coastal Engineering*, **32**, 255–287.

Madsen, P. A., Sørensen, O. R., and Schäffer, H. A. (1997b). Surf zone dynamics simulated by a Boussinesq type model. Part II: surf beat and swash oscillations for wave groups and irregular waves. *Coastal Engineering*, **32**, 289–319.

McKenzie, P. (1958). Rip current systems. *Journal of Geology*, **66**, 103–113.

Mei, C. (1983). *The applied dynamics of ocean surface waves*. John Wiley and Sons.

Miller, C. and Barcilon, A. (1978). Hydrodynamic instability in the surf zone as a mechanism for the formation of horizontal gyres. *J. Geophys. Res.*, **83**(c8), 4107–4116.

Nadaoka, K. and Kondoh, T. (1982). Laboratory measurements of velocity field structure in the surfzone by LDV. *Coastal Engineering in Japan*, **25**, 125–145.

Noda, E. K. (1974). Wave-induced nearshore circulation. *J. Geophys. Res.*, **79**, 4097–4106.

Okaysu, A., Shibayama, T., and Nimura, N. (1986). Velocity field under plunging waves. In *Proc. 20th Coastal Engineering Conference*, pages 660–674, Taipei.

Okaysu, A., Shibayama, T., and Nimura, N. (1988). Vertical variation of undertow in the surf zone. In *Proc. 21th Coastal Engineering Conference*, pages 478–491, Málaga.

Özkan-Haller, H. T. and Kirby, J. T. (1999). Nonlinear evolution of shear instabilities of the longshore current: A comparison of observations and computations. *J. Geophys. Res.*, **104**, 25,953–25,984.

Péchon, P., Rivero, F., Johnson, H., Chesher, T., O'Conner, B., Tanguy, J.-M., Karambas, T., Mory, M., and Hamm, L. (1997). Intercomparison of wave-driven current models. *Coastal Engineering*, **31**, 199–215.

Peregrine, D. H. (1998). Large-scale vorticity generation by breakers in shallow and deep water. In *IUTAM Symposium on Three-dimensional air-sea interactions*, Nice.

Peregrine, D. H. (1999). Surf zone currents. *Theoretical and Computational Fluid Dynamics*, **10**, 295–309.

Peregrine, D. H. and Bokhove, O. (1998). Vorticity and surf zone currents. In *Proc. 26th Coastal Engineering Conference*, Copenhagen. ASCE.

Phillips, O. M. (1977). *The dynamics of the upper ocean*. Cambridge University Press.

Putrevu, U. and Svendsen, I. A. (1991). Wave induced nearshore currents: a study of the forcing, mixing and stability characteristics. (Ph. D. Dissertation), Res. Report CACR-91-11, Center for Applied Coastal Research, Univ. of Delaware.

Putrevu, U. and Svendsen, I. A. (1993). Vertical structure of undertow outside the surf-zone. *J. Geophys. Res.*, **98**, 707–716.

Putrevu, U. and Svendsen, I. A. (1999). Three-dimensional dispersion of momentum in wave-induced nearshore currents. *European Journal of Mechanics-B/Fluids*, pages 409–427.

Quirke, T. T. (1925). The undertow. *Science*, **61**, 468.

Rattanapitikon, W. and Shibayama, T. (2000). Simple model for undertow profile. *Coastal Engineering Journal*, **32**, 1–30.

Rogallo, R. S. and Moin, P. (1984). Numerical simulation of turbulent flows. *Annu. Rev. Fluid Mech.*, **16**, 99–137.

Sanchez-Arcilla, A., Collado, F., Lemos, M., and Rivero, F. (1990). Another quasi-3D model for surf zone flows. In *Proc. 22nd Coastal Engineering Conference*, pages 316–329.

Sanchez-Arcilla, A., Collado, F., and Rodriguez, A. (1992). Vertically varying velocity field in Q-3D nearshore circulation. In *Proc. 23nd Coastal Engineering Conference*, pages 2811–2824.

Sancho, F. and Svendsen, I. A. (1997). Unsteady nearshore currents on longshore varying topographies. (Ph. D. Dissertation), Res. Report CACR-97-10, Center for Applied Coastal Research, Univ. of Delaware.

Sancho, F., Svendsen, I. A., Van Dongeren, A., and Putrevu, U. (1995). Longshore nonuniformities of nearshore currents. In *Proceedings Coastal Dynamics*, pages 425–436.

Sancho, F., Svendsen, I. A., and Putrevu, U. (1999). On the effect of weak longshore topographic variations. Submitted to JGR.

Sasaki, M. (1985). Velocity profiles in nearshore circulation current. *Coastal Engineering in Japan*, **28**, 125–136.

Scotti, A., Meneveau, C., and Lilly, D. (1993). Generalized Smagorinsky model for anisotropic grids. *Phys Fluids A*, **5**, 2306–2309.

Shepard, F. P. (1936). Undertow, rip tide or rip current. *Science*, **84**, 181–182.

Shepard, F. P. and Inman, D. L. (1950). Nearshore water circulation related to bottom topography and wave refraction. *Transactions, American Geophysical Union*, **31**, 196–212.

Shepard, F. P. and Inman, D. L. (1951). Nearshore circulation. In *Proc. 1st Coastal Engineering Conference*, pages 50–59.

Shepard, F. P. and LaFond, E. C. (1939). Undertow. *Science*, **89**, 1–2.

Shepard, F. P., Emery, K. O., and La Fond, E. (1941). Rip currents: a process of geological importance. *Journal of Geology*, **49**, 337–369.

Short, A. D. (1985). Rip-current type, spacing and persistence, Narrabeen Beach, Australia. *Marine Geology*, **65**, 47–71.

Slinn, D. N., Allen, J. S., and Holman, R. A. (2000). Alongshore currents over variable beach topography. *J. Geophys. Res.*, **105**, 16971–16998.

Smagorinsky, J. (1963). General circulation experiments with the primitive equations I. The basic experiment. *Mon. Weath. Rev.*, **91**, 99.

Smith, J. A. and Largier, J. L. (1995). Observations of nearshore circulation: Rip currents. *J. Geophys. Res.*, **100**, 10967–10975.

Sonu, C. J. (1972). Field observations of nearshore circulation and meandering currents. *J. Geophys. Res.*, **77**, 3232–3247.

Sørensen, O. R., Schäffer, H. A., Madsen, P. A., and Deigaard, R. (1994). Wave breaking and induced nearshore circulations. In *Proc. 24th Coastal Engineering Conference*, pages 2583–2594.

Sørensen, O. R., Schäffer, H. A., and Madsen, P. A. (1998). Surf zone dynamics simulated by a Boussinesq type model. Part III. Wave-induced horizontal nearshore circulation. *Coastal Engineering*, **33**, 155–176.

Svendsen, I. A. (1984a). Wave heights and set-up in a surf zone. *Coastal Engineering*, **8**, 303–329.

Svendsen, I. A. (1984b). Mass flux and undertow in a surf zone. *Coastal Engineering*, **8**, 347–365.

Svendsen, I. A. (1987). Analysis of surf zone turbulence. *J. Geophys. Res.*, **92**(C5), 5115–5124.

Svendsen, I. A. and Haas, K. A. (1999). Interaction of undertow and rip currents. In *Proc. Vth COPEDEC 99*, volume I, pages 218–229, Cape Town.

Svendsen, I. A. and Hansen, J. B. (1986). The interaction of waves and currents over a longshore bar. In *Proc. 20th Coastal Engineering Conference*, pages 1580–1594.

Svendsen, I. A. and Hansen, J. B. (1988). Cross-shore currents in surf-zone modelling. *Coastal Engineering*, **12**, 23–42.

Svendsen, I. A. and Lorenz, R. S. (1989). Velocities in combined undertow and longshore currents. *Coastal Engineering*, **13**, 55–79.

Svendsen, I. A. and Putrevu, U. (1990). Nearshore circulation with 3-d profiles. In *Proc. 22nd Coastal Engineering Conference*, volume 1, pages 241–254, Delft. ASCE.

Svendsen, I. A. and Putrevu, U. (1994). Nearshore mixing and dispersion. In *Proc. Roy. Soc. Lond. A(445)*, pages 1–16.

Svendsen, I. A. and Putrevu, U. (1996). Surf zone hydrodynamics. In P. L.-F. Liu, editor, *Advances in Coastal and Ocean Engineering*, volume 2, pages 1–78. World Scientific.

Svendsen, I. A., Schäffer, H. A., and Hansen, J. B. (1987). The interaction between the undertow and boundary layer flow on a beach. *J. Geophys. Res.*, **92**, 11845–11856.

Svendsen, I. A., Haas, K. A., and Zhao, Q. (2000). Analysis of rip current systems. In *Proc. 27th Coastal Engineering Conference*, Sydney. ASCE.

Tam, C. K. (1973). Dynamics of rip currents. *J. Geophys. Res.*, **78**(12), 1937–1943.

Tanaka, H. and Wada, A. (1984). Reproduction of nearshore currents by a mathematical model. *Coastal Engineering in Japan*, **27**, 151–163.

Thompson, R. (1979). Coherence significance levels. *Journal of Atmospheric Science*, **36**, 2020–2021.

Thornton, E. B. (1970). Variation of longshore current across the surf zone. In *Proc. 12th Coastal Engineering Conference*, pages 291–308.

Van Dongeren, A., Sancho, F., Svendsen, I. A., and Putrevu, U. (1994). SHORECIRC: A quasi-3D nearshore model. In *Proc. 24th Coastal Engineering Conference*, pages 2741–2754.

Van Dongeren, A. R. and Svendsen, I. A. (1997). Quasi-3D modeling of nearshore hydrodynamics. (Ph. D. Dissertation), Res. Report CACR-97-04, Center for Applied Coastal Research, Univ. of Delaware.

Van Dongeren, A. R. and Svendsen, I. A. (2000). Nonlinear and 3-d effects in leaky infragravity waves. *Coastal Engineering*, **41**(4), 467–496.

Vos, R. G. (1976). Observations on the formation and location of transient rip currents. *Sediment. Geol*, **16**, 15–19.

Wilcox, D. (1998). *Turbulence Modeling for CFD*. DCW Industries Inc.

Wind, H. G. and Vreugdenhil, C. B. (1986). Rip-current generation near structures. *Journal of Fluid Mechanics*, **171**, 459–476.

Wright, L. and Short, A. D. (1984). Morphydynamic variability of surf zones and beaches: A synthesis. *Marine Geology*, **56**, 93–118.

Wright, L. D., Guza, R. T., and Short, A. D. (1982). Dynamics of a high energy dissipative surf zone. *Journal of Marine Geology*, **45**, 41–62.

Wu, C.-S. and Liu, P. L.-F. (1985). Finite element modeling of nonlinear coastal currents. *J. of Waterway, Port, Coastal and Ocean Engng.*, **111**, 417–432.

You, Z.-J. (1994). A simple model for current velocity profiles in combined wave-current flows. *Coastal Engng.*, **23**, 289–304.

Zyserman, J., Fredsøe, J., and Deigaard, R. (1990). Prediction of the dimensions of a rip current system on a coast with bars. In *Proc. 22th Coastal Engineering Conference*, pages 959–972.